

Light-Induced Cytochrome *c* Redox Mediated Cell Killing

Jordan Cameron Potts, MSci

School of Pharmacy

Thesis Submitted to the University of Nottingham for the degree of Doctor of Philosophy

May 2023

Acknowledgements

First off, I'd like to express sincere thanks to my supervisors, Prof Lluïsa Pérez-García, Prof David Amabilino, and Dr Frankie Rawson. Their consistent support and guidance during my time at the University of Nottingham have been invaluable.

Special appreciation goes to Dr Akhil Jain, whose mentorship has greatly influenced the work presented in this thesis. I'm truly thankful to have had the opportunity to learn from him.

I'm also grateful for the collaboration with the Rawson and Pérez-García group members. Working alongside you all has significantly enriched my learning experience.

To my parents, thank you for your unwavering support throughout my nine years in university. I cannot emphasize enough that this achievement wouldn't have been possible without your sacrifices.

A massive thank you also goes to my girlfriend, Olivia, for standing by me throughout this PhD journey. Your patience and encouragement, especially during those times when I was completely immersed in my work, means more than I can express.

Finally, I dedicate this work to three family members whose memory has been a source of strength during this journey. Firstly, to my Grandad Potts, whose battle with cancer was the reason I applied to this PhD project. Secondly, to Grandad Dyson, who was always keen to hear about my progress. And lastly, to Uncle Mark, whose unwavering support and encouragement ensured my university experience was enjoyable and worthwhile.

Table of Contents

Table of Contents 3
Table of Figures 6
Table of Tables 16
Table of Equations 17
Abbreviations 17
Mathematical Abbreviations 20
Abstract 22
1. Introduction 23
1.1. Aims and Rationale 23
1.2. Introduction 24
1.2.1. Cancer 24
1.2.2. Cancer therapies 25
1.2.3. Gold nanoparticles 29
1.2.4. Cytochrome *c* 39
1.2.5. Fluorescence 44
1.2.6. Gold Nanoparticle Conjugation Strategies for Cytochrome *c* and Zn Porph 47
1.2.7. Electrochemistry 54
1.2.8. Cyclic Voltammetry 54
1.2.9. Differential Pulse Voltammetry 56
1.2.10. Electrochemical applications of Cytochrome *c* 57
1.2.11. Cytochrome *c* in biosensing 58
1.2.12. Cytochrome *c* in biofuels 59
1.3. Objectives 60
2. Synthesis and Characterisation of AuNPs Multifunctionalised with Cyt *c* and Porphyrins 62
2.1. Aims and Objectives 62
2.2. Abstract 62
2.3. Introduction 63
2.4. Methods 65
2.4.1. Materials 65
2.4.2. Synthesis of 20 nm citrate capped AuNPs (cit-AuNPs) 66
2.4.3. Synthesis of 50 nm citrate capped AuNPs (cit-AuNPs) 66
2.4.4. Synthesis of 100 nm citrate capped AuNPs (cit-AuNPs) 66
2.4.5. Functionalisation of 20, 50 and 100 nm cit-AuNPs with PEG 67

2.4.6. Functionalisation of 20, 50 and 100 nm cit-AuNPs with PEG, Cyt *c* and Zn Porph 67
2.4.7. Deconvolution modelling of Cyt *c* and Zn Porph conjugated to AuNPs 68
2.4.8. Functionalisation of 20, 50 and 100 nm cit-AuNPs with MUA 68
2.4.9. Functionalisation of 20, 50 and 100 nm cit-AuNPs with MUA, Cyt *c* and Zn Porph Covalently 68
2.4.10. Functionalisation of 20, 50 and 100 nm cit-AuNPs with MUA, Cyt *c* and Zn Porph Electrostatically 69
2.4.11. LN-MIE-Gans modelling of cit-AuNPs and multi-functionalized AuNPs. 69
2.4.12. Instruments 70
2.5. Results and Discussion 70
2.5.1. Characterisation of Cyt *c* and Zn Porph 70
2.5.2. Synthesis and Characterisation of 20 nm AuNPs with thiol-PEG-carboxyl, Cyt *c* and Zn Porph 71
2.5.3. X-Ray Photoelectron Spectroscopy 80
2.5.4. Characterisation of 20 nm AuNPs with MUA, Cyt *c* and Zn Porphyrin 85
2.5.5. Synthesis, Functionalisation and Characterisation of 50 and 100 nm AuNPs 89
2.6. Conclusion 97
3. Structural and Electrochemical Analysis of Gold Nanoparticles Functionalised with Cytochrome *c* and Zinc Porphyrin 98
3.1. Aims and Objectives 98
3.2. Abstract 98
3.3. Introduction 99
3.3.1. Chapter contents 99
3.3.2. Circular Dichroism 102
3.3.3. ToF-SIMS 103
3.4. Methods: 104
3.4.1. AuNPs Functionalised with Cyt *c* and Zn Porph 104
3.4.2. ToF-SIMS 104
3.4.3. Circular Dichroism 104
3.4.4. Electrochemical Methods 105
3.4.5. Cyclic Voltammetry: 107
3.4.6. Cyclic Voltammetry Analysis 108
3.4.7. Differential Pulse Voltammetry 108
3.4.8. Differential Pulse Voltammetry Analysis: 109
3.4.9. Statistical analysis 110
3.5. Results 110
3.5.1. Circular Dichroism 110
3.5.2. Cyt *c* Ox and Red at different concentrations 110
3.5.3. Investigation on the Structural Change of Cyt *c* after conjugation to AuNPs of different sizes using different ligands and conjugation methods 114
3.6. ToF-SIMS 118

3.7. Cyclic Voltammetry 122
3.8. Differential Pulse Voltammetry 124
3.8.1. Scan rate studies 125
3.8.2. Differential Pulse Voltammetry on AuNPs functionalised with Cyt *c* and Zn Porph 131
3.8.3. Calculating the heterogeneous rate constant for Zn Porph conjugated to multifunctionalised AuNPs 135
3.9. Conclusion 138
4. Biological Studies on MCF-7 Cells after Incubation of Gold Nanoparticles Functionalised with Cyt C and Zinc Porphyrin 141
4.1. Aims and Objectives 141
4.2. Abstract 141
4.3. Introduction 142
4.3.1. Cell Culture Studies with MCF-7 142
4.3.2. Fluorescence microscopy 144
4.3.3. Confocal microscopy 144
4.3.4. Inductively Coupled Plasma Mass Spectrometry 145
4.4. Methods 146
4.4.1. Cell Culture 146
4.4.2. Cellular Uptake Analysis 146
4.4.3. Irradiation of Cells with a 50 mW Monochromatic Green Laser 148
4.4.4. Irradiation of cells with Lumidox® II 96-Position LED Array using Amber Light 148
4.4.5. Presto Blue Metabolic Activity Assay 149
4.4.6. Peroxidase Activity with and without Irradiation with Lumidox® II 96-Position LED Array using Amber Light 149
4.4.7. Differential Nuclear Staining Assay 150
4.4.8. *In Vitro* Singlet Oxygen Detection 150
4.4.9. Statistical analysis 151
4.5. Results 151
4.5.1. Gold Nanoparticle Uptake 151
4.5.2. ICP-MS 152
4.5.3. Confocal microscopy images of Multifunctionalised AuNPs uptake into cells 160
4.6. Catalytic Activity 163
4.6.1. Peroxidase Activity 163
4.7. Apoptotic Ability of Gold Nanoparticles Functionalised with Cyt C and Zinc Porphyrin 168
4.7.1. Irradiated with Monochromatic Green Light 170
4.7.2. Irradiated with Monochromatic Amber Light 173
4.7.3. Optimising the Power of a Lumidox® II 96-position Amber LED array for use in irradiating MCF-7 cells 175

4.8. Effects on AuNPs multifunctionalised Cyt *c* Oxidised and Zn Porph with the AuNP concentration normalised 183
4.8.1. Live/Dead Determination for MCF-7 cells containing Multifucntionalised AuNPs with and without 60 Minutes of Amber Light Treatment 189
4.8.2. Singlet Oxygen Detection of MCF-7 Cells Inoculated with Multifunctionalised AuNPs and Controls with and without Treatment with an Amber LED Array..... 197
4.9. Conclusion 202
5. Conclusion and Future Work 204
5.1. Introduction 204
5.2. Main Findings 204
5.2.1. Chapter 2 - Synthesis and Characterisation of AuNPs Multifunctionalised with Cyt *c* and Porphyrins..... 204
5.2.2. Chapter 3 - Structural and Electrochemical Analysis of Gold Nanoparticles Functionalised with Cytochrome *c* and Zinc Porphyrin 205
5.2.3. Chapter 4 - Biological Studies on MCF-7 Cells after Incubation of Gold Nanoparticles Functionalised with Cyt C and Zinc Porphyrin 206
5.3. Future Work 207
5.4. Conclusion 209
6. Supporting Information 211
7. References 232

Table of Figures

Figure 1. Schematic representation of the proposed AuNP cancer treatment in this work. 24
Figure 2. UV-Vis absorption spectrum of 20 nm cit-AuNPs with an SPR peak at 521 nm..... 34
Figure 3. Schematic representation of the oscillation of electrons across AuNPs in the electromagnetic field of light. Adapted from (Yeh et al., 2012). 35

Figure 4: Schematic representation Turkevich method of AuNPs synthesis, adapted from (Imbraguglio et al., 2013)..... 37
Figure 5. Overview of extrinsic and intrinsic apoptosis pathways. The extrinsic pathway (left side of the figure) begins with an extracellular death ligand binding to a death receptor, forming the DISC and activating caspase-8 or -10. The intrinsic pathway (right side of the figure) is triggered by signals causing outer mitochondrial membrane permeabilisation, releasing proteins such as Cyt *c*, which forms the apoptosome with APAF1 and activates caspase 9. Both pathways converge at the BCL2 family protein BID, with activated caspase-8 promoting BAX and BAK downstream activation (Ow et al., 2008)..... 41
Figure 6. Jablonski diagram showing the mechanism for fluorescence and phosphorescence (Eck, 2014). Bold lines indicate electron states, thin lines represent vibration states between the electron states..... 45
Figure 7. A reactivated biointerface with light or pH double-responsive is manufactured using photocontrolled reversible inclusion and exclusion reactions between the photoresponsive monolayers containing azobenzene and the pH-responsive poly(acrylic acid) polymer that is grafted with cyclodextrin. The double-controlled and reactivated biointerface can be used to reversibly immobilise the redox protein–Cyt c- triggered by dual external stimuli light and pH (Wan et al., 2009). 51
Figure 8: Schematic representation of carbodiimide cross-coupling of Cyt *c* and Zn Porph to AuNPs using NHS as a stabilising agent..... 53
Figure 9. Example cyclic voltammogram demonstrating the difference between the US and IUPAC Convention (Elgrishi et al., 2018). 55
Figure 10. Representation of potential wave form for DPV (Ribeiro et al., 2017). 57
Figure 11. UV-Vis absorption spectra of Cyt *c* Ox (blue line), Cyt *c* Red (red line) and Zn Porph (green line). The inset is a magnified area between 450-650 nm..... 71
Figure 12. Schematic representation of the functionalisation method for AuNP-PEG-Cyt *c*/Zn Porph Cov. 72
Figure 13. Schematic representation of cit-AuNPs as synthesised and when functionalized with thiol-PEG-carboxylic, Cytochrome *c* (Cyt *c*) and Zinc(II) 5-(4-

aminophenyl)-10,15,20-tris-(4-sulfonatophenyl)porphyrin (Zn Porph) (A). Structure of Zn Porph (B). 3D structure crystal of Cyt *c* made from PDB(1 HRC) using Chimera (version 1.16) with blue representing amino acid residues and red representing the porphyrin Heme ring (C). 73
Figure 14. The physicochemical characterisation of AuNPs functionalized with Cyt *c* and Zn Porph was performed using DLS (A), Zeta Potential measurements (B), TEM image and cumulative frequency graph of 20 nm AuNP-PEG-Cyt *C* /Zn Porph produced from analysing 452 AuNPs (C) and UV-visible absorption spectroscopy (D). 76
Figure 15. The Soret band in the Ultraviolet-Visible absorption spectra of AuNP-PEG- Cyt *c* /Zn Porph was deconvoluted to identify 2 fitted components in AuNP-PEG-Cyt *c*/Zn-Porph samples (A) and 3 fitted components in AuNP-PEG-Cyt *c*/Zn-Porph-S2 (B). The peaks were deconvoluted using CASAXPS software. The region of interest was then selected using the regions tool, and then the background setting was changed to 'linear' as it closely represents how the spectra would look without the conjugated molecules. The convoluted peaks in the spectra were then found using the components tab, by adding the components that were thought to be in the region. The components were then fitted to the spectra using the Levenberg-Marquardt algorithm. Figure used in Analytical Chemistry publication (Potts et al., 2023). 80
Figure 16. XPS spectrum in the region of Au4f in Cyt *c* (A) Zn Porph (B) cit-AuNP (C) AuNPs-PEG-Cyt *c* (D), AuNPs-PEG-Zn Porph (E) and AuNPs-PEG-Cyt *c*/Zn Porph (F). 82
Figure 17. XPS spectrum in the region of S2p in Cyt *c* (A) Zn Porph (B) cit-AuNP (C) AuNPs-PEG-Cyt *c* (D), AuNPs-PEG-Zn Porph (E) and AuNPs-PEG-Cyt *c*/Zn Porph (F). 83
Figure 18. XPS spectrum in the region of $Fe2p_{3/2}$ for Cyt *c* (A) AuNP-PEG-Cyt *c* (B) and AuNP-PEG-Cyt *c*/Zn Porph (C). No peaks are visible in any of the XPS spectra for $Fe2p_{3/2}$. 83
Figure 19. XPS spectrum in the region of $Zn2p_{3/2}$ (peak on the right) and $Zn2p_{1/2}$ for Zn Porph (A) AuNP-PEG-Zn Porph (B) and AuNP-PEG-Cyt *c*/Zn Porph (C). 84

Figure 20. Schematic representation of the functionalisation method for AuNP-MUA-Cyt *c*/Zn Porph Cov (A) and AuNP-MUA-Cyt *c*/Zn Porph Electro. 86
Figure 21. Physicochemical characterisation of 20 nm AuNPs functionalised with MUA, Cyt *c* and Zn Porph using DLS (A), zeta potential (B) and UV-Vis absorption spectroscopy (C)..... 88
Figure 22. TEM images of cit-AuNP (A) and AuNP-MUA-Cyt *c*/Zn Porph Cov (B). Images contain cumulative frequency distributions in an insert made of 227 and 40 AuNPs, respectively. 89
Figure 23. The physiochemical characterisation of 50 and 100 nm cit-AuNPs using UV-Vis absorption spectroscopy (A), DLS (B) and Zeta Potential (C). 92
Figure 24. The physiochemical characterisation of multifunctionalised AuNPs using UV-Vis absorption spectroscopy for 50 nm AuNPS (A), 100 nm AuNPs (B) and using DLS for 50 nm AuNPs (C) and 100 nm AuNPs (D). TEM images for 50 nm AuNP-PEG-Cyt *c*/Zn Porph (E) and 100 nm AuNP-PEG-Cyt *c*/Zn Porph (F) with a cumulative frequency distribution included in the insert made using 163, 50 nm AuNPs and 128, AuNPs 100 nm AuNPs. 95
Figure 25. The use of LNMIE-Gans model fitting to 20 nm cit-AuNPs (A) to predict their size (B). 96
Figure 26. Schematic of the three-electrode system used in this work where the electrochemistry of multifunctionalised AuNPs in a PBS solution was measured using an ITO working electrode, Ag/AgCl reference electrode and a platinum wire counter electrode which are connected to a potentiostat and a PC so the sample can be analysed. 106
Figure 27. Comparison between the CD of 20 and 1 μM Cyt c. The CD spectra of 20 μM Cyt c Ox and Red in the Far-UV region (A), near-UV region (B) and Soret region (C). The CD spectra of 1 μM Cyt c Ox and Red in the Far-UV region (D), near-UV region (E) and Soret region (F). 113
Figure 28. Comparison between the CD of Cyt c conjugated to AuNPs using HS-PEG-COOH covalently (with EDC/NHS), MUA covalently (with EDC/NHS) and MUA electrostatically. 20, 50 and 100 AuNP-PEG-Cyt c in the Far-UV region (A), near-UV region (B) and Soret region (C). 20, 50 and 100 AuNP-MUA-Cyt c Cov

in the Far-UV region (D), near-UV region (E) and Soret region (F). 20, 50 and 100 AuNP-MUA-Cyt c Electro in the Far-UV region (G), near-UV region (H) and Soret region (I). 116
Figure 29. ToF-SIMS peak intensity ratio for cysteine/glutamic acid + leucine for Cyt *c* free in solution and bound to 20 nm AuNPs using different ligands and conjugation strategies..... 120
Figure 30. The orientation of Cyt *c* when attached to AuNPs using PEG and MUA ligands covalently or electrostatically was proposed through the use of ToF-SIMS amino acid intensity ratio and literature (Jain et al., 2021). Both covalent and electrostatic conjugation methods identified the binding of AuNPs to the Lys 79 residue of Cyt *c*, with Lys 27 and Lys 25 being potential alternatives (A). The proposed orientation for Cyt *c* bound to AuNPs at the Lys 88 residue was determined when the R value differed by ~50% or greater compared to 100 nm AuNP-MUA-Cyt *c* Electro (B). A 3D model of Cyt *c* was created using the crystal structure of horse heart Cyt *c* from the PDB (1HRC) in Chimera (version 1.15) to label the heme ring and amino acid residues. In the structure of Cyt *c*, the heme/porphyrin ring was red, the Iron (Fe) at the centre of the heme\porphyrin ring was yellow, Cys was black, Glu was magenta, Leu was blue, and Lys was green. 121
Figure 31. Cyclic voltammagrams's at 0.1 $V.s^{-1}$ of Cyt *c* Ox 10 μM free in solution and 20 nm AuNP-PEG-Cyt *c* Ox. Cyclic voltammagrams's run from -0.2 to 0.4 V and PBS was used as the electrolyte. 123
Figure 32. Cyclic voltammagrams's at 0.1 $V.s^{-1}$ of Zn Porph and 20 nm AuNP-PEG-Cyt *c*/Zn Porph. Cyclic voltammagrams's run from -0.2 to 1.2 V and PBS was used as the electrolyte. 124
Figure 33. How DPV oxidation and reduction peaks were analysed in OriginPro (2018). The DPV was first plotted in OriginPro (A), the peak analyser was then selected to make a 4^{th} order polynomial background to fit the DPV trace using 8 nodes with a spline interpolation method selected (B). 128
Figure 34. DPV of all control used in functionalised AuNPs measure between the potentials of -0.2 to 1.2 V using a scan rate of 50 mV/s. 129

Figure 35. Background corrected typical DPV spectra for the oxidation and reduction peaks for Cyt *c* and Zn Porph conjugated to 20 , 50 and 100 nm AuNPs with thiol-PEG-carboxyl covalently or MUA covalently or electrostatically. All DPV displayed were obtained at a scan of 50 mV/s. 131
Figure 36. Heterogeneous rate constant of Cyt *c* oxidised conjugated to multifunctionalised AuNPs with Zn Porph. AuNPs of 20, 50 and 100 nm were functionalised with different ligands and conjugations methods to determine the effects the components have on the heterogenous rate constant of Cyt *c* when compared to Cyt *c* oxidised free in solution..... 135
Figure 37. The heterogeneous rate constant was determined from the first redox peak of Zn Porph, located at 0.4-0.7 V free in solution and conjugated to multifunctionalised AuNPs with Cyt *c* Ox. AuNPs of 20, 50 and 100 nm were functionalised with different ligands and conjugations methods to determine the effects the components have on the heterogenous rate constant of Zn Porph when compared to Zn Porph free in solution. The statistical analysis was performed using a one-way ANOVA with a post-Dunnett test. Determined by DPV..... 137
Figure 38. Growth rate of MCF-7 cells with a doubling time of 36.27 hours and an R^2 of 0.98. Experiments repeated in duplicate, error bars are N=2. 152
Figure 39. The mass of Au in cells or recovered in the supernatant via multifunctionalised AuNPs conjugated with Cyt *c* Ox and Zn Porph using thiol-PEG-carboxyl covalently (A), MUA covalently (B) and MUA electrostatically (C) determined with ICP-MS 155
Figure 40. The number of AuNPs per MCF-7 cell was calculated for multifunctionalised AuNPs conjugated with Cyt c Ox and Zn Porph or Cyt c and Porph using HS-PEG-COOH covalently (A), MUA covalently (B) and MUA electrostatically (C). 159
Figure 41. Confocal microscopy images of MCF-7 cells containing 20 nm AuNP-PEG-Cyt *c*/Zn Porph at 40x magnification (A), 20 nm AuNP-MUA-Cyt *c*/Zn Porph Cov at 20x magnification (B) and 20 nm AuNP-MUA-Cyt *c*/Zn Porph Electro at 20x magnification (C). 161

Figure 42. Confocal microscopy images of MCF-7 cells containing 50 nm AuNP-PEG-Cyt *c*/Zn Porph (A), 50 nm AuNP-MUA-Cyt *c*/Zn Porph Cov (B) and 50 AuNP-MUA-Cyt *c*/Zn Porph Electro (C). All images were acquired at 20x magnification..... 162
Figure 43. Confocal microscopy images of MCF-7 cells containing 100 nm AuNP-PEG-Cyt *c*/Zn Porph (A), 100 nm AuNP-MUA-Cyt *c*/Zn Porph Cov (B) and 100 nm AuNP-MUA-Cyt *c*/Zn Porph Electro (C). All images were acquired at 20x magnification..... 163
Figure 44. Peroxidase activity of 20, 50 and 100 nm AuNPs functionalised with Cyt *c* and Zn Porph (A), AuNP controls and unconjugated molecule controls (B) and PBS, Guaiacol and H_2O_2 controls (C) with no light treatment. Experiment was performed in triplicate and error bars displayed are the standard deviation of the results. P < 0.0005=*** and P < 0.00005=**** vs 20 nm AuNP-PEG-Cyt *c*/Zn Porph for Figure 44A. 165
Figure 45. Peroxidase activity of 20, 50 and 100 nm AuNPs functionalised with Cyt *c* and Zn Porph (A), AuNP controls and unconjugated molecule controls (B) and PBS, Guaiacol and H_2O_2 controls (C) after 60 minutes of treatment with an amber LED array. Experiment was performed in triplicate and error bars displayed are the standard deviation of the results. P<0.00005=**** vs 20 nm AuNP-PEG-Cyt *c*/Zn Porph for Figure 45A. 167
Figure 46. Metabolic activity assessed using a PrestoBlue assay on AuNP controls of different size and concentration (A) and Cyt *c* and Zn Porph controls at different concentrations (B) have on the fluorescence intensity determined by a Presto Blue assay with no cells. Two biological repeats were conducted in triplicate and the error bars are the result of the standard deviation. 169
Figure 47. Effects that AuNPs multifunctionalised with Cyt *c* and Zn Porph or Porph at diameters of 20 nm (A), 50 nm (B) and 100 nm have on the fluorescence intensity determined by a Presto Blue assay with no cells..... 170
Figure 48. UV-Visible absorption spectrum of Zn Porph at 5 μM. Insert shows the Q-bands located between 500 nm to 650 nm and are the region of interest for excitation in this work. 171

Figure 49. Functionalised AuNPs and controls added to MCF-7 cells and irradiated with 50 mW green laser (530 nm) for 30 minutes (A) and temperatures after 30 minutes (B). P<0.005=** P<0.00005=**** 172
Figure 50. Presto Blue assay of 20 nm AuNP-PEG-Cyt c/Zn Porph at different concentrations in MCF-7 cells irradiated by 50 mW green laser (532 nm) for 30 minutes. 173
Figure 51. Lumidox® II 96-position LED array with custom fitted plate to accurately fit a 96 well plate (A). Wavelengths emitted from the different LEDs used in Lumidox® II 96-position LED array (B). 175
Figure 52. Metabolic activity of MCF-7 cells after 30 minutes treatment of monochromatic Amber light from Lumidox® II 96-position Amber LED array at different power levels. No treatment (A), at 55 mW (B), 80 mW (C), 105 mW (D) and 130 mW (E). Key corresponds to fluorescence intensity in RFU. 176
Figure 53. The temperature of the room (A), the array (B) and the plate (C) before and after the treatment of monochromatic Amber light from Lumidox® II 96-position Amber LED array at different power levels. 177
Figure 54. Metabolic activity of MCF-7 cells 24 hours after addition of main samples and controls with 30 min treatment of monochromatic Amber light from Lumidox® II 96-position Amber LED array at different power levels. 30mW (A), 55mW (B), 80mW (C), 105mW (D) and 130mW (E). P<0.05=* P<0.005=** P<0.0005=*** P<0.00005=**** 178
Figure 55. Metabolic activity of MCF-7 cells 24 hours after addition of main samples (Row 1-3) and controls (Row 10-12 and Row 7-12 in column G) with 30 min treatment of monochromatic Amber light from Lumidox® II 96-position Amber LED array at different power levels. 30mW (A), 55mW (B), 80mW (C), 105mW (D) and 130mW (E). Key corresponds to fluorescence intensity in RFU. 180
Figure 56. Metabolic activity of MCF-7 cells 24 hours after addition of 20 nm AuNP controls and unconjugated molecule controls after treatment with monochromatic Amber light from Lumidox® II 96-position Amber LED array at 55 mW for 60 minutes. No Treatment (A) and 60 minutes (B). AuNP and

conjugated molecule controls were also included. P<0.05=* P<0.005=** P<0.0005=*** P<0.00005=**** 181
Figure 57. Metabolic activity of MCF-7 cells 24 hours after addition of 50 nm AuNP controls and unconjugated molecule controls after treatment with monochromatic Amber light from Lumidox® II 96-position Amber LED array at 55 mW for 60 minutes. No Treatment (A) and 60 minutes (B). AuNP and conjugated molecule controls were also included. P<0.05=* P<0.005=** P<0.0005=*** P<0.00005=**** 182
Figure 58. Metabolic activity of MCF-7 cells 24 hours after addition of 100 nmAuNP controls and unconjugated molecule controls after treatment with monochromatic Amber light from Lumidox® II 96-position Amber LED array at 55 mW for 60 minutes. No Treatment (A) and 60 minutes (B). AuNP and conjugated molecule controls were also included. P<0.05=* P<0.005=** P<0.0005=*** P<0.00005=**** 183
Figure 59. Metabolic activity of 20, 50 and 100 nm AuNPs-PEG-Cyt *c*/Zn Porph Ox covalently normalised for AuNPs at 20 μg/mL after treatment with monochromatic Amber light from Lumidox® II 96-position Amber LED array at 55 mW for different amounts of time. No Treatment (A) and 60 minutes (B). AuNP and unconjugated molecule controls were also included. P<0.05=* P<0.0005=*** 184
Figure 60. Metabolic activity of different sized AuNPs functionalised with MUA, Cyt *c* Ox, Zn Porph and Porph covalently normalised for AuNPs at 20 μg/mL after treatment with monochromatic Amber light from Lumidox® II 96-position Amber LED array at 55 mW for different amounts of time. No Treatment (A) and 60 minutes (B). AuNP and conjugated molecule controls were also included. P<0.05=* 186
Figure 61. Metabolic activity of different sized AuNPs functionalised with MUA, Cyt *c* Ox, Zn Porph and Porph covalently normalised for AuNPs at 20 μg/mL after treatment with monochromatic Amber light from Lumidox® II 96-position Amber LED array at 55 mW for different amounts of time. No Treatment (A) and 60

minutes (B). AuNP and conjugated molecule controls were also included. P<0.00005=**** 188
Figure 62. Live/Dead determination of MCF-7 cells containing AuNP-PEG-Cyt *c*/Zn Porph Ox normalised for AuNPs at 20 μg/mL. Before treatment (A) and after treatment with monochromatic Amber light from Lumidox® II 96-position amber LED array at 55 mW for 60 minutes (B). P<0.05=* P<0.005=** P<0.0005=*** P<0.00005=**** 190
Figure 63. Live/Dead determination of MCF-7 cells containing AuNP-MUA-Cyt *c*/Zn Porph Ox Cov normalised for AuNPs at 20 μg/mL. Before treatment (A) and after treatment with monochromatic amber light from Lumidox® II 96-position amber LED array at 55 mW for 60 minutes (B). P<0.05=* P<0.005=** P<0.0005=*** P<0.00005=**** 192
Figure 64. Live/Dead determination of MCF-7 cells containing AuNP-MUA-Cyt *c*/Zn Porph Ox Electro normalised for AuNPs at 20 μg/mL. Before treatment (A) and after treatment with monochromatic Amber light from Lumidox® II 96-position Amber LED array at 55 mW for 60 minutes (B). P<0.05=* P<0.005=** P<0.0005=*** P<0.00005=**** 194
Figure 65. Percentage of Live cells versus the heterogeneous rate constant for Cyt *c* conjugated to 20, 50 and 100 nm AuNP-PEG-Cyt *c*/Zn Porph Ox, AuNP-MUA-Cyt *c*/Zn Porph Ox Cov and AuNP-MUA-Cyt *c*/Zn Porph Ox Electro. 196
Figure 66: Singlet oxygen detection of MCF-7 cells containing AuNPs multifunctionalised of 20 nm cit-AuNPs (A), 50 nm cit-AuNPs (B), 100 nm cit-AuNPs (C), Cyt *c* 2 μM (D), Zn Porph 2 μM (E), live cells (F), and dead cells (G) normalised for AuNPs at 20 μg/mL after treatment with monochromatic Amber light from Lumidox® II 96-position Amber LED array at 55 mW for 60 minutes. 198
Figure 67: Singlet oxygen detection of MCF-7 cells containing AuNP-PEG-Cyt *c*/Zn Porph Ox normalised for AuNPs at 20 μg/mL after treatment with monochromatic Amber light from Lumidox® II 96-position Amber LED array at 55 mW for 60 minuets. 20 nm AuNP-PEG-Cyt *c*/Zn Porph (A), 50 nm AuNP-PEG-Cyt *c*/Zn Porph (B) and 100 nm AuNP-PEG-Cyt *c*/Zn Porph (C)..... 199

Figure 68. Singlet oxygen detection of MCF-7 cells containing AuNP-MUA-Cyt *c*/Zn Porph Ox Cov normalised for AuNPs at 20 μg/mL before and after treatment with monochromatic Amber light from Lumidox® II 96-position Amber LED array at 55 mW for 60 minuets. Before treatment, 20 nm AuNP-MUA-Cyt *c*/Zn Porph Cov (A), 50 nm AuNP-PEG-Cyt *c*/Zn Porph Cov (B) and 100 nm AuNP-PEG-Cyt *c*/Zn Porph Cov (C). 200
Figure 69. Singlet oxygen detection of MCF-7 cells containing AuNP-MUA-Cyt *c*/Zn Porph Ox Electro normalised for AuNPs at 20 μg/mL before and after treatment with monochromatic Amber light from Lumidox® II 96-position Amber LED array at 55 mW for 60 minutes. 20 nm AuNP-MUA-Cyt *c*/Zn Porph Electro (A), 50 nm AuNP-PEG-Cyt *c*/Zn Porph Electro (B) and 100 nm AuNP-PEG-Cyt *c*/Zn Porph Electro (C). 201

Table of Tables

Table 1. Surface chemical composition of AuNPs and their conjugated molecules with controls obtained by XPS 81
Table 2. The effect of the size of AuNP and ligand used in functionalisation has on the theoretical maximum number of Cyt *c* bound to AuNPs if arranged in a monolyer. 91
Table 3. The DPV peak separation of Cyt *c* Ox, Cyt *c* Red and Zn Porph calculated from Figure 34. 130
Table 4: DPV analysis of Cyt *c* in various oxidation states when bound to AuNPs of different sizes and conjugation mechanisms. The table presents the oxidation peak to reduction peak differences (ΔEp) and the associated heterogeneous rate constants (k^0) for each sample. 133
Table 5: DPV analysis of Zn Porph in various oxidation states when bound to AuNPs of differing sizes and through different conjugation techniques. The table shows the differences in oxidation peak to reduction peak (ΔEp) alongside their corresponding heterogeneous rate constants (k0) for each sample configuration. 136

Table 6. The mass of a single 20, 50 and 100 nm AuNP calculated using Equation 10. 156

Table of Equations

Equation 1. 35
Equation 2. 55
Equation 3. 56
Equation 4. 107
Equation 5. 125
Equation 6. 125
Equation 7. 126
Equation 8. 126
Equation 9. 127
Equation 10. 156

Abbreviations

Abbreviation	Definition
Ag/AgCl	Silver/ Silver Chloride (Electrode)
AgNP	Silver Nanoparticle
AMT	Adsorptive-Mediated Transcytosis
APAF1	Apoptotic Protease-Activating Factor-1
ASL	Auxiliary Stabilising Ligands
AuNP	Gold Nanoparticle
BAK	BCL2-Homologous Antagonist Killer
BAX	BCL2 Associated X Protein

BBB	Blood-Brain Barrier
BCL2	Pro-apoptotic B-cell Lymphoma Protein-2
BID	BH3 Interacting-Domain Death Agonist
CD	Circular Dichroism
CE	Counter Electrode
CNT	Carbon Nanotube
CPP	Cell-penetrating Peptide
CRISPR	Cluster Regularly Interspaced Short Palindromic Repeats
CV	Cyclic Voltammetry
Cys	Cysteine
Cyt *c*	Cytochrome *c*
DISC	Death-Inducing Signalling C Complex
DLS	Dynamic Light Scattering
DNA	Deoxyribose Nucleic Acid
DNS	Differential Nuclear Staining
DPV	Differential Pulse Voltammetry
E	Electrochemical Cell
ECM	Extracellular Matrix
EPR	Enhanced Permeability & Retention
EV	Extracellular Vesicle
FSL	Functionalised Stabilising Ligands
FWHM	Full-Width Half Maximum
Glu	Glutamic Acid
GO	Graphene Oxide
HNP	Hybrid Nanoparticle
ICP-MS	Inductively Coupled Plasma Mass Spectrometry
ING4	Inhibitor of Growth 4
ITO	Indium Tin Oxide

LCP	Left-Handed Circularly Polarised Light
Leu	Leucine
Lys	Lysine
MALDI-ToF	Matrix-Assisted Laser Desorption/ Ionisation Time-of-Flight
MNP	Metal Nanoparticle
MS	Mass Spectrometry
MSN	Mesoporous Silica Nanoparticle
MUA	11-Mercaptoundecanoic acid
MWCNT	Multiwalled Carbon Nanotube
NHE	Normal Hydrogen Electrode
NP	Nanoparticle
Ox	Oxidised
PBS	Phosphate Buffer Saline
PEG	Polyethylene glycol
PDT	Photodynamic Therapy
PI	Propium Iodide
PLA	Polylactic Acid
PLGA	Poly(lactic-co-glycolic acid)
PNP	Polymetric Nanoparticle
PS	Photosensitiser
PTEN	Phosphatase and Tensin Homolog
RCP	Right-Handed Circularly Polarised Light
Red	Reduced
RGO	Reduced Graphene Oxide
RMT	Receptor-Mediated Transcytosis
ROS	Reactive Oxygen Species
RSD	Residual Standard Deviation
SAM	Self-Assembled Monolayer
SD	Standard Deviation

SLNP	Solid Lipid Nanoparticle
SPION	Superparamagnetic Iron Oxide Nanoparticle
SPR	Surface Plasmon Resonance
STM	Scanning Tunnelling Microscopy
SWCNT	Single-Walled Carbon Nanotube
t(BID)	Truncated BH3 Interacting-Domain Death Agonist
TEM	Transmission Electron Microscope
ToF-SIMS	Time-of-Flight Secondary Mass Spectroscopy
TPPS	*Meso*-tetrakis(4-sulfonatophenyl)porphyrin
TTF	Tumour Treating Field
UV-Vis	Ultra Violet-Visible
XPS	X-ray Photoelectron Spectroscopy
Zn Porph	Zinc(II) 5-(4-aminophenyl)-10,15,20-tris-(4-sulfonatophenyl)porphyrin

Mathematical Abbreviations

Symbol:	Meaning:	Value (if applicable):
A	Area	
A	Absorbance	
α	Transfer rate constant	0.5 can be assumed but can be calculated
c	Concentration	
d	Distance	
D	Diffusion coefficient	
ε	Extinction coefficient	
$E_{1/2}$	Half peak potential	

$_{E}^{0}$	Standard of species	
Ep	Peak potential	
F	Faraday constant	96 485.33 s A/mol
i	Current	
i_p	Peak current	
k^o	Heterogenous rate constant	
l	Path Length of a spectroscopy cell	
n	Number of electrons	
T	Temperature	Recorded at 22°C
v	Scan rate	
θ	Molar ellipticity	
ΔE	Peak separation	
λ	Wavelength	
ψ	Psi: peak separation function	

Abstract

This research presents a novel cancer treatment strategy employing gold nanoparticles as Cytochrome *c* carriers. Leveraging the protein's inherent apoptotic capabilities, this approach activates the therapeutic potential of Cytochrome c using a porphyrin "trigger" when exposed to monochromatic visible light. This research meticulously details the synthesis, functionalisation, and characterisation of AuNPs with diameters of 20, 50, and 100 nm, utilising many analytical techniques. The AuNPs were functionalised with Cyt c and Zn Porph through two distinct ligands and conjugation strategies, preserving their stability. Our novel spectral deconvolution approach critically ascertains the precise concentration and number of conjugated molecules on AuNPs, setting the stage for an in-depth analysis of their impact, primarily on the redox capabilities of Cyt c. The core objective was to determine if conjugated Cyt c and Zn Porph can instigate apoptosis in cancer cells upon exposure to light.

We examined the electrochemical properties of Cyt c and Zn Porph before and after their conjugation to ascertain any functional alterations. The conjugation process instigated noticeable changes in the structure of Cyt c, dependent on the AuNP size and conjugation methods. ToF-SIMS measurements pinpointed the orientation of Cyt c post-conjugation. Strikingly, while Cyt c showed reduced electron transfer rates post-conjugation, Zn Porph maintained its electron transfer capabilities. Notably, the potential of light-triggered Cyt c activation via Zn Porph remained intact, paving the way for evaluating its anti-cancer efficacy.

Finally, our investigations into the therapeutic application of multifunctionalised AuNPs for cancer therapy revealed that these nanoparticles are proficiently internalised by MCF-7 cells. Their therapeutic potential was realised upon exposure to amber light, leading to significant cellular death. Intriguingly, the size of the AuNPs played a crucial role in enhancing the peroxidase activity of Cyt c. However, certain measurements, such as the PrestoBlue assay, were hindered by fluorescent overlaps, suggesting a need for more apt methodologies. Our findings conclude that AuNPs, when multifunctionalized with Cyt c and Zn Porph and activated by amber light, possess remarkable potential in initiating apoptosis in cancer cells. This pioneering approach holds transformative potential for targeted cancer therapies, marking a pivotal advancement in nanoparticle-based medical interventions.

1. Introduction

1.1. Aims and Rationale

Traditional cancer treatments include surgical intervention (extraction of the tumour), chemotherapy, radiation therapy or a combination of all three fields (Senapati et al., 2018). Although these treatments can effectively kill cancerous cells, they are also nonselective. The resulting effects mean that healthy cells are damaged or killed during treatment, causing the patient unpleasant and unintentional side effects, including hair and appetite loss and nausea, to name but a few (Senapati et al., 2018).

Despite progression in cancer treatment efficacy, the disease remains a global health issue, accounting for one in six deaths worldwide. As of 2020, there were an estimated 19.3 million new cancer cases and approximately 10 million cancer-related deaths worldwide (Debela et al., 2021). This highlights the pressing need for continued innovation and improvement in treatment strategies to minimise mortality rates.

The primary objective of this project was to develop a novel in vitro system to kill cancerous cells, utilising gold nanoparticles (AuNPs) as carriers for Cytochrome *c* (Cyt *c)* and Zinc(II) 5-(4-aminophenyl)-10,15,20-tris-(4-sulfonatophenyl)porphyrin (Zn Porph) to induce apoptosis in cancer cells upon exposure to a specific wavelength of light. As illustrated in Figure 1, the proposed bioelectronic cancer treatment employs AuNPs conjugated with both Cyt *c* and Zn Porph for efficient delivery. Following tumour excision, the multifunctional AuNPs will be administered to nearby tissues, facilitating cellular uptake through endocytosis. Upon light stimulation, Zn Porph serves as an apoptotic activator, transferring energy to Cyt *c*. The energy transfer process triggers a redox change in the heme group's central iron atom within Cyt *c*, shifting from Fe^{2+} (inactive) to Fe^{3+} (active) and consequently inducing apoptosis in the remaining cancer cells. The unique controllability of this apoptosis mechanism distinguishes the proposed

system within the field, with the work in this thesis providing the foundation of what could potentially be a successful cancer treatment.

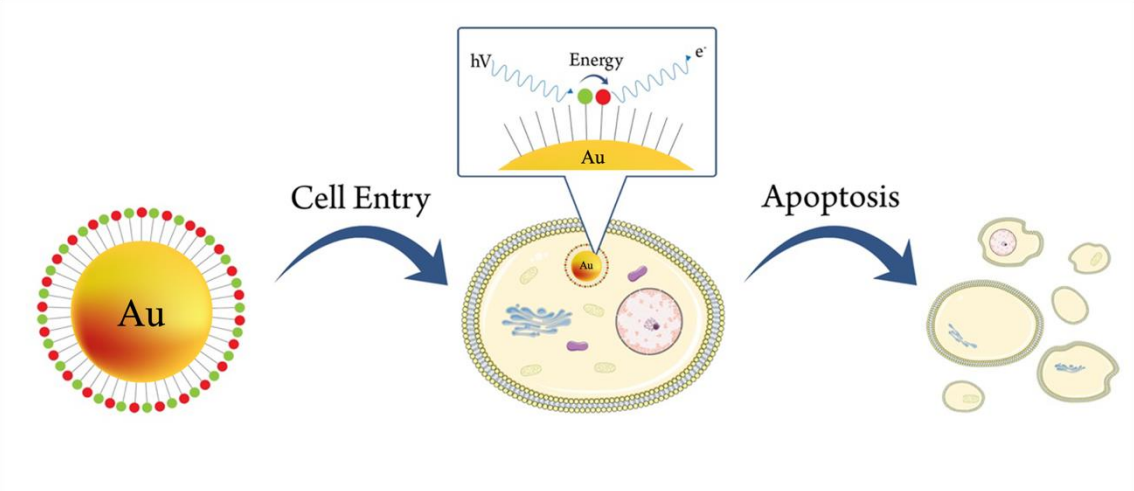


Figure 1. Schematic representation of the proposed AuNP cancer treatment in this work.

1.2. Introduction

1.2.1. Cancer

Cancer represents a considerable global health burden, with tens of millions of people receiving a cancer diagnosis each year and more than half of these cases culminating in fatality (Ma and Yu, 2006). Cancer is currently the second leading cause of death in numerous countries worldwide, successive only to cardiovascular diseases. However, as medical advancements continue to improve the prevention and treatment of cardiovascular diseases, the incidence of such conditions is expected to decline, subsequently elevating cancer to the primary cause of mortality in many nations over the course of this century (Bray et al., 2021).

Elderly populations exhibit a particularly increased susceptibility to cancer, and with the global demographic trend of an ageing population, the disease is expected to remain a significant health concern for the foreseeable future (Bray et al., 2021, Ma and Yu, 2006). This underscores the urgent need to develop innovative cancer treatment approaches including targeted therapies, immunotherapies, and personalised medicine, which can all

improve patient outcomes and reduce mortality rates. Additionally, advancements in early detection and prevention strategies are crucial to mitigating the overall cancer burden.
The interdisciplinary nature of cancer research, which encompasses fields such as genomics, proteomics, bioinformatics and nanotechnology, has the potential to unlock novel insight into the complex mechanisms underpinning the initiation and progression of the disease, the latter being of most interest to this work (Bray et al., 2021, Mosleh-Shirazi et al., 2022).

1.2.2. Cancer therapies

Cancer treatments can vary greatly, each possessing unique therapeutic advantages and limitations (Schirrmacher, 2019). Over the past century, the preferred treatment modalities have included surgical tumour removal, chemotherapy, and radiation therapy (Schirrmacher, 2019, Arruebo et al., 2011). Although these conventional therapies have proven effective in many instances, they face numerous drawbacks such as lack of specificity, cytotoxicity, short half-life, poor solubility, and multidrug resistance, to name a few (Chakraborty and Rahman, 2012, Cheng et al., 2021).

The future of cancer treatment resides in addressing these critical challenges, including combatting drug resistance, optimising drug delivery systems, and reducing damage to healthy cells. New advanced and innovative approaches explore the potential of stem cell therapy, targeted therapy, ablation therapy, gene therapy, natural antioxidants, chemodynamic therapy, sonodynamic therapy, ferroptosis-based therapy, tumour treating field (TTF) therapy, and nanoparticle application; the latter two of which provide the basis for this thesis. These promising avenues are poised to revolutionise the cancer treatment landscape, enhancing selectivity and efficacy while minimising the harmful impact on healthy cells (Debela et al., 2021, Ouyang et al., 2019, Khalil et al., 2019, Padma, 2015, Selmi et al., 2019, Fu et al., 2012, Aghebati-Maleki et al., 2020, Das et al., 2015, Bernardini et al., 2018, Li et al., 2021b, Liang et al., 2020, Luo et al., 2021, Rominiyi et al., 2021).

1.2.2.1. Nanomaterials for Cancer Therapies

Medical nanotechnology utilises nanomaterials, which are materials sized in the range of 1-100 nm and have unique optical, magnetic, and electrical properties more advantageous than traditional macromolecules. These nanomaterials, such as liposomes, solid lipid nanoparticles, dendrimers, carbon nanomaterials, nanoparticles, and metallic nanoparticles, have diverse applications in therapeutic drugs, device design, and manufacture (Ali et al., 2021, Cheng et al., 2021). Each nanomaterial has positive and negative attributes that help ultimately determine which nanomaterials are used in various cancer therapies; this section provides a brief overview of the most widely used nanomaterials and their roles in cancer therapy.

Liposomes, spherical vesicles comprised of phospholipids, can encapsulate hydrophilic and hydrophobic drugs to give protection from degradation (Samad et al., 2007, Torchilin, 2005). Liposomes also offer improved drug pharmacokinetics and targeted drug delivery (Zhang et al., 2008). For example, liposomes coated with polyethylene glycol (PEG) loaded with doxorubicin were used to treat Kaposi's sarcoma in HIV patients, improving the drug's efficacy (James et al., 1994). As of 2023, nine liposomal treatments have received clinical approval for use in various cancers, and an additional eight are undergoing clinical trials (Fulton and Najahi-Missaoui, 2023). This growing number underscores the effectiveness and potential of liposomes as a prominent therapeutic approach in oncology. However, liposomes have limitations including *in vivo* instability, varying drug encapsulation efficiency, and challenges in large-scale production and storage stability (Niza et al., 2021, Van Tran et al., 2019, Mozafari, 2005, Weiner, 1994).

Solid lipid nanoparticles (SLNPs) are colloidal carrier systems with a solid lipid core and a layer of surfactants to prevent aggregation (Yadav et al., 2013, Cheng et al., 2021). They exhibit similar functionality to liposomes but offer better stability and prolonged drug release. The lipidic nature of SLNPs makes them biocompatible, reducing the risk of toxicity which can be a problem for other nanomaterials. The solid matrix can also protect sensitive drugs, decreasing their likelihood of degradation, and broadening the range of

therapeutic agents they can deliver (Sheoran et al., 2022). However, SLNPs may face issues such as unpredictable gelation and low uptake due to their crystalline structure (Iqbal et al., 2012).

Dendrimers (highly branched macromolecules) have a core, multiple branches and functional groups on their surface, making them versatile for drug conjugation and encapsulation, making them great delivery vehicles (Baker Jr, 2009, Lim et al., 2013). Dendrimers have also been shown to have high bioavailability and have been used as contrast agents, although this is dependent on the functional groups on their surface (Bober et al., 2022). Attributes such as enhanced solubility and improved bioavailability of hydrophobic drugs make dendrimers advantageous, however some types of dendrimers, particularly those with cationic surfaces, may exhibit cellular toxicity and accumulation-related toxicity due to the non-biodegradable materials used (Nikzamir et al., 2021, Corrales et al., 2022).

Carbon nanomaterials, including graphene-based nanomaterials and carbon nanotubes, possess unique properties such as electrical, thermal, optical, and mechanical characteristics (Masoudipour et al., 2017, Dong et al., 2017). Graphene oxide (GO) and reduced graphene oxide (rGO) offer greater biocompatibility than graphene, and can be used for targeted therapy and cancer diagnosis (Goenka et al., 2014, Muñoz et al., 2019). However, challenges such as poor solubility, agglomeration, and cellular toxicity must be addressed (Kuilla et al., 2010, Ema et al., 2017).

Carbon nanotubes (CNTs) are rod-shaped structures derived from graphene layers and can be categorised into single-walled carbon nanotubes (SWCNTs) and multi-walled carbon nanotubes (MWCNTs) based on the number of layers present (De Volder et al., 2013). CNTs possess properties such as high electrical and thermal conductivity, high chemical stability, and exceptional tensile strength (De Volder et al., 2013, Simon et al., 2019, Ozgen et al., 2020). However, drawbacks regarding water insolubility and potential toxicity mean surface functionalisation and material modifications must be employed to enhance their bioavailability (Meng et al., 2010, Ozgen et al., 2020). CNTs have

previously been utilised as carriers for anti-cancer drugs, such as doxorubicin, to improve drug accumulation in cells and enhance the drug's anticancer efficacy (Ozgen et al., 2020).

Polymeric nanoparticles (PNPs) main characteristics of biocompatibility, biodegradability and low toxicity make them of great interest (Zielińska et al., 2020). PNPs have diverse applications in drug delivery, diagnostics, and biocompatibility enhancement (De Jong and Borm, 2008, Ferrari, 2005, Malik et al., 2023, Aslan et al., 2013). PNPs can act as drug carriers, offering targeted drug delivery and sustained release (Masood, 2016). However, PNPs have limitations including non-biodegradability (when biodegradability was expected), fragility, toxic solvent residuals, high manufacturing costs, low drug loading efficiency, and aggregation phenomena (Lu et al., 2011, Niza et al., 2021).

Extracellular vesicles (EVs), including exosomes, are phospholipid bilayer vesicles involved in cellular communication and can be utilised for gene therapy in cancer treatment (Batrakova and Kim, 2015). However, EVs have a high clearance rate, lack of uniform isolation and purification, and difficulties in maintaining stability (Niza et al., 2021, Pegtel and Gould, 2019, Jeyaram and Jay, 2018).

Metal nanoparticles (MNPs), including iron oxide, silver, and gold nanoparticles (AuNPs), have diverse applications in biomedical fields (Debela et al., 2021). Superparamagnetic iron oxide nanoparticles (SPIONPs) are used as contrast agents for MRI, targeted drug delivery, treating hyperthermia, and gene therapy (Mody et al., 2010). However, SPIONPs' potential toxicity at high concentrations needs to be addressed (Mody et al., 2010, Alargova et al., 2004). Silver nanoparticles (AgNPs) have the ability to induce cell death in mammalian cells and can enhance radiation sensitivity in cancer therapy (Gibson et al., 2007, Melancon et al., 2011), however their potential toxicity to healthy tissues should be considered (Rodriguez-Garraus et al., 2020, Souza et al., 2018). Gold nanoparticles (AuNPs) however, have many unique attributes that poise them as very attractive for use in cancer therapy; namely high stability, high biocompatibility, easy surface functionalisation, catalytic properties, optical properties and ability to be

synthesised in a variety of shapes and sizes (Sztandera et al., 2019). Numerous studies have previously used AuNPs as delivery systems for anticancer drugs (Jain et al., 2012, Lim et al., 2011), but it is the use of AuNPs in combination therapies which differentiates them from other nanomaterials, and makes them ideal for the applications discussed in this work (Nejati et al., 2022, Park et al., 2019, Al-Shakarchi et al., 2018). The exceptional properties of AuNPs also lends them to theranostic approaches, combining diagnostic imaging with therapeutic intervention (Arruebo et al., 2011). The following section will discuss AuNPs in greater detail, illustrating why they are the best choice of nanomaterial for the work conducted in this thesis.

By harnessing the unique properties of nanomaterials, researchers are developing innovative drug delivery systems, imaging agents, and therapeutic agents that can be tailored to individual patient needs (Sahakyan et al., 2017, Cheng et al., 2021). The potential for targeted and personalised therapy through nanotechnology holds great promise for improving the overall effectiveness of cancer treatments while minimising their associated drawbacks (Dumbrava and Meric-Bernstam, 2018). Continued advancements in this field are expected to revolutionise cancer therapy and contribute to better patient outcomes (Cheng et al., 2021).

1.2.3. Gold nanoparticles

This work utilises AuNPs as carriers for Cyt *c* and Zn Porph, facilitating their internalisation into cancer cells and triggering apoptosis upon exposure to monochromatic light. In the absence of a carrier such as AuNPs, the cellular uptake of Cyt *c* and Zn Porph would be limited due to their hydrophilic nature and the predominantly hydrophobic lipid composition of the cell membrane (Alberts, 2017, Yang and Hinner, 2015). AuNPs are capable of traversing the cell membrane through various mechanisms without compromising cell viability (Lévy et al., 2010). The surface of these nanoparticles can be functionalised with ligands to attach molecules or biomolecules (Lévy et al., 2010), rendering them particularly suitable for this study as they can be conjugated with Cyt *c*

and Zn Porph. The properties of AuNPs are detailed below, providing a clear reasoning as to why they were selected for this work.

Gold nanoparticles (AuNPs) are a specific class of nanomaterials that have garnered significant attention in biotechnology and therapeutic applications due to their unique ability to be internalised by cells with almost no cytotoxic effect and diverse surface functionalities (Yeh et al., 2012, Ramalingam, 2019, Lévy et al., 2010). AuNPs can be functionalised with various biological components, including proteins, antibodies, and oligonucleotides, contributing to their versatility and broad applicability in various biomedical fields (Ramalingam, 2019, Yeh et al., 2012).

AuNPs can be synthesised in a variety of sizes, ranging from 1 nm to 5 μm, and can take on diverse shapes, such as nanorods, nanostars, nanospheres, and nanoclusters (Khan et al., 2014, O'Neal et al., 2004, Chen et al., 2008, Li et al., 2015, Xiao et al., 2020). This versatility in size and shape is a primary factor driving the extensive interest in AuNPs. Different sizes and shapes possess unique properties and applications, making them a valuable asset across various nanotechnology and nanobiomedical industries (Dykman and Khlebtsov, 2011).

The physicochemical properties of functionalised AuNPs can be altered through binding events, thus affecting their redox behaviour, conductivity, and surface plasmon resonance (SPR) (Ramalingam, 2019, Huang and El-Sayed, 2010). As a result, these characteristics can be employed to evaluate the impact of the functionalised nanoparticles in biomedical applications (Huang and El-Sayed, 2010, Yeh et al., 2012).

1.2.3.1. Internalisation Mechanisms of Gold Nanoparticles into Cells

Modulating the size, shape and surface chemistries of AuNPs can change the mechanism by which AuNPs are internalised by cells. The mechanisms for AuNP cellular uptake are endocytosis, passive diffusion, and carrier-mediated transport (Wang et al., 2010, Kapara et al., 2020, Zolghadr and Moosavi, 2019, Song et al., 2021).

Endocytosis can be split into two distinct mechanisms: pinocytosis, involving the internalisation of fluids, molecules and NPs within small vesicles, and phagocytosis, which engulfs large particles (Kuhn et al., 2014). Pinocytosis encompasses macropinocytosis, clathrin and caveolin-mediated endocytosis, and clathrin and caveolin-independent endocytosis (Oh and Park, 2014, Brandenberger et al., 2010). Not all cell types have the machinery to perform all the endocytosis pathways (Douglas et al., 2008) therefore, it is important to consider the targeted cells' endocytosis pathway capabilities when using AuNPs as delivery systems as their size, shape and surface chemistry can be tailored to suit the required pathway. In this work, the size of AuNPs was changed to assess whether a particular size would enable a larger uptake and cause greater cell death. Macropinocytosis can be used to uptake large AuNPs as the pathway can internalise material exceeding 1 μm in diameter. Macropinocytosis is a cellular process activated by signaling cascades involving Rho-family GTPases. This initiates the formation of large membrane protrusions through actin regulation. These protrusions, upon encountering specific molecules or nanoparticles, engulf them and subsequently collapse, fusing with the cell membrane. This process forms large endocytic vesicles, known as macropinosomes (Sousa de Almeida et al., 2021).

Clathrin and caveolin-mediated endocytosis is the result of receptor-mediated endocytosis and is often used to internalise nanoscale materials such as viruses and nanoparticles (Wang et al., 2009, Oh and Park, 2014, Conner and Schmid, 2003, Hillaireau and Couvreur, 2009). Clathrin-mediated endocytosis forms 'coated pits' on the plasma membrane, primarily assembled by clathrin proteins. These pits are invaginated and pinched off to form endocytic vesicles, typically 120 nm in diameter (Conner and Schmid, 2003). Caveolin are flask-shaped invaginations ~50-60 nm in diameter that facilitate the endocytosis of cholesterol and other lipid or protein-coated molecules or NPs that are recognised by caveolin (Conner and Schmid, 2003). Caveolae, a type of cholesterol-rich microdomain on the plasma membrane, and other such microdomains referred to as rafts, approximately 40-50 nm in diameter, can be internalised into endocytic vesicles after freely diffusing on the cell's surface (Conner and Schmid, 2003). Both clathrin and

caveolin-mediated endocytosis pathways have been shown to play a major role in the internalisation of AuNPs (Rattanapinyopituk et al., 2014). Phagocytosis is another form of receptor-mediated endocytosis carried out by macrophages, monocytes, and neutrophils, primarily removing large pathogens or debris like dead cells. This process begins when blood components are identified as foreign, initiating a signalling cascade mediated by Rho-family GTPases that prompts actin assembly, leading to cell surface extensions that engulf these foreign components. Notably, phagocytosis has been observed to internalise AuNPs in macrophages, suggesting potential utility in cancer treatments targeting tumour-associated macrophages (Krpetić et al., 2010).

Passive diffusion has been shown to occur for AuNPs with a diameter of 2-3 nm, as a result of the very small size of the AuNPs making them able to cross the phospholipid bilayer (Sabourian et al., 2020, Rossi and Monticelli, 2016).

Carrier-mediated transport, adsorptive-mediated transcytosis (AMT), and receptor-mediated transcytosis (RMT) are key mechanisms that facilitate transport across cellular barriers. Carrier-mediated transport, driven by specialised proteins, effectively transports various small molecules and may be utilised by small nanoparticles to transport specific drugs (Velasco-Aguirre et al., 2015). AMT, an energy-dependent process, commences with the interaction of a cationic compound with the negatively charged plasma membrane, leading to endocytosis and potentially transcytosis (Pujals et al., 2006, Velasco-Aguirre et al., 2015). This mechanism has been shown to allow the transport of AuNPs functionalised with human serum albumin as previous work has demonstrated that AuNPs using albumin as their stabilising and capping mechanism showed high accumulation in the brain (Sousa et al., 2010, Schäffler et al., 2014). RMT, a highly specific transport method, facilitates the intake of macromolecules at the luminal surface of endothelial cells and their release at the abluminal end (Velasco-Aguirre et al., 2015). This process, involving the identification of a receptor-ligand pair, the formation of an endosome, the transport of the ligand across the cell, and exocytosis at the abluminal side, has been demonstrated with functionalised AuNPs, showing significantly enhanced transport (Shilo et al., 2014).

The ability to modulate the size of AuNPs to utilise the different cellular uptake mechanisms is one of the most attractive features of AuNPs for drug delivery purposes. Modulating the size enables different endocytosis pathways to be utilised, thus, in this project AuNPs of different sizes were used to identify the optimal size of multifunctionalised AuNPs to induce cellular death. Another attractive feature is the ability to synthesis AuNPs in a variety of different shapes.

Gold nanorods have garnered significant interest for their biological applications, as they exhibit distinct absorption properties in visible and near-infrared spectra (Stone et al., 2011). These properties make nanorods suitable for biosensing, gene delivery, and thermal therapy (Khan et al., 2014). Gold nanospheres, on the other hand, are the most prevalent type of nanoparticle, as they can be synthesised with ease, and their size can be precisely controlled. The high absorption coefficient of AuNPs, derived from their high atomic number and electron density, is well-suited for imaging techniques. Additionally, the size of gold nanospheres can be determined using a SPR measured with a UV-Vis absorption spectrophotometer (Hu et al., 2020, Dykman and Khlebtsov, 2011, Yeh et al., 2012).

Overall, the ability for AuNPs to be internalised into cells with low toxicity and the potential to functionalise their surface with molecules and biomolecules makes them an ideal delivery vehicle for Cyt *c* and Zn Porph, as utilised in this work.

1.2.3.2. Gold Nanoparticles and Surface Plasmon Resonance

Most nanomaterials rely on dynamic light scattering (DLS) and transmission electron microscopy (TEM) for accurate size determination (Wilson and Prud'homme, 2021), however the optical properties of AuNPs detailed in this section enables their size and functionality to be assessed using UV-Visible (UV-Vis) absorption spectroscopy (Haiss et al., 2007). The maximum absorbance of a plasmon's surface is known as SPR (Su et al., 2012, Amendola et al., 2017). Using a UV-Vis absorption spectrophotometer, the SPR

peak of AuNPs can be determined by obtaining a UV-Vis absorption spectrum, as demonstrated in Figure 2 (with an SPR peak at 521 nm). Determining the SPR of AuNPs is crucial as it allows for accurate calculation of the size and concentration of AuNPs in a solution (Haiss et al., 2007).

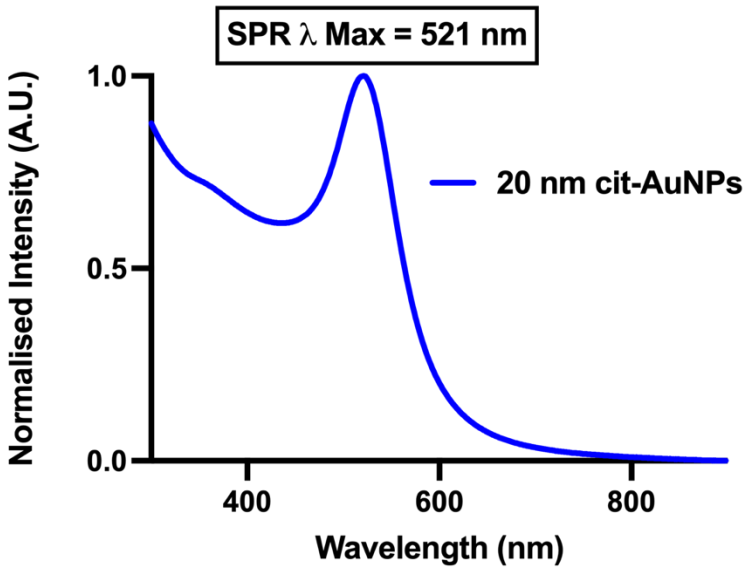


Figure 2. UV-Vis absorption spectrum of 20 nm cit-AuNPs with an SPR peak at 521 nm.

Plasmons, a type of bosonic quasiparticle excitation, are formed by the collective oscillations of free electrons in metals (Amendola et al., 2017). Plasmons can be characterised as a negatively charged electron cloud coherently displaced from its equilibrium position around a lattice of positively charged ions, much like actual plasma (Amendola et al., 2017). One example of this is the relationship between the peak wavelength of light absorbed and the diameter of the AuNP, as depicted in Figure 3. The absorption band results from the collective oscillation of conductor electrons when they are excited by incident photon resonance, known as the surface plasmon band. However, this band is absent in small AuNPs (with a diameter less than 2 nm) and bulk materials.

The plasmon phenomenon is sensitive to several factors, including size, shape, solvent, surface ligand, core charge, temperature, and even proximity to other AuNPs (Toderas et al., 2008, Srivastava et al., 2005, Kelly et al., 2003, Link and El-Sayed, 2000). AuNP

aggregation results in a significant red shift of SPR frequency, an expansion of surface plasmon band, and a colour change of solution from red to blue due to inter-particle plasmon coupling (Su et al., 2003).

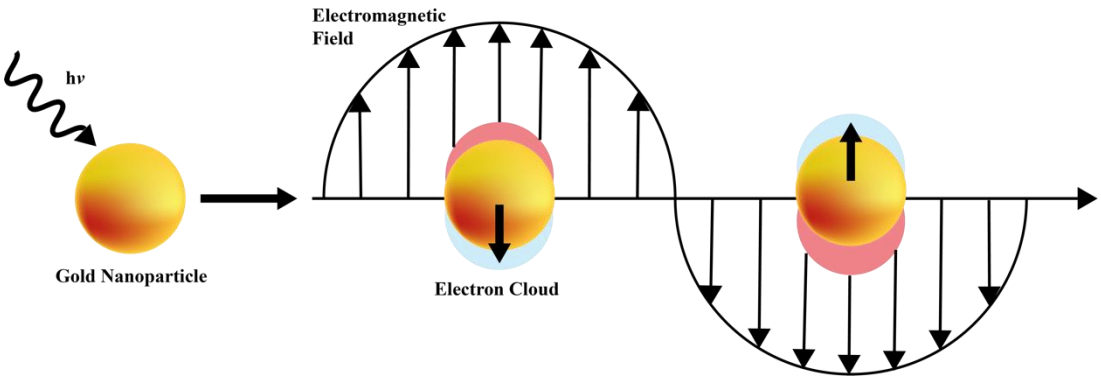


Figure 3. Schematic representation of the oscillation of electrons across AuNPs in the electromagnetic field of light. Adapted from (Yeh et al., 2012).

The size of AuNPs corresponds to a specific extinction coefficient, which is essential for calculations involving Beer-Lambert's law, as shown in Equation 1

$$A = c\varepsilon d$$

Equation 1.

where the absorbance (A) is determined by multiplication of extinction coefficient (Ɛ), distance inside the sample or pathway length (d) and concentration (c) (Mayerhöfer et al., 2016). With a greater AuNP diameter, the SPR peak shifts to the right, resulting in a longer wavelength, as detailed in Table supplementary information 1 (Table SI 1) (Haiss et al., 2007). An increase in the diameter of AuNPs also leads to a higher extinction coefficient, as seen in Table SI 2 (Haiss et al., 2007). To obtain an accurate concentration, the absorbance at 450 nm must be used, as the extinction coefficient value at 450 nm is provided in Table SI 2 . When the absorbance of the SPR and the wavelength of the SPR are known, it is possible to determine the diameter and resulting extinction coefficient. Equation 1. can then be used to calculate the concentration of AuNPs. This is valuable when the AuNPs are required in a specific concentration which can be achieved via

centrifugation and resuspension in a smaller volume, with the ability to dilute by adding more solution. This is a major advantage over other nanoparticle techniques as the concentration can be determined quickly, easily, and cost-effectively using equipment readily available in most labs.

1.2.3.3. AuNP synthesis

AuNPs can be synthesised using various methods, such as the Turkevich method, Brust-Schiffrin method, seed-mediated growth method, and electrochemical synthesis method (Yeh et al., 2012, Turkevich et al., 1951, Brust et al., 1994, Khoury et al., 2018). The size of AuNPs can be easily adjusted during synthesis, leading to a more uniform size distribution with minimal variability (Yeh et al., 2012, Xie et al., 2017). The project detailed in this thesis utilised both the Turkevich and seed-mediated growth methods to synthesise AuNPs due to the ability to control the size and produce water soluble AuNPs. However, other synthesis methods such as the Brust-Schiffrin method and the photochemical method can also be used to synthesis AuNPs.

1.2.3.3.1. Turkevich Method

The Turkevich method describes the reduction of gold ions (Au^{3+}) in the form of tetrachloroauric acid ($HAuCl_4$) to elemental gold (Au^0), by utilising sodium citrate as a reducing agent in an aqueous solution (Turkevich et al., 1951). This reduction process initiates the nucleation of Au^0 followed by the growth phase, ultimately yielding water-soluble AuNPs as illustrated in Figure 4.

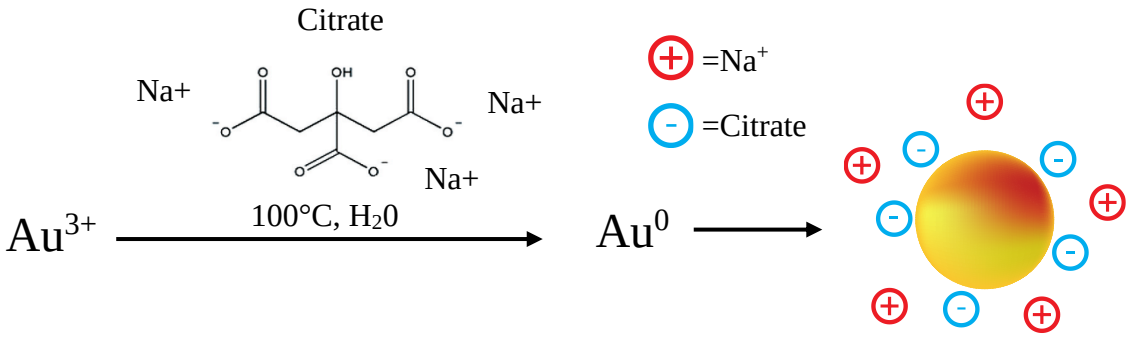


Figure 4: Schematic representation Turkevich method of AuNPs synthesis, adapted from (Imbraguglio et al., 2013)

The size of the AuNPs generated via this method can range from approximately 9 to 120 nm, which is contingent upon the concentration of sodium citrate employed, as well as other experimental parameters including temperature (Kimling et al., 2006). The Turkevich method produces monodispersed AuNPs with a narrow size distribution. By judiciously manipulating the sodium citrate concentration and other experimental variables, researchers can effectively control the size and shape of the resulting AuNPs, tailoring their physicochemical properties to suit specific applications in areas such as biotechnology, catalysis and nanomedicine.

1.2.3.3.2. Gold Nanoparticle Seed Growth Method

Seed-mediated growth is an additional step performed after the Turkevich method that uses cit-AuNP as ‘seeds’, to which additional gold salt is selectively reduced to the surface of AuNPs using hydroquinone and additional citrate (Khoury et al., 2018). Therefore ‘seed’ AuNPs can be ‘grown’ more precisely, making it easier to achieve larger-sized monodispersed AuNPs.

The citrate coating around the AuNPs (cit-AuNPs) can be easily exchanged with thiolated ligands. This adds versatility to the functionalisation of cit-AuNPs, as thiolated ligands can be selected with functional groups for the conjugation of specific molecules.

1.2.3.3.3. Brust-Schiffrin Method

The Brust-Schffrin method produces AuNPs ranging from 1.5 to 5 nm using a two-phase process in which aqueous gold salt is transferred to an organic solvent such as toluene using a phase transfer agent such as tetraoctylammonium bromide (TOAB), followed by a reduction step in the presence of alkanethiol using sodium borohydride ($NaBH_4$). The reduction step causes a colour change from orange to brown in the organic phase, indicating the AuNP formation (Brust et al., 1994, Patil et al., 2023).

1.2.3.3.4. Photochemical Reduction

Photochemical reduction presents an eco-friendly approach to synthesising AuNPs, circumventing the need for chemical reactants that can produce detrimental by-products (Annadhasan et al., 2015). This method combines gold salts with biological extracts or biomolecules, which serve as reducing and stabilising agents (Mukha et al., 2020). The key to this process lies in the inherent capability of certain cellular components to reduce the metal precursor from its trivalent state (Au^{3+}) to its elemental state (Au^0). When facilitated by UV light, this reduction triggers the formation of nucleation centres. These centres subsequently grow and aggregate, culminating in the formation of AuNPs (Jara et al., 2021).

In the context of this research, the aqueous solubility of AuNPs, derived from both the Turkevich method and the seed growth approach, proved to be optimally suited for the intended applications as a cancer therapy.

1.2.3.4. Ligand Exchange on Gold Nanoparticles

A ligand is a molecule that binds to metal atoms, typically through covalent bonds (Ha and Bhagavan, 2023). During the synthesis of AuNPs, certain ligands are employed primarily for stabilisation. However, these initial ligands may lack the specific functional groups necessary for a desired application. As a result, they are often exchanged for more

relevant and functionally appropriate ligands. Ligand exchange reactions facilitate the replacement of ligands on the surface of materials such as AuNPs, thereby tailoring their functionality and optimising material performance (Zhang et al., 2022). The original ligands on the surface of the material, typically employed for stabilisation during synthesis, may not always be suitable for the intended application, so they are exchanged for more suitable ones (Thambiliyagodage, 2022). Some commonly used ligands for functionalising gold nanoparticles include thiols, amines, disulfides, phosphines, and DNA strands (Kalimuthu et al., 2014, Kalimuthu and John, 2010, Zhang et al., 2022, Jain et al., 2021, Zhao et al., 2018, Rodrigues et al., 2014). Stabilising ligands can be classified into two categories: auxiliary stabilising ligands (ASL) and functionalised stabilising ligands (FSL) (Quintana et al., 2020).

The binding strength and size of the ligands influence the rate of reaction and extent of surface functionalisation. The degree of ligand exchange can be controlled by examining the binding strengths of ASL-Au and FSL-Au using scanning tunnelling microscopy (STM). A study of self-assembled monolayers (SAMs) comprising alkyl amines, thiols, and carboxylic acids on Au(111) surfaces revealed that carboxylic acids (-COOH) exhibit a binding strength of 8.4 kJ mol-1 (Au-O), amines (-NH2) have 65 kJ mol-1 (Au-N), and thiols (-SH) display 167 kJ mol-1 (Au-S) (Quintana et al., 2020, Chen et al., 2006). Owing to their superior binding strength, thiols displace the ASL and are frequently employed in ligand exchange processes (Qian et al., 2012, Tsukuda, 2012, Aikens, 2018, Jain et al., 2012).

1.2.4. Cytochrome *c*

Cyt *c* is a 12.3 kDa protein located in the inner mitochondrial membrane, synthesised in the cell cytosol as an apoprotein before being translocated to the mitochondria, where it binds to the heme prosthetic group (Cai et al., 1998). Composed of a 104 amino acid polypeptide chain covalently bound to a central heme group, Cyt *c* exhibits a spherical structure with a diameter of 3.4 nm (Garrido et al., 2006, Kagan et al., 2004). The heme

group imparts redox properties to Cyt *c*, with its iron centre capable of existing in both Fe^{2+} and Fe^{3+} states (Weller et al., 2014).

Cyt *c* serves two primary functions: facilitating electron transfer from complex III to complex IV in the electron transport chain (integral to respiration), while also playing a crucial role in apoptosis (Li et al., 2000). Within the inner mitochondrial membrane, Cyt *c* predominantly exists in a weakly bound state due to limited electrostatic interactions. However, approximately 15% of Cyt *c* is more strongly bound, involving electrostatic and hydrophobic interactions. These different binding strengths confer different functions to Cyt *c*: weakly bound Cyt *c* participates in the electron transport chain and inhibits reactive oxygen species (ROS) formation, while more strongly bound Cyt *c* associates with cardiolipin and exhibits peroxidase activity (Kagan et al., 2004).

The redox state of Cyt *c* influences ROS formation and prevention in weakly and strongly bound Cyt *c*. In the weakly bound state, Fe^{3+} at the heme group's centre is reduced to Fe^{2+} before ROS can form. In the strongly bound state, Fe^{2+} is oxidised to Fe^{3+} in the electron transport chain, enabling free electrons to generate ROS (Brown and Borutaite, 2008).
Apoptosis is another essential function of Cyt *c* and the intrinsic and extrinsic pathways are presented in Figure 5. Cells initiate apoptosis pathways in response to apoptotic stimuli such as metabolic stress or DNA fragmentation (Alvarez-Paggi et al., 2017). Apoptosis can proceed via two primary pathways: the intrinsic (mitochondrial) and extrinsic pathways. The intrinsic pathway is triggered by apoptotic stimuli, leading to the outer mitochondrial membrane's permeabilisation and subsequent release of proteins from the inner mitochondrial membrane into the cytosol. Apoptotic stimuli prompt the split of BH3 interacting-domain death agonist (BID) to form truncated (t)BID, which activates BCL2-associated X protein (BAX) and BCL2 homologous antagonist killer (BAK). BAX and BAK form pores in the outer mitochondrial membrane, allowing Cyt *c* to exit the mitochondria. Once released into the cytosol, Cyt *c* binds to apoptotic protease-activating factor-1 (APAF1), forming an apoptosome. Cysteine proteases, known as caspases, are the primary mediators of apoptosis, with the "initiator" and "executioner" caspases working together to cleave crucial substrates and dismantle the cell. The extrinsic pathway

is initiated by binding an extracellular ligand to a transmembrane death receptor, forming the death-inducing signalling complex (DISC). Procaspase-8 or -10 (the initiator caspases for the extrinsic pathway) bind to DISC producing caspase-8 or -10, which subsequently activate executioner caspases 3 and 7, resulting in apoptosis (Ow et al., 2008).

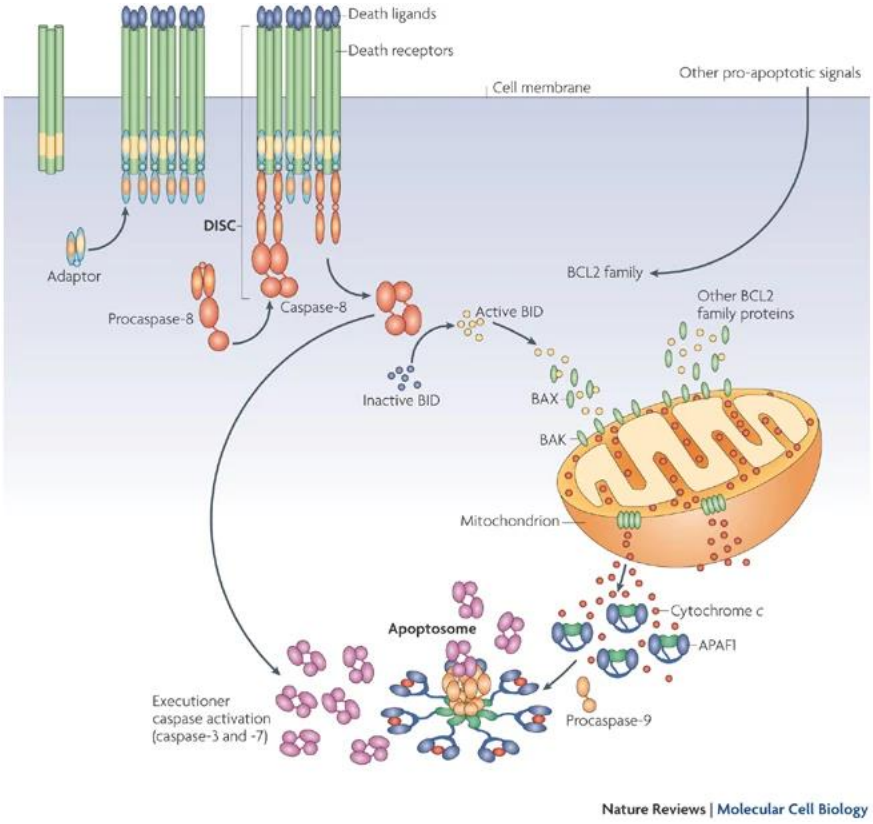


Figure 5. Overview of extrinsic and intrinsic apoptosis pathways. The extrinsic pathway (left side of the figure) begins with an extracellular death ligand binding to a death receptor, forming the DISC and activating caspase-8 or -10. The intrinsic pathway (right side of the figure) is triggered by signals causing outer mitochondrial membrane permeabilisation, releasing proteins such as Cyt *c*, which forms the apoptosome with APAF1 and activates caspase 9. Both pathways converge at the BCL2 family protein BID, with activated caspase-8 promoting BAX and BAK downstream activation (Ow et al., 2008).

By utilising the apoptotic properties of Cyt *c* in drug delivery systems, novel therapeutic options may be developed for treating cancer and other diseases characterised by

dysregulated cell survival and death. Continued research in this area holds promise in greater understanding of the roles Cyt *c* plays in cellular respiration and apoptosis, ultimately contributing to the development of innovative therapeutic interventions that exploit these functions, the latter being of interest in this work.

Due to the role Cyt *c* plays in apoptosis, early work looked at injecting Cyt *c* directly into cells using microneedles in attempt to trigger an apoptotic response. The results showed that 150 minutes after 20 μM of Cyt *c* was injected into cells, ~50% of the cells shown an apoptotic effect (Zhivotovsky et al., 1998). As knowledge in the field progressed, it was found that Cyt *c*'s ability to induce apoptosis was linked to its redox state, as it has been shown that the oxidised form of Cyt *c* (Fe^{3+}) (Cyt *c* Ox) induced caspase activation via the apoptosome, yet reduced Cyt *c* (Fe^{2+}) (Cyt *c* Red) does not induce caspase activation (Brown and Borutaite, 2008). The ability to regulate the apoptotic effect of Cyt *c* poses of great interest for a variety of biomedical applications including cancer therapies (Pessoa, 2022). Thus, there is considerable interest in developing drug delivery systems that exploit this function (Santra et al., 2010). However, the inability of Cyt *c* to cross the cell membrane means it requires conjugation with other materials to successfully enter cells (Slowing et al., 2007). Researchers are exploring various strategies to design and synthesise Cyt *c* conjugates that can effectively transport it across the cell membrane while preserving bioactivity, including the use of nanoparticles, liposomes, and other biocompatible materials that enable the targeted and controlled delivery of Cyt *c* to specific cells or tissues (Al-Shakarchi et al., 2018, Imesch et al., 2013, Barcelo-Bovea et al., 2020, Jain et al., 2021, Santra et al., 2010, Méndez et al., 2014, Malekigorji et al., 2014). Previous examples of Cyt *c* conjugated to nanomaterials to produce an apoptotic effect are detailed below.

Méndez et al., (2014) demonstrated that when Cyt *c* was conjugated to mesoporous silica nanoparticles (MSN) and applied to cells, a 47% increase in cell-free caspase 3- assay was observed when compared to just Cyt *c*. However structural conformation changes were observed in Cyt *c* after conjugation which was thought to reduce the apoptotic effect. Glycosylation was then used to protect Cyt *c* from these conformational changes and as a result the protein was less prone to reduction, meaning a larger percentage of the protein

was present in the oxidised form. When the MSNs functionalised with glycosylated Cyt *c* were applied to cells, an 87% increase in relative caspase activation was observed (Méndez et al., 2014).

Current therapies utilise the apoptotic effect with other treatments to create combined effect cancer treatments. The work by Park et al., (2019) describes the conjugation of Cyt *c* to AuNPs surrounded by single stranded DNA; the opposing isoelectric points of the DNA and the Cyt *c* result in aggregation of the functionalised AuNPs, as pH is decreased the AuNPs aggregate, and when the pH is returned to neutral the AuNPs separate. The treatment takes advantage of the lower pH that is often observed in cancerous environments, which causes the functionalised AuNPs to aggregate. A laser would then be applied to produce a photothermal effect which, in combination with Cyt *c*, can cause apoptosis in the cancerous cells. The aggregation that occurred in the acidic conditions of cancerous cells increased the effectiveness of the treatment, giving evidence of a combined photothermal and Cyt *c* effect (Park et al., 2019).

Another combined approach is shown in the work of Al-Shakarchi et al., (2018), describing hybrid nanoparticles functionalised with anticancer drugs and Cyt *c*. Iron oxide NPs (IONPs) were coated with a gold shell to produce hybrid nanoparticles (HNPs) which were then functionalised with Cyt *c* and the anticancer drugs doxorubicin, paclitaxel, oxaliplatin, vinblastine and vincristine. The functionalised HNPs were then applied to three different cancer cell lines, with results showing that the combination of Cyt *c* and anticancer drugs is more effective in increasing caspase 3 activity (indicating apoptosis) than HNPs functionalised only with anticancer drug or Cyt *c* (Al-Shakarchi et al., 2018). It is clear that the conventional approach of Cyt *c* exclusively conjugated to nanomaterials does not produce enough of an apoptotic effect on target cells to justify it as an effective cancer treatment, thus most recent research focuses on utilising Cyt *c* in a combination therapy. However, despite the acknowledgement that Cyt *c* Ox induces apoptosis and Cyt *c* Red does not, little research is being conducted in exploiting this apoptotic ‘switch’.

Previously, the redox state of Cyt *c* and its link to apoptotic ability was demonstrated in bacteria, which had been shown to oxidise under light and become reduced in dark conditions (Fujita and Myers, 1965). This has also similarly been identified in other heme-based cytochromes in which oxidation occurred through irradiation with a laser (Chauvet et al., 2015). This work therefore focuses on the use of a light source to initiate cellular death, through irradiating Zn Porph to cause excitation and trigger the oxidation of Cyt *c*. The following section addresses why Zn Porph is used in the multifunctionalised AuNPs described in this work.

1.2.5. Fluorescence

Understanding the fluorescence mechanism of Zn Porph, a fluorescent molecule conjugated to AuNPs in this study, is crucial. This comprehension will offer insights into its role in the multifunctionalised AuNP system explored in this work. Fluorescence is a physical process wherein an excited electron releases a photon when it descends to its original or ground state. This is facilitated by electromagnetic waves which impart energy to the electron, thereby pushing it into a high-energy state (Lakowicz, 2007). As the excited electron rapidly reverts to its ground state, it recombines with another electron with a contrasting spin, which remains in its ground state. The photon is then released in this spin-allowed event (Lakowicz, 2007). Luminescence, a broad category that houses both fluorescence and phosphorescence, is clearly represented using a Jablonski diagram (Figure 6) (Murthy and Virk, 2013). Electron states are displayed as bold lines, while vibration states between the electron states are represented by thin lines. Figure 6 details the process of an electron absorbing energy from visible or UV light, causing it to transition from its ground state (S0) to a higher energy state (S1 and beyond). The vibration states are displayed between the electron states such as S1 and S2. The zig-zag line between S1 and S2 illustrates the internal conversion process, showing the return of excited electrons to the lowest vibration state of S1 before emission.

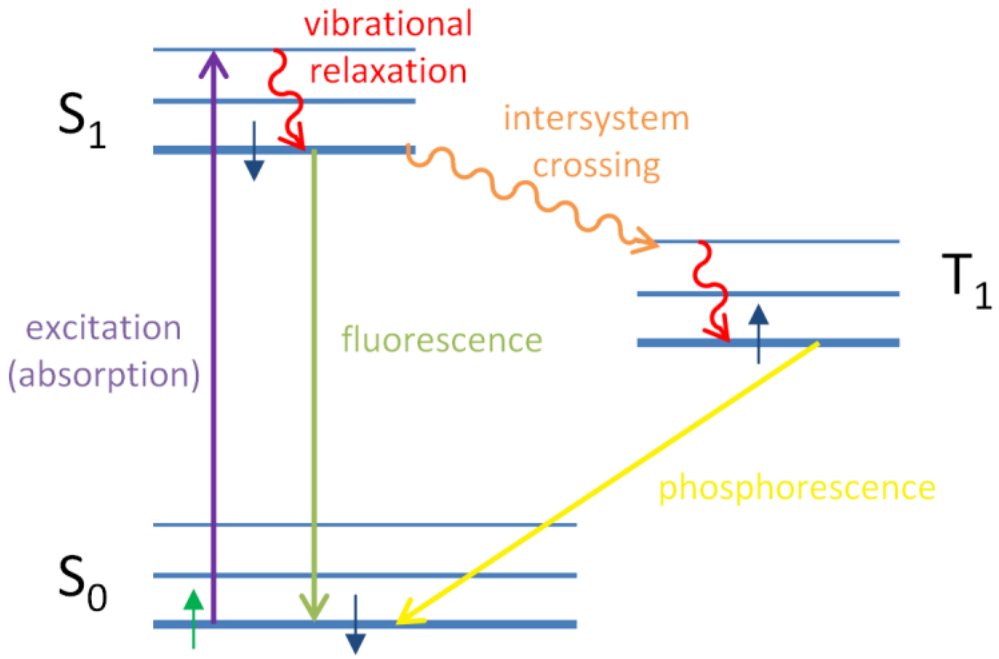


Figure 6. Jablonski diagram showing the mechanism for fluorescence and phosphorescence (Eck, 2014). Bold lines indicate electron states, thin lines represent vibration states between the electron states.

In fluorescence, the electron reverts from S1 to S0, releasing energy in the form of a photon: a phenomenon referred to as fluorescence emission. Contrastingly, phosphorescence involves the conversion of electron spin at S1 to the first triplet state (T1), known as an intersystem crossing. As the electron transitions from T1 back to S0, a photon is emitted, denoted as phosphorescence emission. This photon has a longer wavelength due to its lower energy than that of fluorescence emissions (Lakowicz, 2007). The time of emission varies between fluorescence and phosphorescence, owing to the intersystem crossing in phosphorescence. Fluorescence emissions can occur within a range of 100 picoseconds to 10 microseconds, whereas phosphorescence may extend from 100 microseconds to 10 seconds (Skoog et al., 2007). However, the typical duration for fluorescence emission is around 10 nanoseconds (Lakowicz, 2007).

1.2.5.1. Porphyrins and Photodynamic Therapy

Porphyrins, a class of tetrapyrrole structures, have emerged as promising photosensitiser (PS) candidates for Photodynamic therapy (PDT) due to their fluorescent ability (Abrahamse and Hamblin, 2016). A type of macrocyclic aromatic molecule composed of four pyrrole rings connected by methane bridges, porphyrins are found throughout nature in various types of chlorophylls and heme, making them essential for life (Ptaszek, 2013, Hiroto et al., 2017). Porphyrins can contain a metallic ion such as zinc, iron, gold, platinum, magnesium, aluminium or indium, with each metalloporphyrin possessing differing absorbance and fluorescence properties (Alyousef et al., 2021, Lum et al., 2013). Their unique electronic structure results in characteristic absorption spectra, with the main absorption peak at ~400 nm (Soret band) and smaller peaks in the 500-650 nm range (Q bands) (Ptaszek, 2013). This structure grants porphyrins highly useful for their electronic and spectroscopic properties, suitable for a wide range of applications in photodynamic and photothermal therapies (Bera et al., 2018). To enable even more functionality of porphyrins, functional groups are often added to the outside of the porphyrin rings during synthesis of the molecule or through additional functionalisation to add properties such as greater solubility in aqueous media and enhanced permeability for cancer therapy applications, which is conducted via hydrophilic substitutions (Hiroto et al., 2017).

PDT has emerged as a site-specific cancer treatment with minimal invasiveness, capable of targeting tumour cells without affecting surrounding healthy tissue. This treatment involves administering a photosensitiser PS, a fluorescent molecule that remains within the tumour tissue and is activated using a specific wavelength of light. The excited PS generates ROS, including singlet oxygen, which oxidises critical macromolecules and leads to tumour cell death (Lucky et al., 2015, Sharma et al., 2022, Kwiatkowski et al., 2018). This positively distinguishes PDT from other cancer therapies that have systemic toxicity or that cause collateral tissue damage. In this work, the goal is to harness the excited Zn Porph and, instead of generating ROS, the energy released by the electron as it returns its ground state will be absorbed by Cyt *c*, triggering an electron in the protein

to gain enough energy to cause the oxidation of Cyt *c,* ultimately causing activation of Cyt *c* and killing targeted cells.

1.2.6. Gold Nanoparticle Conjugation Strategies for Cytochrome *c* and Zn Porph

The flexibility to modify ligands on the surface of AuNPs opens the door to multiple conjugation strategies. AuNPs serve as versatile delivery platforms, facilitating the conjugation of various biomolecules including DNA/RNA, aptamers, antibodies, proteins, peptides, drugs, fluorophores, carbohydrates, and targeted molecules (Jazayeri et al., 2016, Patil et al., 2023, Zhang et al., 2019, Al-Shakarchi et al., 2018, Alea-Reyes et al., 2018, Velasco-Aguirre et al., 2015, Jain et al., 2012). For biomolecules with high electrostatic charges, such as DNA/RNA, aptamers, antibodies, proteins, peptides, fluorophores, and carbohydrates, one can replace the ligands on the AuNPs with ones of the opposite charge, leveraging electrostatic interactions for conjugation (Jo et al., 2022, Baio et al., 2013, Trabbic et al., 2021, Zhang et al., 2017, Keleştemur et al., 2017). Additionally, molecules with thiol groups, like certain DNA/RNA, antibodies, proteins, and peptides, can directly bind to AuNPs by displacing the auxiliary stabilising ligands (ASL), thereby allowing for covalent conjugation (Jazayeri et al., 2016). Meanwhile, entities bearing primary amine groups, commonly found in proteins, peptides, and some fluorophores, can be attached to the AuNP surface through carbodiimide chemistry.

To ensure the correct conjugation strategies were chosen for immobilising both Cyt c and Zn Porph to AuNPs, the electrostatic and covalent mechanism discussed in literature were investigated.

1.2.6.1. Electrostatic

1.2.6.1.1. Cytochrome *c*

The immobilisation of organic molecules or biomolecules on AuNPs can be facilitated through ligand exchange (Jain et al., 2012). The most straightforward techniques involve non-covalent binding to the AuNPs, where molecules can attach to the ligands through electrostatic interactions, specific binding affinity, or hydrophobic interactions (Yeh et al., 2012). These non-covalent interactions are widely used in delivery and sensing applications due to their reversible nature and the ease of release facilitated by weak bonding. This work used electrostatic interactions as the sole non-covalent conjugation mechanism.

Cyt *c* has a zeta potential of approximately 10 mV due to lysine residues surrounding the exposed heme edge (Petrović et al., 2005). Consequently, Cyt *c* forms an electrostatic bond with the carboxylic acid of mercaptoundecanoic acid (MUA), a phenomenon often reported in the literature (Murgida and Hildebrandt, 2001).

The redox properties of Cyt *c* are of great interest in biological sensing applications. Chen and colleagues (2002) describe how the redox behaviour of adsorbed Cyt *c* can depend on the ligands used to form a SAM layer on gold electrodes (Chen et al., 2002). The SAM layers are all terminated on the gold electrode with alkanethiols, yet the functional group Cyt *c* binds to is changed. Trimethylammonium and carboxylic acids were close to the formal potential of native Cyt *c*, whereas methyl, amine and aromatic thiol had significant negative shifting in the redox potentials, the result of a more difficult reduction. This suggests that the different functional groups of the SAM layer changed the orientation of the absorbed Cyt *c*, resulting in different redox abilities. The authors suggest that electrochemical measurements can be used for the conformation and orientation of proteins absorbed onto surfaces (Chen et al., 2002).

Further studies were undertaken into the adsorption of Cyt *c* onto SAM-coated electrodes with varying functional groups by Petrović and co-workers (2005). The study mainly focused on the effects that the surface charge of the SAMs had on the redox abilities, which were examined electrochemically (Petrović et al., 2005). Gold electrodes coated SAMs with varying functional groups to immobilise Cyt *c*, these included carbocyclic acid (negatively charged), carboxylic acid and hydroxyl groups (less negatively charged), and electrostatic and covalent and pyridine (neutrally charged). Carboxylic acids were used in the SAMs for their highly negative charge aiding electrostatic absorption of Cyt *c*. The study suggests that the absorption of Cyt *c* onto carboxylic acids changes the redox thermodynamic properties of Cyt *c* significantly. Cyt *c* immobilised to pyridine SAM, which had a neutral charge, showed no significant change in redox abilities when compared to native Cyt *c* . The authors attribute the redox change of Cyt *c* on carbocyclic acid SAMs as the result of the negatively charged SAM. It is suggested that the Debye-Hückel model can be applied to absorbed Cyt *c* to result in the net charge of Cyt *c* being converted from positive to negative. This reversal of the apparent surface charge of Cyt *c* was credited with the inversion of the slope for formal potential versus ionic strength. A shift in formal potential can only occur due to differential binding of two redox forms. When Cyt *c* binds to anionic surfaces, the oxidised form binds stronger than the reduced form (Petrović et al., 2005).

Inspired by the above study, previous work conducted in the Rawson group demonstrated that modifying the ligand's termination functional group influenced the orientation of Cyt *c* on AuNPs (Jain et al., 2021). The terminated functional groups of carboxyl, hydroxyl and amino have negative, neutral, and positive zeta potentials (ζ) respectively. The different charged functional groups would then be attracted to differently charged amino acid residues in Cyt *c*, modulating its orientation. The AuNPs with carboxyl terminated ligands were shown to have had a greater electrostatic interaction with lysine (Lys), whereas the hydroxyl and amino groups were shown to have an electrostatic interaction with glutamic acid (Glu). The cysteine (Cys) residues had been previously reported to be located on the opposite side of the heme group of Cyt *c* to Glu and leucine (Leu), and by using time-of-flight secondary mass spectroscopy (TOF-SIMS), the orientation of Cyt *c*

could be predicted (Jain et al., 2021, Baio et al., 2013). The apoptotic potential of Cyt *c* when conjugated to AuNPs was found to be correlated to its orientation, with the heme group orientated towards the carboxyl group ligand termination demonstrating the lowest ability to induce apoptosis in cancer cells (Jain et al., 2021).

One of the main advantages of using electrostatic binding in Cyt *c* immobilisation is that the bond strength is relatively weak compared to covalent bonds. This means that electrostatic bonding can be utilised in reversible Cyt *c* immobilisation whereby Cyt *c*, once immobilised, can be released when specific environmental changes occur. Wan and colleagues (2009) designed such a system with a photo-responsive azobenzene containing SAM and pH-responsive poly(acrylic acid) polymer with grafted β-cyclodextrin moieties for reversible Cyt *c* immobilisation, which can be triggered by two different external stimuli, as shown in Figure 7 (Wan et al., 2009). The pH-responsive poly(acrylic acid) is electronegative at a neutral pH and binds electrostatically with Cyt *c* (positively charged) at pH 4, the poly(acrylic acid) becomes electroneutral, and Cyt *c* is released. The dual reversibility of the system is attributed to the azobenzene SAM, which under irradiation by light, releases the poly(acrylic acid) with β-cyclodextrin moieties. Therefore, if Cyt *c* has been immobilised onto the poly(acrylic acid), it will also be released (Wan et al., 2009).

To assess the effect of conjugation methods on the functionality of Cyt *c*, the protein was also conjugated to AuNPs using a covalent mechanism.

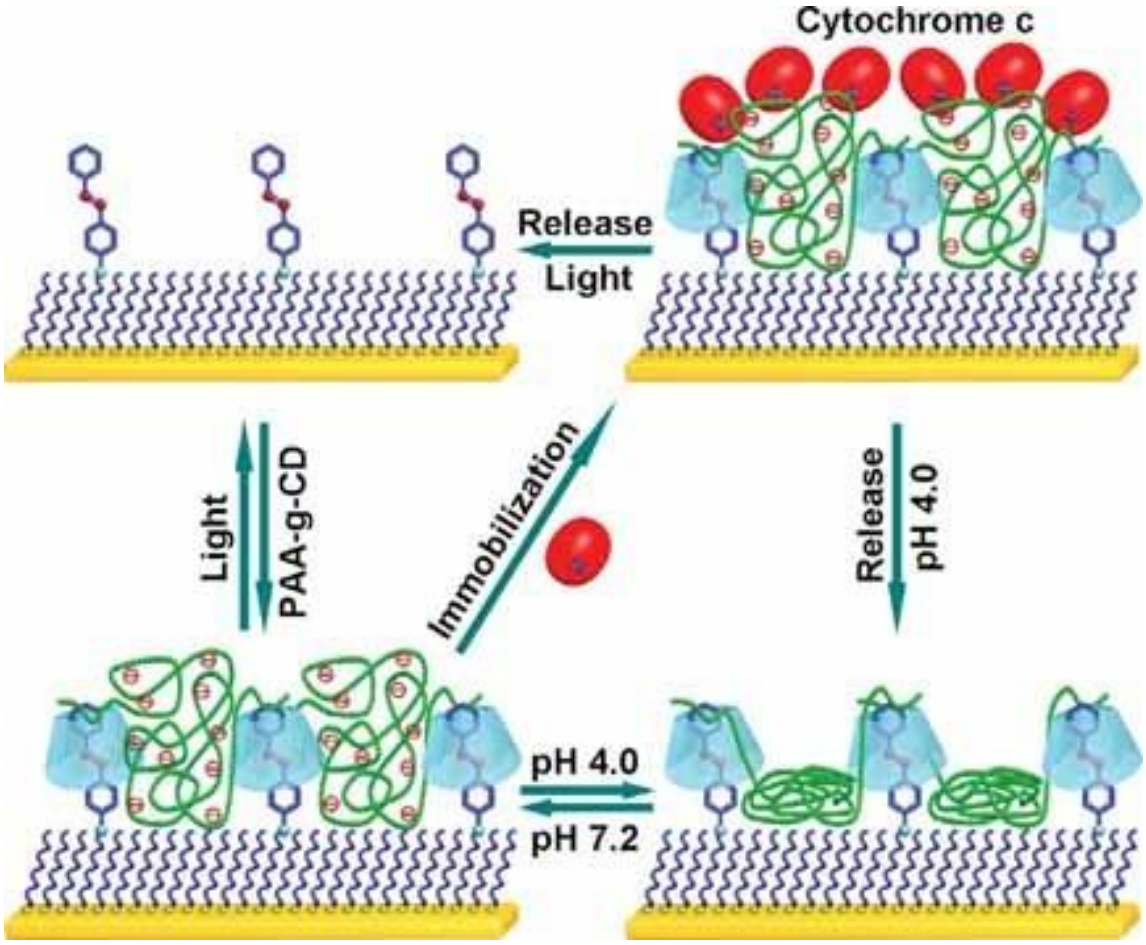


Figure 7. A reactivated biointerface with light or pH double-responsive is manufactured using photocontrolled reversible inclusion and exclusion reactions between the photoresponsive monolayers containing azobenzene and the pH-responsive poly(acrylic acid) polymer that is grafted with cyclodextrin. The double-controlled and reactivated biointerface can be used to reversibly immobilise the redox protein–Cyt c- triggered by dual external stimuli light and pH (Wan et al., 2009).

1.2.6.1.2. Porphyrin

The functional groups surrounding porphyrin rings can be modified to fit their required purpose; combining this with the ability to modify the surface chemistry of AuNPs makes electrostatic conjugation of Porphyrins to AuNPs relatively easy to achieve. It has been previously reported that the negative enthalpy and entropy of a porphyrin such as *meso*-

tetrakis(4-sulfonatophenyl)porphyrin (TPPS) enables electrostatic interactions between the porphyrin and AuNP surface, and can therefore be used as a stabilising agent for AuNPs (Bera et al., 2018). Work by Zeng and colleagues (2018) has shown that AuNPs with their surface modified with chitosan form electrostatic interactions with TPPS, while the porphyrin maintained its functionality for use in PDT for cancer therapy (Zeng et al., 2018). Sousa et al., (2017) also demonstrated that tetraruthenated porphyrin electrostatically deposited on ITO electrodes interacts with AuNPs and dramatically increases the sensitivity of the system to catechol (Sousa et al., 2017).

It can be concluded that porphyrins can be electrostatically conjugated to AuNPs without negatively effecting the functionality of the porphyrins, and can even enhance the fluorescence properties of porphyrins, as it is well reported in literature (Kim et al., 2017) (Francisco et al., 2019).

1.2.6.2. Covalent

Certain systems necessitate the strong adherence of Cyt *c* to a material in order to achieve extensive surface coverage and prevent Cyt *c* from being released. Covalent conjugation is a stronger conjugation force than electrostatic interactions and therefore a better option for systems that may utilise Cyt *c*'s redox ability for biosensing purposes. For accurate detection, the material must firmly bind with Cyt *c*, ensuring that the sensing occurs at the material's surface. If Cyt *c* were to be lost during the sensing process, it would lead to incorrect results due to alterations in the amount of Cyt *c* present on the surface. Murphy and colleagues (2019) exploited the redox properties of Cyt *c* to produce an electrochemical biosensor for the detection of hydrogen peroxide (Murphy et al., 2019). The biosensor comprises of Cyt *c* covalently bound on a carboxyl-functionalised ionic liquid/multiwalled carbon nanotubes hybrid. The carbon nanotubes were functionalised with a ligand terminated with a carboxylic acid; carbodiimide (EDC/NHS) cross-coupling reaction then utilised the free amino group of Cyt *c* with the carbocyclic acid to form an amide bond, as demonstrated in Figure 8(Murphy et al., 2019, Keleştemur et al., 2017).

As outlined above, the ability to modify the functional groups of porphyrins also enables the use of cabodiimide cross-coupling to covalently conjugate the porphyrins to AuNPs. In this work, carbodiimide chemistry converts the electrostatic bond between the carboxylic acid and Cyt *c* or Zn Porph to a covalent amide bond. The schematic representation of the mechanism in Figure 8 shows how EDC in 5.5 to 6.5 pH MES buffer is added to AuNPs functionalised with ligands terminating in a carboxylic acid (in the same buffer solution), which then forms an unstable intermediate. Aqueous NHS is then added to form a stable amine-reactive NHS ester. Then, when a molecule is added to the solution containing a primary amine, such as Cyt *c* or Zn Porph, an amide bond can be formed between the ligand and Cyt *c* or Zn Porph. Previous studies use EDC only to covalently bind Cyt *c* to carboxylic acids; this can be achieved yet it is more prone to hydrolysis of the reaction due to instability (Collinson et al., 1992).

\

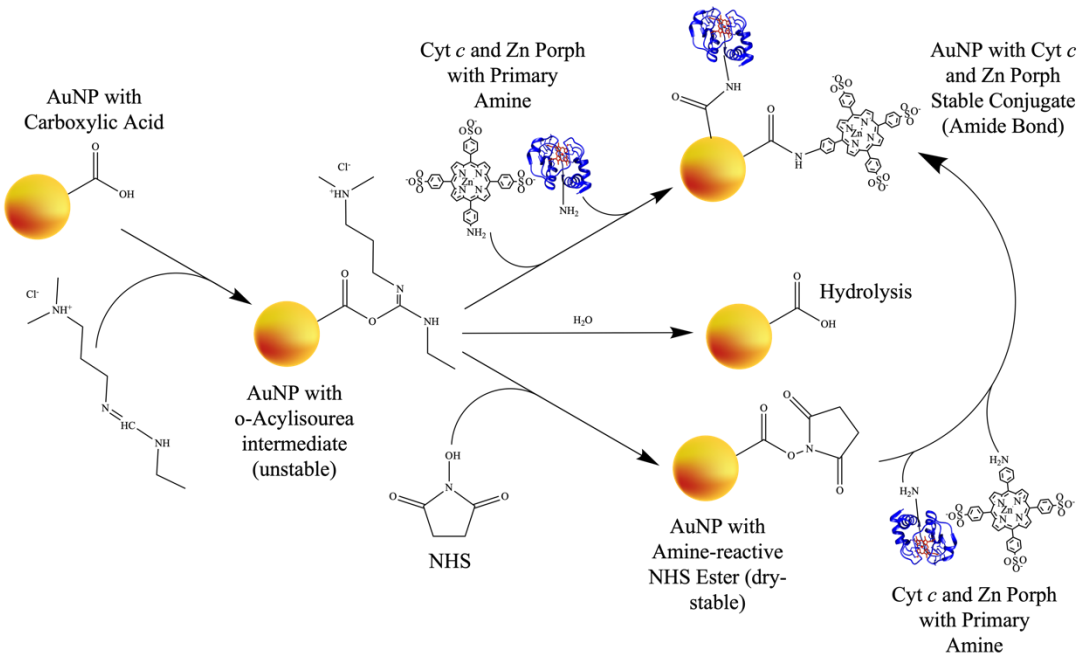


Figure 8: Schematic representation of carbodiimide cross-coupling of Cyt *c* and Zn Porph to AuNPs using NHS as a stabilising agent.

1.2.7. Electrochemistry

One method in which the redox ability of Cyt *c* free in solution can be compared after conjugation to AuNPs utilises electrochemistry. Defined as the application of electricity to chemistry, electrochemistry can be specified as the science of interactions between phases that contain electrons and those that contain ions (Hibbert, 1993). The study of electrochemistry spans biology, chemistry, physics and material sciences. Understanding charge movement and interaction lies in the field of physics, however, understanding charge movement and interactions within a biological setting such as in a cell incorporates materials science of electrodes and organic/ inorganic chemistry due to the species within the cell (Hibbert, 1993). As a result of this involvement throughout the sciences, there is a large spectrum of applications for electrochemistry, including macro and microelectronics, optics, sensors, bioelectronics (Sanjuan-Alberte et al., 2018) and uses within manufacturing, such as in the automotive industry (Schlesinger, 2008). Electrochemistry is an important notion when working with molecules conjugated to nanoparticles, as the electrochemical ability of the molecules may change after conjugation, influencing their function. Due to its redox properties and ability to initiate apoptosis, Cyt *c* is of great interest for electrochemical applications.

1.2.8. Cyclic Voltammetry

Cyclic voltammetry (CV) is a powerful technique which is most commonly used to assess the reduction and oxidation (redox) ability of molecular species (Elgrishi et al., 2018). CV can also be used to study electron transfer kinetics. A cyclic voltammogram commonly resembles Figure 9, where the x-axis is a parameter imposed on the system and the y-axis is the response. In this example, the parameter is the applied potential, and the response is the current (i) (Elgrishi et al., 2018), as shown in Figure 9. The redox peaks produced by 30 µM Cyt *c* free in solution are clearly defined, compared to the control of PBS. Two conventions are commonly used to report on CV data: the US Convention and the IUPAC Convention (Figure 9) (Elgrishi et al., 2018). The example CVs seen in Figure 9 compare

the IUPAC Convention to the US convention and are of 180° rotation of each other. The IUPAC Convention CVs are used in this work, showing the lowest potential on the left and the highest on the right of the *x* axis, with the *y* axis oxidation peak on the upper side of the signal and reduction on the bottom.

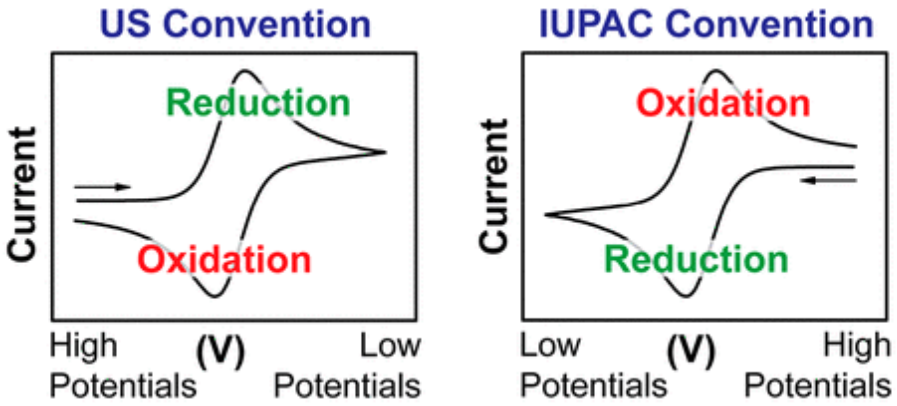


Figure 9. Example cyclic voltammogram demonstrating the difference between the US and IUPAC Convention (Elgrishi et al., 2018).

The Nernst equation (Equation 2) is used to describe the equilibrium in cyclic voltammograms. In Equation 2, the potential of an electrochemical cell (E) relates to the standard of a species (E^0) and the activities of oxidised (Ox) and reduced (Red) components in a system which is at equilibrium.

$$E = E^0 + \frac{RT}{nF} ln \frac{(Ox)}{(Red)} = E^0 + 2.3026 \frac{RT}{nF} log_{10} \frac{(Ox)}{(Red)}$$

Equation 2.

The Nernst equation is effective in predicting how a system will respond to different concentrations of species in solution or a change in the potential at the electrode (Elgrishi et al., 2018). The scan rate is typically expressed in mV per second (mV/s). Increasing the scan rate decreases the size of the diffusion layer, resulting in higher currents. Randles-Sevcik equation (Equation 3) describes how the peak current i_p (amps) increases with the square root of the scan rate v (V/s), where n is the number of electrons in the redox event,

A (cm^2) is the surface area of the electrode, D_0 (cm^2/s) is the diffusion coefficient of the analyte, and C^0 (mol cm^{-3}) is the concentration of the analyte (Elgrishi et al., 2018).

$$i_p = 0.4463\, nFA\, C^0 (\frac{nFvD}{RT})^{\frac{1}{2}}$$

Equation 3.

In this work, equations are combined to determine the heterogeneous rate constant (electron transfer rate) of Cyt *c* when conjugated to AuNPs and when free in solution, to assess the effect the conjugation has on the redox ability of Cyt *c*.

1.2.9. Differential Pulse Voltammetry

Another form of electrochemical technique is differential pulse voltammetry (DPV). In DPV, small amplitude pulses are performed on a linear ramp with the current measured before and after the application of each pulse (Figure 10). The difference in current can then be calculated. The main purpose of the technique is to reduce the background, as the Faraday current is free of capacitive current. DPV being low in capacitive current is therefore advantageous, as this means the technique is highly sensitive to any changes in current. Small steps between pulses means that the redox peaks from the analyte are narrower than other voltammetry techniques, and so DPV is often used for analytes that have close oxidation potentials (Venton and DiScenza, 2020).

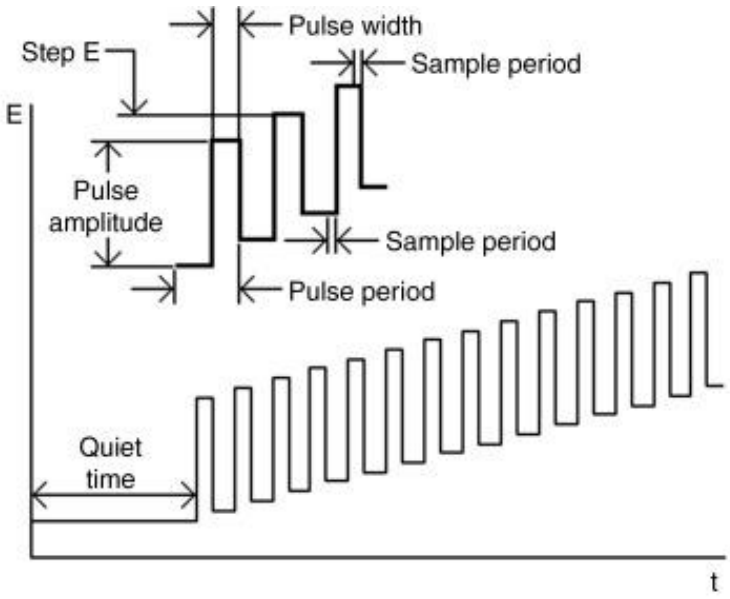


Figure 10. Representation of potential wave form for DPV (Ribeiro et al., 2017).

This technique differs from cycling voltammetry in that there is a linear sweep with interval pulses, compared a cycle of alternating potential from negative to positive or vice versa.

1.2.10. Electrochemical applications of Cytochrome *c*

The redox properties of Cyt *c* are of great use for electrochemical characterisation and applications: for instance, techniques such as CV are ideal for interpreting how the electrochemical properties of the protein change because of environmental or structural alterations. The variances in electrochemical behaviour can indicate a change in function, a particularly significant observation if Cyt *c* is being utilised for one of its numerous biological roles. Wang and colleagues (2019) used Cyt *c* as a model for redox-active proteins and were able to show that when subjected to more acidic pH conditions, the protein would partially unfold, resulting in potential shifts and increased electron transfer rates when compared to Cyt *c* in its native form (Wang et al., 2019). Liu and colleagues (2003) had also previously demonstrated that it was possible to obtain the electron transfer rate for Cyt *c* when conjugated to 11 different SAMs with differing lengths and functional

groups. The electron transfer rate ranged from $\leq 10^{-4}$ to 10^{-1} cm/s, explained by changes in electronic coupling and effective potential near the electrode surface (Liu et al., 2003). As well as the uses electrochemical techniques have in understanding the structure and function of Cyt *c*, other electrochemical applications utilising Cyt *c* include biosensors and biofuels.

1.2.11. Cytochrome *c* in biosensing

Biosensors measure biological or chemical reactions by producing signals corresponding to the concentration of analyte in the reaction. Biosensors are used in disease monitoring, drug discovery, detecting pollutants, disease-causing microorganisms, and markers of diseases in body fluids (e.g., blood, urine, saliva, sweat) (Bhalla et al., 2016). The use of Cyt *c* in biosensing first involves the immobilisation of the protein on electrodes or material such as NPs, which, as previously discussed, can be achieved by electrostatic interaction between the positively charged protein and negatively charged surface (1.2.6.1) or by a covalent mechanism (1.2.6.2) (Aghamiri et al., 2018). Cyt *c* has been immobilised on a variety of materials for use as a biosensor, including but not limited to AuNPs (Jensen et al., 2007), graphene oxide, multi-walled carbon nanotubes (Bathinapatla et al., 2016), single walled carbon nanotubes (Yin et al., 2007), niobium oxide (Xu et al., 2003), cobalt oxide NP (Mohammadi et al., 2011) and cadmium oxide NP (Negahdary et al., 2012). A notable instance of the use of Cyt *c* as a biosensor was conducted by Zhu et al., (2009) where Cyt *c* immobilised on Au/Ag multilayer films was shown to still maintain its enzymatic ability towards H_2O_2, therefore being able to be used as a H_2O_2 biosensor. The work showed the H_2O_2 biosensor to have a high selectivity and low limit of detection, with long stability (Zhu et al., 2009). Another example is provided by Plowman et al., who modified a gold electrode by using 80 nm diameter and 350 nm length gold nanospikes to immobilise the Cyt *c* with a monolayer of the cysteine, resulting in a partial unfolding of the protein. This biosensor was used to measure dopamine via DPV and showed high selectivity when interfering species such as ascorbic acid and uric acid were introduced (Plowman et al., 2010). The applications for Cyt *c* as a biosensor are

ultimately vast as the redox process is very well reported, and so any system that results in a change of the electrochemical properties of Cyt *c* can be detected.

1.2.12. Cytochrome *c* in biofuels

The dwindling reserves of non-renewable fossil fuels forcing the need for alternative sources of electricity with a lower environmental impact makes biological fuels of great interest (Samukaite Bubniene et al., 2022). There are two types of biofuels, microorganism-based biofuel cells (Kisieliute et al., 2019) or enzyme-based biofuel cells (Ramanavicius et al., 2015). A significant advantage of enzymes as catalysts is their high selectivity as they are only able to catalyse specific reactions. This characteristic, along with their general harmlessness, activity at ambient or human body temperatures, and effectiveness in near-neutral pH conditions, makes them well-suited for compatibility with living organisms (Samukaite Bubniene et al., 2022). Moreover, most biofuel cells harness energy from renewable fuels such as ethanol, glucose, sucrose, glycerol, acetate, phenol, lactate, ribitol, and various organics found in wastewater, further emphasising their ecological value (Pant et al., 2010, Yuan et al., 2016). Biofuel cells that utilise enzymes, particularly glucose biofuel cells, are the subject of considerable scientific research due to their immense potential for real-world applications (Samukaite Bubniene et al., 2022). This is largely because living organisms naturally provide an ample and continuously replenishing supply of glucose and oxygen: essential components for these cells (Karajić et al., 2020). A key benefit of these biofuel cells is that their fuel source can be constantly renewed with practically no restrictions. However, they still present a challenge in the form of comparatively low power output. To mitigate this issue, redox mediators are incorporated into the system. This makes Cyt *c* of great interest for enzyme-mediated biofuels as the redox properties of the heme group in the protein can act as intermediaries between the electrode and enzyme, by carrying electrons. Samukaite Bubniene and colleagues (2022) used graphite rods modified with Cyt *c* as a redox mediator to improve electron transfer efficiency (Samukaite Bubniene et al., 2022). The study showed that by increasing the glucose content in the system the current density increased and the equilibrium of the system was reached quicker as the reaction occurred

at a faster rate (Samukaite Bubniene et al., 2022). The electron transport capabilities of Cyt *c* were also utilised in an enzymatic biofuel cell designed by Katz and Willner (2003) where they detail a electro-switchable and tunable biofuel cell that is based on the biocatalysed oxidation of glucose (Katz and Willner, 2003). The anode and the cathode are each covered with a film made of copper and poly(acrylic acid). Pyrroloquinoline quinone and the flavin adenine dinucleotide are attached to this film on the anode, and another molecule, Apo-glucose oxidase, is added to create a glucose oxidase electrode. On the cathode, the same film is used to attach Cyt *c*, which is then connected to cytochrome oxidase. When an electrical charge is applied to the system, the copper in both films undergoes a reodx reaction. This results in an electrically conductive network that connects the glucose oxidase electrode at the anode and the cytochrome oxidase/cytochrome c electrode at the cathode, thus facilitating the flow of electricity (Katz and Willner, 2003).

Overall, the functionality of Cyt *c* appears to be maintained after conjugation, therefore supporting the use case for Cyt *c* in this work as an apoptotic initiator.

1.3. Objectives

The primary objectives of this research are to lay the groundwork for a cancer treatment strategy that prompts death in cancerous cells which have internalised multifunctional AuNPs. This strategy is specifically designed to activate only in the presence of light at a specific wavelength.

In the first experimental chapter of this study, it is hypothesised that the successful synthesis and characterisation of AuNPs will allow for the effective multifunctionalisation with Cyt *c* and Zn Porph. Further, it is expected that through characterisation, the size of the AuNPs can be accurately determined, and the successful conjugation of Cyt *c* and Zn Porph to AuNPs can be confirmed. These steps allowed for precise quantification of the molecules conjugated to AuNPs.

In the subsequent experimental chapter, it is hypothesised that Cyt *c* will maintain its redox properties after being conjugated to AuNPs. The structural characteristics of the protein were compared post-conjugation to its natural form, speculating that the conjugation process may not significantly influence its redox functionalities. Electrochemical techniques, including CV and DPV, will be utilised to evaluate the post-conjugation redox capacities of Cyt *c*.

In the final phase of this study, it is hypothesised that the application and internalisation of multifunctional AuNPs to cancer cells, followed by exposure to a specific light wavelength, would be an effective approach for light-activated cancer therapy. It is anticipated that this novel treatment strategy will demonstrate significant cytotoxicity towards cancer cells while preserving the viability of untreated healthy cells.

2. Synthesis and Characterisation of AuNPs Multifunctionalised with Cyt *c* and Porphyrins

Parts of this chapter have been published in Analytical Chemistry (Potts et al., 2023).

2.1. Aims and Objectives

The primary objectives of the work reported in this chapter are to verify the conjugation of Cyt *c* and Zn Porph to AuNPs, and to accurately measure the concentration and quantity of these molecules per AuNP. Ensuring the precise measurement of the molecules conjugated to AuNPs is crucial for administering an optimal dose, and thus is a vital aspect of this study that is frequently disregarded in the literature.

2.2. Abstract

In this chapter, it is described how AuNPs of 20, 50, and 100 nm in diameter were successfully synthesised and functionalised with Cyt *c* and Zinc(II) 5-(4-aminophenyl)-10,15,20-tris-(4-sulfonatophenyl)porphyrin (Zn Porph). A combination of dynamic light scattering (DLS), zeta potential, UV-Visible absorption spectroscopy (UV-Vis), and X-ray photoelectron spectroscopy (XPS) was employed to characterise the multifunctionalised AuNPs. Thiol-PEG-carboxyl and mercaptoundecanoic acid (MUA) ligands were utilised for covalent and electrostatic conjugation, resulting in stable multifunctionalised AuNPs without aggregation.

A novel deconvolution approach for UV-Visible absorption spectra enabled the accurate determination of the concentrations and exact number of molecules of Cyt *c* and Zn Porph bound to the AuNPs. Precise concentration assessment is critical for subsequent research stages, in order to evaluate the impact of the conjugated molecules. The work in this

chapter lays the foundation for what will ultimately be the purpose of this thesis: to assess whether Cyt *c* and Zn Porph conjugated to AuNPs can induce apoptosis in cancer cells when exposed to a light stimulus.

2.3. Introduction

Current cancer treatments include surgical intervention (extraction of the tumour), chemotherapy, radiation therapy, or a combination of all three fields (Senapati et al., 2018). Although these treatments can be effective in killing cancerous cells, they are also non-selective. Consequently, healthy cells are often damaged or killed during treatment, causing unpleasant and unintentional side effects in the patients, including hair and appetite loss and nausea, to name but a few (Senapati et al., 2018). In this work, an AuNP potential treatment is presented that can be applied to tissue immediately after tumour removal, killing any remaining cancerous cells, and eliminating the need for systemic treatments that can cause healthy cell death.

The ability to functionalise AuNPs with additional molecules has led to an interest in designing more complex systems with multiple molecule types conjugated to each AuNP, known as multifunctionalised AuNPs. These multifunctionalised AuNPs have a significant advantage over AuNPs conjugated with just one type of molecule, as they can be used for much broader applications (Mieszawska et al., 2013); an example is in drug delivery systems, where a targeting agent and drug are conjugated to the surface of the particle to direct the effect of the drug to a specific cell type or region (Hosta-Rigau et al., 2010, Mohamed et al., 2014, Taghdisi et al., 2016).

In this chapter, the synthesis and characterisation of multifunctionalised AuNPs utilising the apoptotic ability of Cyt *c* for cancer treatment are described. The concentration of the conjugated molecules on the surface of the AuNPs is an important factor that determines its nano-bio interactions and, eventually, its biological function. In pharmaceutical applications, the concentration of the conjugated molecules is a significant factor in modulating drug dose thresholds. In biosensing, the minimum concentration of analyte

that can be detected is known as its limit of detection or sensitivity (Bhalla et al., 2016). Working beyond the limit of detection will make the results inaccurate and invalid; consequently, there is a need to develop a simple, robust, and fast analytical method to facilitate surface quantification of AuNPs functionalised with more than one molecule. The group has previously reported on the development of a multifunctional AuNP system functionalised with Cyt *c* for cell-induced apoptosis (Jain et al., 2021). Cyt *c* is a biomolecule of interest due to its redox properties, which make it useful for biosensing and its ability to induce apoptosis, lending it to applications in drug delivery (Manickam et al., 2017, Guo et al., 2018, Delinois et al., 2021). UV-visible absorption spectroscopy was utilised to quantitate the presence of Cyt *c* on AuNPs functionalised with ligands of varying electrostatic charge (Jain et al., 2021). The presence of monolayers or multilayers is also important to establish, particularly when considering the concentration of drugs or biomolecules conjugated to AuNPs, as a multilayer may interfere with their function, leading to an inaccurate representation of drug/biomolecule delivery or activity.

The concentration of biomolecules conjugated to AuNPs can be determined using additional photometric and fluorometric assays. These involve monitoring the change in absorbance intensity before and after a molecule is conjugated or by fluorescently tagging the biomolecules and observing a rise in fluoresce after conjugation is confirmed. The intensity change in both methods can be used to calculate the concentration of conjugated molecules (Geißler et al., 2021). More costly techniques, such as matrix-assisted laser desorption/ionisation time of flight (MALDI-TOF) mass spectrometry (MS), can be used to quantify proteins conjugated to NPs, by digesting the proteins and analysing the peptide fragments after the addition of an isotope-labelled internal standard (Ju and Yeo, 2012). The analytical methodology used to determine the exact concentration of each functional molecule in a multifunctionalised material is not often thoroughly described in the literature. Furthermore, the analysis of multifunctionalised AuNPs by UV-vis absorption spectroscopy is complicated by the molecular complexity caused; for example, conjugated molecules, such as porphyrins and Cyt *c*, have similarities in their absorption spectrums, which could lead to erroneous calculated values.

To address the above problem, this chapter reports a new analysis protocol to quantify a model multifunctionalised AuNP system that would allow the accurate calculation of the concentration of different molecules attached to the surface of AuNPs. Initially, AuNPs with a diameter of 20 nm and 50 nm were synthesised and functionalised with Zn Porph and Cyt *c*. Using CASA-XPS, a method was devised to deconvolute the merged absorption spectra of the two types of conjugated molecules. This enabled an accurate identification of the peak heights of each conjugated molecule, thus the concentrations could be calculated for each. The outlined method can be used as a guide by researchers to tailor conjugation parameters for obtaining multifunctionalised AuNPs for the desired application.

In this work, the materials are characterised using UV-Vis, DLS, TEM and XPS to successfully confirm and calculate the coverage of the functionalisation.

2.4. Methods

2.4.1. Materials

Equine heart cytochrome *c* (Cyt *c*) (≥ 95%), *N*-(3-dimethylaminopropyl)-*N*′-ethylcarbodiimide hydrochloride (EDC), gold(III) chloride trihydrate ($HAuCl_4 \cdot 3H_2O$) (99.99%), thiol-PEG-carboxyl (HS-PEG-COOH) (2000 Da), 2-(*N*-morpholino)ethanesulfonic acid, 4-morpholineethanesulfonic acid monohydrate (MES monohydrate) (≥99.0%), *N*-hydroxysuccinimide (NHS) (98%), sodium citrate tribasic dihydrate (99%) were purchased from Sigma Aldrich. 5-(4-Aminophenyl)-10,15,20-tris-(4-sulfonatophenyl)porphyrin (Porph) and Zinc(II) 5-(4-aminophenyl)-10,15,20-tris-(4-sulfonatophenyl)porphyrin (Zn Porph) were purchased from Porphychem, France. Milli-Q® water at a resistivity of 18.2 MΩ provided by Milli-Q® direct water purification system was used for experiments.

2.4.2. Synthesis of 20 nm citrate capped AuNPs (cit-AuNPs)

1 mL of $HAuCl_4.3H_2O$ (39.38 mg, 0.1 mol) was added to 89 mL of Milli-Q® water and was brought to boil under constant stirring. Aqueous sodium citrate solution (38.8 mM, 10 mL) was rapidly added to the boiling solution, causing a colour change from yellow to burgundy. The solution was boiled for 10 minutes before allowing it to cool down at room temperature under stirring. The solution was then filtered using a 0.22 μm nylon filter to remove any large aggregates and stored at 4 °C until further use.

2.4.3. Synthesis of 50 nm citrate capped AuNPs (cit-AuNPs)

A total of 100 μL of $HAuCl_4.3H_2O$ (1% W/V) was added to a scintillation vial containing 9.488 mL of Milli-Q® water, before the addition of 20 nm AuNPs (290 μL) which was then set to stir at room temperature for 10 minutes. 22 μL of Sodium citrate tribasic dihydrate (1% W/V) was then added to the stirring solution and immediately followed by the addition of 100 μL of Hydroquinone (30 mM). The solution rapidly changed colour and was mixed for a further 10 minutes. The obtained coloured solution was filtered using 0.22 μm filter and stored at 4 °C until further use.

2.4.4. Synthesis of 100 nm citrate capped AuNPs (cit-AuNPs)

A total of 100 μL of $HAuCl_4.3H_2O$ (1% W/V) was added to a scintillation vial containing 9.748 mL of Milli-Q® water before the addition of 20 nm AuNPs (30 μL), which was then set to stir at room temperature for 10 minutes. 22 μL of Sodium citrate tribasic dihydrate (1% W/V) was then added to the stirring solution and immediately followed by the addition of 100 μL of Hydroquinone (30 mM). The solution rapidly changed colour and was mixed for a further 10 minutes. The obtained coloured solution was filtered using 0.22 μm filter and stored at 4 °C until further use.

2.4.5. Functionalisation of 20, 50 and 100 nm cit-AuNPs with PEG

A 1 mL solution of aqueous thiol-PEG-carboxl (2000 Da, 1 mM) was added to 20 mL of 20 nm or 50 nm cit-AuNPs under stirring and left overnight. The following day the solution was washed twice using centrifugation at 13,400 rpm for 30 minutes to form a pellet of AuNP functionalised with PEG-COOH (AuNP-PEG). The pellet was then resuspended in ultrapure water and stored at 4°C until further use.

2.4.6. Functionalisation of 20, 50 and 100 nm cit-AuNPs with PEG, Cyt *c* and Zn Porph

For covalent conjugation of Cyt *c* and Zn Porph on to 20, 50 and 100 nm AuNPs, a fresh EDC/NHS mix solution was made by adding EDC (19.17 mg, 100 μmol) and NHS (23 mg, 200 μmol) in 1 mL of MES buffer (10 mM, pH 5). A total of 100μL of EDC/NHS mix was added to the 1 mL aqueous solution of thiol-PEG-carboxyl (2000 Da, 1 mM) and was left stirring for 1 hour. To this solution, aqueous Cyt *c* (1 mL, 200 μM) and aqueous Zn Porph (1 mL, 200 μM) were added under constant stirring, the solution was then left stirring for 24 hours. For the synthesis of AuNP-PEG-Cyt *c,* only Cyt *c* (1 mL, 200 μM) was added, and in AuNP-PEG-Zn Porph, only Zn Porph (1 mL, 200 μM) was added to the EDC/NHS activated thiol-PEG-carboxyl. After the solution was stirred for 24 hours, 20 mL of 20, 50 or 100 nm cit-AuNPs were added and mixed for a further 24 hours. The solution was then centrifuged at 13,400 rpm for 3 cycles using Milli-Q® water to remove any unbound Cyt *c* and Zn Porph. The obtained pellet was resuspended in 1 mL of Milli-Q® water to yield a monodispersed sample of AuNP-PEG-Cyt *c*/Zn Porph.

2.4.7. Deconvolution modelling of Cyt *c* and Zn Porph conjugated to AuNPs

Deconvolution of the UV-visible absorption spectrum to confirm the conjugation of Cyt *c* and Zn Porph was performed using CASA-XPS. The absorption spectra of the chosen samples were imported into CASA-XPS as text files. The graph was then plotted, and the x-axis was changed to start with the smallest number near the origin. The region of interest was then selected using the regions tool, and the background setting was changed to 'linear' as this closely represents how the spectra would look without the conjugated molecules. The convoluted peaks in the spectra were then found using the components tab, by adding the components that were thought to be in the region. The components were then fitted to the spectra using Levenberg-Marquardt algorithm LN (LN-MIE-Gans) fitting. The resulting spectra data was copied to Microsoft Excel before being added to GraphPad Prism 9 for analysis.

2.4.8. Functionalisation of 20, 50 and 100 nm cit-AuNPs with MUA

A 1 mL solution of MUA (1 mM) in 90:10 Milli-Q® water: ethanol was added to 20 mL of 20 nm or 50 nm cit-AuNPs under stirring and left overnight. The following day the solution was washed twice using centrifugation at 13,400 rpm for 30 minutes to form a pellet of AuNP functionalised with MUA (AuNP-MUA). The pellet was then resuspended in ultrapure water and stored at 4 °C until further use.

2.4.9. Functionalisation of 20, 50 and 100 nm cit-AuNPs with MUA, Cyt *c* and Zn Porph Covalently

For covalent conjugation of Cyt *c* and Zn Porph onto 20, 50 and 100 nm AuNPs, a fresh EDC/NHS mix solution was made by adding EDC (19.17 mg, 100 µmol) and NHS (23 mg, 200 µmol) in 1 mL of MES buffer (10 mM, pH 5). A total of 100µL of EDC/NHS

mix was added to the 1 mL of MUA (1 mM) in a 90:10 Milli-Q® water: ethanol solution and was left stirring for 1 hour. To this solution, aqueous Cyt *c* (1 mL, 200 μM) and aqueous Zn Porph (1 mL, 200 μM) were added under constant stirring, and left stirring for 24 hours. After 24 hours, 20 mL of 20, 50 or 100 nm cit-AuNPs were added and mixed for a further 24 hours. The solution was then centrifuged at 13,400 rpm for three cycles using Milli-Q® water to remove any unbound Cyt *c* and Zn Porph. The obtained pellet was resuspended in 1 mL of Milli-Q® water to yield a monodispersed sample of AuNP-MUA-Cyt *c*/Zn Porph Cov.

2.4.10. Functionalisation of 20, 50 and 100 nm cit-AuNPs with MUA, Cyt *c* and Zn Porph Electrostatically

For electrostatic conjugation of Cyt *c* and Zn Porph on to 20, 50 and 100 nm AuNPs, aqueous Cyt *c* (1 mL, 200 μM) and aqueous Zn Porph (1 mL, 200 μM) were added to the 1 mL of MUA (1 mM) in a 90:10 Milli-Q® water:ethanol solution and left stirring for 24 hours. After 24 hours, 20 mL of 20, 50 or 100 nm cit-AuNPs were added and mixed for a further 24 hours. The solution was then centrifugation at 13,400 rpm for three cycles using Milli-Q® water to remove any unbound Cyt *c* and Zn Porph. The obtained pellet was resuspended in 1 mL of Milli-Q® water to yield a monodispersed sample of AuNP-MUA-Cyt *c*/Zn Porph Electro.

2.4.11. LN-MIE-Gans modelling of cit-AuNPs and multi-functionalized AuNPs

Model fitting on AuNP spectra to predict their size was conducted on Wolfram Mathematica using the LNMG Fit 1.0 model obtained from the literature (Amendola and Meneghetti, 2009).

2.4.12. Instruments

Ultraviolet-Visible absorption (UV-vis absorption) spectra were obtained using a Varian Cary 50 bio-UV-visible absorption spectrophotometer. Centrifugation was performed on a Spectrafuge 24D. The transmission electron microscope (TEM) images were captured using JEOL FX 2000 TEM at 200 kV. The histogram of AuNP size distribution was determined from the TEM images using ImageJ® software. Dynamic light scattering (DLS) and Zeta potential experiments were conducted on a Malvern Zetasizer nano.

2.5. Results and Discussion

2.5.1. Characterisation of Cyt *c* and Zn Porph

The research presented in this thesis is centred on the delivery of Cyt *c* and Zn Porph to cancer cells, with the aim of initiating apoptosis through a photo-induced energy transfer event between Zn Porph and Cyt *c*. This process results in the oxidation and subsequent activation of Cyt *c*. To achieve this objective, the successful conjugation of Cyt *c* and Zn Porph to a specialised delivery system is required, along with the determination of their respective concentrations to establish a direct correlation between these components.

Cyt *c* and Zn Porph possess porphyrin moieties within their structures, giving rise to prominent and distinct peaks in their ultraviolet-visible (UV-Vis) absorption spectra. As depicted in Figure 11, the Soret band peaks at 408 nm for oxidised Cyt *c* (Cyt *c* Ox) and 415 nm for reduced Cyt *c* (Cyt *c* Red) correspond to literature values (Fisher et al., 1973). The Soret band peak for Zn Porph can be identified at 423 nm.

Although the Soret band peak shift between Cyt *c* Ox and Cyt *c* Red is relatively small, a notable difference is observed in the 500-600 nm spectral region. The spectrum for Cyt *c* Ox in this region displays a smooth, singular peak, whereas Cyt *c* Red exhibits two distinct, sharp peaks (Figure 11). Furthermore, the Q bands of Zn Porph can be identified within the same spectral region, specifically at approximately 560 nm and 600 nm.

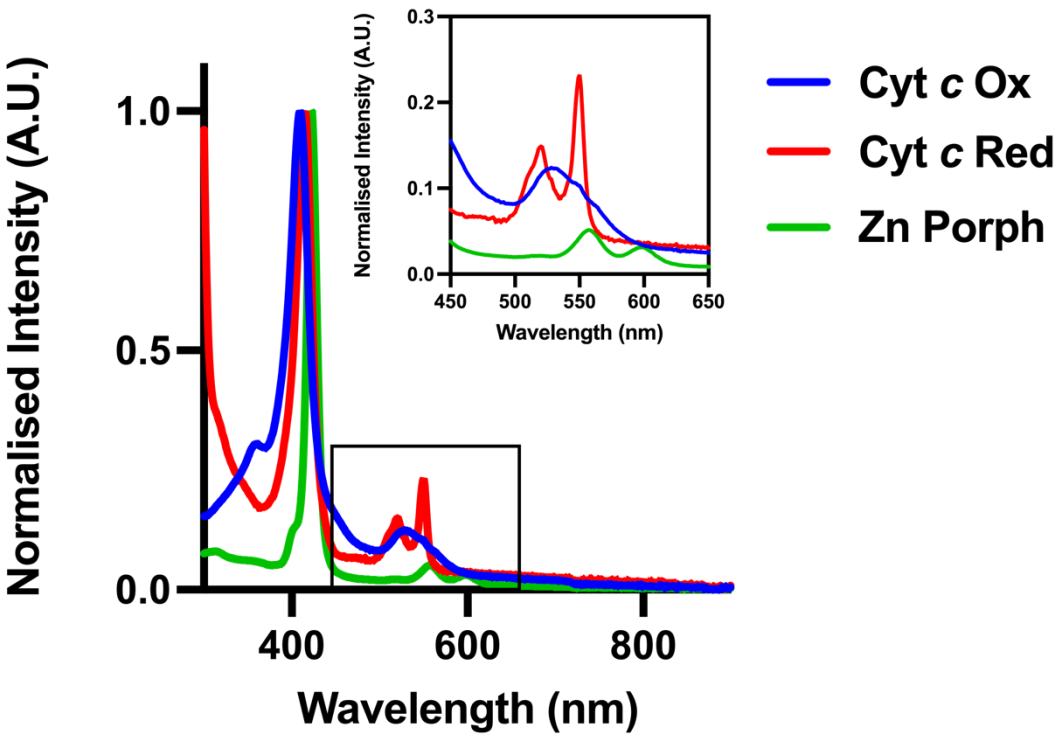


Figure 11. UV-Vis absorption spectra of Cyt *c* Ox (blue line), Cyt *c* Red (red line) and Zn Porph (green line). The inset is a magnified area between 450-650 nm.

In this work, gold nanoparticles (AuNPs) are the carrier for the delivery of conjugated Cyt *c* and Zn Porph , enabling uptake of Cyt *c* and Zn Porph into cancerous cells for cancer treatment.

2.5.2. Synthesis and Characterisation of 20 nm AuNPs with thiol-PEG-carboxyl, Cyt *c* and Zn Porph

To begin this project, AuNPs were synthesised and functionalised with Cyt *c* and Zn Porph. The Turkevich method was employed to synthesise cit-AuNPs with a diameter of approximately 20 nm, as detailed in section 2.4.2. The freshly prepared cit-AuNPs were functionalised with thiol-PEG-carboxyl with Cyt *c* and Zn Porph covalently conjugated using carbodiimide coupling chemistry (AuNP-PEG-Cyt *c*/Zn Porph), represented in Figure 12.

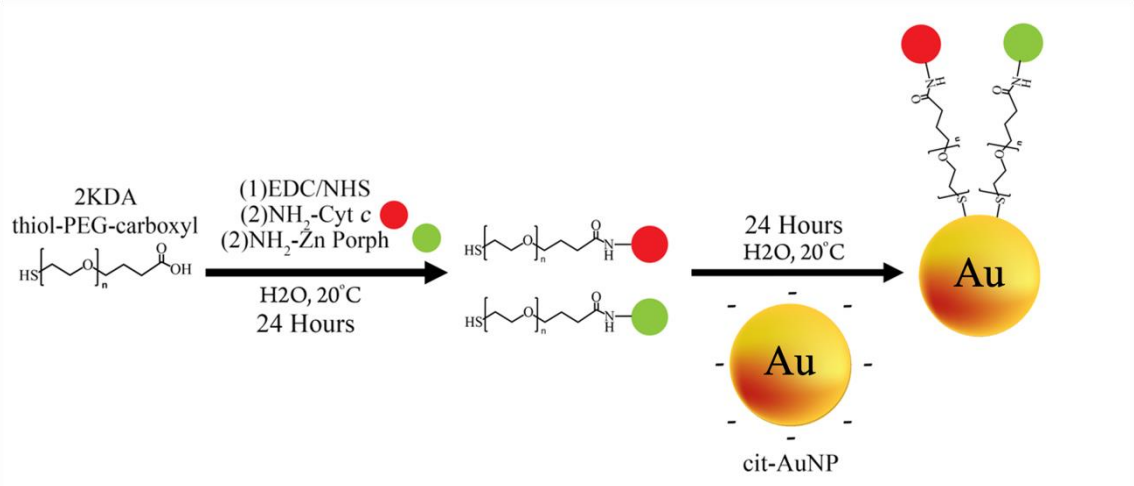


Figure 12. Schematic representation of the functionalisation method for AuNP-PEG-Cyt *c*/Zn Porph Cov.

The AuNPs used in this work are depicted in Figure 13A and are named the cit-AuNPs, AuNP-PEG, AuNP-PEG-Zn Porph, AuNP-PEG-Cyt *c* and AuNP-PEG-Cyt *c*/Zn Porph. The structure of Zn Porph and Cyt *c* are displayed in Figure 13B and C, respectively.

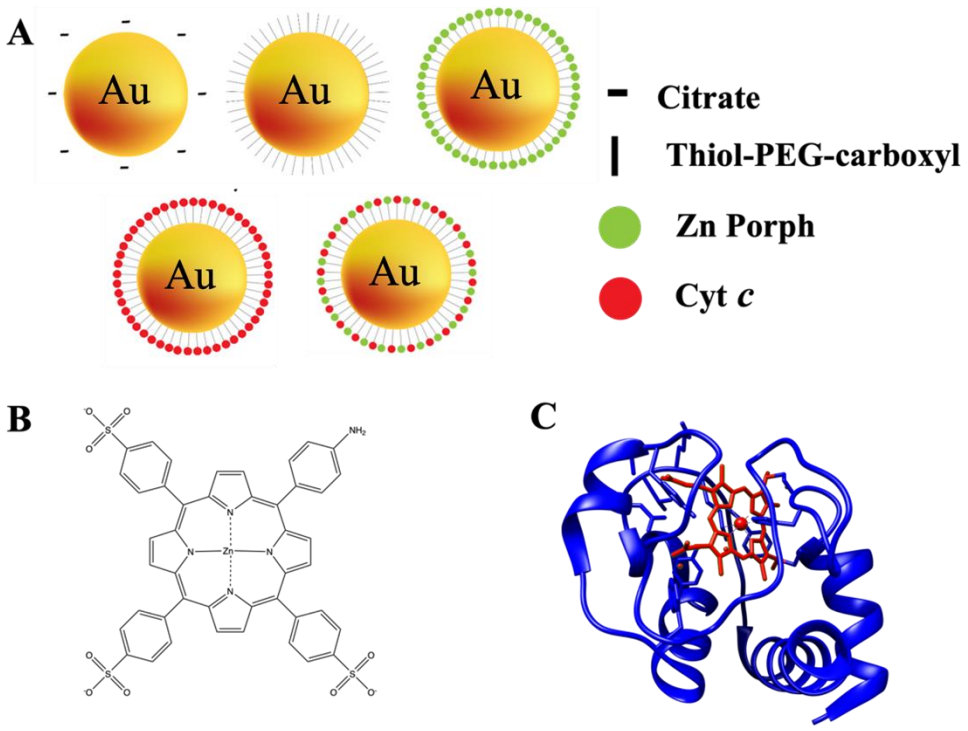


Figure 13. Schematic representation of cit-AuNPs as synthesised and when functionalized with thiol-PEG-carboxylic, Cytochrome *c* (Cyt *c*) and Zinc(II) 5-(4-aminophenyl)-10,15,20-tris-(4-sulfonatophenyl)porphyrin (Zn Porph) (A). Structure of Zn Porph (B). 3D structure crystal of Cyt *c* made from PDB(1 HRC) using Chimera (version 1.16) with blue representing amino acid residues and red representing the porphyrin Heme ring (C).

The physical characterisation of the multifunctionalised AuNPs was conducted to enable the quantification of the conjugated molecules. Initially, light scattering techniques were performed to assess the change in hydrodynamic diameter (h_d) and zeta potential of cit-AuNPs, AuNPs-PEG, and AuNP-PEG-Cyt *c*/Zn Porph samples. The length of the fully extended thiol-PEG-carboxyl (2000 Da) is ca. 7.9 nm, while the diameters of Cyt *c* and Zn Porph are ca. 3.4 nm and around ca. 1.6 nm respectively (calculated using ChemDraw3D) (Garrido et al., 2006). The h_d of cit-AuNPs, AuNP-PEG and AuNP-PEG-Cyt *c*/Zn Porph were measured using DLS (Figure 14A). This analysis revealed a difference in the h_d of the Cit-AuNPs from 19.6 ± 1.0 nm (PDI 0.301) to 33.54 ± 0.50 nm (PDI 0.297) in AuNP-PEG, and to 38.9 ± 1.1 nm (PDI 0.388) for AuNP-PEG-Cyt *c*/Zn

Porph, suggesting successful conjugation. The zeta potential measurements provide insight into the change in surface chemistry, shown by measuring the potential difference between the stationary fluid attached to the particle and the dispersion medium itself (Jain et al., 2021). Hence, the zeta potential was used to confirm the successful conjugation of molecules to AuNPs. The zeta potential measurement of cit-AuNPs was recorded to be -36.77 ± 2.33 mV, which is a slightly lower value compared to -30.77 ± 1.4 mV for AuNP-PEG. Cyt *c* is known to have a positive zeta potential measurement, exhibited on the AuNP-PEG-Cyt *c* samples at +14.7 ± 0.9 mV, which confirms successful conjugation of Cyt *c* on PEG functionalised AuNPs (Figure 14B) (Jain et al., 2021). However, the zeta potential values of AuNP-PEG-Zn Porph at -27.3 ± 0.0 mV indicate the successful conjugation of Zn Porph due to the slight change compared to AuNP-PEG. The change in zeta potential values from -27.3 ± 0.0 mV for AuNP-PEG-Zn Porph to +10.8 ± 0.2 mV in AuNP-PEG-Cyt *c*/Zn Porph samples verifies the effective binding of both Cyt *c* and Zn Porph to AuNPs-PEG.

TEM was carried out to analyse the morphology, aggregation, and size of surface functionalised AuNPs. TEM analysis revealed that the AuNP-PEG-Cyt *c*/Zn Porph particles are monodispersed, and that the functionalisation process does not cause any aggregation (Figure 14C). Furthermore, the cumulative frequency graph (inset of Figure 14C) displays a mean average diameter of AuNP-PEG- Cyt *c*/Zn Porph samples to be around 19.15 ± 2.12 nm (Gaussian fit). The size discrepancy between TEM and DLS is because DLS measures the h_d of particles in dispersion, while TEM images provide information about the particle size in the dry state. DLS can differentiate between the cit-AuNPs and the multifunctionalised AuNPs as the h_d varies due to the change in the organic layer surrounding the AuNPs; however, the contrast produced in TEM would not be great enough to determine the change in diameter.

To further confirm the successful conjugation of Cyt *c* and Zn Porph with AuNP, UV-visible absorption spectroscopy was performed; this is widely used to characterise the size, concentration and conjugation of AuNPs (Haiss et al., 2007). The maximum absorbance (located between 500 and 600 nm) in a typical UV-vis absorption spectrum of

AuNPs, also known as the SPR peak, is indicative of their size. Once the size and the extinction coefficient of the AuNPs are known, their concentration can be calculated using the Beer-Lambert law (Haiss et al., 2007, Grimsley and Pace, 2004, Fonin et al., 2014). Porphyrins are commonly conjugated to nanomaterials for fluorescent tagging and photodynamic therapy (Tsolekile et al., 2020, Kou et al., 2017, Sharma et al., 2022, García Calavia et al., 2018). The UV-vis absorption spectra of AuNPs synthesised in this work are reported in Figure 14D, revealing that the SPR peak of the AuNPs remains in the same position at 521 nm for all the samples except AuNP-PEG-Cyt *c*, in which it has red-shifted to 525 nm, indicating a change in surface chemistry. This could be attributed to the successful functionalisation of Cyt *c* onto AuNP-PEG. Moreover, the full-width half maximum (FWHM) of the SPR peak increased in all the functionalised AuNP samples when compared to the spectrum of cit-AuNPs, suggesting an increase in polydispersity of the functionalised AuNPs. This could be the result of agglomerates which could form in the colloidal dispersions. The increase in intensity between 650-700 nm in AuNP-PEG-Cyt *c* is the likely result of small aggregates caused by protein-nanoparticle interactions between Cyt *c* conjugated to AuNPs. Cit-AuNPs and AuNPs-PEG do not show any absorption peaks other than the SPR, whereas free Cyt *c* and Zn Porph exhibit additional peaks, with their UV-visible absorption spectra shown in Figure SI 1A. The Soret band peaks at 408 nm and 415 nm correspond to oxidised (Cyt *c* Ox) and reduced Cyt *c* (Cyt *c* Red), respectively, aligning with literature values (Fisher et al., 1973). The absorption peak at 423 nm corresponds to Zn Porph (Figure SI 1A). After conjugation to AuNPs, the Soret band peak of Cyt *c* was located at 410 nm, suggesting that the Cyt *c* conjugated to the AuNPs exists in both oxidised and reduced forms. Meanwhile, the Zn Porph Soret band is evident at 430 nm, which is red shifted when compared to free Zn Porph in solution at 423 nm. This redshift after conjugation to AuNPs could be attributed to J-type aggregation formed between neighbouring chromophores (in this case Zn Porph) attached close to each other in a nanoparticle (Maiti et al., 1998). It is evident from Figure 14D that in multifunctional AuNP-PEG-Cyt *c*/Zn Porph samples, the Soret band peaks of Cyt *c* and Zn Porph overlap, consequently, the exact peak of each of the components is difficult to determine. Importantly, this poses the risk of erroneous calculations to determine the accurate concentrations of these molecules. The overlapping spectra of Cyt *c* Ox and Zn

Porph (Figure SI 1B) and Cyt *c* Red and Zn Porph (Figure SI 1C) free in solution support the spectrum depicted in Figure 14D showing how the absorbance peaks convolute and make it impossible to accurately determine the peak. Therefore, the deconvolution of the overlapping spectra of Cyt *c* Ox and Zn Porph and Cyt *c* Red and Zn Porph (Figure SI 1D and Figure SI 1E) is essential as it allows the hidden peaks to be revealed, and therefore the absorbance of each peak to be identified for further quantification purposes.

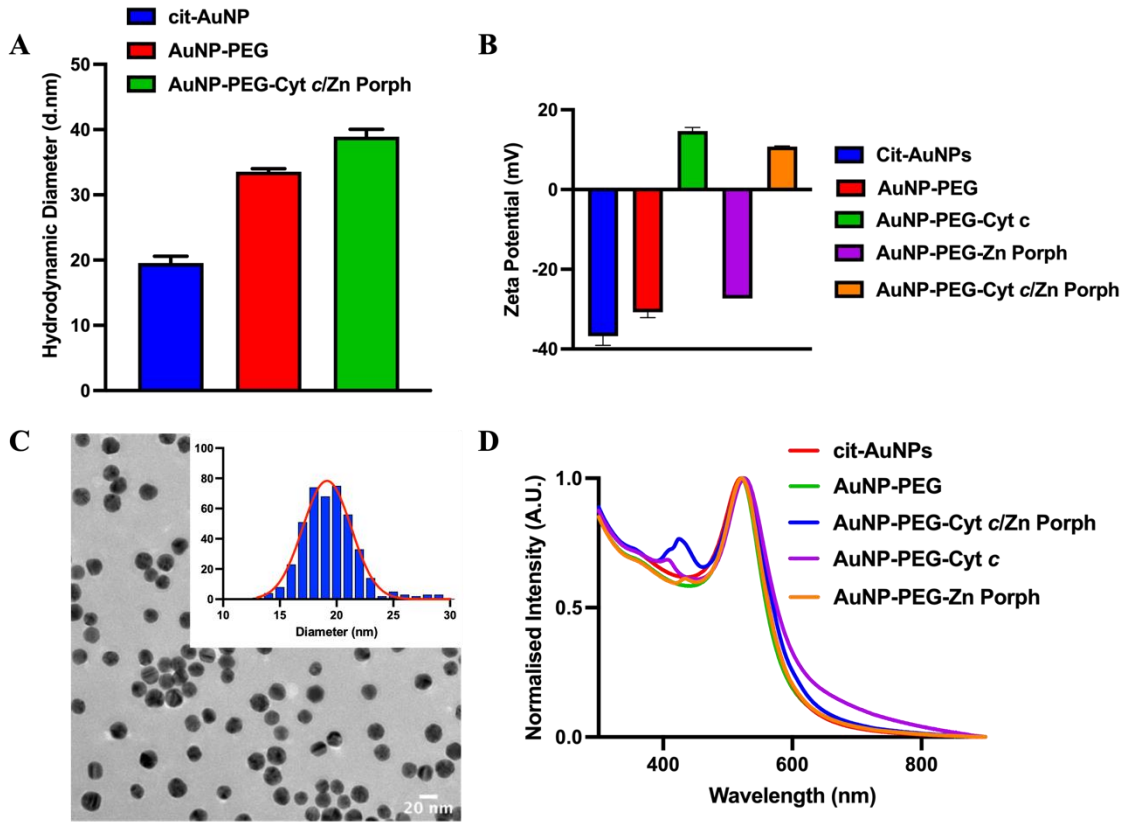


Figure 14. The physicochemical characterisation of AuNPs functionalized with Cyt *c* and Zn Porph was performed using DLS (A), Zeta Potential measurements (B), TEM image and cumulative frequency graph of 20 nm AuNP-PEG-Cyt *C* /Zn Porph produced from analysing 452 AuNPs (C) and UV-visible absorption spectroscopy (D).

The spectral overlap of the Soret band of Cyt *c* and Zn Porph (Figure SI 1A) prevents the identification of individual Soret peak heights in AuNP-PEG-Cyt *c*/Zn Porph. Therefore, deconvolution of the Soret band of AuNP-PEG-Cyt *c*/Zn Porph was conducted to

accurately find the contributions of Cyt *c* and Zn Porph in the functionalised AuNP samples (Figure 15A). The Soret band was selected as a region of interest in CASA-XPS, and two components (the first for Cyt *c* and the second for Zn Porph) were selected to fit in the AuNP-PEG-Cyt *c*/Zn Porph absorption spectrum shown in Figure 15A. These were located at 415 nm, attributed to Cyt *c*, and at 430 nm for Zn Porph. The components were fitted using the Levenberg-Marquardt algorithm fitting, which resulted in a good fit with a residual standard deviation (RSD) of 0.006. The fit confirms that only two components are located within the peak and that the deconvolution can accurately determine the heights of the hidden peaks.

To confirm the precision of the analysis method, another sample of AuNP-PEG-Cyt *c*/Zn Porph (AuNP-PEG-Cyt *c*/Zn Porph-S2) with a different shaped Soret band peak was deconvoluted (Figure 15B). The sample was made using the same component concentrations as AuNP-PEG-Cyt *c*/Zn Porph, but the AuNP concentration was reduced from 0.26 nM to 1.21 nM (Table S1). When the Soret band of Figure 15B is compared to Figure 15A, it appears as a different shape with shoulders on each side of the peak. In this case, fitting the deconvoluted spectrum with just two components resulted in a large RSD suggesting the presence of another component. Therefore, the third component at 423 nm, which corresponds to the absorption peak of the unconjugated free Zn Porph (Figure SI 1A), was added to improve the fit. The fitting resulted in an RSD of 0.002 (Figure 15B). The inclusion of a third component supposes that free unconjugated Zn Porph is still present in the solution together with the Zn Porph conjugated to AuNPs, therefore suggesting that further purification of the sample is required. Notably, the formation of Zn Porph J-aggregates can also be identified using this method, which is of great importance as the fluorescence properties of porphyrins depend on their aggregation state and local environment (Scolaro et al., 2005, Siggel et al., 1996). The presence of J-aggregates was also observed when deconvoluting the UV-Vis absorption spectra of free Cyt *c* Ox and Zn Porph in water (Figure SI 1D). Figure 15B also shows a wider SPR peak cresting at around 553 nm, due to the higher concentration of Zn Porph and Cyt *c* in the sample; therefore, Cyt *c*'s peak at 500-600 nm and the Q bands of Zn Porph from 550-650 nm influence the spectrum more in Figure 15B than in Figure 15A. Further

characterisation of the sample in Figure 15B by TEM indicated that no aggregation of the AuNPs occurred (Figure SI 3A) as the diameter was determined to be 19.3 ± 2.5 nm. However, the mean diameter of the DLS (Figure SI 3B) shows a h_d of 43.0 ± 0.9 nm (PDI 0.353), a direct result of the aggregation of a small percentage of AuNP in the sample (Figure SI 3C).

Identification of unbound molecules in AuNP-PEG-Cyt *c*/Zn Porph-S2 using the deconvolution method is essential to ensure the accuracy of the concentration of molecules bound to AuNP. Excess unbound molecules would influence other analytical techniques and experiments; hence it is important to remove the unbound molecules once identified. The deconvolution method should be used regularly together with UV-Vis for accurate quantification of bound molecules. This is particularly imperative in applications such as drug delivery, where UV-vis absorption is often used to quantify surface-conjugated molecules.

To further the impact of this method, the concentration of surface functionalised molecules conjugated to AuNP was calculated for both AuNP-PEG-Cyt *c*/Zn Porph samples in Figure 15A and B. The number of each bound molecule was calculated from the UV-visible absorption spectrum shown in Figure 15A and B using the Beer-Lambert law. The extinction coefficient of the 20 nm AuNPs (5.41×10^{8} M^{-1} cm^{-1}) was divided by the minimum absorbance value between the SPR peaks and the conjugated molecule peaks. Based on the above method, the calculated concentrations of 1.21 nM and 0.26 nM were obtained for samples AuNP-PEG-Cyt *c*/Zn Porph and AuNP-PEG-Cyt *c*/Zn Porph S2, respectively Figure 15A and B. These values can then be multiplied by Avogadro's constant (6.022×10^{23}) to give 7.30×10^{14} and 1.55×10^{14} AuNPs per litre for each above sample respectively.

The quantity of Cyt *c* and Zn Porph molecules per litre can also be found by first calculating their concentration and, subsequently, the number of molecules per AuNP. For the concentration, the height of the deconvoluted peaks was found by subtracting the background from the spectra. The absorbance peak heights were then divided by the

extinction coefficients of Cyt *c* (101600 M^{-1} cm^{-1}) and Zn Porph (57940 M^{-1} cm^{-1}, calculated from a concentration curve in Figure SI 2) resulting in the bound concentrations (Caesar et al., 2009). The concentration of Cyt *c* for the AuNP-PEG-Cyt *c*/Zn Porph sample (Figure 15A) was calculated to be 0.42 μM, corresponding to 2.53×10^{17} Cyt *c* molecules per litre. Similarly, the concentration of Zn Porph was calculated for the AuNP-PEG-Cyt *c*/Zn Porph sample (Figure 15A) was calculated to be 1.30 μM, with an ensuing 7.83×10^{17} Zn Porph molecules per litre. By dividing the number of Cyt *c* and Zn Porph molecules per litre by the number of AuNPs per litre, the quantity of each molecule was calculated to be 346 and 1073, respectively. The AuNP concentration of AuNP-PEG-Cyt *c*/Zn Porph-S2 (Figure 15B) was calculated to be 0.26 nM, with 1.55×10^{14} AuNPs per litre. The concentrations of Cyt *c* and Zn Porph in AuNP-PEG-Cyt *c*/Zn Porph-S2 were calculated to be 0.40 μM and 1.16 μM, which is equivalent to 2.4×10^{17} and 6.99×10^{17} molecules per litre, respectively. Thus, the number of molecules bound to each AuNP was calculated to be 1545 Cyt *c* and 4500 Zn Porph. The Zn Porph free solution in this sample was also calculated to have a concentration of 1.11 μM. The quantity of conjugated molecules for AuNP-PEG-Cyt *c*/Zn Porph-S2 (Figure 15B) is more than four times the quantity conjugated to AuNP-PEG-Cyt *c*/Zn Porph (Figure 15A), suggesting that the free Zn Porph in solution hinders accurate determination of the number of molecules bound to AuNPs. The deconvolution of peaks on multifunctional AuNPs provides valuable information about the quality and concentration of conjugated molecules while also providing insight into whether the material needs to be purified further.

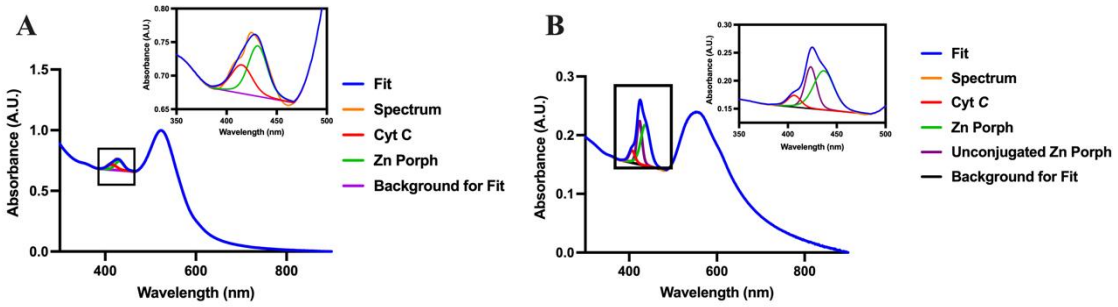


Figure 15. The Soret band in the Ultraviolet-Visible absorption spectra of AuNP-PEG-Cyt *c* /Zn Porph was deconvoluted to identify 2 fitted components in AuNP-PEG-Cyt *c*/Zn-Porph samples (A) and 3 fitted components in AuNP-PEG-Cyt *c*/Zn-Porph-S2 (B). The peaks were deconvoluted using CASAXPS software. The region of interest was then selected using the regions tool, and then the background setting was changed to 'linear' as it closely represents how the spectra would look without the conjugated molecules. The convoluted peaks in the spectra were then found using the components tab, by adding the components that were thought to be in the region. The components were then fitted to the spectra using the Levenberg-Marquardt algorithm. Figure used in Analytical Chemistry publication (Potts et al., 2023).

2.5.3. X-Ray Photoelectron Spectroscopy

X-ray photoelectron spectroscopy (XPS) was used to examine the chemical composition of functionalised AuNPs and their respective controls. The elemental peaks derived from the XPS spectra of Cyt *c*, Zn Porph and cit-AuNPs controls along with AuNPs-PEG-Cyt *c*, AuNPs-PEG-Zn Porph and AuNPs-PEG-Cyt *c*/Zn Porph are presented in Table 1.

Table 1. Surface chemical composition of AuNPs and their conjugated molecules with controls obtained by XPS

	Binding Energy (eV)				
Sample	$Au4f_{7/2}$	$Au4f_{5/2}$	$S2p_{3/2}$	$Zn2p_{3/2}$	$Zn2p_{1/2}$
Cyt *c*	-	-	160.2	-	-
Zn Porph	-	-	165.3	1018.6	1041.5
cit-AuNP	80.0	83.6	-	-	-
AuNP-PEG-Cyt *c*	80.7	84.3	160.4	-	-
AuNP-PEG-Zn Porph	80.5	84.1	161.0	1018.6	1041.5
AuNP-PEG-Cyt *c*/Zn Porph	80.4	84.0	160.5	-	-

To confirm the presence of metallic Au (Au^0) from AuNPs the XPS spectra of Au4f were investigated and displayed in Figure 16A-F. Au4f presents doublet characteristics, with peaks corresponding to $Au4f_{7/2}$ and $Au4f_{5/2}$ at 84.0 and 87.6 eV, respectively (Devia et al., 2006). Figure 16A to C presents the XPS spectra of Cyt *c*, Zn Porph and cit-AuNPs, respectively. Figure 16A and B show an absence of distinctive peaks, as expected. Figure 16C displayed peaks around the 80 and 84 eV range, resonating with both $Au4f_{7/2}$ and $Au4f_{5/2,}$ respectively but shifted 4eV. This is a 4 eV shift from the reported value of Au^0 in the literature, caused by the differing binding energies in variously sized AuNPs. The AuNPs referenced in the literature had a diameter of 3-5 nm, while this thesis utilised 20 nm AuNPs (Casaletto et al., 2006, Vollath et al., 2018). Figure 16D to F are the functionalised samples of AuNP-PEG-Cyt *c*, AuNP-PEG-Zn Porph and AuNP-PEG-Cyt

c/Zn Porph, further highlighting the presence of Au^0 in the samples. A consistent observation across the spectra is the peak alignment ~80 eV and ~84 eV corresponding to $Au4f_{7/2}$ and $Au4f_{5/2}$ for for the functionalised AuNPs, validating the presence of Au^0. The spectra accentuate the role of AuNP size in influencing XPS binding energies, with the observed binding energy shift underscoring the Au^0 presence in the analysed AuNPs. Table 1 shows that all samples with AuNP show peaks ~80 eV, corresponding to $Au4f_{7/2}$ and all AuNP peaks ~84 eV corresponding to $Au4f_{5/2}$.

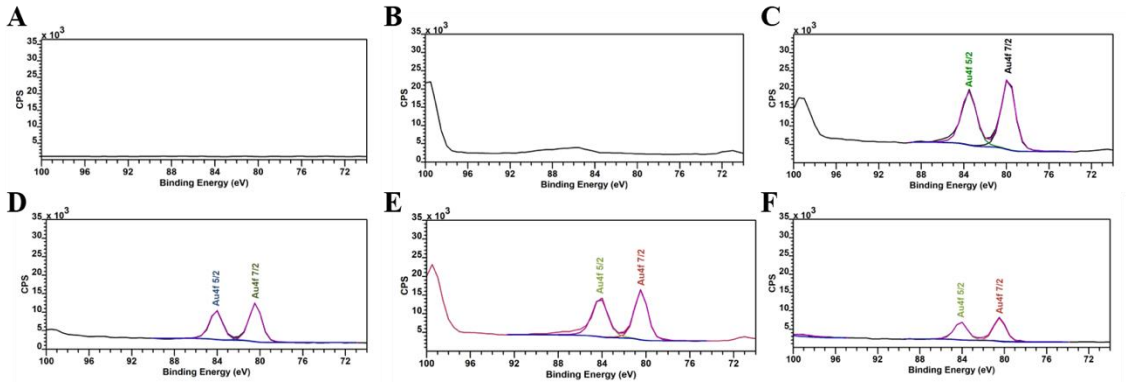


Figure 16. XPS spectrum in the region of Au4f in Cyt *c* (A) Zn Porph (B) cit-AuNP (C) AuNPs-PEG-Cyt *c* (D), AuNPs-PEG-Zn Porph (E) and AuNPs-PEG-Cyt *c*/Zn Porph (F).

To identify sulphur in the samples the binding energy of the S 2p region was assessed. The S 2p region comprises duplet peaks S $2p_{3/2}$ and S $2p_{1/2}$ with a peak separation of 1.2 eV with areas at a 2:1 ratio (Sun et al., 2006). The binding energy of the $S2p_{3/2}$ peak in Figure 17A-F and Table 1 verifies that a thiol-PEG-carboxylic acid SAM exists on the functionalised AuNPs. During the functionalisation process, the thiol group in thiol-PEG-carboxylic acid replaces the citrate on cit-AuNPs. Although sulphur is present in the structures of Cyt *c* and Zn Porph, it is not found in cit-AuNPs. It corresponds to approximately 162 eV for bound thiols, 164 eV for unbound thiols (Castner et al., 1996), and 166.6 eV for sulfonates (Baltrusaitis et al., 2007). The binding energies for Cyt *c* and Zn Porph are 160.2 eV and 165.3 eV, respectively, in line with the literature values for bound thiols and sulfonate-containing molecules (Castner et al., 1996, Baltrusaitis et al., 2007). The binding energies for AuNP-PEG-Cyt *c*, AuNP-PEG-Zn Porph, and AuNP-PEG-Cyt *c*/Zn Porph are 160.4 eV, 161.0 eV, and 160.5 eV, respectively, further

confirming the presence of bound thiols as per the literature values. The presence of S $2p_{1/2}$ at around half the area of S $2p_{3/2}$ also supports the assumption tha the sulphur is bound to Au.

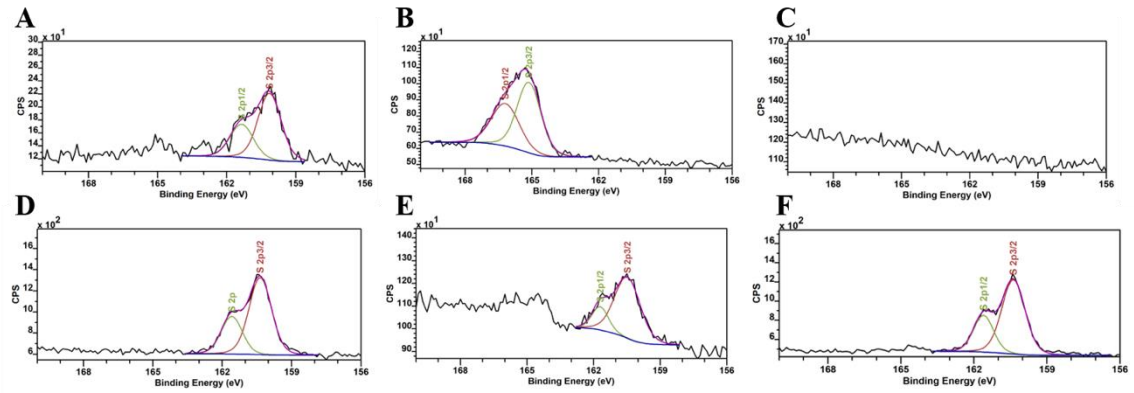


Figure 17. XPS spectrum in the region of S2p in Cyt *c* (A) Zn Porph (B) cit-AuNP (C) AuNPs-PEG-Cyt *c* (D), AuNPs-PEG-Zn Porph (E) and AuNPs-PEG-Cyt *c*/Zn Porph (F).

Unique to Cyt *c* in the samples, iron is centrally located within the heme group of the protein. In XPS spectra, the expected iron peak should fall between ~708-715 eV according to literature for Fe2p3/2 (Grosvenor et al., 2004). However, no significant peaks were detected in this region for any of the samples, including Cyt *c*, AuNP-PEG-Cyt *c*, and AuNP-PEG-Cyt *c*/Zn Porph as depicted in Figure 18A-C. This can be attributed to the presence of only a single iron atom in each Cyt *c* molecule, resulting in its minimal quantity within a sample, making detection challenging.

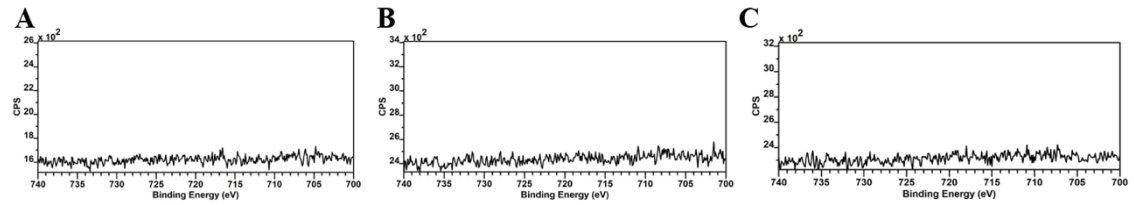


Figure 18. XPS spectrum in the region of $Fe2p_{3/2}$ for Cyt *c* (A) AuNP-PEG-Cyt *c* (B) and AuNP-PEG-Cyt *c*/Zn Porph (C). No peaks are visible in any of the XPS spectra for $Fe2p_{3/2}$.

Zinc, the element specific to Zn Porph, is situated at the centre of the porphyrin ring. The XPS spectrum of Zinc displays two distinct Zn2p peaks with binding energies of 1021.9 eV and 1044.8 eV for $Zn2p_{3/2}$ and $Zn2p_{1/2}$, respectively, and a spin-orbit split of 22.9 eV (Kumar et al., 2014). The presence of both peaks in the XPS spectra verifies the existence of zinc in Zn Porph and AuNP-PEG-Zn Porph as seen in Figure 19A-B, with binding energies of 1018.6 eV and 1041.5 eV for $Zn2p_{3/2}$ and $Zn2p_{1/2}$. The AuNPs-PEG-Cyt *c*/Zn Porph sample as seen in Figure 19C, however, did not exhibit Iron or Zinc in its XPS spectrum, as no significant peaks were observed at the relevant binding energies. Similar to the solitary iron atom in Cyt *c*, Zn Porph contains only a single zinc atom. This likely explains its lack of peaks in AuNP-PEG-Cyt *c*/Zn Porph, as Zn Porph would compete with Cyt *c* for ligand binding. Consequently, its concentration in the sample would be low, rendering its detection difficult.

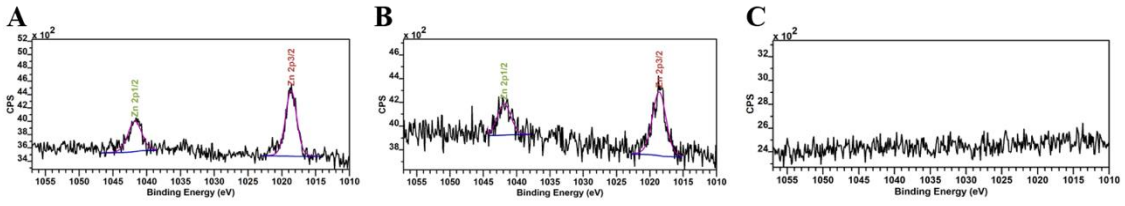


Figure 19. XPS spectrum in the region of $Zn2p_{3/2}$ (peak on the right) and $Zn2p_{1/2}$ for Zn Porph (A) AuNP-PEG-Zn Porph (B) and AuNP-PEG-Cyt *c*/Zn Porph (C).

These absences of Fe and Zn peaks may be attributed to the relatively large size of Cyt *c* molecules (3.4 nm), which could shield both the central Iron and the Zinc in Zn Porph, thereby preventing X-rays from dislodging enough of each element to form significant peaks in the XPS spectrum. The difficulty in detecting the Iron peak of Cyt *c* is well-documented in the literature, as the Heme group is centrally located within the structure of Cyt *c* and is thus shielded by amino acid residues, making the single Iron atom in each Cyt *c* molecule challenging to detect (Mukherjee et al., 2015). Similarly, the Zinc in Zn Porph is positioned at the centre of its structure, with only one atom per molecule, complicating its detection. The substantial size difference between the molecules (Cyt *c* at 12,384 Da and Zn Porph at 984 Da) suggests that X-rays are more likely to identify the

Zinc in Zn Porph than the Iron in Cyt *c*. Consequently, XPS does not seem to be a suitable technique in verifying the conjugation of Cyt *c* and Zn Porph to AuNPs.

2.5.4. Characterisation of 20 nm AuNPs with MUA, Cyt *c* and Zn Porphyrin

It was hypothesised that the close proximity between the AuNPs and Cyt *c* when conjugated could impact the redox capability of Cyt *c* and subsequently affect the multifunctionalised AuNPs' cellular uptake (Jo et al., 2022, Neeves et al., 2007, Pons et al., 2006). The length of the thiol-PEG-carboxyl 2 kDa ligand was calculated to be ~7.9 nm, and to test this hypothesis another ligand, 11-mercaptoundecanoic acid (MUA), was employed. MUA, which also terminates in a thiol and carboxyl group, has a shorter length of ~1.4 nm, as determined using ChemDraw 3D software.

Additionally, it was hypothesised that covalent conjugation of Cyt *c* to AuNPs could alter Cyt c's structure and function (Jain et al., 2021). Therefore, electrostatic conjugation of Cyt *c* and Zn Porph on AuNPs was performed using MUA. Electrostatic conjugation was not conducted on PEG functionalised AuNPs, as PEG has an inherent repulsion to proteins. Therefore, covalent conjugation was used to ensure the conjugation of Cyt *c* to the PEG functionalised AuNPs (Meziadi et al., 2022). The conjugation of Cyt *c* and Zn Porph to AuNPs utilising MUA covalently is detailed in 2.4.10 and electrostatically in 2.4.9, both are schematically represented in Figure 20A and B, respectively.

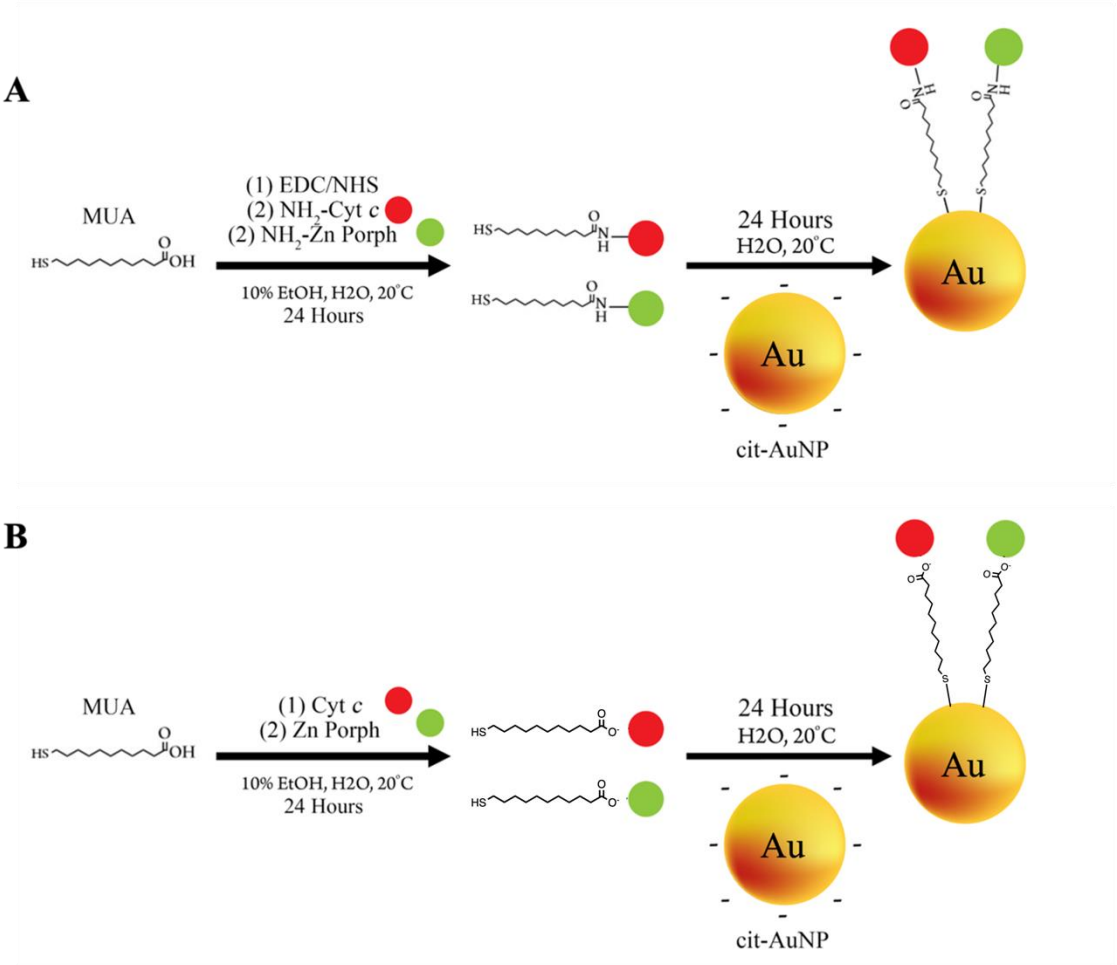


Figure 20. Schematic representation of the functionalisation method for AuNP-MUA-Cyt *c*/Zn Porph Cov (A) and AuNP-MUA-Cyt *c*/Zn Porph Electro.

Physicochemical characterisation of the 20 nm AuNPs functionalised with MUA, Cyt *c* and Zn Porph (Figure 21A-C) was undertaken to identify whether the AuNPs were reflective of those functionalised with thiol-PEG-carboxyl. The results of the DLS analysis indicate that the h_d of 20 nm AuNPs increased from 19.57 ± 1.03 nm (PDI of 0.335) in cit-AuNPs to 26.32 ± 0.75 nm (PDI of 0.215) in AuNP-MUA, confirming the attachment of MUA to the AuNPs (Figure 21A). The conjugation of Cyt *c* and Zn Porph to AuNP-MUA using both covalent and electrostatic methods also showed an increase in h_d, with values of 126.20 ± 10.35 nm (PDI of 0.467) and 124.3 ± 6.54 nm (PDI of 0.407) respectively. This significant increase in hd suggests multiple layers of Cyt *c* and Zn Porph form on the AuNP-MUA.

The ζ also confirms the successful conjugation of Cyt *c* and Zn Porph to AuNPs, as the ζ decreases from -36.77 ± 2.33 mV in cit-AuNPs to -42.23 ± 2.01 mV in AuNP-MUA. The ζ for AuNP-MUA-Cyt *c*/Zn Porph conjugated using covalent and electrostatic methods had increased to values of -29.57 ± 1.69 mV and -14.00 ± 0.36 mV, respectively (Figure 21B). The positive ζ of Cyt *c* is due to the increase in ζ for AuNP-MUA-Cyt *c*/Zn Porph conjugated using covalent and electrostatic methods compared to cit-AuNPs and AuNP-MUA. The lower ζ of AuNP-MUA-Cyt *c*/Zn Porph conjugated using covalent and electrostatic methods when compared to AuNP-PEG-Cyt *c*/Zn Porph is likely due to the higher concentration of Zn Porph, which has a negative ζ.

The UV-Vis absorption spectra showed little difference between the SPR peak and shape of cit-AuNPs and AuNP-MUA, but AuNP-MUA-Cyt *c*/Zn Porph conjugated using covalent and electrostatic methods both showed double peaks in the Soret region, which can be attributed to Cyt *c* (~410 nm) and Zn Porph (~432 nm for J-aggregates) (Figure 21C). A redshift in the SPR peak was also observed for both AuNP-MUA-Cyt *c*/Zn Porph conjugated using covalent and electrostatic methods at 543 and 556 nm, respectively, from the 521 nm of cit-AuNPs. This red-shifted SPR peak and the general broadening of the peak can be attributed to the aggregation of the sample and the increased polydispersity of the AuNP size. However, this is also a result of the functionalisation of AuNPs, as their surface is less accessible due to the conjugated Cyt *c* and Zn Porph, and therefore the plasmon produced by the AuNPs is affected (Szunerits et al., 2014). The DLS size distribution for 20 nm AuNPs before and after functionalization is displayed in Figure SI 5A.The combination of the results from the h_d, □ and UV-Vis absorption spectra collectively confirm the successful conjugation of Cyt *c* and Zn Porph to AuNP-MUA using both covalent and electrostatic conjugation methods.

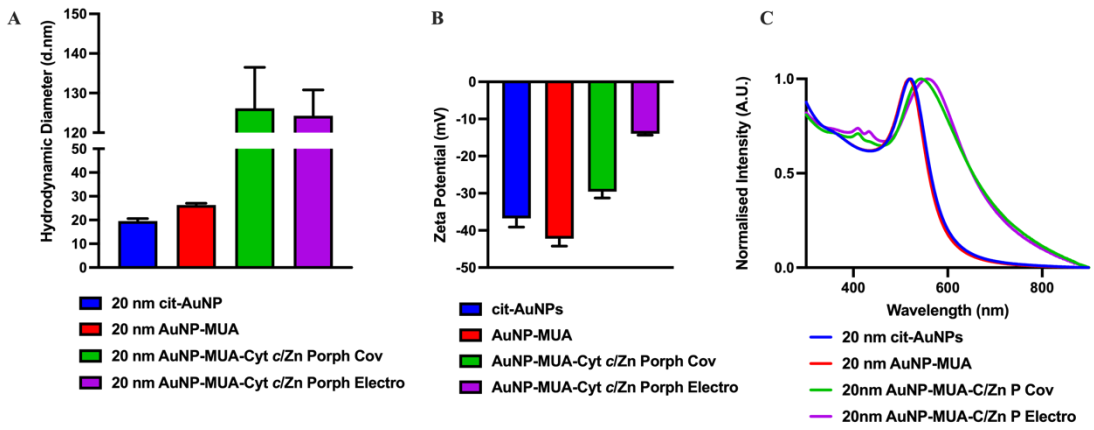


Figure 21. Physicochemical characterisation of 20 nm AuNPs functionalised with MUA, Cyt *c* and Zn Porph using DLS (A), zeta potential (B) and UV-Vis absorption spectroscopy (C).

TEM images of cit-AuNPs and AuNP-MUA-Cyt *c*/Zn Porph Cov were taken to assess whether the functionalisation process resulted in any AuNP size changes (Figure 22A and B). The images show that the AuNPs are mostly spherical in shape uniform diameters. The mean particle diameters of 19.5 ± 2.5 nm for cit-AuNPs (calculated from 227 AuNPs) and 19.3 ± 2.5 nm for AuNP-MUA-Cyt *c*/Zn Porph Cov (calculated from 40 AuNPs). Since the h_d and UV-Vis spectra of 20 nm AuNP-MUA-Cyt *c*/Zn Porph Cov and 20 nm AuNP-MUA-Cyt *c*/Zn Porph Electro were similar, it can be inferred that there is no aggregation present in the AuNP-MUA-Cyt *c*/Zn Porph Electro.

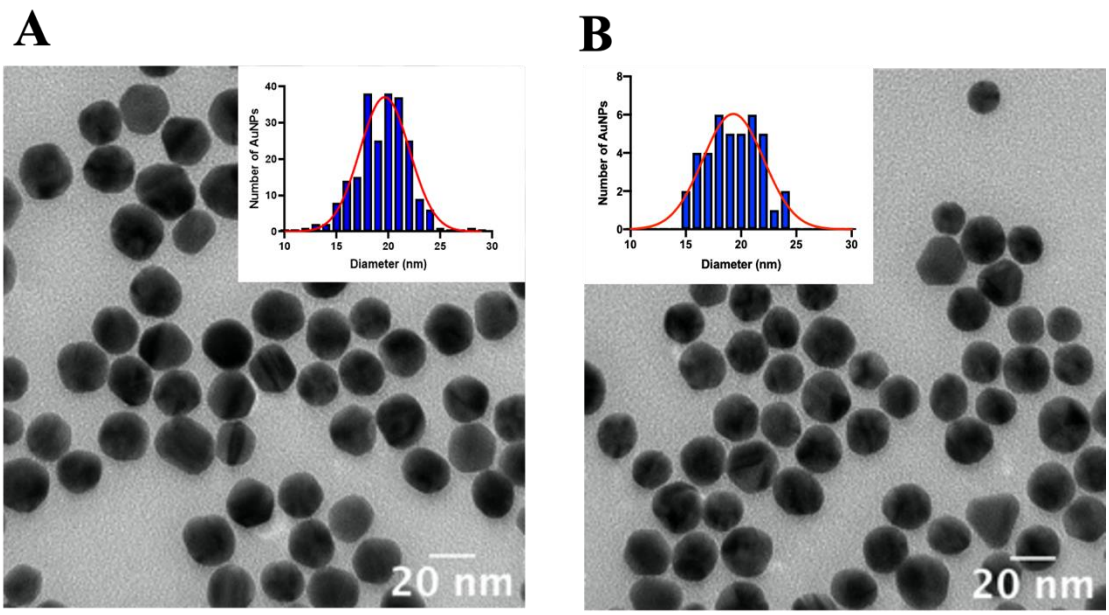


Figure 22. TEM images of cit-AuNP (A) and AuNP-MUA-Cyt *c*/Zn Porph Cov (B). Images contain cumulative frequency distributions in an insert made of 227 and 40 AuNPs, respectively.

This confirmed that Cyt *c* and Zn Porph could be successfully conjugated to AuNPs using different ligands and conjugation mechanisms, and that their concentrations could be accurately determined.

2.5.5. Synthesis, Functionalisation and Characterisation of 50 and 100 nm AuNPs

In this work, it was of great interest to functionalise Cyt *c* and Zn Porph onto AuNPs of different sizes to assess how the size of the AuNP affects cellular uptake and, subsequently, the ability of Cyt *c* and Zn Porph to induce apoptosis when irradiated with light.

The extracellular matrix (ECM) plays a pivotal role in dictating the mobility of nanoparticles (NPs) around cells. The collagen fibril inter-spacing of the ECM typically

ranges between 20 to 40 nm. This means NPs below this size range can navigate through the ECM more easily. However, it's essential to note that the ability of NPs to move through the ECM isn't solely dependent on their size. Factors such as the nanoparticles' hydrodynamic diameter and surface charge can also influence their mobility through the ECM (Neeves et al., 2007, Pons et al., 2006).

Once Nps have navigated past the ECM, their size significantly impacts their ability to enter cells. Smaller nanoparticles are generally more easily internalised by cells than larger ones. One primary reason for this is the large surface area to volume ratio of smaller NPs, which facilitates their entry into the cell membrane (Montis et al., 2018, Panyam et al., 2003).

Despite this, previous reports suggest that the uptake of AuNPs is greatest for those with a diameter of around 50 nm (Chithrani et al., 2006, Carnovale et al., 2019). Theoretical models propose that the optimal particle size for cellular uptake via endocytosis is determined by the competition between diffusion kinetics and thermodynamic driving forces (Gao et al., 2005). For NPs smaller than the optimal size, the increased elastic energy coupled with the bending of the membrane results in a reduced driving force, requiring smaller NPs to aggregate in order to create a sufficient driving force for successful internalisation into cells (Augustine et al., 2020). Larger NPs, on the other hand, accommodate many receptors on the cells surface over a large area during uptake, leading to a lower internalisation (Augustine et al., 2020, Gao et al., 2005).

It has been previously shown that a specific quantity of "activated" Cyt *c* is necessary to initiate the apoptosis process. For example, previous work conducted by Slee et al., 1999 suggests that Cyt *c* induced apoptotic changes to nuclei at concentrations as low as 80 nM (Slee et al., 1999). It can be deduced that a greater number of smaller functionalised AuNPs would have to be taken up by cells compared to larger AuNPs to induce apoptosis. The larger the AuNP, the greater it's surface area; therefore, more Cyt *c* and Zn Porph can be conjugated per AuNP, as shown in Table 2. Despite this, there is a drawback to functionalising larger AuNPs, as their size may result in reduced uptake due to reduced

ability to pass the ECM, as the depletion of free receptors limits the ligand bind energy forming a large membrane curvature, of which AuNPs of 80 nm or larger struggle to overcome (Wang et al., 2010).

Table 2. The effect of the size of AuNP and ligand used in functionalisation has on the theoretical maximum number of Cyt *c* bound to AuNPs if arranged in a monolyer.

Sample	Diameter (nm)	Surface area (nm^2)	Theoretical Maximum Number of Cyt *c* per AuNP if Arranged in a Monolayer	Theoretical Maximum Number of Zn Porph per AuNP if Arranged in a Monolayer
20 nm AuNP-PEG	35.8	4026.4	1184	2517
20 nm AuNP-MUA	22.8	1633.1	480	1021
50 nm AuNP-PEG	65.8	13602.0	4001	8501
50 nm AuNP-MUA	52.8	7604.7	2237	4753
100 nm AuNP-PEG	115.8	42127.6	12390	26330
100 nm AuNP-MUA	102.8	33199.9	9765	20750

Seed-mediated AuNP growth was used to synthesize 50 and 100 nm AuNPs, as described in sections 2.4.3 and 2.4.4 respectively. The quantity of 20 nm cit-AuNP seeds needed to produce 50 and 100 nm cit-AuNPs was determined by adding different volumes of the seeds while keeping the volumes and concentrations of the $HAuCl_4$, sodium citrate and hydroquinone the same (Figure SI 4 and Table SI 4). The resulting 50 and 100 nm cit-AuNPs were analysed using UV-Vis, DLS, and Zeta potential techniques, as illustrated in Figure 23A-C. According to UV-vis measurements, the diameters of these AuNPs were 52 and 101 nm, and the DLS calculations for their h_d were 60.39 ± 0.99 and 105.00 ± 7.24 nm, respectively, as shown in Figure 23A-B. The h_d values were larger than the UV-vis sizes, as anticipated, because the Stokes-Einstein equation used for the DLS calculation considers not only the core of the particle but also the surface structures that interact with the solution. Comparatively, UV-vis measures the SPR produced by the AuNPs' core and excludes the surface structures. The ζ of the cit-AuNPs were approximately -35 mV, indicating moderate electrostatic stability, as demonstrated in Figure 23C (Pochapski et al., 2021).

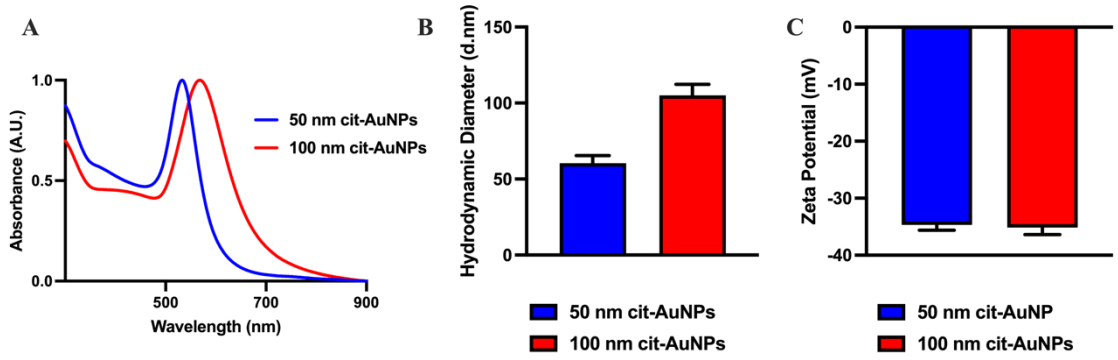


Figure 23. The physiochemical characterisation of 50 and 100 nm cit-AuNPs using UV-Vis absorption spectroscopy (A), DLS (B) and Zeta Potential (C).

The 50 nm and 100 nm gold AuNPs were functionalised with Cyt *c* and Zn Porph using thiol-PEG-carboxyl and MUA through covalent and electrostatic methods. Characterisation was carried out using UV-vis absorption spectroscopy and DLS (Figure 24).

The UV-Vis absorption spectroscopy of the 50 nm cit-AuNPs exhibited an SPR peak at 529 nm, as also observed for 50 nm AuNP-MUA. However, SPR redshift and peak broadening occurred for the 50 nm AuNP-PEG, 50 nm AuNP-PEG-Cyt *c*/Zn Porph, 50 nm AuNP-MUA-Cyt *c*/Zn Porph Cov, and 50 nm AuNP-MUA-Cyt *c*/Zn Porph Electro at 536, 539, 542, and 541 nm, respectively. These redshifted SPR peaks and peak broadening indicate changes in surface chemistry due to Cyt *c* and Zn Porph functionalisation. In the Soret band region, 50 nm cit-AuNP, 50 nm AuNP-PEG, and 50 nm AuNP-MUA showed no peaks as expected, while 50 nm AuNP-PEG-Cyt *c*/Zn Porph, 50 nm AuNP-MUA-Cyt *c*/Zn Porph Cov, and 50 nm AuNP-MUA-Cyt *c*/Zn Porph Electro displayed peaks at ~410 nm, attributed to Cyt *c*, and at ~432 nm, attributed to Zn Porph, (Figure 24A).

For the 100 nm cit-AuNPs, 100 nm AuNP-PEG, and 100 nm AuNP-MUA, the UV-Vis absorption spectroscopy revealed an SPR peak at 563 nm. In contrast, SPR redshift and peak broadening were observed for 100 nm AuNP-PEG-Cyt *c*/Zn Porph, 100 nm AuNP-MUA-Cyt *c*/Zn Porph Cov, and 100 nm AuNP-MUA-Cyt *c*/Zn Porph Electro at 580, 575, and 579 nm, respectively. The redshifted SPR peak and peak broadening suggest changes in surface chemistry due to functionalisation with Cyt *c* and Zn Porph. As expected, the Soret band regions of cit-AuNP 100 nm, AuNP-PEG 100 nm and AuNP-MUA 100 nm showed no peaks. In contrast, AuNP-PEG-Cyt *c*/Zn Porph 100 nm, AuNP-MUA-Cyt *c*/Zn Porph Cov, and 100 nm AuNP-MUA-Cyt *c*/Zn Porph Electro displayed peaks at ~410 nm, attributed to Cyt *c*, and at ~432 nm, attributed to Zn Porph (Figure 24B).

The DLS results showed that the h_d of 50 nm AuNPs increased as expected. The h_d increased from 49.21 ± 0.81 nm (with a polydispersity index, PDI, of 0.263) for 50 nm cit-AuNPs to 65.64 ± 1.28 nm (PDI of 0.139) and 52.79 ± 1.09 nm (PDI of 0.129) for 50 nm AuNP-PEG and 50 nm AuNP-MUA, respectively. For 50 nm AuNP-PEG-Cyt *c*/Zn Porph, 50 nm AuNP-MUA-Cyt *c*/Zn Porph Cov, and 50 nm AuNP-MUA-Cyt *c*/Zn Porph Electro, the h_d values were larger than anticipated at 311.0 ± 22.4 nm (PDI of 0.428), 127.1 ± 1.6 nm (PDI of 0.237), and 831.0 ± 37.5 nm (PDI of 0.252), respectively. This suggests the presence of multilayers on the functionalised AuNPs. Although the increased diameters could imply aggregation, aggregation typically involves a significant increase

in PDI, often above 0.7. Thus, the considerable increase in h_d is more likely due to the formation of Cyt *c* and Zn Porph multilayers (Danaei et al., 2018) (Figure 24C).

The DLS results for 100 nm AuNPs showed an expected increase in h_d. For 100 nm cit-AuNPs, the h_d was 106.9 ± 1.9 nm (with a PDI of 0.051), while for 100 nm AuNP-PEG and 100 nm AuNP-MUA, the h_d values were 128.3 ± 3.4 nm (PDI of 0.057) and 112.7 ± 1.5 nm (PDI of 0.043), respectively. The h_d values for 100 nm AuNP-PEG-Cyt *c*/Zn Porph, 100 nm AuNP-MUA-Cyt *c*/Zn Porph Cov, and 100 nm AuNP-MUA-Cyt c/Zn Porph Electro were larger than anticipated, measuring 183.4 ± 30.3 nm (PDI of 0.242), 136.0 ± 2.9 nm (PDI of 0.136), and 206.3 ± 1.0 nm (PDI of 0.159), respectively. These results suggest the presence of multilayers on the functionalised AuNPs just as in the 50 nm multifunctionalised AuNPs (Danaei et al., 2018) (Figure 24D).

To investigate the possibility of aggregation, TEM analysis was conducted on the 50 nm and 100 nm AuNP-PEG-Cyt *c*/Zn Porph samples (shown in Figure 24E and F, respectively). The images in Figure 24E show AuNPs of slightly varying size and with a mostly spherical morphology but does contain some cylindrical morphologies. The morphologies of the 100 nm AuNP-PEG-Cyt *c*/Zn Porph samples in Figure 24F appear more spherical and of a more uniform size than when compared to 50 nm AuNP-PEG-Cyt *c*/Zn Porph sample. The mean diameter of the 50 nm AuNP-PEG-Cyt *c*/Zn Porph sample was measured to be 40.3 ± 14.3 nm, based on an evaluation of 163 AuNPs, while the 100 nm AuNP-PEG-Cyt *c*/Zn Porph sample exhibited an average size of 101.4 ± 9.0 nm, derived from 128 AuNPs. If aggregation had occurred, the frequency distribution would display an increase in AuNP diameter, leading to a higher average size. However, this increase was not observed, and there seemed to be no overlapping clusters, which are often associated with aggregation (Nam et al., 2009). The lack of aggregation seen in the TEM images supports the hypothesis that the SPR peak broadening, red-shifting in UV-Vis absorption spectroscopy, and the increase in h_d in DLS for the multifunctionalised AuNPs are all due to the formation of Cyt *c* and Zn Porph multilayers on the AuNPs. However, when observing the DLS size distribution for 50 and 100 nm AuNPs in Figure SI 5B and C, there appear to be aggregates forming in the solution. This is likely the result

of the conjugated molecules bound to AuNPs interacting with the conjugated molecules bound to other AuNPs.

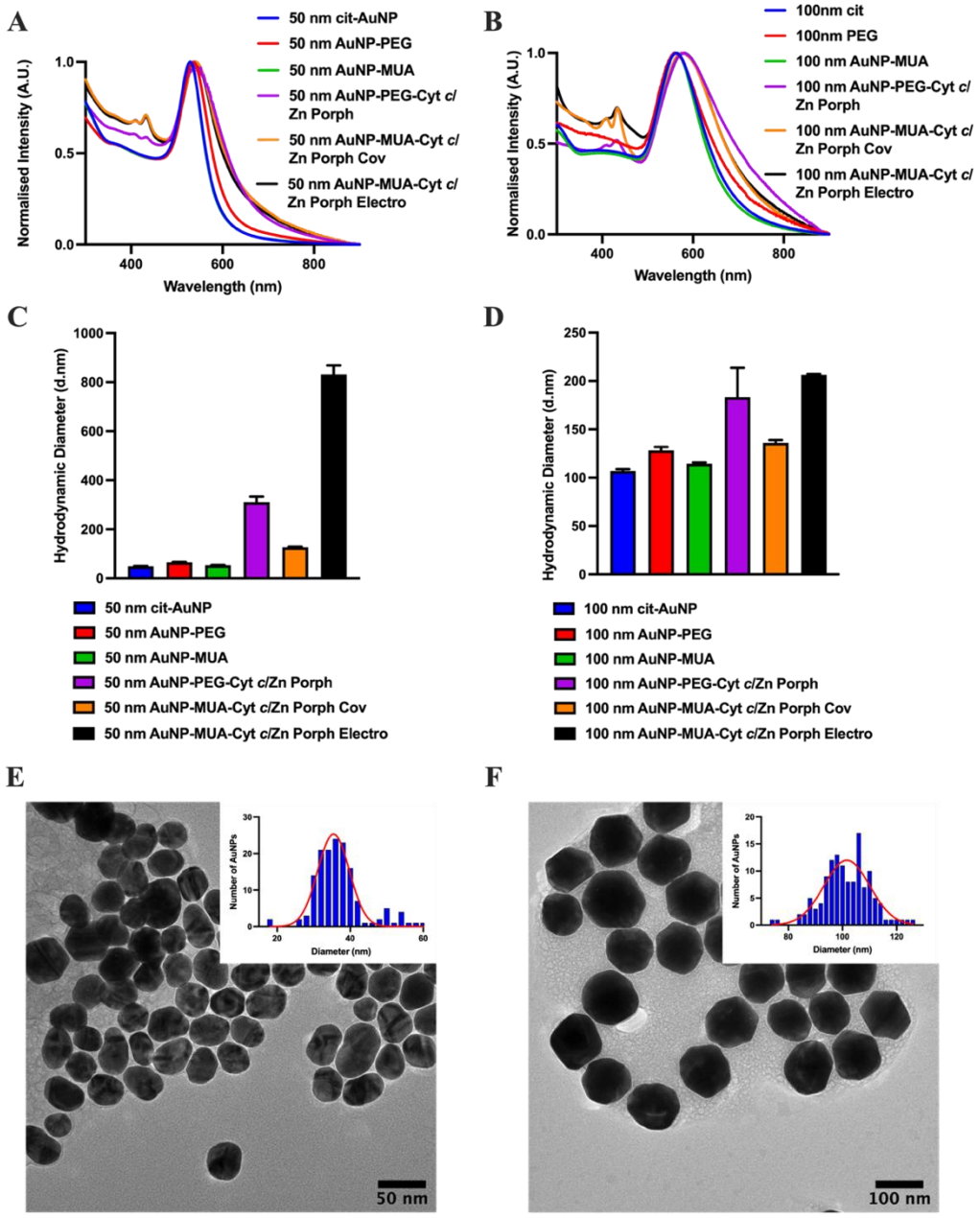


Figure 24. The physiochemical characterisation of multifunctionalised AuNPs using UV-Vis absorption spectroscopy for 50 nm AuNPS (A), 100 nm AuNPs (B) and using DLS for 50 nm AuNPs (C) and 100 nm AuNPs (D). TEM images for 50 nm AuNP-PEG-Cyt *c*/Zn Porph (E) and 100 nm AuNP-PEG-Cyt *c*/Zn Porph (F) with a cumulative frequency distribution included in the insert made using 163, 50 nm AuNPs and 128, AuNPs 100 nm AuNPs.

Deconvolution was not conducted on the SPR peak of AuNPs between 500 and 600 nm, as this region was attributed to the SPR peak of the AuNPs. The LN-MIE-Gans model fitting of 20 nm AuNPs, taken from literature, evidences this (Figure 25A), as it can predict the radius of the AuNPs based on the fit of the model to the spectra (Figure 25B) (Amendola and Meneghetti, 2009). For the spectrum of 20 nm cit-AuNPs, the radius is predicted to be 10 nm with a resultant predicted diameter of 20 nm. This predicted diameter correlates with those calculated previously for cit-AuNPs, from the TEM at 19.15 ± 2.12 nm and DLS at 19.57 ± 1.03 nm; therefore, it can be assumed that the only region of interest for deconvolution in these examples is within the Soret band region.

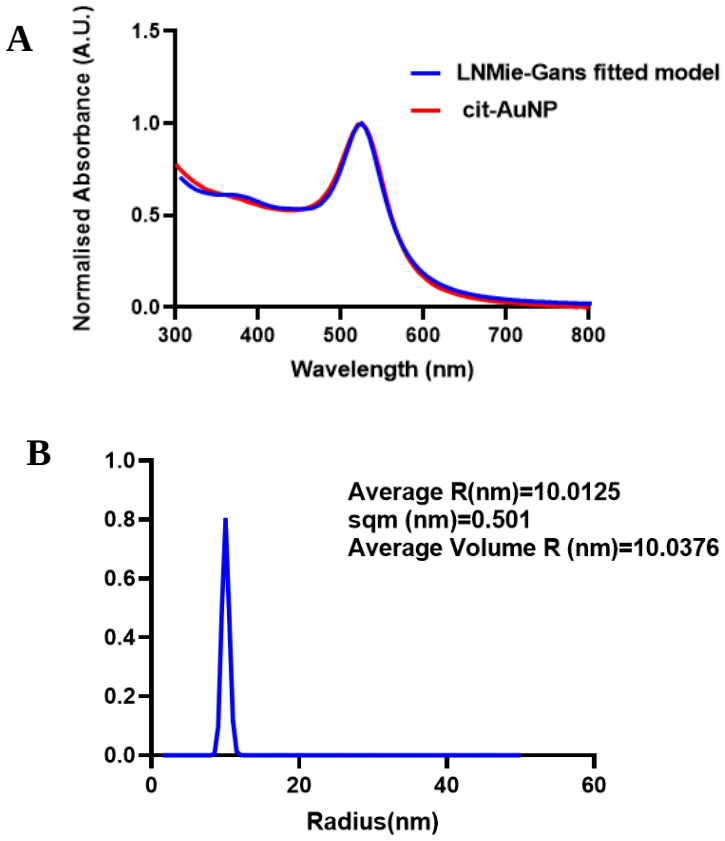


Figure 25. The use of LNMIE-Gans model fitting to 20 nm cit-AuNPs (A) to predict their size (B).

2.6. Conclusion

In this chapter, the 20, 50 and 100 nm AuNPs have all shown to have been successfully synthesised, functionalised with Cyt *c* and Zn Porph, and characterised using a combination of DLS, Zeta potential, UV-Vis absorption spectroscopy and XPS. The conjugation of Cyt *c* and Zn Porph to AuNPs was achieved using thiol-PEG-carboxyl and MUA ligands with both covalent and electrostatic conjugation mechanisms, and without causing aggregation of the AuNPs.

This novel approach to deconvolution of UV-Vis absorption spectra enables the accurate determination of the concentration of Cyt *c* and Zn Porph, as well as the exact number of molecules that are bound to AuNPs to be found. It is crucial to pinpoint the precise concentration of the conjugated molecules for the subsequent stages in this research, as this will clarify their impact. The following phase involves examining whether functionalisation approach and particle size influence the redox capabilities of Cyt *c*. Any change in the redox ability or structure may indicate a change in function which will be assessed. Ultimately, the goal is to determine whether Cyt *c* and Zn Porph when conjugated to AuNPs can trigger apoptosis in cancer cells, upon exposure to a light stimulus.

3. Structural and Electrochemical Analysis of Gold Nanoparticles Functionalised with Cytochrome *c* and Zinc Porphyrin

3.1. Aims and Objectives

In this chapter, the electrochemical ability of Cyt *c* and Zn Porph free in solution is compared to Cyt *c* and Zn Porph conjugated to AuNPs with varying components. The main goal of the work described in this chapter was to identify if the conjugation of Cyt *c* to AuNPs enforced structural change which could influence its electrochemical behaviour and therefore its function in the proposed cancer treatment in this work.

3.2. Abstract

Following the successful conjugation of Cyt *c* and Zn Porph to AuNPs described in the previous chapter, the present study aimed to assess the electrochemical properties of these molecules. It was important to determine whether conjugation to multifunctionalised AuNPs affected the structure and function of Cyt *c*, which is critical for inducing apoptosis in cancer cells. For this reason, Circular Dichroism (CD) was utilized to examine changes in the structure of Cyt *c* after conjugation to AuNPs, and TOF-SIMS to determine its spatial orientation. The electrochemical properties of Cyt *c* and Zn Porph conjugated to AuNPs were evaluated using cyclic voltammetry (CV) and differential pulse voltammetry (DPV). However, the high charging current produced by the AuNP-functionalised samples in CV meant it was difficult to determine accurately the heterogeneous rate constant (k^0) of Cyt *c* or Zn Porph. Therefore, a new method was developed using DPV, allowing the accurate identification of peak current and potential of both Cyt *c* and Zn Porph when conjugated to AuNPs, thereby enabling their k^0 values to be ascertained. The findings indicated that the k^0 value of Cyt *c* conjugated to multifunctionalised AuNPs was

lower than that of Cyt *c* free in solution, likely due to the structural changes observed in the CD data. The orientation of Cyt *c* did not appear to be influential upon the k^0 values, while the effect of ligand packing density in AuNPs and the size of the AuNPs were more significant. The k^0 values of Zn Porph also showed a decrease after conjugation, but this was not significant. Nevertheless, it was found that the electrochemical abilities of both Cyt *c* and Zn Porph were retained after conjugation to AuNPs, and all samples were therefore used for *in vitro* studies as reported in the next chapter.

3.3. Introduction

3.3.1. Chapter contents

In the previous chapter, the characterisation indicated the successful conjugation of Cyt *c* and Zn Porph to AuNPs. The next step in this research was to assess whether the redox ability of Cyt *c* was affected when conjugated to AuNPs. The ability for Cyt *c* to induce apoptosis upon redox change (Ow et al., 2008), known as 'activation', made it ideal for use in this project; however, the redox ability of Cyt *c* still needs to be present after conjugated to AuNPs to induce apoptosis. By varying the conjugation strategies, SAM ligands, and AuNP size, this study aimed to identify which formulations maintained, enhanced, or reduced the redox ability of Cyt *c*. This information would help determine whether changing the redox abilities of Cyt *c* when conjugated to AuNPs affects their ability to induce apoptosis in cancer cells.

Different sizes of AuNPs were used (20, 50 and 100 nm) to establish whether this influenced the redox ability of Cyt *c*. The hypothesis is that larger AuNPs may allow for increased electron transfer rate, while smaller AuNPs with a larger cumulative surface area of gold could have a greater influence on the redox ability of Cyt *c*. Different sized AuNPs would also allow for different amounts of Cyt *c* to be conjugated to each particle, due to different surface areas; ergo, larger AuNPs would allow for the conjugation of a greater quantity of Cyt *c*.

A previous study conducted by Romanovskaia et al., 2022 found that smaller AuNPs had stronger electrochemical interactions when oxidising with L-cysteine (a thiol containing amino acids), possibly due to the formation of agglomerates (Romanovskaia et al., 2022). The overall greater surface area of smaller AuNPs in a given volume could accommodate more Cyt *c*, which may affect the electron transfer rate.

The ligands were varied in this research to assess the impact of distance on the redox ability of Cyt *c* when conjugated to AuNPs. Both ligands used had a thiol termination group for strong Au-S bonding to form SAMs (Villarreal et al., 2017), and a carboxyl group for electrostatic or covalent bonding (Jain et al., 2021, Tollefson et al., 2019, Zhang et al., 2017). Ligand length was the main differentiation between the two, with 11-mercaptoundecanoic acid (MUA) being ~1.4 nm in length and thiol-PEG-carboxyl 2 kDa being ~7.9 nm (length determined via ChemDraw 3D). Both ligands have been previously used in literature in conjugation with Cyt *c* and had demonstrated a redox ability (Millo et al., 2009, Oviedo-Rouco et al., 2020, Jain et al., 2021, Pessoa, 2022). Alternating ligand length tested whether the proximity of conjugated molecules to AuNPs affected their redox ability, with the hypothesis being that increased distance would result in less influence from AuNPs and their electrochemical enhancing properties (Jo et al., 2022). Previous work produced by Barfidokht et al., 2013 has shown that increasing the distance between a redox molecule and an electron-rich node can reduce electron transfer abilities, as seen with ruthenium hexane (Barfidokht et al., 2013). Although this system differs, the principle may still apply to Cyt *c* and the iron at the centre of the heme contained within the protein and is responsible for the electron transfer abilities.

Multiple methods of conjugating Cyt *c* to the ligand of the AuNPs were trialled to investigate their effect on the redox ability of Cyt *c*. Previous work conducted in the Rawson group showed that modifying the ligand's termination functional group influenced the orientation of Cyt *c* (Jain et al., 2021). The terminated functional groups of carboxyl, hydroxyl and amino have negative, neutral, and positive zeta potentials (ζ) respectively. The different charged functional groups would then be attracted to differently charged amino acid residues in Cyt *c*, modulating its orientation. The AuNPs

with carboxyl terminated ligands were shown to have had a greater electrostatic interaction with lysine (Lys), whereas the hydroxyl and amino groups were shown to have an electrostatic interaction with glutamic acid (Glu). The cysteine (Cys) residues had been previously reported to be located on the opposite side of the heme group of Cyt *c* to Glu and leucine (Leu), and by using time-of-flight secondary mass spectrometry (TOF-SIMS), the intensity values can then be used to help understand the orientation of Cyt *c* (Jain et al., 2021, Baio et al., 2013). The apoptotic potential of Cyt *c* when conjugated to AuNPs was found to be correlated with its orientation, with the heme group orientated towards the carboxyl group ligand termination demonstrating the lowest ability to induce apoptosis in cancer cells (Jain et al., 2021). However, this thesis aimed to examine the effect that covalent conjugation has on the redox ability of Cyt *c*, as this could provide an inherently stronger and longer lasting bond with the conjugated molecules. Carbodiimide (EDC/NHS) is a well-known method used in conjugation through establishing amide linkages (Keleştemur et al., 2017). Cyt *c* has many amino groups, so carboxyl-terminated ligands were used to compare Cyt *c*'s redox ability when conjugated to AuNPs either electrostatically or covalently utilising EDC/NHS. The hypothesis was that stronger covalent conjugation may influence the secondary and tertiary structures of the Cyt *c*, potentially affecting its redox ability.

This chapter also investigates how Zn Porph affected the redox ability of Cyt *c* when conjugated to AuNPs. Previous work by Sanjuan-Alberte et al., 2019 demonstrated that Zn(II) meso-tetrakis(4-carboxyphenyl)porphyrin sodium salt (Na-ZnTCPP) conjugated to AuNPs could produce fluorescence in cells when stimulated with an electrical field (Sanjuan-Alberte et al., 2019). Based on this finding, a similar porphyrin with a Zn ion in the porphyrin ring was chosen, Zn Porph. The goal was to use monochromatic visible light to excite Zn Porph, with the energy released as the Zn Porph returns to its ground state resulting in the 'activation' of Cyt *c*, subsequently inducing apoptosis in cancerous cells.

3.3.2. Circular Dichroism

Circular dichroism (CD) is a spectroscopic technique that measures the differential absorption between left-handed circularly polarized light (LCP) and right-handed circularly polarized light (RCP) components by a chiral molecule in solution (Greenfield, 2006). CD spectroscopy can provide information about the secondary structure and conformational changes of chiral molecules such as proteins, nucleic acids, and carbohydrates, when in solution. The basic principle of CD spectroscopy relies on chiral molecules absorbing circularly polarized light differently than achiral molecules. When circularly polarized light passes through a solution of chiral molecules, the two components will experience different amounts of absorption depending on the orientation and electronic structure of the chiral molecule (Greenfield, 2006, Garab and van Amerongen, 2009). The difference in absorption between the LCP and RCP components is measured using a detector, such as a photodiode. The CD signal is calculated as the difference in absorbance between the two light components and is usually reported in units of molar ellipticity (θ) or delta epsilon ($\Delta\varepsilon$), which represent the magnitude of the CD signal.

CD spectra can then provide information about the secondary structures of proteins, such as the alpha-helices and beta-sheets, by analysing the shape and magnitude of the CD signal at specific wavelengths (Greenfield, 2006, Garab and van Amerongen, 2009).

CD spectra of Cyt *c* have previously shown two negative bands at ~208 nm and ~222 nm, and a positive band at ~190 nm; alpha-helices have a characteristic positive peak at ~190 nm and a negative peak at ~208 nm, while beta-sheets have a negative peak at ~218 nm. The intensity and shape of these bands can be used to estimate the percentage of alpha-helical content in the protein, as well as in monitoring changes in the secondary structure of the protein under different conditions (Sreerama et al., 2000, Jain et al., 2021). The tertiary structures of Cyt *c* can be understood by its CD spectrum, as two minima at 282 nm and 288 nm can be attributed to Tryptophan residues (Vinogradov and Zand, 1968)

and the Soret region (between 360 nm to 450 nm) can be attributed to the amino acid residues located close to the heme ring (Jain et al., 2021).

Changes in the structure of a protein or nucleic acid can also be monitored using CD spectroscopy, such as the folding or unfolding of a protein or the melting of a DNA duplex (Greenfield, 2006, Garab and van Amerongen, 2009). CD will be used in this study to determine if any structural changes occur after Cyt *c* is conjugated to multifunctionalised AuNPs.

3.3.3. ToF-SIMS

Time-of-Flight Secondary Ion Mass Spectrometry (ToF-SIMS) is a surface analysis technique used to determine the chemical composition and molecular structure of solid surfaces with high sensitivity and specificity. The technique can provide spatial resolution at less than 1 μm and is widely used in materials science, surface chemistry, and biomedicine (Belu et al., 2003). The ToF-SIMS instrument consists of a primary ion source, a sample stage, and a mass spectrometer. The primary ion source generates a beam of high-energy primary ions, which are directed towards the sample's surface. The primary ions cause the emission of secondary ions on impact, which are then accelerated towards the mass spectrometer. The mass spectrometer separates the secondary ions based on their mass-to-charge ratio (m/z) and detects their intensity (Belu et al., 2003).

ToF-SIMS can be used to analyse a wide range of materials, including inorganic materials, organic materials, and biological samples. It can provide information about the elemental composition of a sample as well as the molecular composition of its surface. The technique can identify specific molecules and their functional groups, making it useful for analysing complex mixtures, such as polymers and biological tissues (Belu et al., 2003).

ToF-SIMS has been previously used by the Rawson group to predict the orientation of Cyt *c* conjugated to AuNPs (Jain et al., 2021). This same application will be used with the Cyt *c* conjugated to AuNPs but different conjugations will be used in this study to

determine whether the conjugation stratergy affects the orientation and then link the findings to the redox ability of Cyt *c*.

3.4. Methods:

3.4.1. AuNPs Functionalised with Cyt *c* and Zn Porph

Prepared as described in section 2.4.8 to 2.4.10. The only difference is that the final pellet was suspended in 10 mM PBS.

3.4.2. ToF-SIMS

The ToF-SIMS analysis was conducted in accordance with the work produced by Jain et al., 2021. Microscopy glass slides were cleaned with IPA and left to dry overnight before drop-casting the Cyt c functionalized AuNPs onto them. ToF-SIMS analysis was performed on each AuNP sample using a TOF SIMS IV system from ION-TOF GmbH (Münster, Germany), acquiring spectra for positively charged secondary ions. A 25 keV Bi3+ primary ion beam was used in the high current bunched mode to deliver 0.3 pA, and raster scanning was performed 30 times over a 100 x 100 μm^2 area, with a total dose kept below the static limit of 10^{12} ions/cm^2. To prevent charge build-up, a low-energy (20 eV) electron flood gun was utilized. The ToF analyzer was set to a 200 μs cycle time, providing a mass range of 0-3492 mass units. Six spectra were collected from different regions of each sample, and control spectra of only cit-AuNPs were also obtained.

3.4.3. Circular Dichroism

CD spectra were recorded in the Far and near UV as well as the Soret region at 20 °C on a Chirascan CD spectrophotometer (Applied Photophysics) equipped with a temperature control unit TC125 (Quantum Northwest). All the AuNP samples functionalised with Cyt *c* and Cyt *c* Ox and Red free in solution were dispersed in 10 mM PBS at pH 7.4. Three

spectra were taken for each sample and averaged. A quartz cuvette with an optical path length of 1 mm was employed for all CD measurements.

3.4.4. Electrochemical Methods

This section makes constant reference to the works of (Bard and Faulkner, 2002, Elgrishi et al., 2018, Compton and Banks, 2018).

Electrochemistry is essentially the study of electron flow in chemical reactions. The faradaic electrochemical experiments in this work rely on a three-electrode system as shown in Figure 26. The working electrode is the site of the desired reaction, which in this work is an indium tin oxide (ITO) coated glass. A reference electrode plays a crucial role in the electrode system as it provides a known, established potential against which the potential of the system is measured. A silver/silver chloride (Ag/AgCl) reference electrode is also employed to maintain a very stable potential, achieved through the equilibrium of a redox system that sustains consistent concentrations of both reduced and oxidised species. The counter electrode, a platinum wire in this system, establishes a complete circuit.

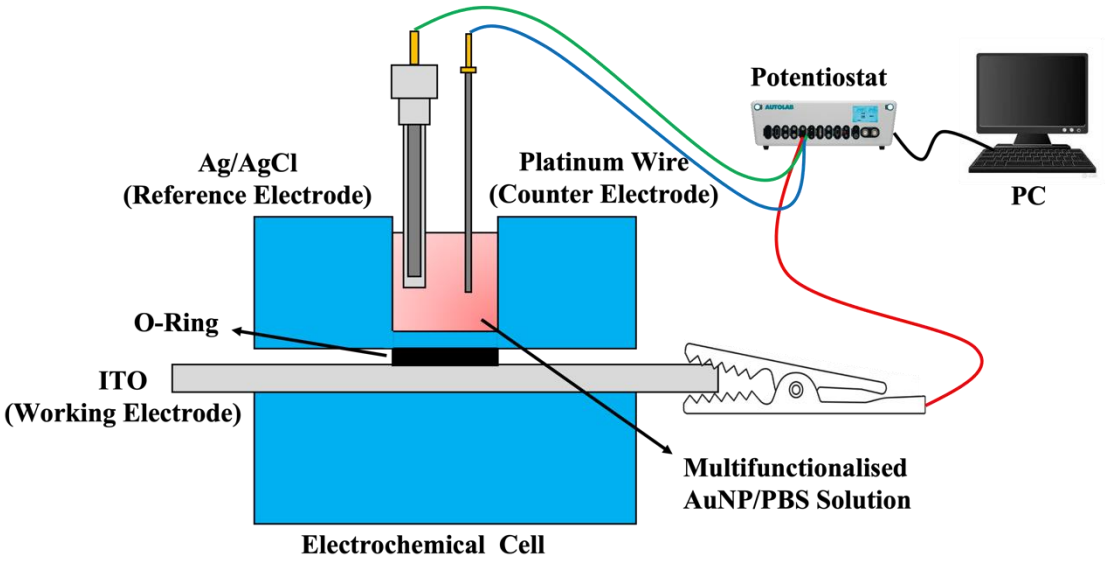


Figure 26. Schematic of the three-electrode system used in this work where the electrochemistry of multifunctionalised AuNPs in a PBS solution was measured using an ITO working electrode, Ag/AgCl reference electrode and a platinum wire counter electrode which are connected to a potentiostat and a PC so the sample can be analysed.

A core principle in electrochemical processes is Butler-Volmer kinetics, which implies that an electrode's current hinges on its potential, assuming that both the reduction and oxidation reactions are taking place on the same electrode. This correlation between current and potential is reflected in a plethora of electrochemical formulas, some of which are used to determine redox capabilities of Cyt *c* natively and when conjugated to multifunctionalised AuNPs.

Normal hydrogen electrodes (NHE) were traditionally used as reference electrodes with a standard potential of 0 at all temperatures, however due to difficulties maintaining known values of hydrogen pressure, temperature and concentration constant, this reference electrode is difficult to work with. An Ag/AgCl reference electrode was chosen for this work as it is an affordable and simple to construct option that is readily available commercially. An Ag/AgCl electrode is based on the half-reaction shown in Equation 4, with a formal potential of 0.199 vs NHE at 25°C 157 (White, 1990).

$$AgCl_{(s)} + e^{-} \rightarrow Ag_{(s)} + Cl_{(aq)}$$

Equation 4.

This is the half-reaction for a silver chloride cell (s represents solid, aq represents aqueous). An AgCl electrode comprises a silver wire cloaked in silver chloride and dipped in saturated potassium chloride, typically isolated from the bulk solution by a porous frit. Using a reference electrode (platinum wire) enables the measurement of the potential difference across an electrochemical cell.

The solution in which the electrodes are immersed must also be controlled and contain an analyte and electrolyte. The compound set to be reduced or oxidised is called the 'analyte'. Interactions between the analyte and the electrode may occur through quantum mechanical tunnelling, so it's critical that the analyte be within 10-20 Å of the electrode surface. Consequently, the potential decline between the electrode surface and the bulk solution should take place over a similar distance for successful reduction or oxidation of the analyte. If this condition is not met, only a portion of the potential decline will be available to facilitate the electron transfer, necessitating equation modifications. Such modifications are known as 'Frumkin corrections' and will not be covered further in this work. Electrochemists deliberately introduce high volumes of supporting electrolyte to compress the potential drop within 20 Å of the working electrode surface to sidestep this issue. These solutions are ideally inactive at the potential range being studied. The electrochemical experiments within this thesis used 10 and 25 mM phosphate buffered saline (pH 7) as the supporting electrolyte, which is suitable for biological studies.

3.4.5. Cyclic Voltammetry:

Cyclic voltammetry was conducted on a Metrohm Autolab M204 potentiostat in a three Electrode setup which was placed within a Faraday cage. The counter electrode consisted of a platinum wire, the reference electrode was Ag/AgCl and the working electrode was indium tin oxide (ITO). ITO-coated glass was cut to approximately 10mm x 20mm,

washed with acetone, isopropan-2-ol and water and dried with Nitrogen gas. The ITO was then assembled in an electric chemical cell with an exposed working area of 38.48 mm^2 defined by a silicone "O" ring. A new ITO working electrode was used for every sample. The Cyt *c* free in solution and AuNPs with conjugated Cyt *c* were dispersed in PBS at varying concentrations determined by UV-Vis spectroscopy. CVs were conducted at a potential range of -0.2 V to 0.4 V with a start potential of -0.2 V and switching of 0.4 V and end of -0.2 V and -0.2 V to 1.2 V with a start potetial of -0.2 V and switching of 1.2 V and end of -0.2 V using scan rates varying between 50 $mV.s^{-1}$ to 2 $V.s^{-1}$.

3.4.6. Cyclic Voltammetry Analysis

The peak current and potential position for both redox peaks were calculated in Origin Pro. Firstly, the data was split into two sections; the oxidation peak data which ranged from -0.2 to 0.4 V, and the reduction peak data from 0.4 to -0.2 V (the second part of the potential cycle). Each section of the cyclic voltammogram was then plotted and the background was subtracted. To background subtract, a 4^{th} order polynomial fit was selected and nodes were placed along the cyclic voltammogram to act as anchors. The region of interest for Cyt *c*, between -0.1 V and 0.2 V, was left clear of nodes in both the oxidation and reduction data sets, allowing a background to be created in this region. The interpolation method was changed from line to Spline and background then subtracted. The resulting data was plotted in GraphPad Prism 9 and the area under the graph function was utilised to obtain the peak height and position. This was repeated for the oxidation and reduction peaks for the scan rate of each sample.

3.4.7. Differential Pulse Voltammetry

Differential pulse voltammetry was conducted in accordance to section 3.4.5, with the exception of running the potential from -0.2 V to 0.4 V or -0.2 to 1.2 V for the oxidation peaks. The potentials were then reversed for the reduction peaks. Scan rates varied from 50 $mV.s^{-1}$ to 10 $mV.s^{-1}$. A voltage amplitude of 25 mV was utilised on all samples.

3.4.8. Differential Pulse Voltammetry Analysis:

The peak current and potential position for both redox peaks was calculated in Origin Pro. The data sets for the redox peaks were stored as different files as DPV increases or decreases potential in a linear sweep, therefore the data does not have to be split as in section 3.4.6. The oxidation data ranged from -0.2 V to 0.4 V for Cyt *c* free in solution or bound to AuNPs, and from -0.2 V to 1.2 V when the system contained both Cyt *c* and porphyrins free in solution or bound to AuNPs. For the reduction data, the inverse potentials were applied from 0.4 V to -0.2 V for Cyt *c* free in solution or bound to AuNPs, and from 1.2 V to -0.2 V for the Cyt *c* and porphyrins free in solution. Each section of the cyclic voltammogram was then plotted and background subtracted. To background subtract, a 4^{th} order polynomial fit was selected, and nodes were placed along the cyclic voltammogram at points acting as anchors. The region of interest for Cyt *c* between -0.1 V and 0.2 V was left clear of nodes, allowing a background to be created in this region. The region of interest for the porphyrins ranged between 0.3 V to 0.6 V for the first redox peak, and 0.7 V to 1 V for the second peak; both regions were left clear of nodes allowing a background to be created in both. The interpolation method was changed from line to Spline and the background was subtracted. The resulting data were plotted as a new graph in Origin Pro and using the quick peaks tool the region of interest mentioned previously was selected. The baseline mode was set to 2^{nd} derivative with the range of curve within ROI selected, and the smoothing method used for the baseline was adjacent-averaging with a maximum of 8 anchor points and the connect method set as the line. The peak finding method was set to a local maximum determined by 15 local points, and peak filtering was turned on to a threshold height of 20%. Once the peaks were identified by the software, their heights and position were output to a table.

3.4.9. Statistical analysis

Statistical analysis was performed in GraphPad Prism v9.4.0 software (GraphPad Software, Inc). Data are shown as mean ± SD unless stated otherwise in the section. For comparison between data and single control, a one-way ANOVA with a Dunnett test was used, $P \leq 0.05$ was significant. For the histograms that used a normal frequency distribution, a non-linear curve was plotted with a Guassian fit, the result of which was presented as mean ± SD.

3.5. Results

3.5.1. Circular Dichroism

3.5.2. Cyt *c* Ox and Red at different concentrations

The CD spectra of Cyt *c* were recorded at two different concentrations, 20 μM and 1 μM, to determine whether the maxima and minima peaks changed as signal-to-noise ratio changed (lower Cyt *c* concentration should have a larger signal-to-noise ratio) (Figure 27A-F). The higher concentration of Cyt *c* was utilised to obtain an accurate CD spectrum, while the lower concentration was employed to represent the amount of Cyt *c* that is usually conjugated to AuNPs. In the Far-UV CD spectra (in the range of 180-260 nm), the double minima in molecular ellipticity located at 208 and 222 nm and the positive band at ~190 nm can be identified for Cyt *c* Ox and Red in both 20 μM (Figure 27A) and 1 μM (Figure 27D). The double minima and positive band signify the α helical content, which can be associated the catalytic ability of the protein (Greenfield, 2006). The double minima are more defined for Cyt *c* Red than Cyt *c* Ox in both Figure 27A and Figure 27D, insinuating a greater α helical content. The near-UV CD spectra in the range of 260-360 nm showed a double minimum at 282 nm 288 nm for both Cyt *c* Ox and Red at 20 μM (Figure 27 B), which can be associated with Tryptophan residues indicative of the tertiary structure (Vinogradov and Zand, 1968). Only the minimum at 288 nm are visible in Cyt

c Ox and Red at 1 μM, with the 282 nm band appearing to blue shift to ~275 nm (Figure 27E), as the signal to noise ratio must be too large to detect this minimum at 282 nm. The CD spectra was also obtained in the Soret region (360-450 nm), enabling further understanding of the tertiary structure of Cyt *c*, as the Soret region can be attributed to the amino acid residues near the heme ring of Cyt *c* (Figure 27C and F). The 20 μM Cyt *c* Ox and Red showed maxima at 405 and 408 nm respectively, with minima both at 416 nm. 20 μM Cyt *c* Red also displayed an additional maximum at 431 nm (Figure 27C). For 1 μM Cyt *c* Ox and Red, the maxima and minima were blue shifted to 403 and 412 nm respectively, with 1 μM Cyt *c* Red displaying the same maxima as 20 μM Cyt *c* Red at 431 nm. This data, therefore, shows that lower Cyt *c* concentrations, comparable to those observed in AuNP samples conjugated with Cyt *c*, produce high signal to noise background resulting in spectra of Near-UV CD and Soret region CD that are more difficult to interpret. CD was conducted for Cyt *c* conjugated to AuNPs using HS-PEG-COOH covalently (with EDC/NHS), MUA covalently (with EDC/NHS), and MUA electrostatically to investigate the conjugation's effect on the structure of the protein.

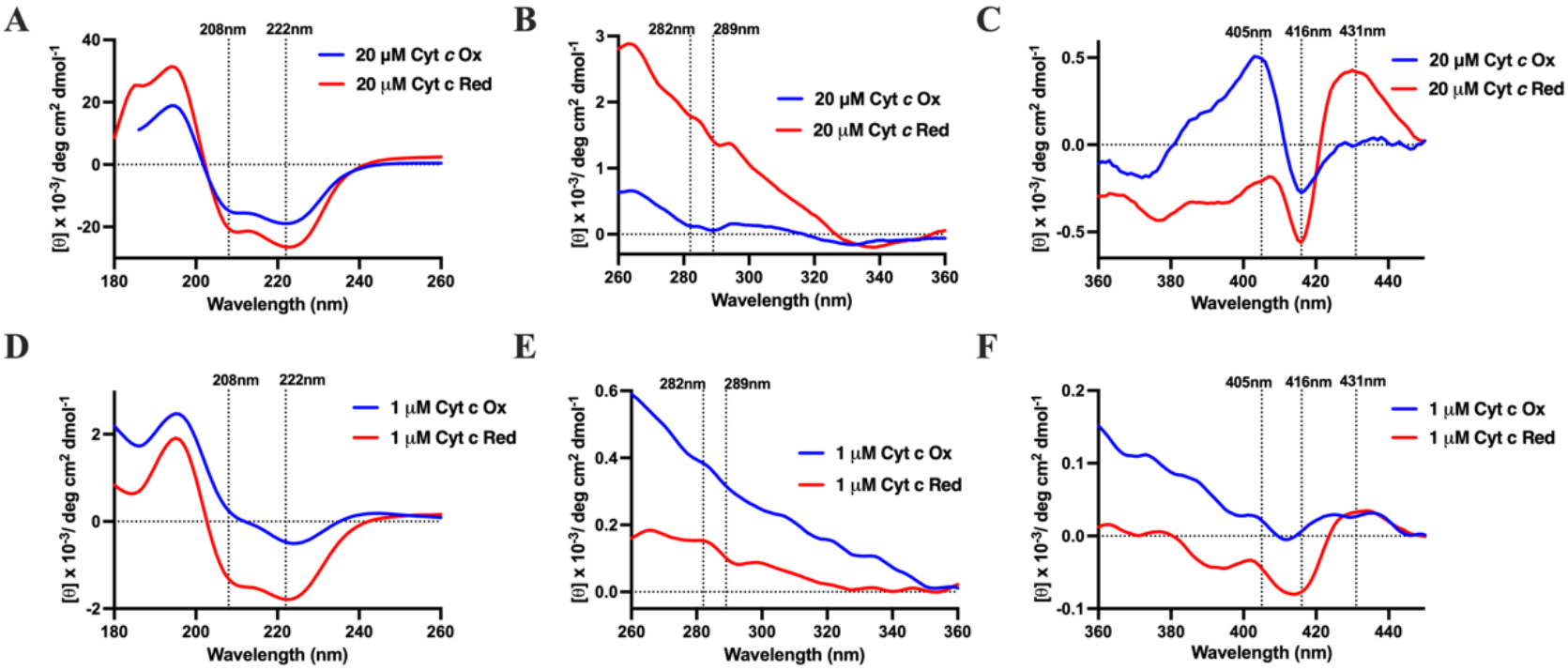


Figure 27. Comparison between the CD of 20 and 1 μM Cyt c. The CD spectra of 20 μM Cyt c Ox and Red in the Far-UV region (A), near-UV region (B) and Soret region (C). The CD spectra of 1 μM Cyt c Ox and Red in the Far-UV region (D), near-UV region (E) and Soret region (F).

3.5.3. Investigation on the Structural Change of Cyt *c* after conjugation to AuNPs of different sizes using different ligands and conjugation methods

For the Cyt *c* covalently bound to AuNPs using HS-PEG-COOH (with EDC/NHS), the Far-UV region for all of the samples (Figure 28A) demonstrated clear minima at 208 and 222nm, the same positions seen with Cyt *c* free in solution (Figure 27A and D), suggesting no change in the secondary structure of Cyt *c*. The CD spectra for the 20 nm AuNPs are more defined; this is most comparable to Cyt *c* Red, despite Cyt *c* Ox being used in this functionalisation method. (Figure 28A). Cyt *c* functionalised using MUA covalently (with EDC/NHS) showed less defined CD spectra when compared to Cyt *c* free in solution (Figure 27A and D), although the position of one minimum at 208 nm was maintained (Figure 28D). Despite this, the minima at 222 nm was red-shifted to 227 nm, suggesting a change in α helical content and therefore an alteration in the secondary structure of Cyt *c*. Cyt *c* functionalised using MUA electrostatically presented minima at 208 nm, but showed the 222 nm minima to be red shifted to 225 nm for the 20 nm AuNPs, and to 227 nm for 50 and 100 nm AuNPs, once again suggesting changes in α helical content and subsequently in the secondary structure (Figure 28G). The definition of the CD Far-UV spectra becomes lesser as the AuNP size deceased for Cyt *c* conjugated to MUA electrostatically, likely the result of a lower overall content of Cyt *c* in the samples with larger AuNPs. The CD spectra in the near-UV region showed a double minima at 282 nm and 289 nm for all Cyt *c* conjugated to AuNPs using HS-PEG-COOH (Figure 28B) and MUA covalently (Figure 28E), indicating tertiary structure (signified by Tryptophan residues) remained unchanged (Figure 27B and E). The 20 and 100 nm AuNP-MUA-Cyt *c* Electro samples also showed these double minima at 282 nm and 289 nm, suggesting they too have an unchanged tertiary structure, whereas these minima are not visible for 50 nm AuNP-MUA-Cyt *c* Electro, indicating a change in the tertiary structure of this sample. The CD spectra in the Soret region for Cyt *c* conjugated to AuNPs (Figure 28C, F and I for Cyt *c* conjugated to AuNPs using HS-PEG-COOH covalently, MUA

covalently, and MUA electrostatically, respectively) differed from that observed of the Cyt *c* free in solution (Figure 27C and F). The positive maxima for Cyt *c* conjugated to AuNPs with HS-PEG-COOH were located at 403, 410 and 405 nm for 20, 50 and 100 nm AuNP samples respectively. The minima were not present in 50 nm AuNP samples but appeared at 420 nm for both the 20 and 100 nm samples (Figure 28C). These changes in the maxima and minima indicate a structural change around the heme moiety of Cyt *c*. The structural changes are similarly observed for both Cyt *c* conjugated to AuNPs using MUA covalently and electrostatically (Figure 28F and I), as the shape of the spectra and positions of maxima and minima all differ from Cyt *c* Ox or Red free in solution.

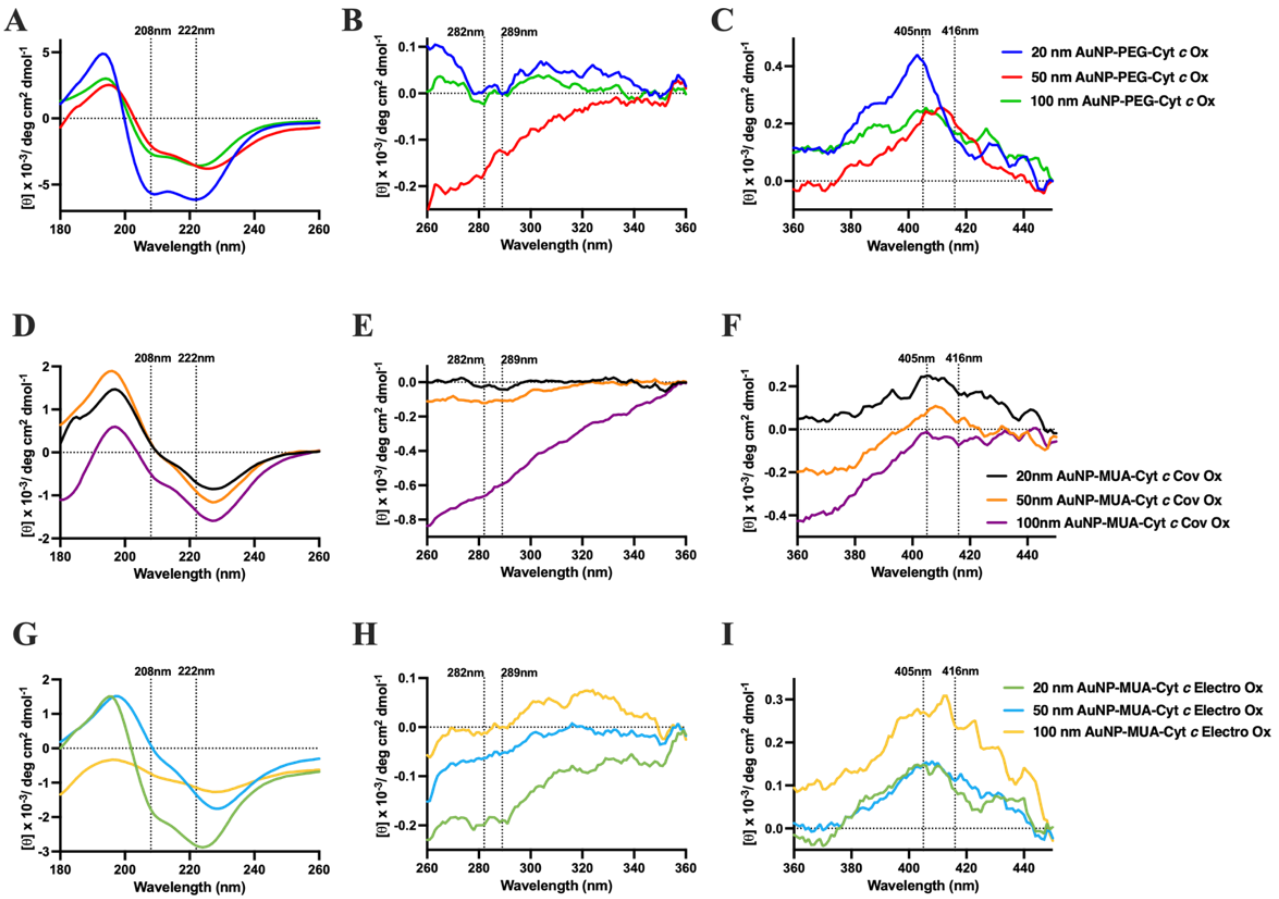


Figure 28. Comparison between the CD of Cyt c conjugated to AuNPs using HS-PEG-COOH covalently (with EDC/NHS), MUA covalently (with EDC/NHS) and MUA electrostatically. 20, 50 and 100 AuNP-PEG-Cyt c in the Far-UV region (A), near-UV region (B) and Soret region (C). 20, 50 and 100 AuNP-MUA-Cyt c Cov in the Far-UV region (D), near-UV region (E) and Soret region (F). 20, 50 and 100 AuNP-MUA-Cyt c Electro in the Far-UV region (G), near-UV region (H) and Soret region (I).

The CD spectra indicate that Cyt *c* undergoes structural changes when conjugated to AuNPs using different ligands and methods of conjugation. It was observed that Cyt *c* conjugated to AuNPs using thiol-PEG-carboxyl experienced minimal changes, as evidenced by alterations in only the CD spectra in the Soret region (indicating modifications in the heme group's structure). However, when Cyt *c* was conjugated to AuNPs using MUA through covalent and electrostatic interactions, the secondary and tertiary structures of Cyt *c* were altered. No specific correlation could be identified to determine the effect of the conjugation method, as Cyt *c* showed similar secondary and tertiary distortion when conjugated to AuNPs both covalently and electrostatically. The significant differences between Cyt *c* conjugated to AuNPs with HS-PEG-COOH and MUA is the length of the ligand and the chemical composition.

The 2 kDa PEG ligand, with a predicted length of ~7.9 nm (determined via ChemDraw3D), offers a relatively large buffer between Cyt *c* and the AuNP surface. This spacing, coupled with the innate flexibility of PEG (Shi et al., 2021), likely minimises steric hindrance and interactions with the AuNP, resulting in the observed minimal structural perturbations. PEG is commonly known to repel proteins, therefore it would be easy to assume that this repulsion would cause structural changes to proteins, however, the changes were not as large as expected (Meziadi et al., 2022). Conversely, MUA's shorter stature, with a length of ~1.4 nm, ensures Cyt *c* remains near the AuNP. This closeness intensifies potential interactions, possibly leading to the increased structural distortions seen when Cyt *c* binds both covalently and electrostatically to AuNPs. Given the increased absorption and light scattering properties of AuNPs in the visible and Near-UV regions, these may further complicate the structural analysis, causing challenges in identifying spectral maxima and minima, and resulting in spectral shape changes. Beyond these physical considerations, the unique chemistry of each ligand plays a pivotal role. While both ligands possess carboxylic functionalities, their distinct spatial orientations and lengths might foster varying interactions with Cyt *c*. Specifically, MUA's inherent chemical properties might prompt unique interactions or steric hindrances not evident with thiol-PEG-carboxyl. Consequently, MUA emerges as the more influential ligand,

primarily due to its closer positioning to the AuNPs surface and the potential for stronger chemical interactions.

3.6. ToF-SIMS

In this work, ToF-SIMS was used to investigate whether the orientation of Cyt *c* conjugated to AuNPs varied with different AuNP sizes and ligands. Earlier studies by Baio et al., 2013, found that cysteine residues (Cys) were situated close to the heme moiety of Cyt *c*, while glutamic acid (Glu) and leucine residues (Leu) were located on the opposite side of the heme moiety. The study used ToF-SIMS to compare the secondary ion intensity related to cysteine residues to that of glutamic acid and leucine. The researchers were then able to determine the orientation of Cyt *c* by calculating the ratio R=ICys/(ILeu+IGlu) (Baio et al., 2013). By virtue of this previous work, the Rawson group proposed that Cyt *c* within AuNP-COOH-Cyt *c* would have an orientation in which the heme ring is positioned near the protein-ligand interface, with the positively charged residues lysine (Lys 79) electrostatically interacting with the carboxylic group. This orientation would bring the Cys residues nearer to the carboxylic group, leading to reduced secondary ion intensity detected by ToF-SIMS. In both studies, it has been suggested that a change in R of ~50% or greater indicates a 180° rotation in orientation.

Figure 29 displays the ToF-SIMS peak intensity ratios R=ICys/(ILeu+IGlu) for Cyt *c* that is conjugated to 20, 50, and 100 nm AuNPs using thiol-PEG-COOH covalently (with EDC/NHS), MUA covalently (with EDC/NHS), and MUA electrostatically. The comparison is made against 100 nm AuNP-MUA-Cyt *c* Electro: the closest match to the work by Jain et al., 2021 which predicts the orientation of the heme of Cyt *c* to be towards the terminated carboxyl group (Jain et al., 2021). The results in this work show that 20 and 50 nm AuNP-MUA-Cyt *c* Electro and 20 nm AuNP-MUA-Cyt c Cov have an R difference of ~50% or greater, when compared to 100 nm AuNP-MUA-Cyt *c* Electro, indicating an orientation change. The R value suggests that Cys residues in the Cyt *c* of 20 and 50 nm AuNP-MUA-Cyt c Electro and 20 nm AuNP-MUA-Cyt *c* Cov have a higher

intensity than Glu or Leu residues and thus must be orientated away from the AuNP. The longer ligand, thiol-PEG-carboxyl, did not show a change in R value for Cyt *c* conjugated to any size AuNP, only the 20 and 50 nm AuNPs functionalised with MUA showed a change. These results indicate that the orientation of Cyt *c* is influenced by the AuNPs themselves and orientation change is more prevalent in the weakly bound electrostatic samples. The samples with smaller AuNPs have more individual AuNPs contained in a given mass of Au, and so the positively charged Lys residues may be more influenced by the electron-rich AuNPs in the solution. The Lys residues are mostly located near the Cys residues, exposing the heme ring more and producing a higher Cys residue intensity value. Glu is negatively charged and so may be repelled by the electron rich AuNPs and appears at a lower intensity as Glu and Leu (both located at the opposite side of the heme ring when compared to Cys) would be hidden more by the Cyt c structure for the samples with a more exposed heme ring of Cyt *c*. The secondary ion intensity from the heme moiety consisting an iron-porphyrin fragments ($C_{34}H_{33}N_4O_4Fe^+$ – 617.186 u, 618.12 u and 619.12 u) were analysed and also support the findings as the changes in intensity match the aforementioned results (Figure SI 6).

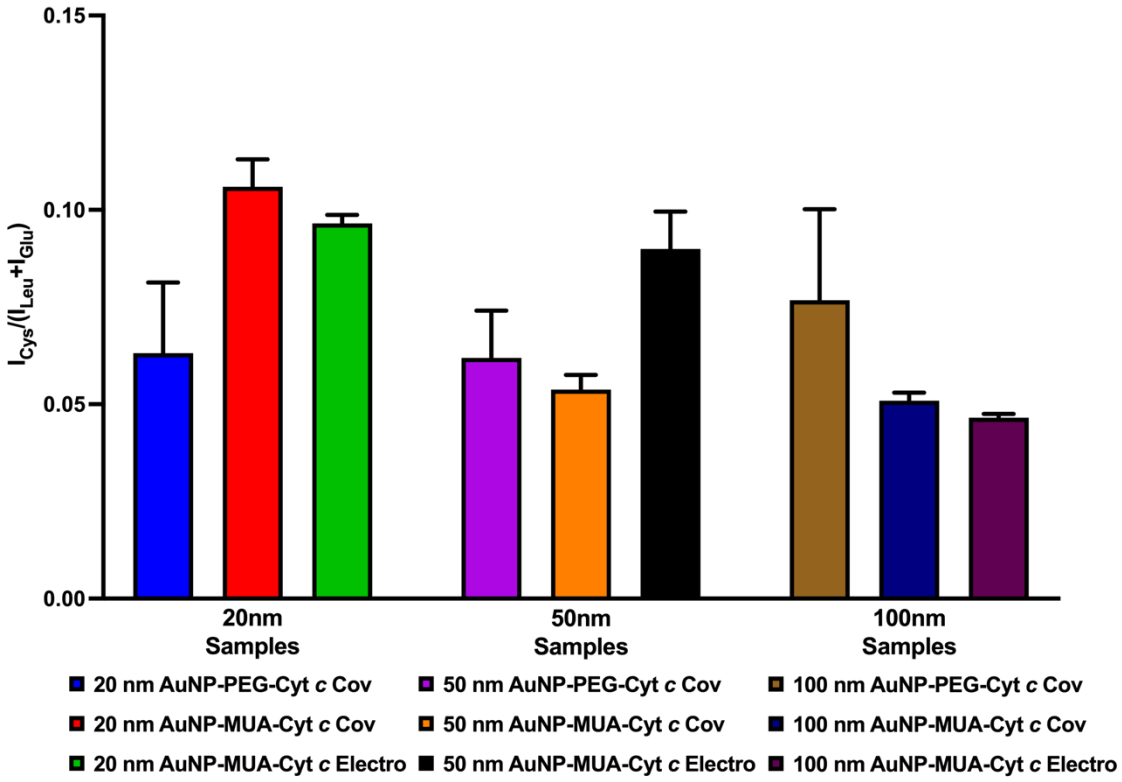


Figure 29. ToF-SIMS peak intensity ratio for cysteine/glutamic acid + leucine for Cyt *c* free in solution and bound to 20 nm AuNPs using different ligands and conjugation strategies

The suggested orientations of Cyt *c* conjugated to AuNPs are displayed in Figure 30A and B. The samples which did not show a large divergence in R value when compared to 100 nm AuNP-MUA-Cyt *c* Electro are presented in Figure 30A with the ligand termination conjugated to Lys 79 following Jain et al., 2021. The Lys residues are a likely point for conjugation as they are positively charged, so would naturally have electrostatic interaction with the carboxyl group, while also containing amino groups which are required for covalent conjugation using EDC/NHS (Biedulska et al., 2021). Lys 25 and 27 are also highlighted as they too are potential conjugation sites and may be the result of variation in the amino acid intensity values. The predicted orientation of 20 and 50 nm AuNP-MUA-Cyt *c* Electro and 20 nm AuNP-MUA-Cyt *c* Cov is represented in the schematic from Figure 30B. Conjugation to Lys 88 would cause the heme to be more

exposed, resulting in increased Cys residue intensity and a lower Glu and Leu intensity as observed in Figure 29.

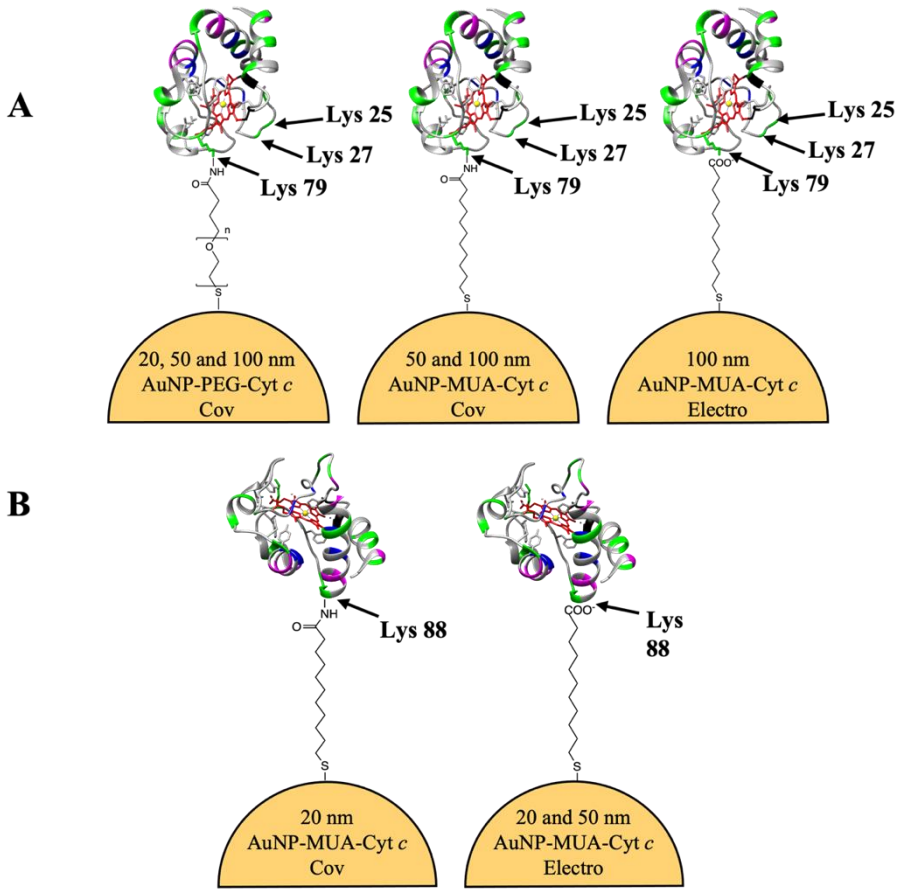


Figure 30. The orientation of Cyt *c* when attached to AuNPs using PEG and MUA ligands covalently or electrostatically was proposed through the use of ToF-SIMS amino acid intensity ratio and literature (Jain et al., 2021). Both covalent and electrostatic conjugation methods identified the binding of AuNPs to the Lys 79 residue of Cyt *c*, with Lys 27 and Lys 25 being potential alternatives (A). The proposed orientation for Cyt *c* bound to AuNPs at the Lys 88 residue was determined when the R value differed by ~50% or greater compared to 100 nm AuNP-MUA-Cyt *c* Electro (B). A 3D model of Cyt *c* was created using the crystal structure of horse heart Cyt *c* from the PDB (1HRC) in Chimera (version 1.15) to label the heme ring and amino acid residues. In the structure of Cyt *c*, the heme/porphyrin ring was red, the Iron (Fe) at the centre of the heme\porphyrin ring was yellow, Cys was black, Glu was magenta, Leu was blue, and Lys was green.

The next phase of this work was in determining whether the orientation of Cyt *c* conjugated to AuNPs played any role in its electrochemical ability.

3.7. Cyclic Voltammetry

Cyclic voltammetry (CV) was conducted on Cyt *c* free in solution and Cyt *c* conjugated to AuNPs to establish whether the redox ability of Cyt *c* is retained after conjugation. The heme group in Cyt *c*, containing Fe at its centre, is responsible for the observed redox couple at approximately 0.09 V (oxidation peak) and 0.039 V (reduction peak), as shown in Figure 31 (Yagati et al., 2012). The surface reactive groups of Cyt *c*, including carboxylic, amine, hydroxyl, and thiols, undergo protonation and deprotonation, but these events do not coincide with the redox peaks produced by the heme's Fe (Chen et al., 2002).The heme group in Cyt *c* plays a crucial role in the protein's primary functions, such as within the electron transport chain, where it facilitates electron transfer from complex II to complex III. Cyt *c* is also involved in apoptosis, acting as the first reversible point to trigger the process via 'activation' of the Cyt *c*, resulting from a redox change caused by cellular damage or stress factors (Garrido et al., 2006). Any change in electrochemical activity may indicate a change in function, hence it is essential to understand the cause of any changes.

Figure 31 demonstrates that accurate determination of the redox peaks of Cyt *c* is not possible when it is conjugated to AuNPs. This is due to the presence of a high number of AuNPs in the solution results in a high charging current, masking the characteristic peaks of Cyt *c*. As a result, it is not possible to conduct further analysis on the cyclic voltammograms.

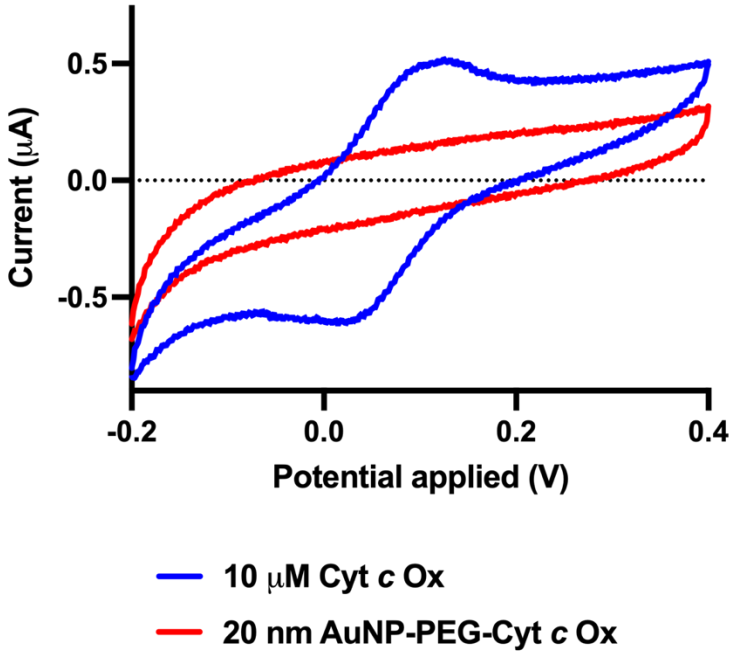


Figure 31. Cyclic voltammagrams's at 0.1 $V.s^{-1}$ of Cyt *c* Ox 10 μM free in solution and 20 nm AuNP-PEG-Cyt *c* Ox. Cyclic voltammagrams's run from -0.2 to 0.4 V and PBS was used as the electrolyte.

The redox peaks produced by Zn Porph are identified at a higher potential than those of Cyt *c* (Figure 32); these are evident at 0.65 and 0.95 V, with only one reduction peak being identified at 0.60 V. The high charging current caused by the AuNPs also significantly affects the visibility of redox peaks for Zn Porph when conjugated to AuNPs.

It was therefore concluded that the only way to accurately identify the redox peaks of Cyt *c* and Zn Porph when conjugated to AuNPs would be by reducing the charging current. Utilising differential pulse voltammetry (DPV) would overcome this problematic high charging current.

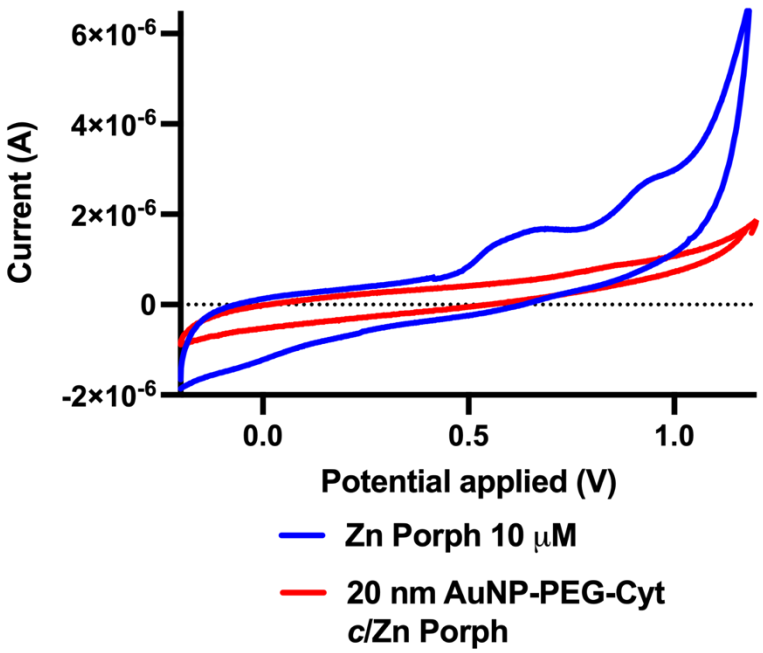


Figure 32. Cyclic voltammagrams's at 0.1 $V.s^{-1}$ of Zn Porph and 20 nm AuNP-PEG-Cyt *c*/Zn Porph. Cyclic voltammagrams's run from -0.2 to 1.2 V and PBS was used as the electrolyte.

3.8. Differential Pulse Voltammetry

Differential Pulse voltammetry (DPV) was conducted due to its high sensitivity to changes in current, high resolution of peak-shaped response, and the decreased background and double layer effects (Molina et al., 2011). In this thesis, a novel approach has been taken to differential pulse voltammetry, by setting out to identify the electron transfer rate between Cyt *c* and porphyrins, and the electrodes. Yet as previously shown in the cyclic voltammograms, identifying the redox peaks produced by Cyt *c* and Zn Porph was difficult due to the high charging current caused by the multifunctional AuNPs. To eliminate the possibility of human error, a new analysis method was devised to precisely determine the height and position of the redox peaks for both Cyt *c* and Zn Porph. Previous work using 1.6 nm AuNPs coated with hexanethiolate ligands demonstrated a similar difficulty in identifying a defined peak in the CVs, however through DPV as many as 13 peaks could be resolved due to the suppression of working electrode background currents

(Miles and Murray, 2003). In this study, the new approach involved varying the scan rates of DPV on both the oxidation and reduction peaks, to obtain an average electron transfer rate for each component in each sample.

3.8.1. Scan rate studies

In research previously carried out by the Rawson group, the heterogeneous rate constant was calculated from CVs (Hicks et al., 2017). In this present work, a scan rate study is performed using DPV by running a forward potential sweep, immediately followed by sweeping the potential backwards to best replicate the conditions used in CV. This was then repeated at scan rates decreasing from 50 to 10 mV/s, with the ultimate goal of calculating the electron transfer rate of Cyt *c* and Zn Porph conjugated to AuNPs. To calculate the electron transfer rate k^0 (heterogeneous rate constant), numerous equations were combined. In the work produced by Hicks et al., 2017 the k^0 value was determined using Equation 5.

$$\psi = k^0 \left[\frac{\pi D n v F}{RT}\right]^{-0.5}$$

Equation 5.

Where ψ is a function of the peak separation, D is the diffusion coefficient, n is the number of electrons transferred in the redox reaction, v is the scan rate, F is the Faraday constant, R is the gas constant, and T is the temperature (Lavagnini et al., 2004, Hicks et al., 2017). Equation 5 was rearranged to find the heterogenous rate constant as shown in Equation 6.

$$k^0 = \frac{\psi}{\left[\frac{\pi D n v F}{RT}\right]^{-0.5}}$$

Equation 6.

From Equation 6 there are still two unknown factors that needed to be determined to complete the equation, ψ and D. For calculating ψ, Equation 7 was used

$$\psi = 2.18(\frac{\alpha}{\pi})^{0.5} exp\left[-\left(\frac{\alpha^2 F}{RT}\right) n\Delta E_p\right]$$

Equation 7.

Where *a* is the transfer rate coefficient, assumed to be 0.5 (Hicks et al., 2017), and ΔE_p is the peak separation. 20 details the name of each symbol used in the equations and the value of the constants.

Equation 6 and Equation 7 were then combined to create Equation 8

$$k^0 = \frac{2.18\left(\frac{\alpha}{\pi}\right)^{0.5} exp\left[-\left(\frac{\alpha^2 F}{RT}\right) n\Delta E_p\right]}{\left[\frac{\pi D n v F}{RT}\right] - 0{\cdot}5}$$

Equation 8.

Where *D* is the diffusion coefficient, *n* is the number of electrons transferred in the redox reaction, *F* is the Faraday constant, *R* is the gas constant, *T* is the temperature (Lavagnini et al., 2004, Hicks et al., 2017), *a* is the transfer rate coefficient assumed to be 0.5 following literature, and ΔE_p is the peak separation (value of all constants included in Mathematical Abbreviations).

Only the value of *D* now remains unknown in calculating k^0; this can be determined using Equation 3, the Randles-Sevcik equation. The electrode surface area, *A*, has been calculated previously as 38.48 mm^2 in a previous study by Jain et al. (2021). The

concentration of the analyte, C^0, was determined through UV-Vis spectroscopy, as outlined in section 2.4.7; the number of electrons transferred in the redox event was assumed to be 1 (Elgrishi et al., 2018, Garrido et al., 2006); the scan rate (v) was varied between 50 to 10 mV/s; temperature was recorded to be 22°C, room temperature. Equation 2 was then rearranged to derive Equation 9, for calculating the diffusion coefficient.

$$D = \frac{(i_p)^2 RT}{(0.4463nC^0AF)^2 nfV}$$

Equation 9.

Once the diffusion coefficient had been calculated, all the values could then be inputted into Equation 4 to give the k^0 value. The k^0 value was determined for Cyt *c* free in solution and bound to AuNPs using Equations 5-9.

For accurate measurement of the oxidation and reduction peak heights and positions, a polynomial fit was applied to the background subtracted DPV of each sample. This was necessary due to the complex shape of the voltammogram. DPV experiments were conducted on PBS (25 mM) and AuNPs, which did not show significant peaks. Therefore, any deviations from the DPV shape of PBS and AuNPs were attributed to the conjugated molecules. The DPVs were plotted in OriginPro (2018) (Figure 33A) and peak analysis was performed by selecting the "Peak Analyzer" from the "Analysis" tab. "Subtract Baseline" and "User-Defined Baseline Mode" were selected, and the 1st and 2nd derivatives were chosen as the methods for finding anchor points. Adjacent-averaging smoothing was used with a window size of 3, threshold of 0.05, and 8 anchor points were selected. The software automatically placed anchor points on the voltammogram, and minor adjustments were made to ensure that each anchor point was positioned before and after the regions of interest. Once the anchor points were in the correct position, the interpolation method “Spline” was selected to create a smooth curve fitting the shape of the voltammograms. The "Finish" button was then selected on the peak analyser (Figure

33B). The background-subtracted voltammogram was plotted, and the "Quick Peaks" option was selected from the "Gadgets" section. The region of interest box (ROI) was positioned over the peak, and if found, the peak height and position were output into a table. This method was conducted for each sample at scan rates of 50 mV/s, 25 mV/s, and 10 mV/s for both the oxidation and reduction peaks to obtain the most accurate measurements.

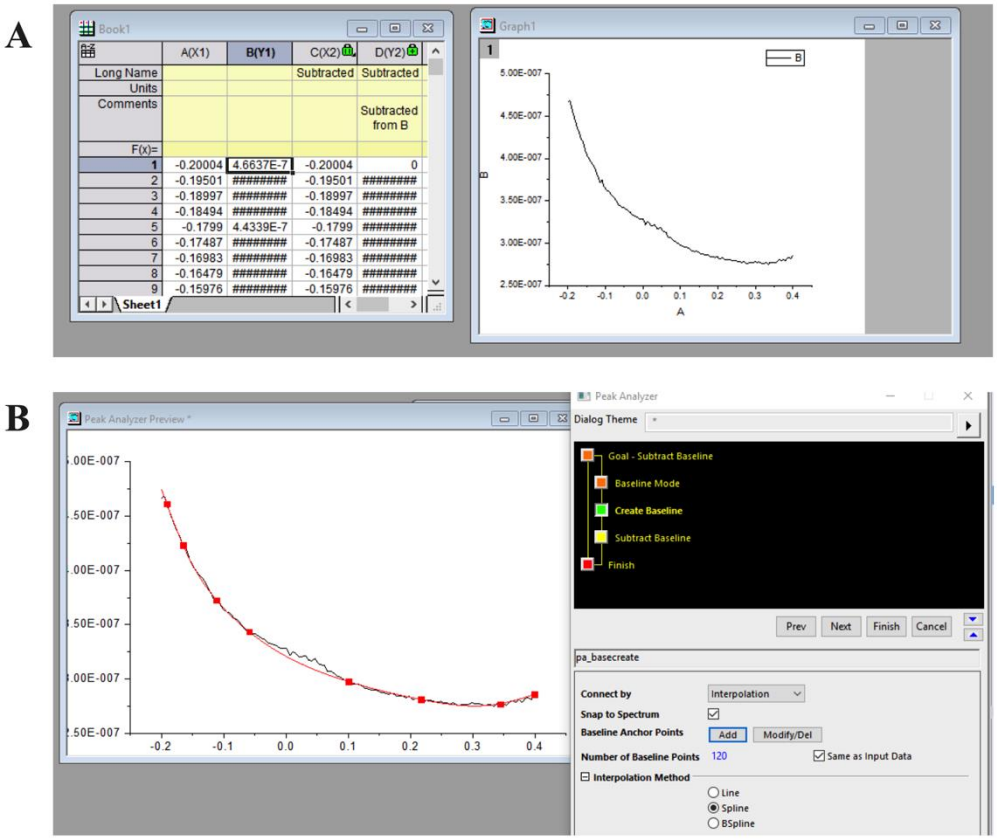


Figure 33. How DPV oxidation and reduction peaks were analysed in OriginPro (2018). The DPV was first plotted in OriginPro (A), the peak analyser was then selected to make a 4th order polynomial background to fit the DPV trace using 8 nodes with a spline interpolation method selected (B).

Previous studies have shown that the k^0 values of Cyt *c* bound to gold electrodes via 11 different SAMs ranged from 10^{-4} to approximately 10^{-1} cm/s (Liu et al., 2003). Liu et al., (2003) discovered a correlation between the hydrogen bonding capability of the SAM and

the k^0 value of Cyt *c*, suggesting that the k^0 value is dependent upon factors such as outer-sphere reorganization energy, the double layer current (background current), and the electronic coupling between the different SAMs and Cyt *c*. Given the similarities between the work of Liu et al. (2003) and this thesis, it was essential to determine the k^0 values of Cyt *c* bound to AuNPs of different sizes, with ligands of varying lengths, and various methods of conjugation. This analysis was crucial in determining whether any of these factors influenced the k^0 value. Moreover, comparing the k^0 value with biological data assisted in ascertaining whether the k^0 value affects the apoptotic ability of Cyt *c*.

DPV tested the controls used in multifunctionalised AuNPs and determined whether the redox peaks of Cyt *c* and Zn Porph could be identified. As shown in Figure 34, the redox peaks for Zn Porph, Cyt *c* Ox, and Cyt c Red were all easily identifiable. However, only one peak was visible for Zn Porph, unlike in the molecule's CV in which multiple peaks were shown. In the case of AuNPs and PBS, DPV did not show any redox peaks, except for a very small peak at ~1.0 V for 20 nm cit-AuNPs, which could potentially interfere with the DPV spectra of the 20 nm multifunctionalised Cyt *c* and Zn Porph, as a result no analysis was conducted in this region.

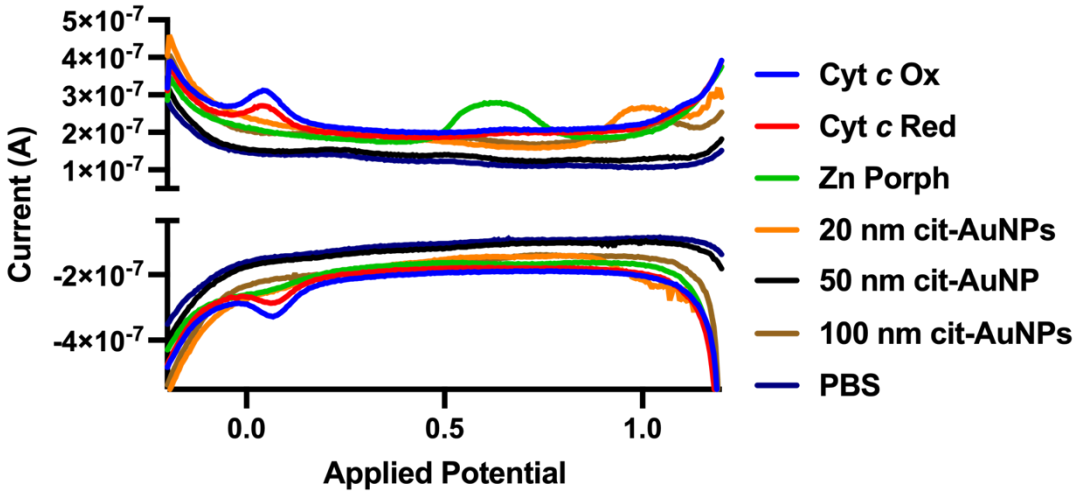


Figure 34. DPV of all control used in functionalised AuNPs measure between the potentials of -0.2 to 1.2 V using a scan rate of 50 mV/s.

The peak potentials of Cyt *c* identified using DPV differ from those determined by CV, likely due to variations in the techniques. DPV measures the current response to a series of voltage pulses, while CV measures the current response to a linearly increasing or decreasing voltage sweep. The differences in the experimental conditions can cause variations in the observed peak potentials, as the behaviour of the electrode surface may differ between the two techniques (Bard and Faulkner, 2002). For a reversible and fast, one-electron transfer, the expected peak-to-peak separation (ΔEp) is known to be 57 mV at room temperature (Elgrishi et al., 2018). In the case of Cyt *c*, the ΔEp values for the Ox and Red forms were calculated from Figure 34 to be 19 and 27 mV, respectively, suggesting surface chemistry is confined (Eckermann et al., 2010). These small ΔEp values suggest that a portion of the response is from surface-confined Cyt *c* (Kalimuthu et al., 2014), which enables rapid electron transfer. Such a rapid transfer would not be possible if Cyt *c* were freely diffusing throughout the electrolyte (Bard and Faulkner, 2002). In contrast, the peak separation of Zn Porph was found to be 56 mV, indicating a fast, reversible one-electron transfer event.

Table 3. The DPV peak separation of Cyt *c* Ox, Cyt *c* Red and Zn Porph calculated from Figure 34.

Control Sample	Oxidation Ep (V)	Reduction Ep (V)	ΔEp (Peak Separation) (mV)
Cyt *c* Ox	0.048	0.067	19
Cyt *c* Red	0.050	0.077	27
Zn Porph	0.624	0.680	56

3.8.2. Differential Pulse Voltammetry on AuNPs functionalised with Cyt *c* and Zn Porph

3.8.2.1. Calculating the heterogeneous rate constant for Cyt *c* conjugated to multifunctionalised AuNPs

DPV was performed on 20, 50 and 100 nm AuNP-PEG-Cyt *c*/Zn Porph Ox, AuNP-MUA-Cyt *c*/Zn Porph Ox Cov and AuNP-MUA-Cyt *c*/Zn Porph Ox Electro (Figure SI 7). To ensure that the peak current and potential position were as accurate as possible, the DPVs were background subtracted as detailed in 3.8.1 (Figure 35A-I).

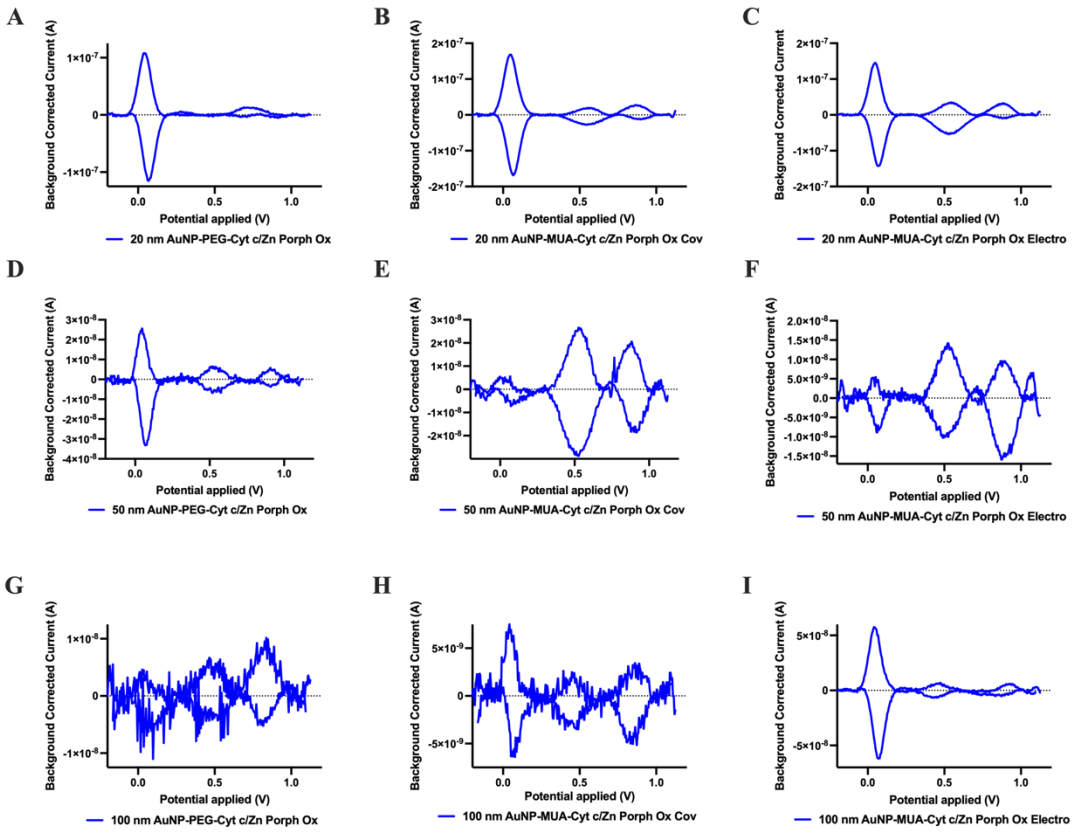


Figure 35. Background corrected typical DPV spectra for the oxidation and reduction peaks for Cyt *c* and Zn Porph conjugated to 20 , 50 and 100 nm AuNPs with thiol-PEG-carboxyl covalently or MUA covalently or electrostatically. All DPV displayed were obtained at a scan of 50 mV/s.

Table 4 displays the calculated change in potential energy (ΔEp) for the Cyt *c* that was conjugated to the multifunctional AuNPs, using the redox peaks from Figure 35A-I. The concentration of the Cyt *c* conjugated to AuNPs was normalised to 2 μM via dilution or concentration steps (the concentration of Cyt *c* and Zn Porph conjugated to AuNPs can be seen in Table SI 3). A relationship between the ΔEp and the size of the AuNPs appears to exist, with an increase in ΔEp observed as the size of the AuNPs increases suggesting slower electron transfer kinetics (Elgrishi et al., 2018), except for the case of 100 nm AuNP-MUA-Cyt c/Zn Porph Ox Electro. This correlation between the size of AuNPs and the ΔEp of Cyt *c* conjugated to them could be the result of the quantity of AuNPs in the samples, as there is an overall greater surface area of Au in the AuNP samples utilising smaller AuNPs. The electron-rich AuNPs may therefore help mediate the reversibility of Cyt *c*, this is supported by work which has shown that AuNPs can act as electrocatalysts (Li et al., 2021a). Another perspective is that the correlation between the size of the AuNPs and the ΔEp of Cyt *c* may be due to the number of AuNPs in the sample. The multifunctionalised AuNP samples were normalised for Cyt *c* concentration, and the smaller AuNPs have less Cyt *c* per individual AuNP, therefore, there are more AuNPs in the solution compared to the larger AuNPs and so there is a greater chance of a portion of the AuNPs being surface confined. However, as previously stated, the concertation of analyte at the surface of the electrode is regarded as the bulk concentration (Bard et al., 2022), so may not influence the ability to determine the kinetics of the electrons moving between the multifunctionalised AuNPs and the electrode.

Table 4: DPV analysis of Cyt *c* in various oxidation states when bound to AuNPs of different sizes and conjugation mechanisms. The table presents the oxidation peak to reduction peak differences (ΔEp) and the associated heterogeneous rate constants (k^0) for each sample.

Sample	ΔEp (mV)	Mean Heterogeneous Rate Constant (k^0) (cm/s)
20 nm AuNP-PEG-Cyt c/Zn Porph Ox	23.66	$7.69 \times 10^{-3} \pm 4.95 \times 10^{-3}$
20 nm AuNP-MUA-Cyt c/Zn Porph Cov Ox	11.9	$3.26 \times 10^{-3} \pm 1.27 \times 10^{-3}$
20 nm AuNP-MUA-Cyt c/Zn Porph Ox Electro	21.98	$3.16 \times 10^{-3} \pm 1.25 \times 10^{-3}$
50 nm AuNP-PEG-Cyt c/Zn Porph Ox	25.32	$6.41 \times 10^{-3} \pm 1.88 \times 10^{-3}$
50 nm AuNP-MUA-Cyt c/Zn Porph Ox Cov	28.70	$9.89 \times 10^{-5} \pm 1.90 \times 10^{-5}$
50 nm AuNP-MUA-Cyt c/Zn Porph Ox Electro	32.04	$8.24 \times 10^{-4} \pm 2.71 \times 10^{-4}$
100 nm AuNP-PEG-Cyt c/Zn Porph Ox	40.44	$6.85 \times 10^{-4} \pm 3.70 \times 10^{-4}$
100 nm AuNP-MUA-Cyt c/Zn Porph Cov Ox	42.93	$3.37 \times 10^{-4} \pm 8.71 \times 10^{-5}$
100 nm AuNP-MUA-Cyt c/Zn Porph Ox Electro	23.62	$3.67 \times 10^{-4} \pm 2.02 \times 10^{-4}$
Cyt *c* Ox	18.61	$1.25 \times 10^{-2} \pm 2.42 \times 10^{-3}$
Cyt *c* Red	27.03	$9.00 \times 10^{-3} \pm 7.37 \times 10^{-4}$

The heterogeneous rate constants for Cyt *c* conjugated to multifunctionalised AuNPs were calculated from the DPVs of Figure 35A-I, tabulated in Table 4 and displayed in Figure 36. The k^0 value of Cyt *c* Red was shown to be lower than that of Cyt *c* Ox, this may be the result of the tertiary structural changes identified in CD in section 3.5.2.

All the samples in Figure 36 had a lower k^0 value than Cyt *c* Ox, but only 20 nm AuNP-PEG-Cyt *c*/Zn Porph Ox was shown to not have a greatly significantly different value when compared to Cyt *c* Ox. This overall indicates that the electron transfer rate of Cyt *c* is lower when conjugated to AuNPs, likely the result of the change in secondary and

tertiary structures as observed in the CD spectra of Cyt *c* conjugated to AuNPs outlined in section 3.5.3. The CD spectra of Cyt *c* conjugated to 20 nm AuNP-PEG-Cyt *c* Ox showed the greatest similarity to that of Cyt *c* Ox free in solution, signalling that the structure of the Cyt *c* conjugated to 20 nm AuNP-PEG-Cyt *c*/Zn Porph Ox was the most comparable to Cyt *c* Ox free in solution. As a result, the electrochemical function (k^0 value) of Cyt *c* within both samples was comparable.

The Cyt *c* conjugated to AuNPs using thiol-PEG-carboxyl was hypothesised to have a lower k^0 value than Cyt *c* conjugated to AuNPs using MUA, due to its proximity to AuNPs and the predicted orientation of Cyt *c*. However, it appears to only be the proximity of Cyt *c* to AuNPs that negatively effects the k^0 value, and this influence becomes more significant as the size of AuNPs increases (Figure SI 8). Literature suggests that the protein binding constant increases as AuNP size increases, which can cause structural changes to the protein and affect function (Lacerda et al., 2010). The CD spectra displayed in section 3.5.3 supports the literature as the Cyt *c* conjugated to 20 nm AuNPs showed less structural change than the Cyt *c* conjugated to 50 and 100 nm AuNPs, resulting in higher k^0 values for the 20 nm AuNPs. The higher protein packing density that is observed in larger AuNPs in section 2.5.5 and as evidenced in literature may also be the result of the lower Cyt *c* k^0 value, as the heme of Cyt *c* is less accessible when conjugated to 100 nm AuNPs (Lacerda et al., 2010). The packing density may also explain why the AuNPs functionalised with thiol-PEG-carboxyl showed the highest k^0 values, whereas the k^0 value of AuNPs multifunctionalised using MUA covalently and electrostatically were very similar to each other (Figure SI 8). The longer length of thiol-PEG-carboxyl would result in less conjugated Cyt *c* per unit of volume when compared to the amount of Cyt *c* conjugated to MUA, therefore being more accessible to electrons.

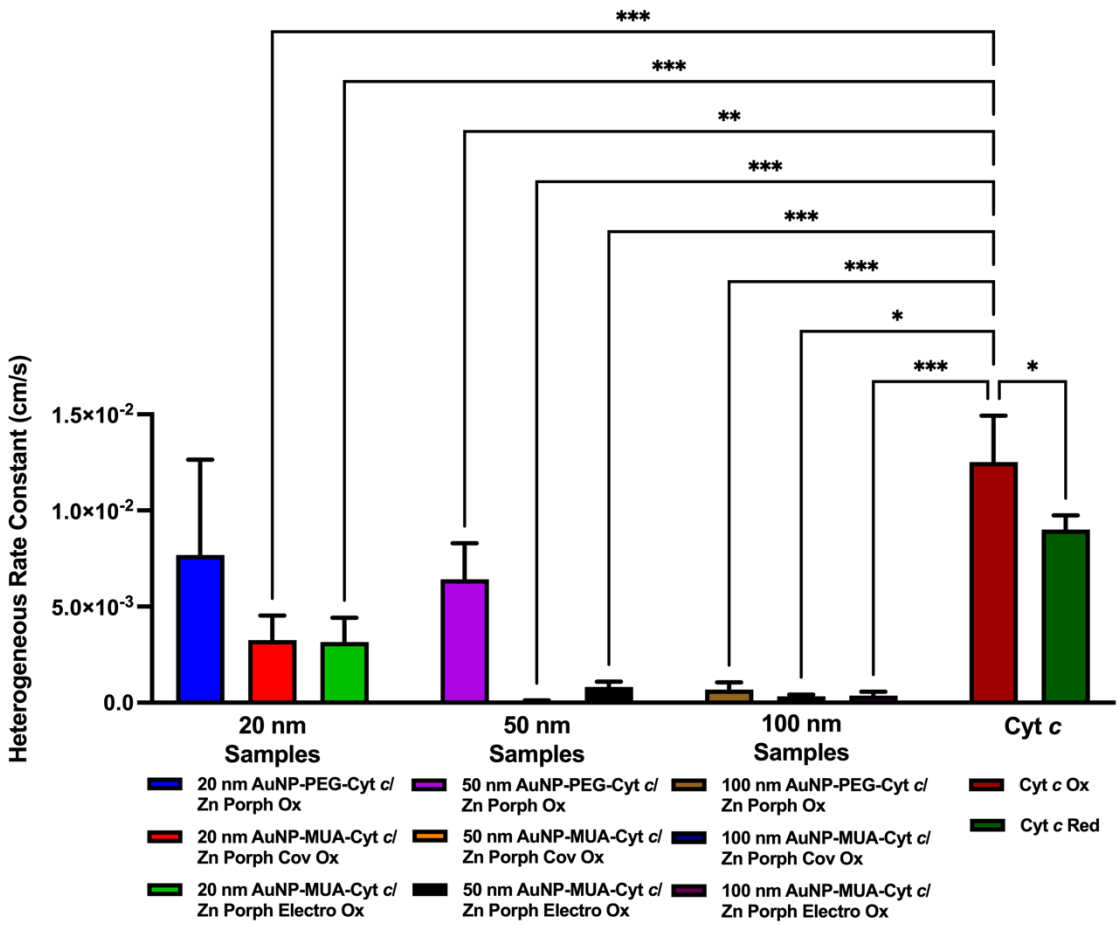


Figure 36. Heterogeneous rate constant of Cyt *c* oxidised conjugated to multifunctionalised AuNPs with Zn Porph. AuNPs of 20, 50 and 100 nm were functionalised with different ligands and conjugations methods to determine the effects the components have on the heterogenous rate constant of Cyt *c* when compared to Cyt *c* oxidised free in solution.

3.8.3. Calculating the heterogeneous rate constant for Zn Porph conjugated to multifunctionalised AuNPs

The k^0 value of Zn Porph was also essential to determine, to assess the effect, if any, conjugation had upon the electrochemical ability of Zn Porph. A change in electrochemistry may indicate an inability to provide an energy source to Cyt *c*, which could make the treatment ineffective. The ΔEp showed that in general, the peak separation

of Zn Porph decreased after conjugation to AuNPs, indicating either sample deposition on the ITO electrode or the ability for AuNPs to enhance the reversibility of the Zn Porph. A large ΔEp value was evident for 20 nm AuNP-PEG-Cyt *c*/Zn Porph Ox, suggesting that the system is electrochemically irreversible (Elgrishi et al., 2018). The irreversibility of Zn Porph conjugated to 20 nm AuNP-PEG-Cyt *c*/Zn Porph Ox could be the result of the Cyt *c* blocking the accessibility of Zn Porph, resultantly decreasing the kinetics between Zn Porph and the electrode surface.

Table 5: DPV analysis of Zn Porph in various oxidation states when bound to AuNPs of differing sizes and through different conjugation techniques. The table shows the differences in oxidation peak to reduction peak (ΔEp) alongside their corresponding heterogeneous rate constants (k0) for each sample configuration.

Sample	ΔEp (mV)	Mean Heterogeneous Rate Constant (k^0) (cm/s)
20 nm AuNP-PEG-Cyt c/Zn Porph Ox	265.30	$3.02 \times 10^{-3} \pm 3.28 \times 10^{-3}$
20 nm AuNP-MUA-Cyt c/Zn Porph Cov Ox	28.40	$1.37 \times 10^{-3} \pm 7.11 \times 10^{-4}$
20 nm AuNP-MUA-Cyt c/Zn Porph Ox Electro	9.90	$7.55 \times 10^{-4} \pm 3.90 \times 10^{-4}$
50 nm AuNP-PEG-Cyt c/Zn Porph Ox	25.30	$3.14 \times 10^{-4} \pm 1.33 \times 10^{-4}$
50 nm AuNP-MUA-Cyt c/Zn Porph Ox Cov	20.00	$1.19 \times 10^{-4} \pm 3.50 \times 10^{-5}$
50 nm AuNP-MUA-Cyt c/Zn Porph Ox Electro	45.20	$3.27 \times 10^{-4} \pm 6.77 \times 10^{-5}$
100 nm AuNP-PEG-Cyt c/Zn Porph Ox	8.50	$1.80 \times 10^{-4} \pm 1.50 \times 10^{-4}$
100 nm AuNP-MUA-Cyt c/Zn Porph Cov Ox	22.80	$8.61 \times 10^{-5} \pm 5.98 \times 10^{-5}$
100 nm AuNP-MUA-Cyt c/Zn Porph Ox Electro	36.80	$1.43 \times 10^{-5} \pm 4.61 \times 10^{-6}$
Zn Porph	55.50	$3.38 \times 10^{-3} \pm 4.07 \times 10^{-3}$

The k^0 values of Zn Porph were determined by analysing the DPV data with background correction (examples shown in Figure 35A-I and summarised in Table 5). The results indicated that there was no significant alteration in the k^0 values of Zn Porph after

conjugation to multifunctionalised AuNPs of varying sizes and using different ligands and conjugation methods when compared to Zn Porph free in solution (Figure 37). However, the standard deviation (SD) of Zn Porph in solution was relatively large, making it difficult to determine the exact impact of the conjugation to AuNPs. Nonetheless, the mean k^0 values of Zn Porph conjugated to multifunctionalised AuNPs were observed to be lower than the Zn Porph in solution.

The k^0 values of Zn Porph conjugated to AuNPs were statistically compared to each other to identify whether any component significantly affected the electrochemical ability of Zn Porph (Figure SI 9). The results show that the size of AuNPs and the lengths of the linker most greatly affected the k^0 values of Zn Porph conjugated to AuNPs, as also observed in Cyt *c* conjugated to AuNPs. The Zn Porph conjugated to 50 and 100 nm AuNPs showed a significant difference from each other, with the mean k^0 values being lowest for Zn Porph conjugated to 100 nm AuNPs. This is presumptively the result of higher amounts of Zn Porph and Cyt *c* bound to each of the larger AuNPs, decreasing the accessibility of each of the conjugated molecules and therefore slowing the rate of electron transfer.

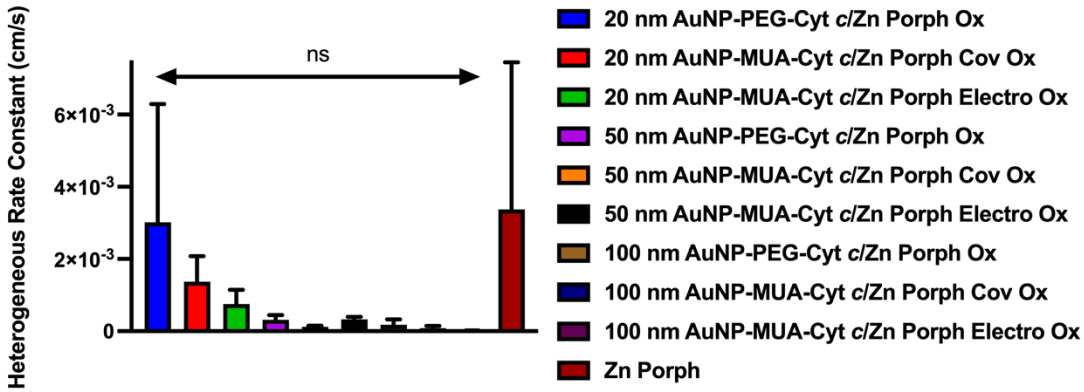


Figure 37. The heterogeneous rate constant was determined from the first redox peak of Zn Porph, located at 0.4-0.7 V free in solution and conjugated to multifunctionalised AuNPs with Cyt *c* Ox. AuNPs of 20, 50 and 100 nm were functionalised with different ligands and conjugations methods to determine the effects the components have on the heterogenous rate constant of Zn Porph when compared to Zn Porph free in solution. The

statistical analysis was performed using a one-way ANOVA with a post-Dunnett test. Determined by DPV.

Overall, the calculated k^0 values for Cyt *c* are lower after conjugation to multifunctionalised AuNPs, the likely result of structural changes observed in the CD spectra. The k^0 values can be correlated to the packing density influenced by the ligand length, as longer ligands would have a lower packing density making the Cyt *c* more accessible to electrons. The larger AuNPs have been previously shown to conjugate stronger to proteins than smaller AuNPs, which can have a greater effect on structural change of Cyt *c* (as observed in the CD) and therefore its electrochemical ability. The Zn Porph showed no significant change in k^0 value after conjugation to multifunctionalised AuNPs, attributed to the large SD of Zn Porph free in solution. Comparison between the k^0 values of Zn Porph conjugated to differing sizes of multifunctionalised AuNPs concluded that the larger AuNPs reduce the electron transfer ability of Zn Porph due to the higher number of conjugated molecules per AuNP, meaning the molecules are less accessible to electrons.

3.9. Conclusion

In this chapter, we report how the electrochemical ability of Cyt *c* and Zn Porph was assessed both before and after conjugation to AuNPs to observe whether any changes occurred. A change in the electrochemical activity of Cyt *c* or Zn Porph after conjugation may result in a change in function, resulting in the molecules being unusable for the cancer treatment theorised in this work.

The structural changes in Cyt *c* were evaluated following its conjugation to AuNPs and compared to the native Cyt *c* in its oxidized and reduced states. Conjugation of Cyt *c* to AuNPs led to alterations in both secondary and tertiary structures, with thiol-PEG-carboxyl functionalised AuNPs causing the least amount of structural change when compared to MUA-based covalent and electrostatic conjugation methods. This suggests that either the proximity of Cyt *c* to the AuNP or the packing density is responsible for the structural changes observed. An increase in the size of AuNPs was found to have a

negative impact on the structure of the conjugated Cyt *c*, with the larger AuNPs causing greatest changes in structure. This supports the premise that changes in structure are primarily due to variations in packing density. Covalent conjugation methods were initially hypothesized to have a greater impact on the structure of Cyt *c* due to the strength of the bond compared to an electrostatic interaction. However, these methods in fact caused less structural change than AuNP-MUA-Cyt *c* Ox electro conjugation. All the Cyt *c* conjugated to AuNPs showed CD spectra similar to that of Cyt *c* Red, despite Cyt *c* Ox being used for functionalisation; this indicates the reduction of Cyt *c* occurring during the functionalisation process.

Using ToF-SIMS, the orientation of Cyt *c* following its conjugation to AuNPs was confirmed. The intensity ratio of the majority of Cyt *c* conjugated to AuNPs did not show a significant enough difference (~50% intensity difference indicates a change in orientation) to indicate a change in orientation from that reported in Jain et al., 2021 (Jain et al., 2021). Those Cyt *c* molecules that did exhibit a change in orientation were conjugated to MUA using covalent and electrostatic techniques. Therefore, it can be established that the conjugation method did not affect the orientation significantly, moreover, the ligand used in the conjugation method was responsible for this change in orientation. A higher packing was density observed on AuNPs utilising MUA as a ligand due to its shorter length, when compared to that observed from the longer thiol-PEG-carboxyl.

The k^0 values calculated for Cyt *c* were found to be reduced after conjugation to multifunctionalised AuNPs, assumably due to the observed structural changes in the CD spectra. These k^0 values are thought to be related to the packing density caused by the length of the ligand, with longer ligands resulting in lower packing density and increased accessibility to electrons. Larger AuNPs have been previously demonstrated to form stronger conjugates with proteins than smaller AuNPs, which can have a more significant impact on both structure (as seen in the CD spectra) and function. The orientation of Cyt *c* conjugated to AuNPs appeared not to have a significant effect on the k^0 values. In contrast, the k^0 values of Zn Porph exhibited no significant change after conjugation to multifunctionalised AuNPs, by virtue of the high SD of Zn Porph in solution. A

comparison of the k^0 values of Zn Porph conjugated to multifunctionalised AuNPs indicated that larger AuNPs result in decreased electron transfer ability, due to the higher number of conjugated molecules per AuNP, which can reduce the accessibility of the molecules to electrons.

Although the electron transfer rate was altered, the overall redox capabilities of Cyt *c* and Zn Porph prevailed even after their conjugation to AuNPs. This suggested that the proposed activation of Cyt *c* through Zn Porph upon exposure to light was feasible. The following chapter evaluates the proposed cytotoxicity in cancer cells.

4. Biological Studies on MCF-7 Cells after Incubation of Gold Nanoparticles Functionalised with Cyt C and Zinc Porphyrin

4.1. Aims and Objectives

This chapter aims to determine whether Cyt *c* and Zn Porph conjugated to AuNPs can induce an apoptotic response in cancer cells after internalisation, and when triggered by a light stimulus.

The above will be accomplished by conducting *in vitro* experiments, employing diverse assays, and utilising imaging techniques to assess the potential of Cyt *c* and Zn Porph conjugated to AuNPs in inducing apoptosis upon triggering.

4.2. Abstract

This chapter presents a study on the effectiveness of multifunctionalised AuNPs as a cancer treatment, specifically on breast cancer (MCF-7) cells. ICP-MS and confocal microscopy were used to identify the uptake of multifunctionalised AuNPs into MCF-7 cells, with no visible AuNPs attached to the outside of the cells. The study also showed the peroxidase activity of Cyt *c* was maintained and even enhanced after conjugation to multifunctionalsied AuNPs. The live/dead study demonstrated that the addition of multifunctionalised AuNPs significantly decreased the percentage of live cells within samples after only 60 minutes of treatment with the amber LED array. The study concludes that AuNPs multifunctionalised with Cyt *c* and Zn Porph are internalised into MCF-7 cells successfully and have the ability to induce cell death when triggered via an

amber light source exciting Zn Porph and transferring its energy to Cyt *c* enabling the 'activation' of Cyt *c*.

4.3. Introduction

The previous chapter identified that the structure and electron transfer rate of Cyt *c* altered after conjugation to multifunctionalised AuNPs. This prompted the investigation into whether these structural modifications affected the potential of Cyt *c* to instigate apoptosis in cancerous cells, and ultimately be used as an anticancer therapy. The current chapter presents the biological investigations conducted on MCF-7 cells to determine the apoptotic ability of the multifunctional AuNPs conjugated with Cyt *c* and Zn Porph, when activated with a light stimulus. The uptake of each AuNP formulation was analysed to identify the most efficient AuNP delivery system. The apoptotic potential of Cyt *c* linked to AuNPs was evaluated to establish which AuNP-ligand formulation demonstrated the optimal redox capacity when present inside cells. All samples used in the preceding chapter were also used in this chapter to gain a comprehensive understanding of how the electrochemical and structural alterations observed in the Cyt *c* following its conjugation to AuNPs impacted its ability to trigger apoptosis when activated via a light stimulus.

4.3.1. Cell Culture Studies with MCF-7

This study focuses on proof of concept data for the treatment of breast cancer, namely the most widely diagnosed cancer and the leading cause of cancer deaths in females (Comsa et al., 2015). While the treatment described in this research is intended for use in all solid tumour-like cancers, the cell studies conducted here specifically targeted MCF-7 breast cancer cells to combat this problem. Breast cancer tumours are typically removed through common procedures, and current treatments have proven effective with 90% of patients surviving for 5 years and 80% living for 10 years (Nardin et al., 2020). However, nearly 30% of patients with breast cancer experience a recurrence of the disease during follow-up, with the highest percentage occurring in the first 5 years (10.4%) (Colleoni et al.,

2016). The probability of breast cancer recurrence is linked to the oestrogen receptor status of patients, as oestrogen receptor-negative patients typically experience recurrence earlier during follow-up compared to oestrogen receptor-positive patients (whose recurrence usually appears later in follow-ups, between years 5 to 10) (Colleoni et al., 2016). Pedersen et al. (2021) studied 36,924 women with breast cancer and found that 2595 (15.53%) developed late breast cancer, 10 to 32 years after the primary diagnosis. Women with high lymph node burden, large initial tumour mass, and oestrogen receptor-positive tumours have an increased risk of late breast cancer recurrence (Pedersen et al., 2021). In the cancer treatment detailed in this study, the multifunctionalised AuNPs would be applied to the tissue surrounding the area where the tumour was just extracted during the keyhole surgery that typically occurs for breast cancer tumour removal. The AuNPs would then be left to enter targeted cancer cells for 24 hours before the tissue is illuminated with monochromatic light, triggering the activation of the Cyt *c* conjugated to the AuNPs within the cancer cells, initiating cell death and killing the remaining cancerous tissue. If this treatment were to be advanced, this additional step in cancer therapy could potentially decrease the chance of breast cancer recurrence, thus increasing the life expectancy of breast cancer patients over the remaining portion of their life. The long-term goal would be for the treatment to be applied after any solid tumour removal.

MCF-7 cells are a human breast cancer cell line that is widely employed in research. Initially obtained from a 69-year-old woman with metastatic breast cancer in 1970, these cells have become one of the most extensively studied and thoroughly characterised breast cancer cell lines. MCF-7 cells are considered hormone receptor-positive, denoting that they express receptors for progesterone and/or oestrogen. This feature makes them a valuable tool for investigating the mechanisms of hormone-responsive breast cancer, devising novel therapies for this disease, and as mentioned earlier, developing remedies to avert the recurrence of breast cancer (Comsa et al., 2015). Apart from their hormonal properties, MCF-7 cells are also noteworthy for their capability to create mammospheres *in vitro:* three-dimensional formations that mimic mammary gland tissue (Wang et al., 2014). This attribute is advantageous for exploring the behaviour of breast cancer cells in a more intricate microenvironment. Overall, MCF-7 cells are an invaluable resource for

advancing our comprehension of breast cancer biology and when devising new treatments for this disease.

4.3.2. Fluorescence microscopy

Fluorescence microscopy is a type of optical microscopy that uses fluorescent probes to visualize biological samples. The sample is labelled with fluorescent molecules or dyes that emit light of a particular wavelength, when excited by a light source. The excitation light is filtered to ensure that only the desired wavelength reaches the sample. The emitted light is then captured and visualized using specialized equipment such as filters, dichroic mirrors, and objective lenses, allowing for high-resolution imaging of biological structures and processes (Sanderson et al., 2014, Lakowicz, 1999). Fluorescence microscopy is a powerful tool for studying biological samples and has a wide range of applications in various fields. It allows researchers to visualize specific molecules or structures, track the movement of molecules in live cells, and study the dynamics of biological processes in real time (Sanderson et al., 2014).

4.3.3. Confocal microscopy

Confocal microscopy is a type of optical microscopy used in biological research to create high-resolution 3D images of biological samples. A focused laser beam is used to excite fluorescent molecules within a sample, with a pinhole aperture eliminating out-of-focus light; this results in sharper, more detailed images when compared to fluorescence microscopy (Sanderson et al., 2014, Elliott, 2020). Unlike conventional fluorescence microscopy which uses xenon arc or mercury vapour lamps, confocal microscopy scans the laser beam across the sample in a series of planes, producing optical sections to create a three-dimensional image of the sample (Wright and Wright, 2002). (Sanderson et al., 2014, Elliott, 2020) This technique is particularly useful for studying cells, tissues, neurons in the brain (Elliott, 2020) and nanoparticle internalisation (Gottstein et al., 2013), which is the main use case in this work.

4.3.4. Inductively Coupled Plasma Mass Spectrometry

Inductively Coupled Plasma Mass Spectrometry (ICP-MS) is a method used to detect and measure trace elements and isotopes in samples. A sample is firstly ionized in a high-temperature gas, where the ions can then be separated and measured using a mass spectrometer. This technique is highly sensitive, being able to detect elements at very low levels. ICP-MS is used in many fields, including environmental monitoring, geochemistry, materials science, and biological research (Wilschefski and Baxter, 2019).

ICP-MS can be used for the quantitative analysis of AuNPs in *in vitro* studies, whereby the nanoparticles are exposed to biological systems such as cell cultures or biological fluids; thus, the method is of interest to the work in this chapter. In the *in vitro* studies, ICP-MS is used to measure the concentration of AuNPs in the sample, providing insight into the uptake of AuNPs by cells, tissues or organs, and the distribution of the nanoparticles in the system. Typically, the samples are first digested with acids to dissolve the biological components and release the AuNPs for analysis. The sample is then introduced into the ICP-MS instrument, where the AuNPs are ionized and detected by the mass spectrometer (Noireaux et al., 2019, Gray et al., 2013). Using ICP-MS for *in vitro* studies of AuNPs can yield crucial insights into the behaviour of these nanoparticles within biological systems. For instance, ICP-MS can help examine the influence of various factors, such as particle size, surface chemistry, and concentration on AuNP uptake and distribution (Jain et al., 2021). Additionally, ICP-MS can be used to measure the release of AuNPs from cells or tissues; this is particularly important for understanding their potential biological toxicity and environmental impact (Noireaux et al., 2019, Gray et al., 2013).

ICP-MS is, therefore, a highly effective technique for the quantitative analysis of AuNPs in *vitro* studies, providing invaluable insights into the behaviour of these nanoparticles within biological systems.

4.4. Methods

4.4.1. Cell Culture

Breast cancer cell line MCF-7 were purchased from ATCC, USA and cultured in DMEM (Gibco) with 10% foetal bovine serum (FBS) and 1% penicillin/streptomycin. The MCF-7 cells were maintained in an incubator with a humidified atmosphere containing 5% CO_2.

4.4.2. Cellular Uptake Analysis

4.4.2.1. MCF-7 Growth Curve

To calculate the double time of MCF-7 cells, 7.0 x 10^5 MCF-7 cells were seeded in T-25 flask and incubated for 24, 48, 72 and 96 hours. After each time interval, the media was removed, and cells were washed with PBS before being trypsinised (2 mL) for 5 minutes. 3 mL of media was then added to the plate before 50 μl of the solution was combined with 50 μl of trypan blue. The media/trypan blue solution was then added to a haemocytometer and the viable cells were counted. The method was repeated for 2 plates at each time point.

4.4.2.2. ICP-MS

For cellular uptake analysis by ICP-MS, 9.0 x 10^4 MCF-7 cells were seeded on 24 well plates and incubated at 37 °C for 24 hours. After 24 hours, the culture medium was replaced with meda ium containing 20 μg/ml of the multifunctionalised AuNPs seen in

Figure 39 and incubated for 24 hours. After the incubation period, the media was removed, and the cells washed 3 times to remove any unbound AuNPs. The cells were then trypsinised with the control cells from each plate being used for a trypan blue cell viability assay. The cell suspension was centrifuged at 300 g for 5 minutes. The supernatant was then removed and centrifuged again at 14,100g for 10 minutes. The pellet from both the

main cell suspension and supernatant was digested overnight with 50 μl of aqua regia, with the 20, 50 and 100 nm controls all requiring 300 μl of aqua regia. The main cell suspension solutions and supernatant were then diluted using milliQ® water to reach a final acid concentration of 0.5%. The final acid concentration of the AuNP controls once diluted was 2%. The samples were then analysed using ICP-MS (iCAPQ Thermo Fischer).

To determine the quantity of AuNPs present in each cell, the mass of AuNPs of various sizes was calculated. Next, the overall number of AuNPs in the cells was obtained by dividing the mass of Au in the cell by the mass of a single AuNP. The number of AuNPs per cell was then determined by dividing the number of cells in the controls by the number of AuNPs. This method has been adapted from works previously conducted in the Rawson group (Jain et al., 2021, Sanjuan-Alberte et al., 2019).

4.4.2.3. Confocal Laser Scanning Microscopy

For cellular uptake analysis by ICP-MS, 9.0 x 10^5 MCF-7 cells were seeded on 24 well plates and incubated at 37 °C for 24 hours. After 24 hours, the culture medium was replaced with a medium containing 20 μg/ml of the multifunctionalised AuNPs seen in

Figure 39 and incubated for 24 hours. After the incubation period, the media was removed, and the cells were washed three times to remove any unbound AuNPs. The cells were then fixed with 4% paraformaldehyde for 15 minutes before staining with actin phalloidin for 30 minutes and DAPI for 20 minutes; the cells were also washed three times with PBS between each staining process. The plate was then imaged using the Leica SP8 LIGHTNING confocal microscopy with 10 to 40x objective. The nuclei, actin and porphyrin from nanoparticles were imaged using DAPI, FITC and mPlum filters respectively. The mCherry filter was also included due to some overlap with the emission spectra of Zn Porph. Images were analysed using ImageJ.

4.4.3. Irradiation of Cells with a 50 mW Monochromatic Green Laser

For each multifunctionalised AuNP sample and control, 10,000 MCF-7 cells (100 μL) were seeded in triplicate into Corning™ Costar™ 96-well cell culture treated, flat bottom microplates. The cells were incubated for 24 hours, the medium was then removed and cells were washed three times with PBS before 20 μg/mL of multifunctionalised AuNPs and control in medium (100 μL) were added to wells. The controls of Cyt *c* and Zn Porph free in solution were added to cells at a final concentration of 2 μM in cell culture medium (100 μL). The 96-well plate was then incubated for another 24 hours. The medium was removed from the well and washed three times with PBS to remove excess multifunctional AuNPs or controls, after which fresh medium was added. The green laser (532 nm) was placed in a clamp stand 30 cm above a 96-well plate, and the laser point aligned to the centre of each well before irradiation for 5 to 30 minutes. Triplicate samples were conducted on each plate. Assays were conducted either immediately after irradiation or between 4 to 24 hours after being returned to the incubator.

4.4.4. Irradiation of cells with Lumidox® II 96-Position LED Array using Amber Light

For each multifunctionalised AuNP sample and control, 7,500 MCF-7 cells (100 μL) were seeded in triplicate into Corning™ Costar™ 96-well cell culture treated, flat bottom microplates. The cells were incubated for 24 hours, the medium was removed, and cells were washed three times with PBS before 20 μg/mL of multifunctionalised AuNPs and control in medium (100 μL) were added to each well. The controls that did not contain AuNPs (Cyt *c* and Zn Porph) were added to cells at a final concentration of 2 μM in a cell culture medium (100 μL). The 96-well plate was then incubated for another 24 hours; the medium was then removed from the well and washed three times with PBS to remove excess multifunctional AuNPs or controls before the fresh medium was added. The 96-

well plate containing MCF-7 cells with multifunctionalised AuNPs was placed onto the Lumidox® II 96-Position LED Array with a custom fitting, designed specifically for the cell culture plates used. The array was fitted with a lens mat and active cooling base. The setting of 'Stage 2' was selected, producing 55 mW of amber light per well. Once the plate was correctly fitted, the 96-position array and the self-timer were set to either 15, 30 or 60 minutes, the device was started, and irradiation began on the cells. The cells were then returned to the incubator for 24 hours before any assays was conducted.

4.4.5. Presto Blue Metabolic Activity Assay

The method for 4.4.4 was followed for cells treated with amber light and without treatment. The media from each well was then replaced with media containing 10% PrestoBlue and incubated for 2 hours at 37°C. The coloured solution was then transferred to a black bottomed 96-well plate where the fluorescence of the solution was read using a TECAN Infinite 2000 plate reader at an excitation of 570 nm and an emission of 600 nm.

4.4.6. Peroxidase Activity with and without Irradiation with Lumidox® II 96-Position LED Array using Amber Light

The peroxidase activity of Cyt *c* free in solution and conjugated to multifunctionalised AuNPs was determined from the oxidation of Guaiacol (2-methoxyhenol) by H_20_2 with and without Cyt *c* present. The peroxidase activity of Cyt *c* was also determined with and without irradiation with monochromatic amber light (590 nm). The multifunctionalised AuNPs (1 mL) at concentrations of 6.25, 12.5 and 25 μg/mL were added to Guaiacol (1 mL at 2.5 μM) and H_20_2 (1 mL at 2.5 μM) before incubating for 5 minutes; absorption was recorded at 470 nm. For the controls of PBS (1 mL) that the multifunctionalised AuNPs were suspended in, Guaiacol (1 mL at 2.5 μM) and H_20_2 (1 mL at 2.5 μM) absorbance were recorded at 470 nm. The samples irradiated with monochromatic amber

light (590 nm) were left exposed to the light for 30 minutes before the peroxidase activity was evaluated.

4.4.7. Differential Nuclear Staining Assay

Differential nuclear staining (DNS) using Hoechst and propidium iodide (PI) was conducted to determine the proportion of live to dead cells. Cells were allocated at a concentration of 7.55 x 10^3 cells in each well of 96-well glass-bottomed dark plates. Following a 24-hour incubation, the culture medium was substituted 20 mg/mL of multifunctionalised AuNPs and control in medium (100 mL) and allowed to incubate for an additional 24 hours. The medium was removed from the cells and washed three times with PBS to remove excess multifunctionalised AuNPs or controls. The medium was replaced with treated with a PI solution (0.25 mg mLin PBS) for 10 minutes at ambient temperature. After double rinsing with PBS, Hoechst was administered to each well and incubated for 20 minutes at room temperature, protected from light. Images were captured using a Nikon Eclipse Ti fluorescence microscope, utilizing the DAPI and mCherry filters.

4.4.8. *In Vitro* Singlet Oxygen Detection

MCF-7 cells were seeded on tissue culture-treated black glass bottom 96-well plates at a density of 7.5 x 10^3 cells per well and incubated for 24 hours at 37 °C with a humidified atmosphere containing 5% CO_2. The medium was then removed, and cells were washed three times with PBS before 20 μg/mL of multifunctionalised AuNPs and control in medium (100 μL) were added to wells and incubated for 24 hours. After the incubation, the medium was removed from the cells and washed three times with PBS to remove excess multifunctionalised AuNPs or controls. The medium was replaced with a singlet oxygen sensor green (SOSG) (10 μM) in PBS solution and incubated for 20 minutes. The 96-well plate was then placed onto the Lumidox® II 96-Position LED Array and irradiated for 30 minutes at 55 mW per well. The cells were then washed and the green

fluorescence of SOSG caused by $^1O_2$ generation was imaged using a Nikon Eclipse Ti with a FITC filter. Images were analysed using ImageJ.

4.4.9. Statistical analysis

Statistical analysis was performed in GraphPad Prism v9.4.0 software (GraphPad Software, Inc). Data are shown as mean ± SD unless stated otherwise in the section. For comparison between data and single control, a one-way ANOVA with a Dunnett test was used, $P \leq 0.05$ was significant.

4.5. Results

4.5.1. Gold Nanoparticle Uptake

The doubling time of MCF-7 cells was calculated by seeding two plates for T=0, 24, 48, 72 and 96 hours; the cells were then counted from each plate using a haemocytometer and trypan blue as described in 4.4.2.1. The doubling time was calculated to be 36.27 hours, correlating closely to the literature value of 35 hours (Larsson et al., 2008). The MCF-7 cells are therefore representative of the cells used in the literature and are used in the rest of this study.

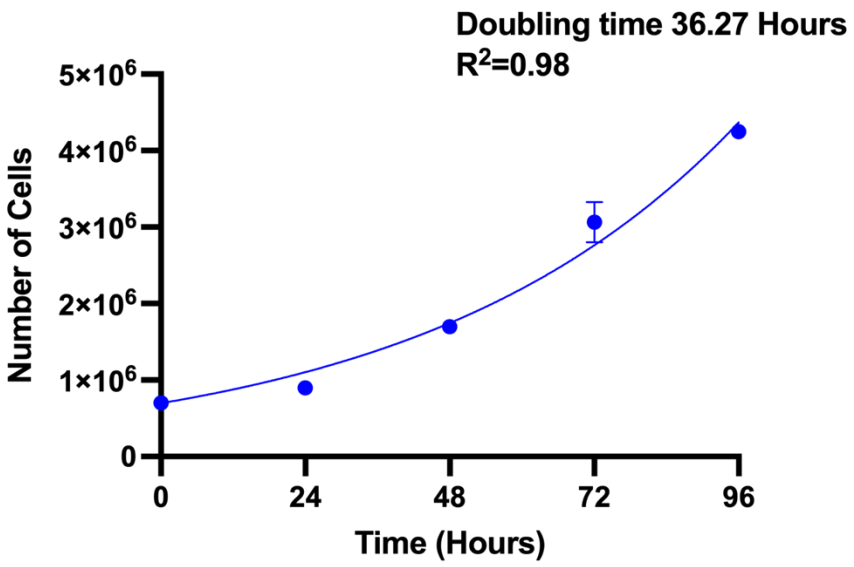


Figure 38. Growth rate of MCF-7 cells with a doubling time of 36.27 hours and an R^2 of 0.98. Experiments repeated in duplicate, error bars are N=2.

4.5.2. ICP-MS

The mobility of NPs around cells is largely influenced by the ECM. Specifically, the spacing between collagen fibrils in the ECM usually varies from 20 to 40 nm. NPs smaller than this range tend to traverse the ECM more proficiently. Nonetheless, particle size isn't the sole determinant of their movement through the ECM. Aspects like the hydrodynamic diameter and surface charge of the nanoparticles also play crucial roles in modulating their progression within the ECM (Tomasetti and Breunig, 2018, Neeves et al., 2007, Pons et al., 2006). After passing tthe ECM barriers, the size of the NPs becomes a significant factor determining their cellular uptake. In general, cells more readily internalise smaller Nps. This preferential uptake is attributed to the advantageous surface area to volume ratio of smaller NPs, which enhances their assimilation by the cell membrane (Montis et al., 2018, Panyam et al., 2003).

Despite this, previous reports suggest that the uptake of AuNPs is greatest for those with a diameter of around 50 nm (Chithrani et al., 2006, Carnovale et al., 2019). Theoretical

models propose that the optimal particle size for cellular uptake is determined by the competition between diffusion kinetics and thermodynamic driving forces (Gao et al., 2005). For NPs smaller than the optimal size, the increased elastic energy coupled with the bending of the membrane results in a reduced driving force, requiring smaller NPs to aggregate in order to create sufficient driving force for successful internalisation into cells (Augustine et al., 2020). Larger NPs, on the other hand, accommodate many receptors over a large area during uptake, leading to low internalization of larger AuNPs (Augustine et al., 2020, Gao et al., 2005). In this thesis, the internalization of 20, 50, and 100 nm AuNPs, multifunctionalised with Cyt *c* and Zn Porph in MCF-7 cells, was evaluated. Thiol-PEG-carboxyl and MUA were used as ligands to conjugate Cyt *c* to Zn Porph, with the theory that the longer length of thiol-PEG-carboxyl would reduce the uptake of AuNPs compared to those functionalised with MUA, as the hydrodynamic diameter would be larger and thus internalise less. The conjugation method was also alternated to identify whether this played any role in the internalisation of the multifunctionalised AuNPs, as a change in surface charge has previously been shown to affect internalisation of AuNPs into cancerous cells (Liu et al., 2020). Changing the AuNP size, ligand length and conjugation method to Cyt *c* and Zn Porph enables an optimal multifunctionalised AuNP system to be chosen to initiate cell death in cancerous cells when irradiated with monochromatic light.

AuNPs functionalised with Cyt *c* and Zn Porph were introduced to MCF-7 cells at 20 μg/mL, and their uptake and distribution were analysed using ICP-MS. The results are presented in Figure 39A-C and Tables S1-S3. The mass of AuNPs internalised in MCF-7 cells and the mass of AuNPs present in the supernatant after centrifugation of the cells were measured. The uptake of AuNPs was found to be poor for all samples, particularly for the 20 nm AuNP-PEG-Cyt *c*/Zn Porph Ox sample, which had a mass of only 0.09 ± 0.02 μg/mL. In contrast, the mass of Au recovered from the MCF-7 cells containing 50 nm and 100 nm AuNP-PEG-Cyt *c*/Zn Porph Ox samples was 1.43 ± 0.38 and 2.98 ± 1.07 μg/mL, respectively. The mass of Au recovered from the supernatant was higher for the 20 nm AuNP-PEG-Cyt *c*/Zn Porph Ox sample at 2.76 ± 0.25 μg/mL, indicating that less Au was internalised within the cells.

In Figure 39B, AuNPs were multifunctionalised with Cyt *c* Ox and Zn Porph using MUA ligands covalently. The mass of Au internalised in MCF-7 cells was similar for both 20 nm and 50 nm multifunctionalised AuNPs. However, the mass of Au internalized in cells for 100 nm AuNP-MUA-Cyt *c*/Zn Porph Ox Cov and 100 nm AuNP-MUA-Cyt *c*/Porph Ox Cov was much higher at 14.24 ± 1.64 μg/mL and 8.17 ± 0.53 μg/mL, respectively. The mass of Au recovered from the supernatants was highest for the 20 nm AuNPs, followed by 50 nm and then 100 nm multifunctionalised AuNPs.

In Figure 39C, AuNPs were multifunctionalised with Cyt *c* Ox and Zn Porph using MUA ligands electrostatically. The 20 nm multifunctionalised samples in Figure 39C showed an Au mass of 10.00 ± 3.81 μg/mL for 20 nm AuNP-MUA-Cyt *c*/Zn Porph Ox Electro, a substantial increase when compared to the Au mass in Figure 39A and B. This increase was also observed in Figure 2C for 50 nm and 100 nm multifunctionalised samples.

The AuNP-MUA-Cyt *c*/Zn Porph electro samples showed the bester overall uptake when compared to AuNP-PEG-Cyt *c*/Zn Porph Cov and AuNP-MUA-Cyt *c*/Zn Porph Cov samples. This suggests that the covalent conjugation method has a negative effect on the uptake of the multifunctionalised AuNPs. Electrostatic interactions might bestow Cyt *c* with surface properties that are more conducive to cell internalisation, such as charge and hydrophobicity.

To investigate the reason for the difference in uptake between Figure 2A-C, the number of AuNPs per MCF-7 cell was calculated.

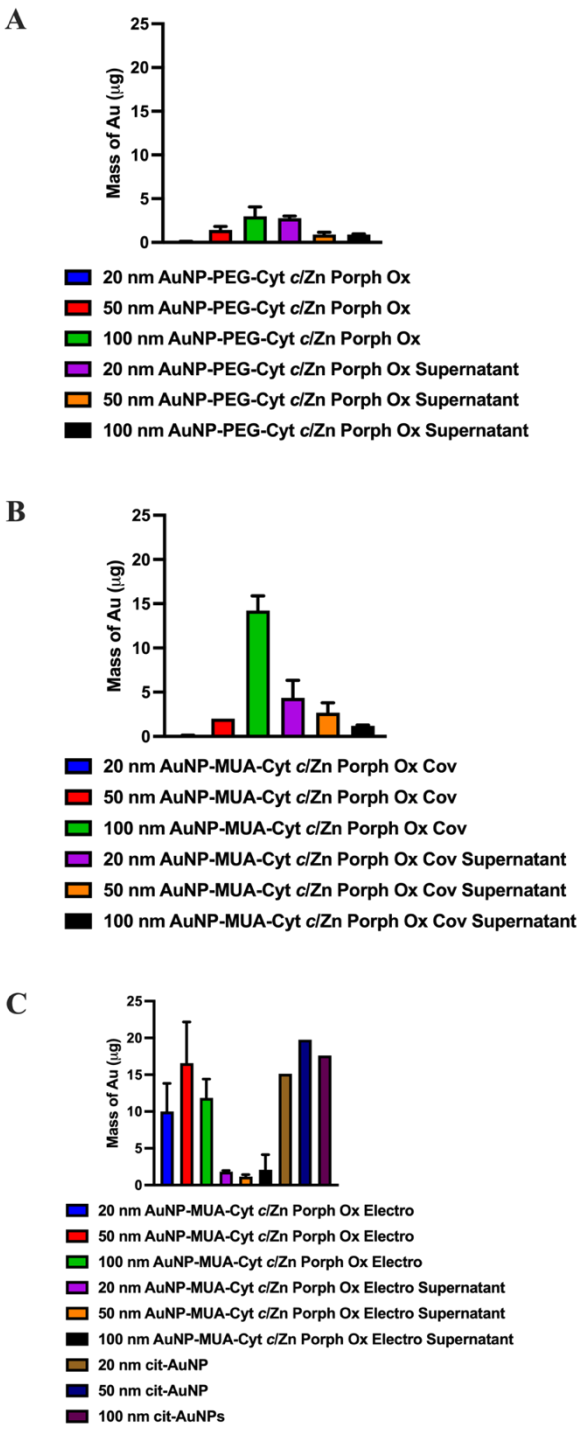


Figure 39. The mass of Au in cells or recovered in the supernatant via multifunctionalised AuNPs conjugated with Cyt *c* Ox and Zn Porph using thiol-PEG-carboxyl covalently (A), MUA covalently (B) and MUA electrostatically (C) determined with ICP-MS

To calculate the number of AuNPs per MCF-7 cell, the mass of a single 20, 50 and 100 nm AuNP was first established. Dividing the total mass of Au into the cells by the mass of a single AuNP then gives the number of AuNPs in the entire sample. Cells were counted from the control wells onto the plate to give an average number of cells per sample; the number of AuNPs calculated to be in the sample can then be divided by the number of cells per well to verify the quantity of AuNPs per MCF-7 cell. The mass of a single spherical particle can be calculated using Equation 10.

$$m = \left(\frac{\pi}{6}\right) D^3 \rho$$

Equation 10.

where D (cm) is the diameter of the particle and ρ (g/cm^2) is the density of the material. In the case of the AuNPs used in this work, the diameters are 20, 50 and 100 nm and the density of Au is 19.32 g/cm^2. The mass of a single particle is then given in grams (g); multiplying the mass by 1 x 10^6 converts the mass in micrograms (μg), a more useful unit for applications of AuNPs. The mass of a single AuNP with a diameter of 20, 50 or 100 nm is displayed in Table 6.

Table 6. The mass of a single 20, 50 and 100 nm AuNP calculated using Equation 10.

Diameter (nm)	Diameter (cm)	Pie/6	D cubed (cm)	Density (g/cm3)	Mass of Single Particle (μg)
20.00	2.00 x 10^{-6}	0.52	8.00 x 10^{-18}	19.30	8.08 x 10^{-11}
50.00	5.00 x 10^{-6}	0.52	1.25 x 10^{-16}	19.30	1.26 x 10^{-9}
100.00	1.00 x 10^{-6}	0.52	1.00 x 10^{-15}	19.30	1.01 x 10^{-8}

After calculating the amount of AuNPs in a sample, the quantity was divided by the number of cells counted in the controls of each plate. This step was taken to identify how the mass of internalised Au in cells correlates with the number of AuNPs (Figure 40A-C and Table SI 6-8). The average number of cells for the MCF-7 cells used in Figure 40A-C was counted to be 161,250, 200,000 and 145,000, respectively. In Figure 40A, the mean

number (standard deviation included) of 20 and 50 nm AuNPs per cell was relatively alike each other at 7002 ± 1488 to 7025 ± 1890, respectively, while the 100 nm AuNPs samples showed 1828 ± 655 AuNPs per cell. The expected outcome would have been to see 20 nm AuNPs internalised in MCF-7 cells the most, followed by 50 nm samples and then 100 nm samples. It is generally recognised that smaller particles with larger curvature interact with a lower number of cell surface receptors, requiring less energy to be internalised (Carnovale et al., 2019). However, as the literature suggests, 50 nm AuNPs usually show the best cellular uptake (Chithrani et al., 2006, Carnovale et al., 2019).

For 20, 50 and 100 nm AuNP-MUA-Cyt *c*/Zn Porph Ox Cov, the mean number of AuNPs internalised in MCF-7 cells was found to be 6828 ± 2189,7960 ± 12 and 7046 ± 812 respectively (Figure 40B). The results indicate no real change from the 20 and 50 nm AuNP-PEG- Cyt *c*/Zn Porph Ox, but a large increase when compared to the 100 nm AuNPs.

The 20 and 50 nm AuNP-MUA-Cyt *c*/Zn Porph Ox Electro showed much greater internalisation into MCF-7 cells at 885,318 ± 325,278 and 90,439 ± 30,610 respectively (Figure 40C), when compared to AuNPs-PEG-Cyt *c*/Zn Porph Ox and AuNP-MUA-Cyt *c*/Zn Porph Ox Cov (Figure 40A and B). The 100 nm AuNP-MUA-Cyt *c*/Zn Porph Ox Electro samples had only 8079 ± 1750 AuNPs per MCF-7 cells, closely matching the result of the 100 nm AuNP-MUA-Cyt *c*/Zn Porph Ox Cov (Figure 40B).

The findings from Figure 3A-C are intriguing as they suggest that the number of multifunctional AuNPs internalised is significantly influenced by the method used to conjugate Cyt *c* and Zn Porph The greater h_d of thiol-PEG-carboxyl functionalised AuNPs the internalisation into MCF-7 cells is less impacted compared to those AuNPs functionalised with MUA for 20 and 50 nm AuNPs. However, for 100 nm AuNPs, the increase in h_d is more pronounced, and fewer 100 nm AuNP-PEG-Cyt *c*/Zn Porph were internalised into MCF-7 cells than 100 nm AuNP-MUA-Cyt c/Zn Porph Ox Cov and Electro. The inconsistency in the internalisation of multifunctionalised AuNPs is likely dependent on the orientation of Cyt *c*, as observed in the previous chapter (section 4.6),

where 20 and 50 nm AuNP-MUA-Cyt *c*/Zn Porph Ox Electro exhibited a different Cyt *c* orientation based on varying amino acid intensities. Cyt *c* in this orientation, the negatively charged Glu residues of Cyt *c* would be positioned towards the ligand termination and AuNPs, with the outer part of Cyt *c* containing numerous positively charged Lys residues being attracted to the negatively charged surface of MCF-7 cells (Dhiman et al., 2004). Prior research has demonstrated that the biomolecules functionalised to AuNPs can increase their internalisation into cells (Escudero-Francos et al., 2017, Albanese et al., 2012, Chaudhuri et al., 2011).

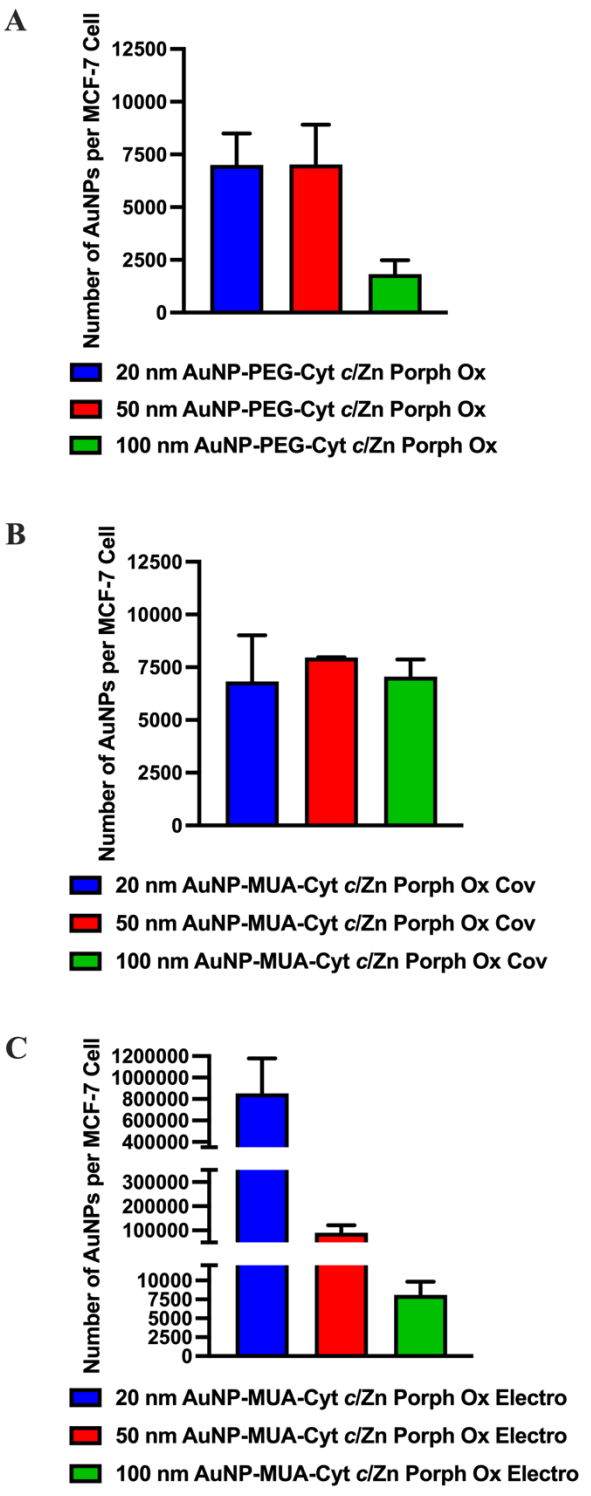


Figure 40. The number of AuNPs per MCF-7 cell was calculated for multifunctionalised AuNPs conjugated with Cyt c Ox and Zn Porph or Cyt c and Porph using HS-PEG-COOH covalently (A), MUA covalently (B) and MUA electrostatically (C).

The impact of sedimentation rate on the internalisation of AuNPs is often overlooked when discussing the effect of the size of the AuNPs. This study involved adding AuNPs to MCF-7 cells in a media volume of 100 μL, which approximately equates to half the height of the average well depth of a 96-well plate, as the plate has a maximum fill volume of 200 μL. The sedimentation rate of AuNPs with varying diameters was previously calculated by Midelet et al. (2017) over a distance of 1 cm, but for this study, the distance was adjusted to 0.5 cm. Literature showed that 20 nm AuNPs would take 515 hours to sediment, 50 nm AuNPs would take 82.5 hours, and 100 nm AuNPs would take 20.7 hours (Midelet et al., 2017). Therefore, after 24 hours of incubation in MCF-7 cells, 100% of 100 nm AuNPs would have sedimented but only ~30 % of 50 nm AuNPs and ~5% of 20 nm AuNPs. The remaining 20 and 50 nm AuNPs in suspension are influenced by Brownian motion, which increases during incubation at 37°C (Michaelides, 2015). This suggests that AuNPs that are attracted to the cell surface are more likely to interact and be internalised, rather than remaining in suspension. This is important for this study because the goal is to use AuNPs transporting as much Cyt *c* and Zn porph as possible into the cells to induce cell death when activated via monochromatic light; if the multifunctionalised AuNPs do not sufficiently internalised, there will be no chance to assess if the mechanism can induce cell death.

4.5.3. Confocal microscopy images of Multifunctionalised AuNPs uptake into cells

The internalisation of multifunctionalised AuNPs in MCF-7 cells was evaluated by observing Z-stacks using confocal microscopy. To observe the cells, Alexa Fluor™ 488 Phalloidin was used as a stain and excited with a 488 nm laser. Excitation of Zn Porph conjugated to multifunctionalised AuNPs was achieved using the 405, 532, and 635 nm lasers for the Soret band and Q-bands, and their emissions were combined to obtain overall fluorescence from Zn Porph. To determine the location of the multifunctionalised AuNPs, images were captured from beneath the cells, with Z-positions increasing until a complete cross-section was obtained, allowing for the MCF-7 cells and

multifunctionalised AuNPs to be seen three-dimensionally. The aim of this study was to confirm that the multifunctionalised AuNPs were fully internalised in the MCF-7 cells and not just conjugated to surface proteins. The results showed that the AuNPs (coloured red) were internalised in the MCF-7 cells (coloured green) inoculated with 20, 50, and 100 nm multifunctionalised AuNPs, with no fluorescence detected outside the cells from the Zn Porph conjugated to AuNPs (Figure 41A-C, Figure 42A-C and Figure 43A-C, respectively). The maximum intensity of the Z-stacks are displayed in Figure SI 10A-C, Figure SI 11A-C and Figure SI 12A-C for 20, 50 and 100 nm multifunctionalised AuNPs, respectively and clearly show the presence of the multifunctionalsied AuNPs in MCF-7 cells.

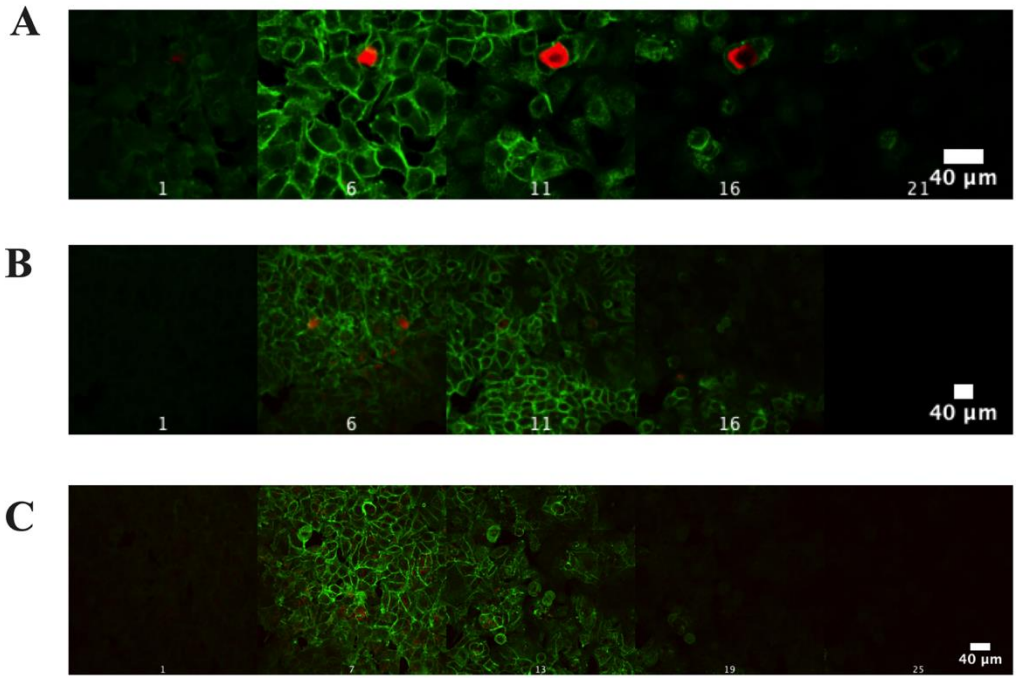


Figure 41. Confocal microscopy images of MCF-7 cells containing 20 nm AuNP-PEG-Cyt *c*/Zn Porph at 40x magnification (A), 20 nm AuNP-MUA-Cyt *c*/Zn Porph Cov at 20x magnification (B) and 20 nm AuNP-MUA-Cyt *c*/Zn Porph Electro at 20x magnification (C).

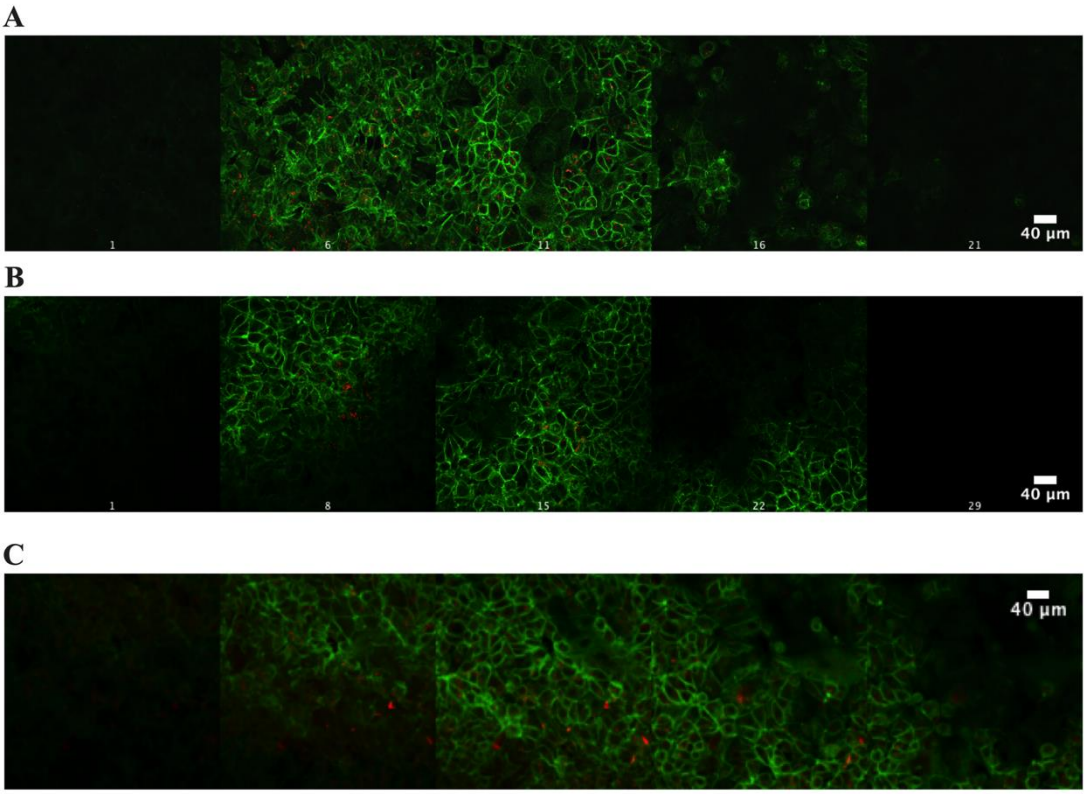


Figure 42. Confocal microscopy images of MCF-7 cells containing 50 nm AuNP-PEG-Cyt *c*/Zn Porph (A), 50 nm AuNP-MUA-Cyt *c*/Zn Porph Cov (B) and 50 AuNP-MUA-Cyt *c*/Zn Porph Electro (C). All images were acquired at 20x magnification.

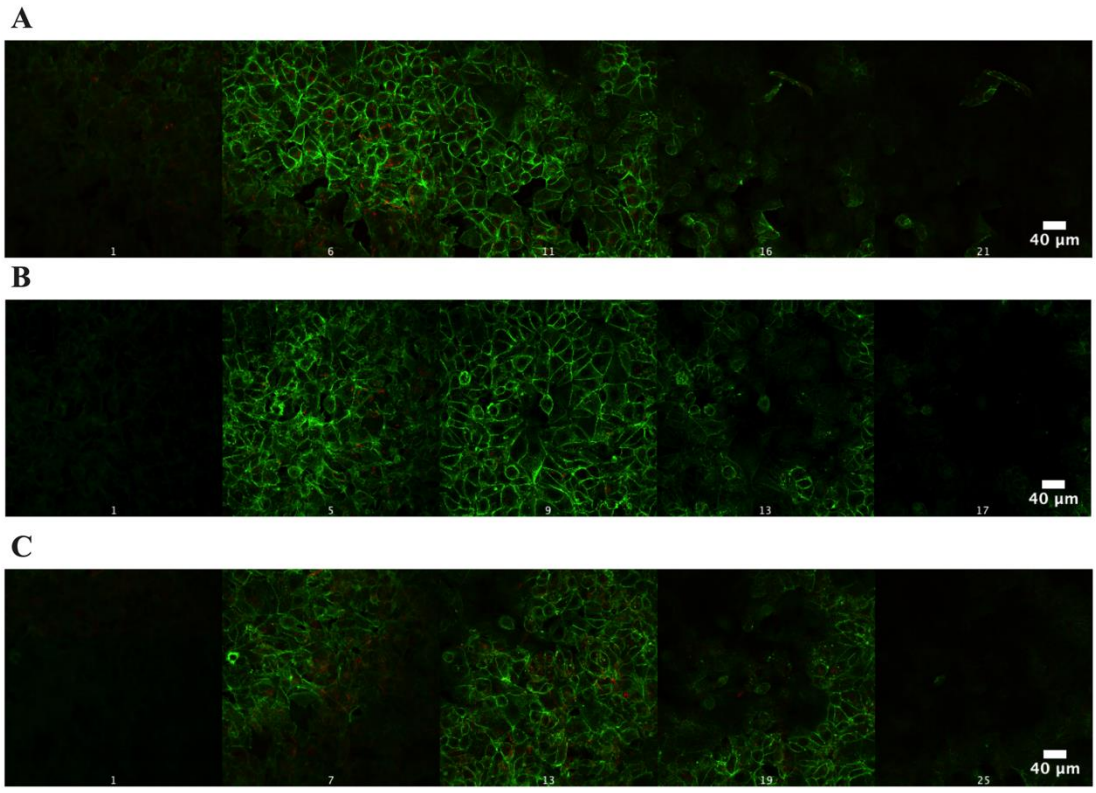


Figure 43. Confocal microscopy images of MCF-7 cells containing 100 nm AuNP-PEG-Cyt *c*/Zn Porph (A), 100 nm AuNP-MUA-Cyt *c*/Zn Porph Cov (B) and 100 nm AuNP-MUA-Cyt *c*/Zn Porph Electro (C). All images were acquired at 20x magnification.

4.6. Catalytic Activity

4.6.1. Peroxidase Activity

In addition to the role Cyt *c* plays in the electron transport chain and apoptotic initiator, the protein has been previously shown to possess a peroxidase activity (Yin et al., 2017). One of the main apoptosis pathways involves H_2O_2 production in the mitochondria (Lee et al., 2011). Cyt *c* uses H_2O_2 to catalyse the oxidation of cardiolipin in the mitochondrial membrane (Kagan et al., 2005, McClelland et al., 2014). As a result, the damaged membrane releases proapoptotic factors into the cytoplasm, resulting in cell death (Kagan et al., 2005, Kitt et al., 2017). The peroxidase mechanism is similar to that of other

peroxidases (Veitch, 2004, Volkov et al., 2011) where H2O2 reacts with Fe(III) resting state at the centre of the heme of Cyt *c*, producing a compound I-type intermediate Fe(IV)=O heme and an adjacent radical (Lawrence et al., 2003). The newly formed radicals react with O_2 to form stable oxidation products (Xu and Chance, 2007). This cycle typically consumes external substrates but also oxidises Cyt *c* and results in its deactivation (Kathiresan and English, 2017, Yin et al., 2017). Therefore, it was hypothesised that the secondary and tertiary structural changes observed for Cyt *c* as a result of the different conjugation strategies used to bind Cyt *c* to 20, 50 and 100 nm AuNPs (section 4.5) may affect Cyt *c*'s functions such as its peroxidase activity. To investigate whether the observed differences in the secondary and tertiary structure of Cyt *c* in CD affected peroxidase activity, the peroxidase activity of multifunctionalised AuNPs with Cyt *c* and Zn Porph, and the control samples, was evaluated. Previous studies have shown that changes in the tertiary structure of Cyt *c* can increase the accessibility of the heme ring within the molecule, resulting in enhanced peroxidase activity. Guaiacol was used in these studies as an oxidation indicator, as it turns from a colourless solution to a coloured solution that absorbs light at 420-470 nm in the presence of H_2O_2. (Tarpani et al., 2019, Weinkam et al., 2010).

Results showed that before any irradiation, the peroxidase activity of 50 and 100 nm multifunctionalised AuNPs conjugated with Cyt *c* and Zn Porph was significantly higher than that of the 20 nm samples at concentrations of 12.5 and 25 μg/mL (Figure 44A). The controls (Figure 44B and C) demonstrated that only the 20, 50, and 100 nm cit-AuNPs had slightly greater peroxidase activity as the concentration of cit-AuNPs was increased. As cit-AuNPs have been previously shown to have a low peroxidase-like ability (Huang et al., 2020), a small increase in absorbance was expected. These findings suggest overall that conjugating Cyt *c* to AuNPs increases peroxidase activity, and that larger AuNPs have a more significant impact on enhancing peroxidase activity. This observation has already been observed in the Rawson group as Jain et al., (2021) showed that the peroxidase acitivty of Cyt *c* increased after conjugation to AuNPs (Jain et al., 2021).

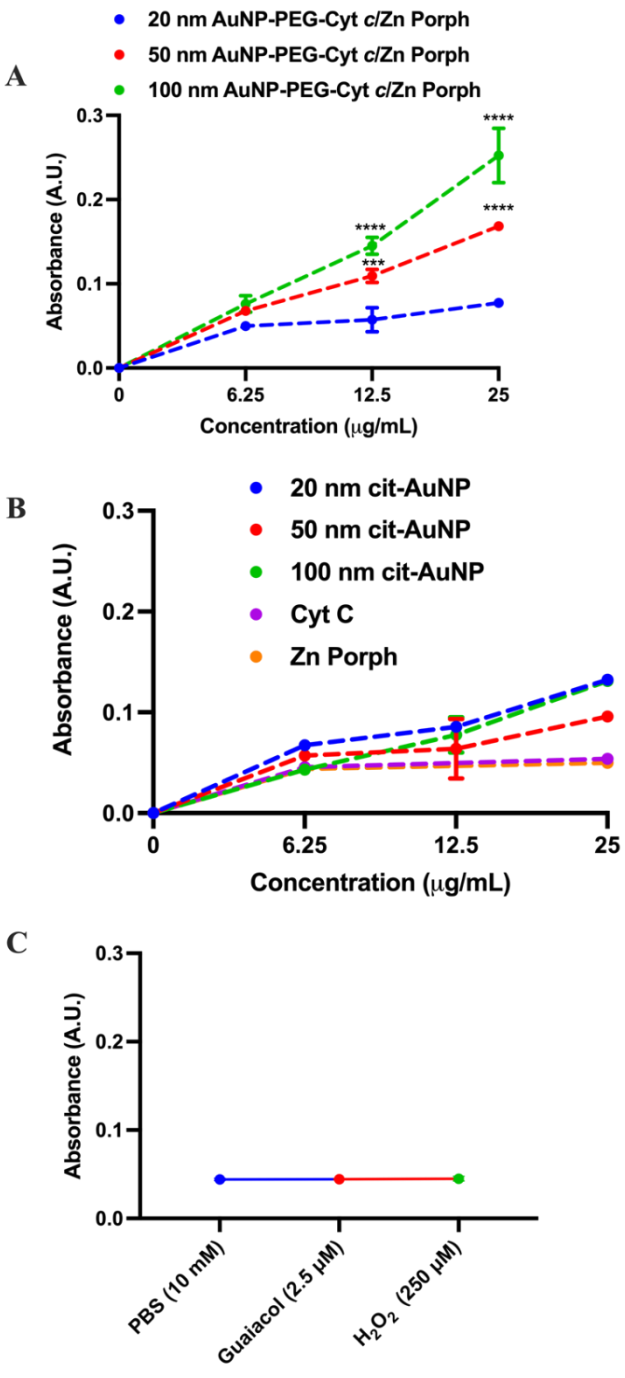


Figure 44. Peroxidase activity of 20, 50 and 100 nm AuNPs functionalised with Cyt *c* and Zn Porph (A), AuNP controls and unconjugated molecule controls (B) and PBS, Guaiacol and H_2O_2 controls (C) with no light treatment. Experiment was performed in triplicate and error bars displayed are the standard deviation of the results. P < 0.0005=*** and P < 0.00005=**** vs 20 nm AuNP-PEG-Cyt *c*/Zn Porph for Figure 44A.

To evaluate whether irradiation treatment affected the peroxidase ability of Cyt *c*, the peroxidase activity of multifunctionalised AuNPs was then measured after exposure to an amber light LED array. After 60 minutes of treatment (length of treatment justified in section 4.7.3), the peroxidase activity of 50 and 100 nm AuNPs-PEG-Cyt *c*/Zn Porph was significantly higher than that of the 20 nm samples at concentrations of 6.25, 12.5, and 25 μg/mL (Figure 45A). In contrast, the controls of the cit-AuNPs, Cyt *c* free in solution, Zn Porph free in solution, PBS, guaiacol (2.5 μM) and H_2O_2 (250 μM) (Figure 45B and C) did not exhibit any changes after treatment. The results indicate that the treatment does not substantially affect Cyt c's peroxidase capabilities, suggesting that it does not interfere with with Cyt c's redox potential. Consequently, one can infer that no structural degradation occurs during the 60-minute treatment period.

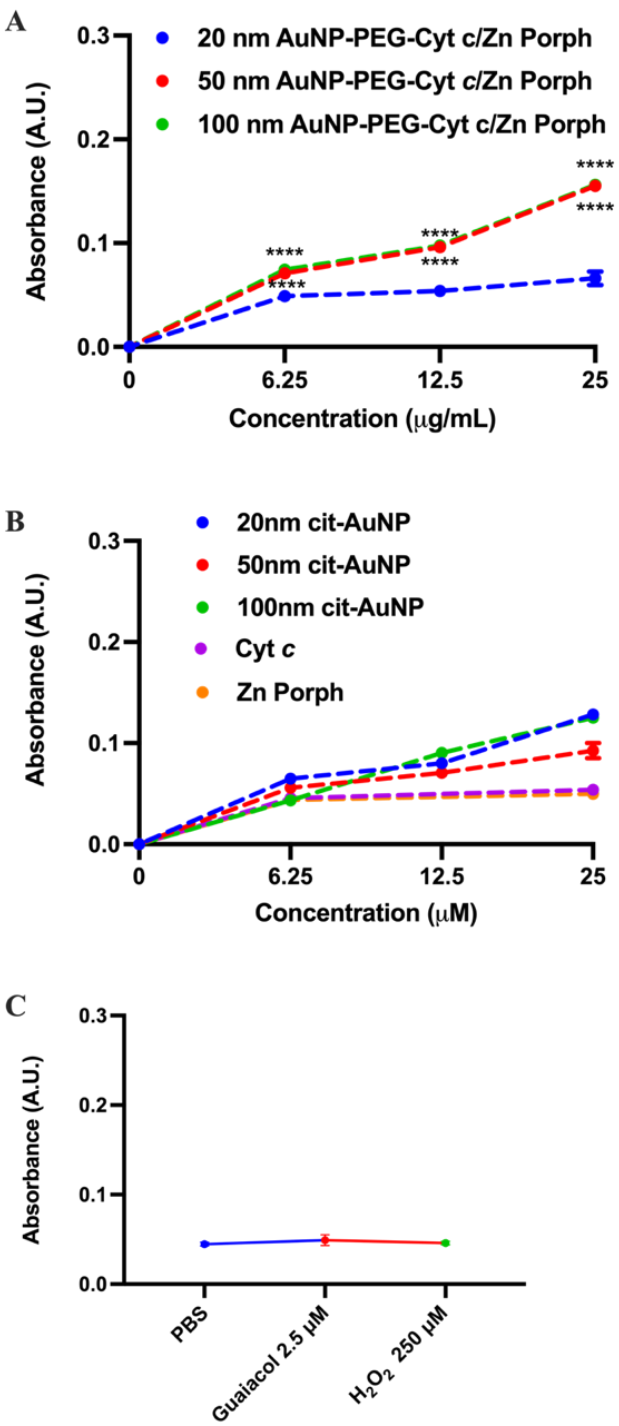


Figure 45. Peroxidase activity of 20, 50 and 100 nm AuNPs functionalised with Cyt *c* and Zn Porph (A), AuNP controls and unconjugated molecule controls (B) and PBS, Guaiacol and H_2O_2 controls (C) after 60 minutes of treatment with an amber LED array. Experiment was performed in triplicate and error bars displayed are the standard deviation of the results. P<0.00005=**** vs 20 nm AuNP-PEG-Cyt *c*/Zn Porph for Figure 45A.

4.7. Apoptotic Ability of Gold Nanoparticles Functionalised with Cyt C and Zinc Porphyrin

After the peroxidase assay confirmed that Cyt *c* maintained its functionality after conjugation to AuNPs then next step was to assess the ability for Cyt *c* to induce apoptosis in cancer cells. Prior to evaluating the apoptotic potential of multifunctionalised AuNPs using the Presto Blue metabolic assay, control experiments were conducted (Figure 41A and B) using cit-AuNPs, single functionalsed AuNPs with Cyt *c* or Zn Porph and the unbound Cyt *c* and Zn Poprh at different concentrations. First, AuNP controls (cit-AuNP) of 20, 50 and 100 nm diameters were added to the Presto Blue assay without cells to determine whether the AuNPs themselves influenced the assay (Figure 46A). Although a small increase in fluorescence was observed for most of the control AuNPs, indicating increased fluorescence, this increase was not significant. There was no clear relationship between fluorescence increase and the size or concentration of the control AuNPs, which was important to establish accurate assay results. Previous work showed that AuNPs of ~33 nm exhibited significant metal-enhanced fluorescence, whereas 18 and 160 nm AuNPs did not (Pawar et al., 2019). Additionally, controls for molecules conjugated to AuNPs were tested against the Presto Blue assay to determine their influence (Figure 46B). Cyt *c* demonstrated a significant increase in fluorescence intensity at 2.5 and 10 μM, indicating an increase in metabolic activity if cells were present. This was important to note before using Cyt *c* in cell studies. Presto Blue relies on resazurin, which causes fluorescence when reduced through cellular respiration to form resorufin, accepting electrons from NADPH, FADH, FMNH, NAD and cytochromes (Al-Nasiry et al., 2007, Xu et al., 2015). Therefore, Cyt *c* can increase fluorescence intensity in the Presto Blue assay. Similarly, Zn Porph is a fluorescence-producing molecule, so it was crucial to ensure that the excitation/emission wavelength of the Presto Blue assay did not overlap with that of Zn Porph, causing it to fluoresce and influence the assay results. Zn Porph controls showed a slight increase in fluorescence intensity, indicating slightly heightened metabolic activity, but as no cells were included it can be inferred that the molecules themselves caused the slight increase. However, as previously noted, this result was not significant.

Based on these results, it can be inferred that AuNPs multifunctionalised with both Cyt *c* and Zn Porph might display slightly increased metabolic activity compared to the control consisting only of the Presto Blue solution. This is due to the fact that all the components that make up these multifunctionalised AuNPs demonstrate enhanced metabolic activity. Thus, any decrease in metabolic activity compared to the control cells indicates reduced activity due to cellular death.

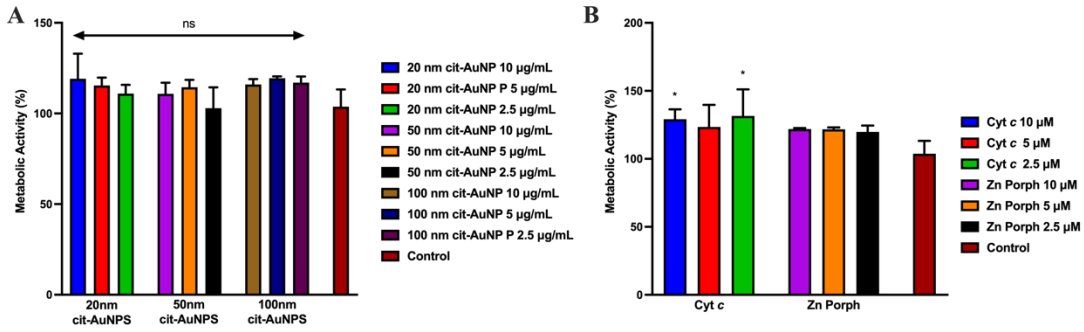


Figure 46. Metabolic activity assessed using a PrestoBlue assay on AuNP controls of different size and concentration (A) and Cyt *c* and Zn Porph controls at different concentrations (B) have on the fluorescence intensity determined by a Presto Blue assay with no cells. Two biological repeats were conducted in triplicate and the error bars are the result of the standard deviation.

To determine whether AuNPs multifunctionalised with Cyt *c* and Zn Porph would lead to a slight increase in the apparent metabolic activity of PrestoBlue in the absence of cells, experiments were conducted (Figure 47A-C). The results showed that the multifunctionalised AuNPs with diameters of 20 nm (Figure 47A), 50 nm (Figure 47B), and 100 nm (Figure 47C) displayed slight increases in mean fluorescence intensity, indicating a slightly higher apparent metabolic activity. The slight increase in fluorescence increase observed in cells caused by Cyt *c* and AuNPs, may hide the actual apoptotic ability of the samples after treatment with amber light.

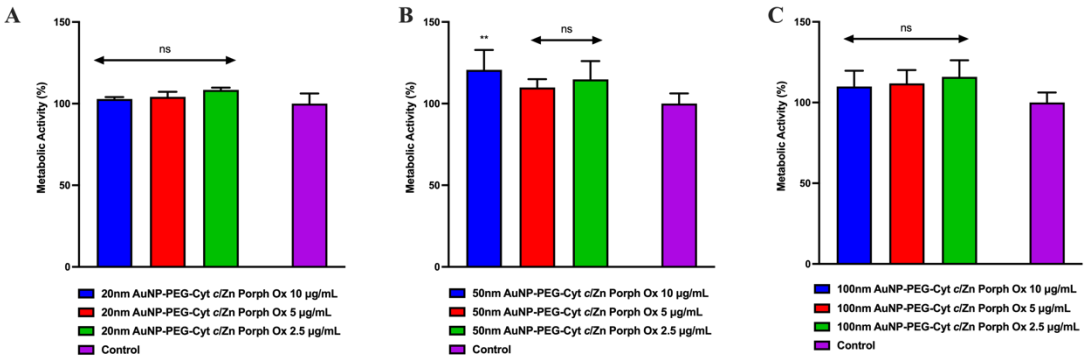


Figure 47. Effects that AuNPs multifunctionalised with Cyt *c* and Zn Porph or Porph at diameters of 20 nm (A), 50 nm (B) and 100 nm have on the fluorescence intensity determined by a Presto Blue assay with no cells.

4.7.1. Irradiated with Monochromatic Green Light

To avoid damaging cells by inducing oxidative stress, the Soret band region of Zn Porph was not used in this study, as previous research has shown that shortwave length visible light (385-405 nm) can cause such damage (Lawrence et al., 2018). Instead, the Q-bands of Zn Porph were targeted for excitation, as shown in the insert from Figure 48. The Q-bands of Zn Porph range from 500 to 650 nm with multiple peaks. Although the 532 nm monochromatic green laser (50 mW) purchased in the research group did not hugely overlap with the absorption spectrum of Zn Porph, an experiment was still conducted using the green laser to attempt to induce apoptosis in cancer cells containing AuNPs functionalised with Cyt *c* and Zn Porph.

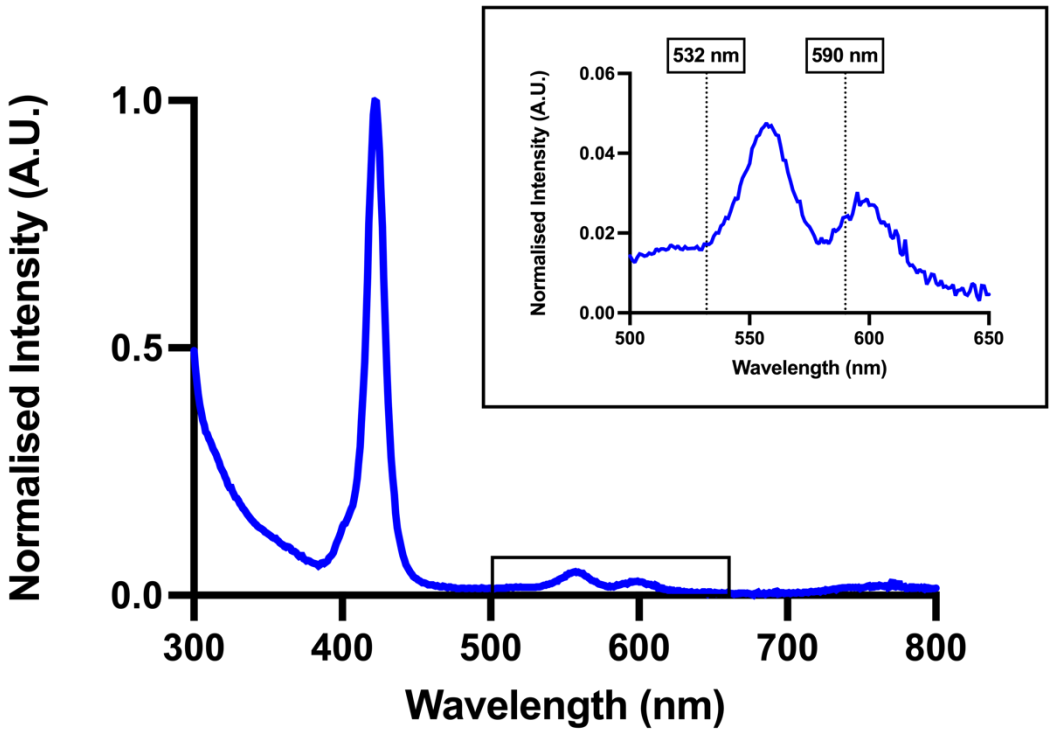


Figure 48. UV-Visible absorption spectrum of Zn Porph at 5 μM. Insert shows the Q-bands located between 500 nm to 650 nm and are the region of interest for excitation in this work.

To achieve this, the 50 mW green laser was positioned in a clamp stand 30 cm above a 96-well plate containing MCF-7 cells with multifunctionalised AuNPs and controls, and the wells were irradiated for 30 minutes each in triplicate. To prevent cellular death because of inhospitable conditions, all samples were arranged on separate 96-well plates, and the PrestoBlue assay was performed as described in 4.4.5. The results revealed that there was no significant decrease in the metabolic activity in any of the samples in Figure 49A. However, Cyt *c* ox and Zn Porph significantly increased the metabolic activity of the MCF-7 cells, likely due to the molecules enhancing the reduction of resazurin to resorufin. The temperatures of the wells containing the samples were recorded after 30 minutes of irradiation, showing no significant changes from room temperature. An increase in temperature could result in cell death, making this an essential observation (Figure 49B).

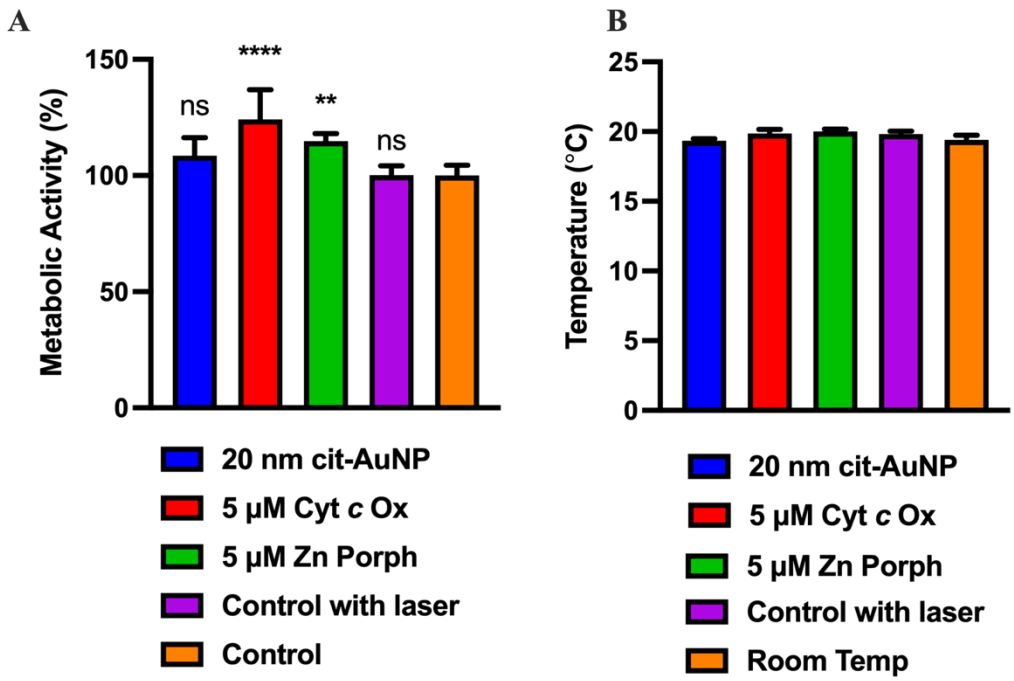


Figure 49. Functionalised AuNPs and controls added to MCF-7 cells and irradiated with 50 mW green laser (530 nm) for 30 minutes (A) and temperatures after 30 minutes (B). P<0.005=** P<0.00005=****

To determine the suitability of the green laser to the study, a PrestoBlue assay was performed on MCF-7 cells that were exposed to 20 nm AuNP-PEG-Cyt *c*/Zn Porph and irradiated for 30 minutes. The cells were incubated for 24 hours after irradiation to enable the effects of reduced metabolic activity to be more easily identified.

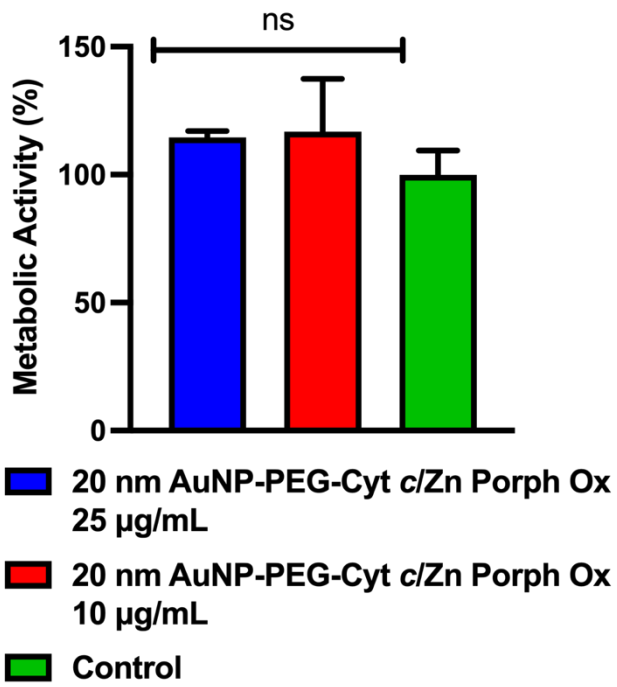


Figure 50. Presto Blue assay of 20 nm AuNP-PEG-Cyt c/Zn Porph at different concentrations in MCF-7 cells irradiated by 50 mW green laser (532 nm) for 30 minutes.

4.7.2. Irradiated with Monochromatic Amber Light

Previous attempts at using a green laser to trigger Cyt *c* activation were unsuccessful and posed several issues. Firstly, the laser had a narrow beam, and could only focus on one well at a time, making the experimentation very time-consuming. The removal of the lid of the well plate was also required as it caused the laser to diffract, reducing the amount of light reaching the cells. Additionally, conducting the experiments outside of a biological safety cabinet made the cells more prone to fungal infections, which could negatively affect the results. These issues made the system unsuitable for the current work, which required numerous samples to accurately determine the contributions of each component in the multifunctionalised AuNPs.

The solution to these problems was found in the form of a Lumidox® II 96-position LED array, which could irradiate all 96 positions in a 96-well plate simultaneously, making it 96 times faster than the green laser (Figure 51A). The LED array came equipped with a custom-fitted white plate specifically designed for Corning™ Costar™ 96-well cell culture-treated flat bottom microplates and was calibrated to ensure precise LED mW per well. The LED array was also modulated to control the LED power at different stages and included an active cooling base to prevent overheating.

Before purchasing the device, it was crucial to determine the appropriate colour of LEDs to excite the Q-bands of the porphyrin. The wide spectra of the amber LEDs deemed this colour the most suitable for exciting the multiple peaks that appear throughout the 500 to 650 nm region of the porphyrin's spectra (Figure 51B). Although green LEDs may have also been suitable for the work, the high cost of previous experiments meant that only the amber LED array was purchased.

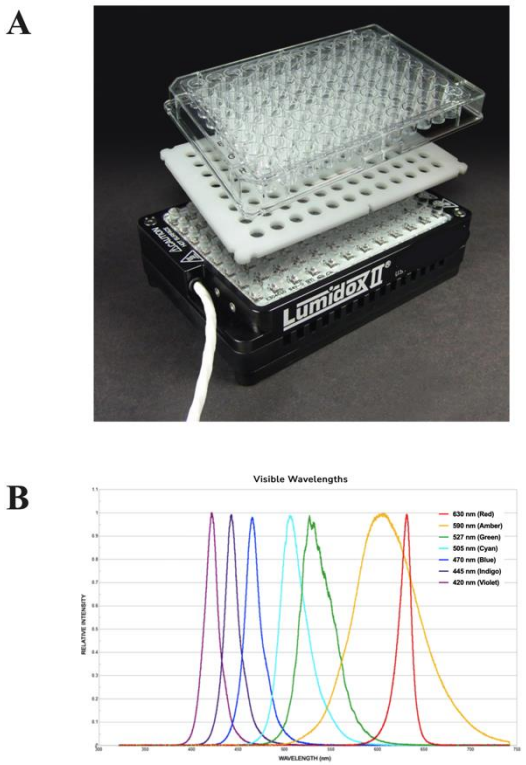


Figure 51. Lumidox® II 96-position LED array with custom fitted plate to accurately fit a 96 well plate (A). Wavelengths emitted from the different LEDs used in Lumidox® II 96-position LED array (B).

4.7.3. Optimising the Power of a Lumidox® II 96-position Amber LED array for use in irradiating MCF-7 cells

Before exposing MCF-7 cells to multifunctionalised AuNPs, it was necessary to optimise the LED array parameters, which are the power level setting and the length of time to apply the light to the cells. MCF-7 cells were seeded in all wells of a 96-well plate, and a PrestoBlue assay was performed to evaluate cell viability. The cells were either untreated (Figure 52A) or irradiated with 55, 80, 105, and 130 mW (Figure 52B to E, respectively) for 30 minutes. The results indicated that an increase in power led to a decrease in cell metabolic rate, insinuating cell death. The darker centres of the heat maps in Figure 52C to E reflect lower metabolic activity, indicating that cells at the centre of the array were

more affected by the increase in power, likely due to the higher heat produced by the LEDs in that region.

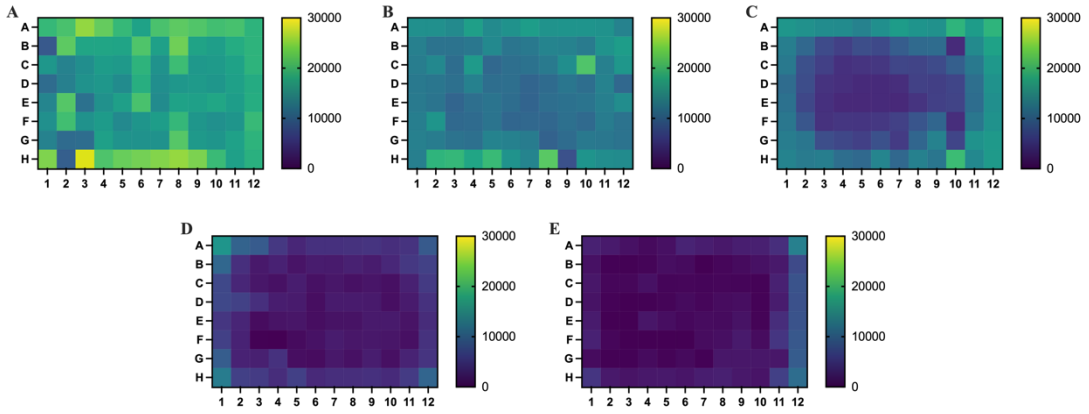


Figure 52. Metabolic activity of MCF-7 cells after 30 minutes treatment of monochromatic Amber light from Lumidox® II 96-position Amber LED array at different power levels. No treatment (A), at 55 mW (B), 80 mW (C), 105 mW (D) and 130 mW (E). Key corresponds to fluorescence intensity in RFU.

To determine whether the decreased metabolic activity observed in Figure 52A-E was due to an increase in LED array power, the temperatures of the room, LED array, and cell culture plate were all measured (Figure 53A-C). The room temperature remained constant at 21-22°C throughout the experiment (Figure 53A), but it was apparent that increasing the power from 55 mW to 130 mW caused the temperature of the LED array (Figure 53B) and cell culture plate (Figure 53C) to rise from approximately 38°C to 60°C. At 55 mW, the LED array temperature of approximately 38°C was close to the MCF-7 cell's habitable temperature of ~37°C, and thus did not significantly impact their metabolic activity. However, at power levels between 80 to 130 mW, temperatures ranging from 40-60°C were recorded; this can cause cellular stress by affecting protein unfolding, protein aggregation, DNA damage, stalling of replication, and plasma membrane permeability, (Roti Roti, 2008).

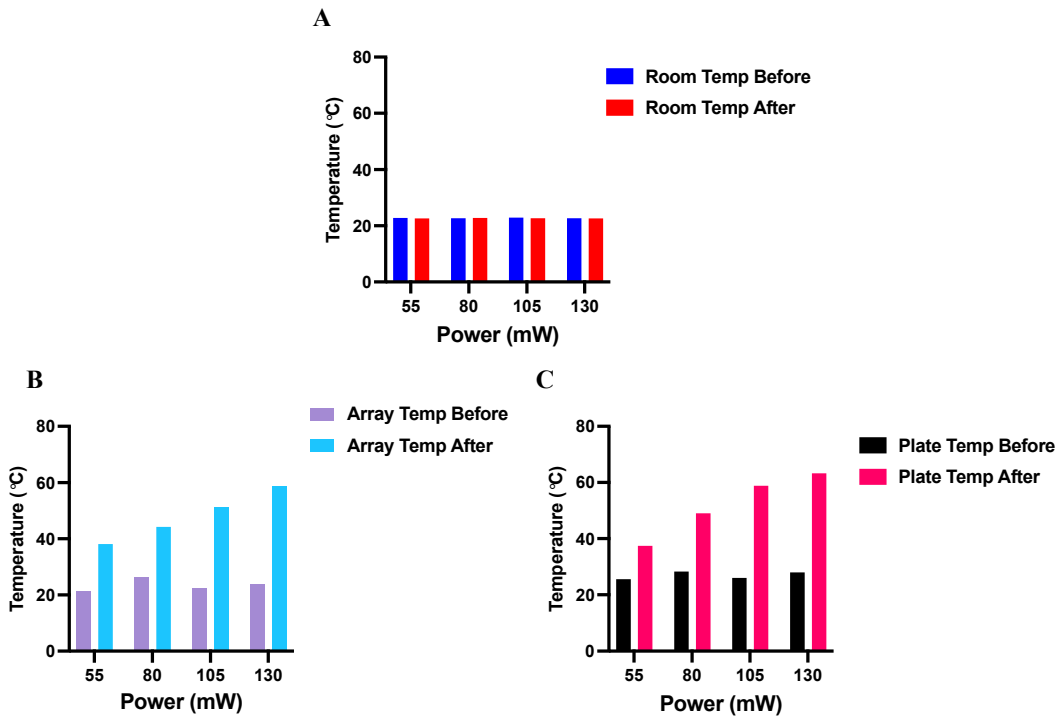


Figure 53. The temperature of the room (A), the array (B) and the plate (C) before and after the treatment of monochromatic Amber light from Lumidox® II 96-position Amber LED array at different power levels.

The metabolic activity of MCF-7 cells treated with multifunctionalised AuNPs and controls was evaluated 24 hours after being exposed to different powers of the amber LED array (Figure 54A-E). MCF-7 cells were treated with 20, 50, and 100 nm AuNP-PEG-Cyt *c*/Zn Porph at a concentration of 20 μg/mL, while controls of 20, 50, and 100 nm cit-AuNPs were also administered at the same concentration. Furthermore, Cyt *c* and Zn Porph were added to MCF-7 cells at a concentration of 1 μM. No significant disparity in metabolic activity was seen between the control cells and the multifunctionalised AuNP samples and AuNP controls when irradiated with the amber LED array at 30 mW (Figure 54A). At 55 mW, MCF-7 cells containing 20 nm AuNP-PEG-Cyt *c*/Zn Porph showed significantly higher metabolic activity than the control (Figure 54B). However, 50 nm and 100 nm AuNP-PEG-Cyt *c*/Zn Porph irradiated at this power both exhibited a decrease in metabolic activity, indicating that the Cyt *c* had been activated successfully and cell death had occurred; despite this, the results were not significantly different from the control

(Figure 54B). AuNP controls and unconjugated molecule controls were also not significantly different from the control cells, suggesting no cellular death occurred. At 80 mW (Figure 54C), the 20 nm AuNP-PEG-Cyt *c*/Zn Porph once again showed a higher mean metabolic rate, but the results were not significant due to the large standard deviation. Comparatively, both the 50 nm and 100 nm AuNP-PEG-Cyt *c*/Zn Porph samples demonstrated a significant reduction in metabolic activity when compared to the control. None of the AuNP controls or unconjugated molecule controls showed any significant differences in metabolic activity when compared to the control cells, suggesting they do not cause cellular death after irradiation. Samples irradiated at 105 mW (Figure 54D) and 130 mW (Figure 54E) displayed the same trend as the samples irradiated at 80 mW, but the results were not significantly different from the controls due to the large standard deviations.

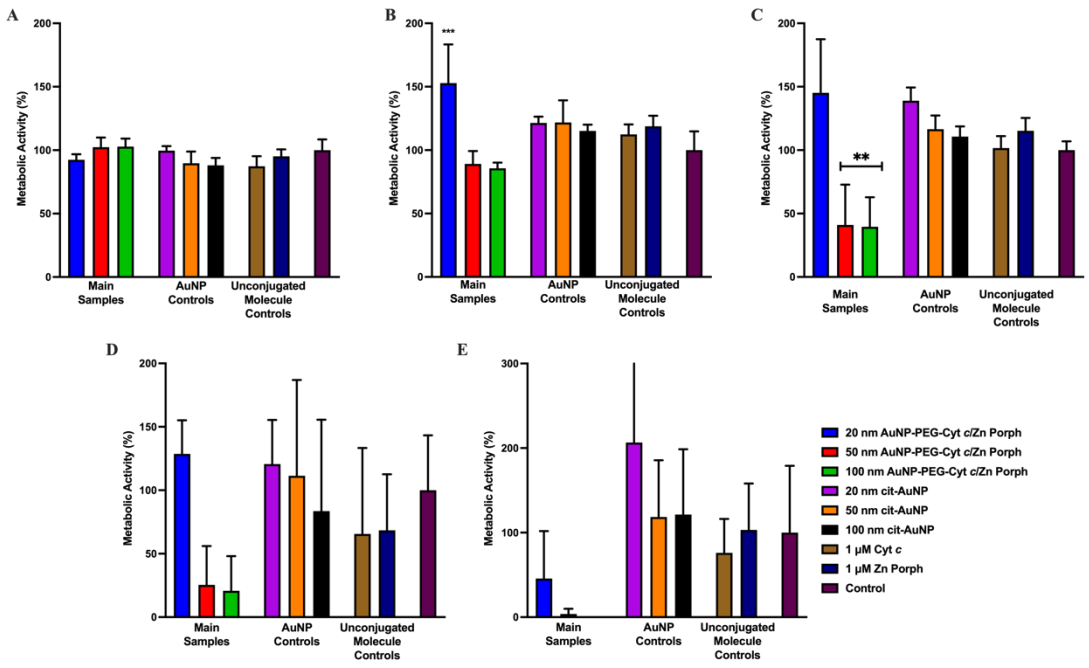


Figure 54. Metabolic activity of MCF-7 cells 24 hours after addition of main samples and controls with 30 min treatment of monochromatic Amber light from Lumidox® II 96-position Amber LED array at different power levels. 30mW (A), 55mW (B), 80mW (C), 105mW (D) and 130mW (E). P<0.05=* P<0.005=** P<0.0005=*** P<0.00005=****

The results of Figure 54 were further analysed by creating a heat map to investigate whether avoiding the centre of the plate could mitigate the negative effects of high temperatures on MCF-7 cells (Figure 18A-E). The samples were arranged between columns 1-12 and rows A-F, with multifunctionalised AuNPs in columns 1-3 and control samples in columns 10-12. The control cells were located in columns 7-12 in row G. The centre of the 96 well plates was left blank as that is the area that showed a significant reduction on the metabolic activity of cells which was a result of high temperatures. The heat map revealed that at 30 mW (Figure 55A) and 55 mW (Figure 55B), the power did not have a significant impact on the metabolic activity of MCF-7 cells, regardless of their location on the plate. However, at 80 mW (Figure 55C), 105 mW (Figure 55D) and 130 mW (Figure 55E), the metabolic activity of the cells towards the centre of the plate was significantly lower than those at the edges with increasing effect. This observation could explain the large standard deviation observed in the PrestoBlue assay for the samples in Figure 54C-E. While Figure 54C showed a promising increase in metabolic activity for the 20 nm AuNP-PEG-Cyt *c*/Zn Porph sample, there was still a notable decrease in metabolic activity of the cells closer to the centre of the plate compared to those at the edges. Therefore, the 80, 105, and 130 mW power stages were not used in subsequent experiments.

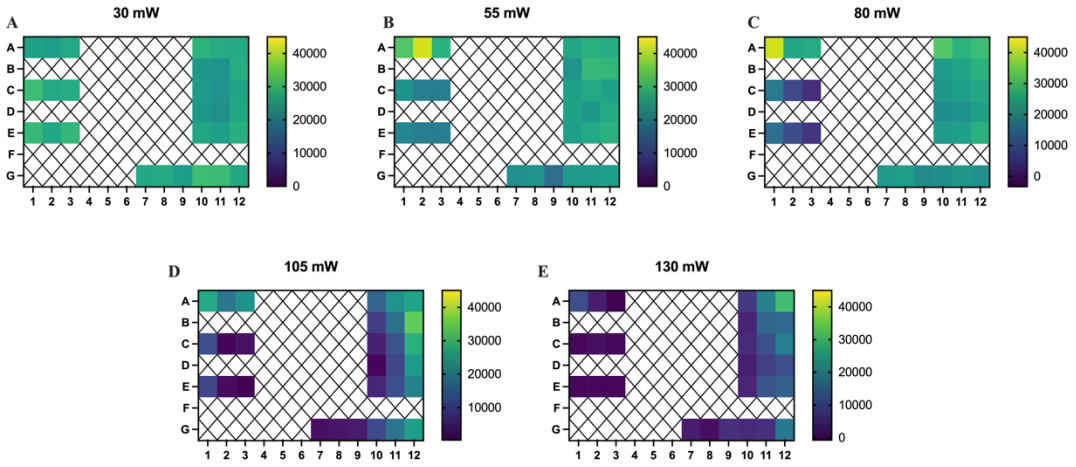


Figure 55. Metabolic activity of MCF-7 cells 24 hours after addition of main samples (Row 1-3) and controls (Row 10-12 and Row 7-12 in column G) with 30 min treatment of monochromatic Amber light from Lumidox® II 96-position Amber LED array at different power levels. 30mW (A), 55mW (B), 80mW (C), 105mW (D) and 130mW (E). Key corresponds to fluorescence intensity in RFU.

4.7.3.1. Effect of Size of AuNPs on Ability to Induce Apoptosis when Irradiated at Different Time Lengths

The metabolic activity of MCF-7 cells containing 20 nm AuNP controls and unconjugated molecule control was tested 24 hours after being irradiated for 60 minutes (Figure 56A-B). For the MCF-7 cells that received no irradiation (Figure 56A), there was a significantly greater metabolic activity for the AuNP control compared to the control, which may be the result of the AuNPs increasing the reduction rate of resazurin to resorufin. The MCF-7 cells irradiated for 60 minutes showed no significant change in metabolic rate from the controls (Figure 56B). The data shown in Figure 56A-B demonstrates that 20 nm AuNPs functionalised with Cyt *c* and Zn Porph can cause a significant increase in the fluorescence intensity produced in the PrestoBlue assay, suggesting an increase in the metabolic activity of MCF-7 cells, but is more likely the AuNPs increasing the reduction rate of resazurin to resorufin.

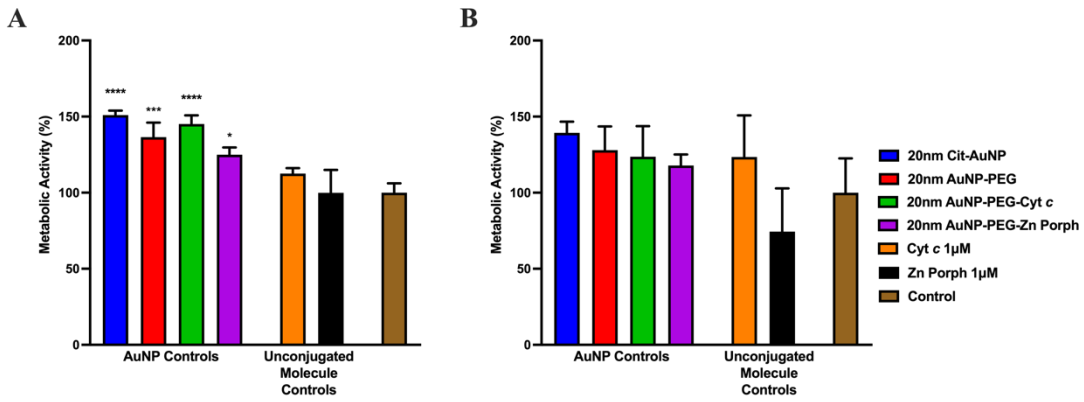


Figure 56. Metabolic activity of MCF-7 cells 24 hours after addition of 20 nm AuNP controls and unconjugated molecule controls after treatment with monochromatic Amber light from Lumidox® II 96-position Amber LED array at 55 mW for 60 minutes. No Treatment (A) and 60 minutes (B). AuNP and conjugated molecule controls were also included. P<0.05=* P<0.005=** P<0.0005=*** P<0.00005=****

The metabolic activity of MCF-7 cells containing 50 nm AuNP controls and unconjugated molecule control was also tested 24 hours after being irradiated for 60 minutes (Figure 57A-B). For the samples that received no irradiation (Figure 57A) there was no significant change in the metabolic activity when compared to the control. Samples irradiated for 60 minutes (Figure 57B) all showed increased 'apparent' metabolic activity compared to the control but only 50 nm cit-AuNPs are significantly different.

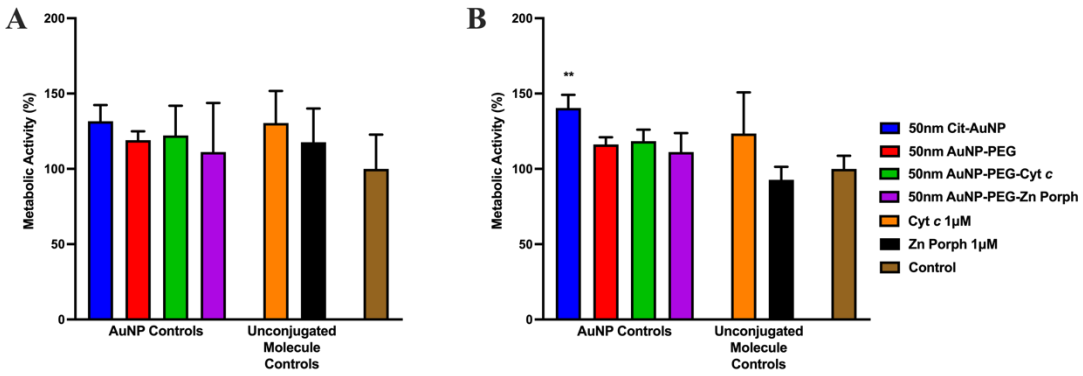


Figure 57. Metabolic activity of MCF-7 cells 24 hours after addition of 50 nm AuNP controls and unconjugated molecule controls after treatment with monochromatic Amber light from Lumidox® II 96-position Amber LED array at 55 mW for 60 minutes. No Treatment (A) and 60 minutes (B). AuNP and conjugated molecule controls were also included. P<0.05=* P<0.005=** P<0.0005=*** P<0.00005=****

Finally, the metabolic activity of MCF-7 cells containing 100 nm AuNP controls and unconjugated molecule control was tested 24 hours after irradiation for 60 minutes (Figure 58A-B). The 100 nm AuNP controls and unconjugated molecule controls followed the same trends as 20 and 50 nm controls (Figure 56 and Figure 57 A-D) with no significant decreases. Only significant increases were observed in the AuNP controls as a result of enhanced fluorescence ability, not indicative of an increase in metabolic rate.

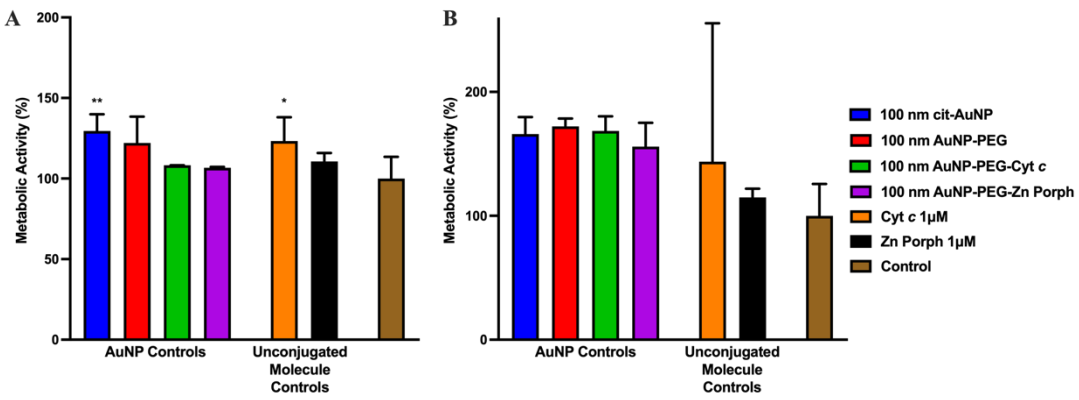


Figure 58. Metabolic activity of MCF-7 cells 24 hours after addition of 100 nmAuNP controls and unconjugated molecule controls after treatment with monochromatic Amber light from Lumidox® II 96-position Amber LED array at 55 mW for 60 minutes. No Treatment (A) and 60 minutes (B). AuNP and conjugated molecule controls were also included. P<0.05=* P<0.005=** P<0.0005=*** P<0.00005=****

In this section, no single functionalised AuNPs caused a toxic effect, but often showed increased metabolic activity. As discussed previously, cit-AuNPs, Cyt *c* and Zn Porph can contribute slightly to the fluorescence intensity of the PrestoBlue assay, which can result in an artificial increase in metabolic activity. The next stage of the study was to evaluate the impact of multifunctionalised AuNPs with sizes of 20, 50, and 100 nm on the metabolic activity of MCF-7 cells after amber light stimulation.

4.8. Effects on AuNPs multifunctionalised Cyt *c* Oxidised and Zn Porph with the AuNP concentration normalised

Determining whether the ligand and method used to conjugate Cyt *c* and Zn Porph to AuNPs affected the metabolic ability of MCF-7 cells was another crucial phase. The metabolic activity of MCF-7 cells containing 20, 50 and 100 nm AuNPs-PEG-Cyt *c*/Zn Porph Ox (main samples), 20, 50 and 100 cit-AuNPs (AuNP controls) and Cyt *c* and Zn Porph (unconjugated molecule controls) was determined after no treatment (Figure 59A) and after irradiation for 60 minutes (Figure 59B). The samples both before and after

treatment did not show significant differences from the control MCF-7 cells, indicating no overall apoptotic effect was induced by the 20, 50 and 100 nm AuNPs-PEG-Cyt *c*/Zn Porph Ox.

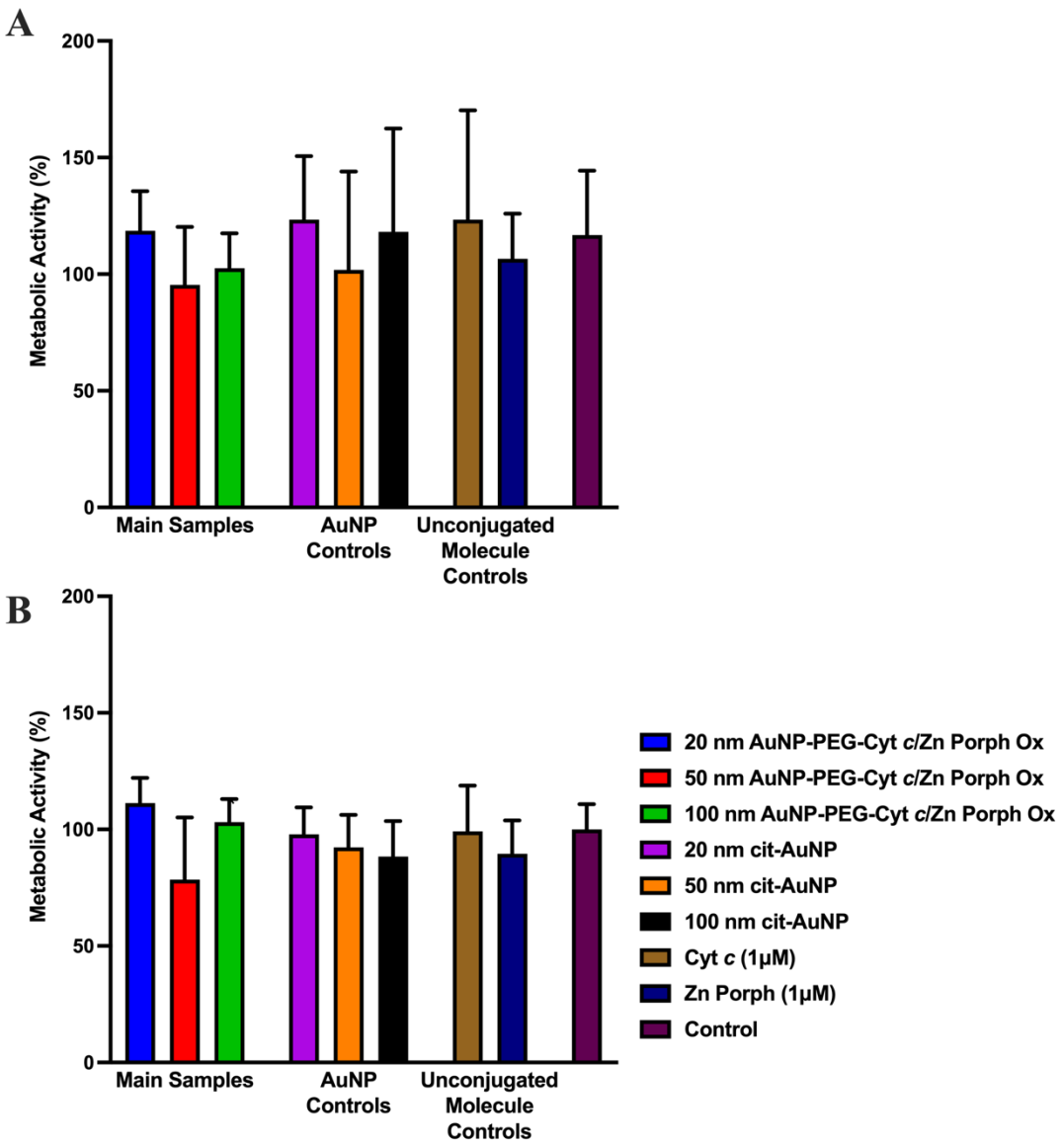


Figure 59. Metabolic activity of 20, 50 and 100 nm AuNPs-PEG-Cyt *c*/Zn Porph Ox covalently normalised for AuNPs at 20 μg/mL after treatment with monochromatic Amber light from Lumidox® II 96-position Amber LED array at 55 mW for different amounts of time. No Treatment (A) and 60 minutes (B). AuNP and unconjugated molecule controls were also included. P<0.05=* P<0.0005=***

The metabolic activity of MCF-7 cells containing 20, 50 and 100 nm AuNPs-MUA-Cyt *c*/Zn Porph Ox Cov (main samples), 20, 50 and 100 cit-AuNPs (AuNP controls) and Cyt *c* and Zn Porph (unconjugated molecule controls) was determined after no treatment (Figure 60A) and after irradiation for 60 minutes (Figure 60B). The only sample that showed any significant reduction from the control was the 100 nm cit-AuNPs in the plates untreated with amber light, potentially a result of the high uptake of the larger AuNPs causing a slightly toxic effect to the MCF-7 cells (Avishek Chakraborty and Ankita Das and Sreyan Raha and Ananya, 2020). Reduced metabolic activity was observed for MCF-7 cells inoculated with 50 and 100 nm AuNPs-MUA-Cyt *c*/Zn Porph Ox Cov after treatment, indicating the effectiveness of the treatment, yet these results were not significant enough to draw on.

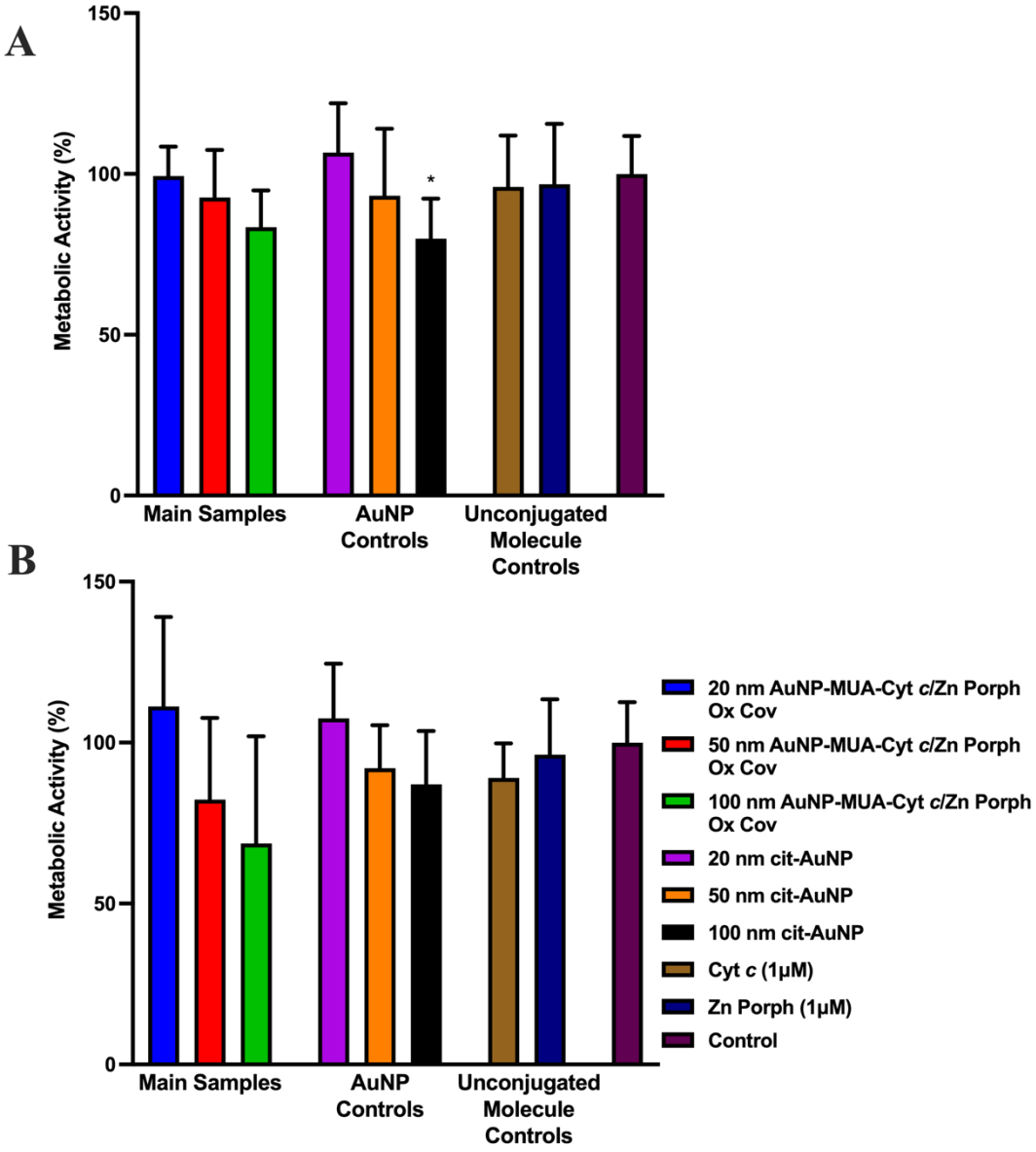


Figure 60. Metabolic activity of different sized AuNPs functionalised with MUA, Cyt *c* Ox, Zn Porph and Porph covalently normalised for AuNPs at 20 μg/mL after treatment with monochromatic Amber light from Lumidox® II 96-position Amber LED array at 55 mW for different amounts of time. No Treatment (A) and 60 minutes (B). AuNP and conjugated molecule controls were also included. P<0.05=*

The metabolic activity of MCF-7 cells containing 20, 50 and 100 nm AuNP-MUA-Cyt *c*/Zn Porph Ox Electro (main samples), 20, 50 and 100 cit-AuNPs (AuNP controls) and

Cyt *c*, Zn Porph and Porph (unconjugated molecule controls) was also determined after no treatment (Figure 61A) and after irradiation for 60 minutes (Figure 61B). As expected, the untreated samples did not yield a significant change in the metabolic activity of MCF-7 cells from the control (Figure 61A). The samples irradiated for 60 minutes did however exhibit a significant reduction in the metabolic activity of MCF-7 cells containing 100 nm AuNP-MUA-Cyt *c*/Zn Porph. This appears to be the result of the activation of Cyt *c* via Zn Porph after irradiation causing cellular death (Figure 61B). The remaining main samples, AuNP controls and the unconjugated molecule controls all showed no change in the metabolic activity of MCF-7 cells when compared to the control.

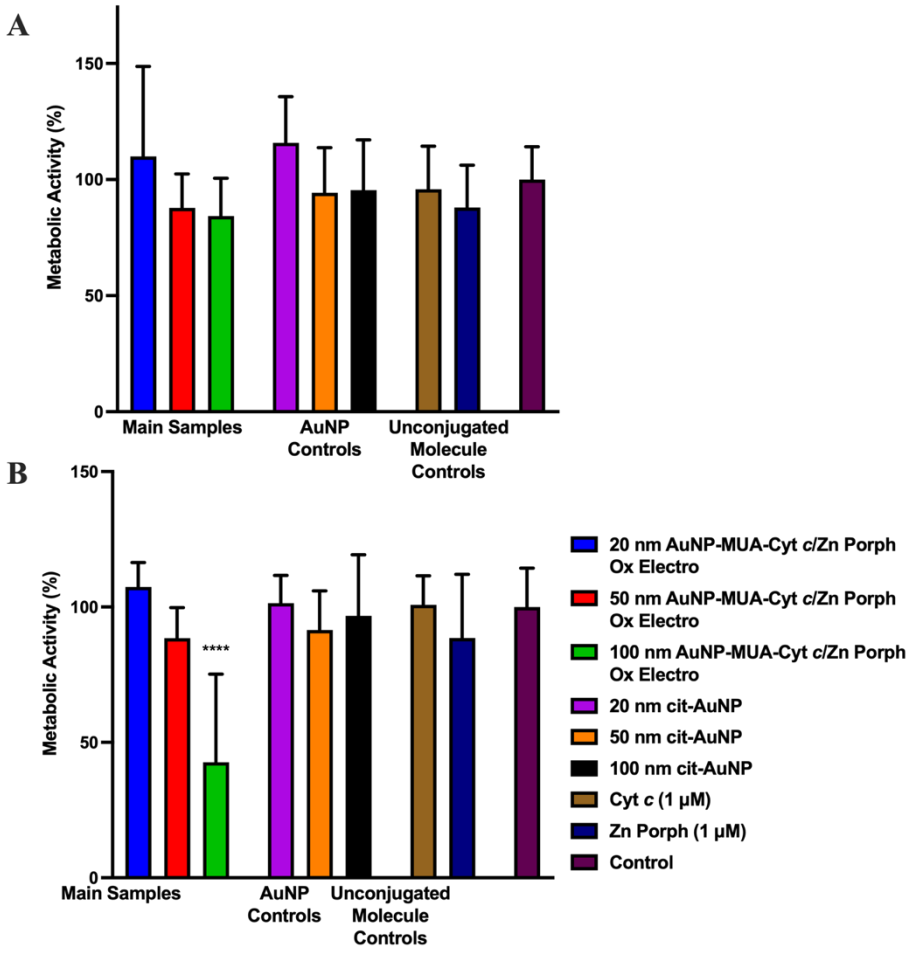


Figure 61. Metabolic activity of different sized AuNPs functionalised with MUA, Cyt *c* Ox, Zn Porph and Porph covalently normalised for AuNPs at 20 µg/mL after treatment with monochromatic Amber light from Lumidox® II 96-position Amber LED array at 55 mW for different amounts of time. No Treatment (A) and 60 minutes (B). AuNP and conjugated molecule controls were also included. P<0.00005=****

The results from the PrestoBlue assays suggest that only 100 nm AuNP-MUA-Cyt *c*/Zn Porph Electro can induce apoptosis in cells. However, prior studies had indicated that both AuNPs and Cyt c could enhance the fluorescence intensity generated by the PrestoBlue assay. This effect may potentially hinder the assay's ability to detect the metabolic activity of MCF-7 cells and, ultimately, cellular mortality.

To help identify the effect of multifuntionalised AuNP treatment, live/dead staining was next conducted.

4.8.1. Live/Dead Determination for MCF-7 cells containing Multifucntionalised AuNPs with and without 60 Minutes of Amber Light Treatment

MCF-7 cells were subjected to Differential Nuclear Staining (DNS) using Hoechst and propidium iodide (PI) dyes to determine the number of viable and dead cells, both with and without exposure to 60 minutes of amber LED array irradiation. Hoechst and PI are DNA-intercalating dyes, with Hoechst staining the nucleus of all cells, and PI staining only the DNA of dead cells (Lema et al., 2011). By subtracting the number of dead cells from the total number of cells within a given sample and dividing the outcome by the total number of cells, the percentage of live cells was calculated for all samples treated with and without the amber LED array (Figure 62A-B). The MCF-7 cells were inoculated with different samples, including 20, 50 and 100 nm AuNP-PEG-Cyt *c*/Zn Porph Ox (main samples), 20, 50 and 100 cit-AuNPs (AuNP controls) and Cyt *c* Ox and Zn Porph (unconjugated molecule controls). Control groups of live MCF-7 cells (cells only) and dead MCF-7 cells (cells treated with MeOH for 15 minutes) were used to assess the effectiveness of the treatment. The overlays of Hoechst (coloured green) and PI (coloured red) before and after treatment were presented in Figure SI 13A-J and Figure SI 14, respectively.

The percentage of live cells in untreated MCF-7 cells decreased when exposed to all main samples and AuNP controls, relative to MCF-7 cells alone. This could be due to the samples interacting with the cells for 24 hours, creating more stress than in the live cell control. Meanwhile, the dead cells control had significantly fewer live cells than the MCF-7containingontaing the main samples, AuNP controls, and unconjugated molecule controls, indicating that most cells were viable. (Figure 62A).

After 60 minutes of treatment with the amber LED array, the percentage of live cells observed in the main samples was significantly reduced, with the largest decrease seen in the 20, 50 and 100 nm AuNP-PEG-Cyt *c*/Zn Porph samples. This suggests that the

PrestoBlue assay may not be suitable for this work, as the fluorescence of resorufin may be enhanced by the AuNPs and conjugated molecules, resulting in the insignificant amount of cellular death previously assumed. The reduction in the percentage of live cells in the main samples indicates that Cyt *c* is activated by the amber LED array in MCF-7 cells, suggesting that it is the Cyt *c* that is the main cause of apoptosis.

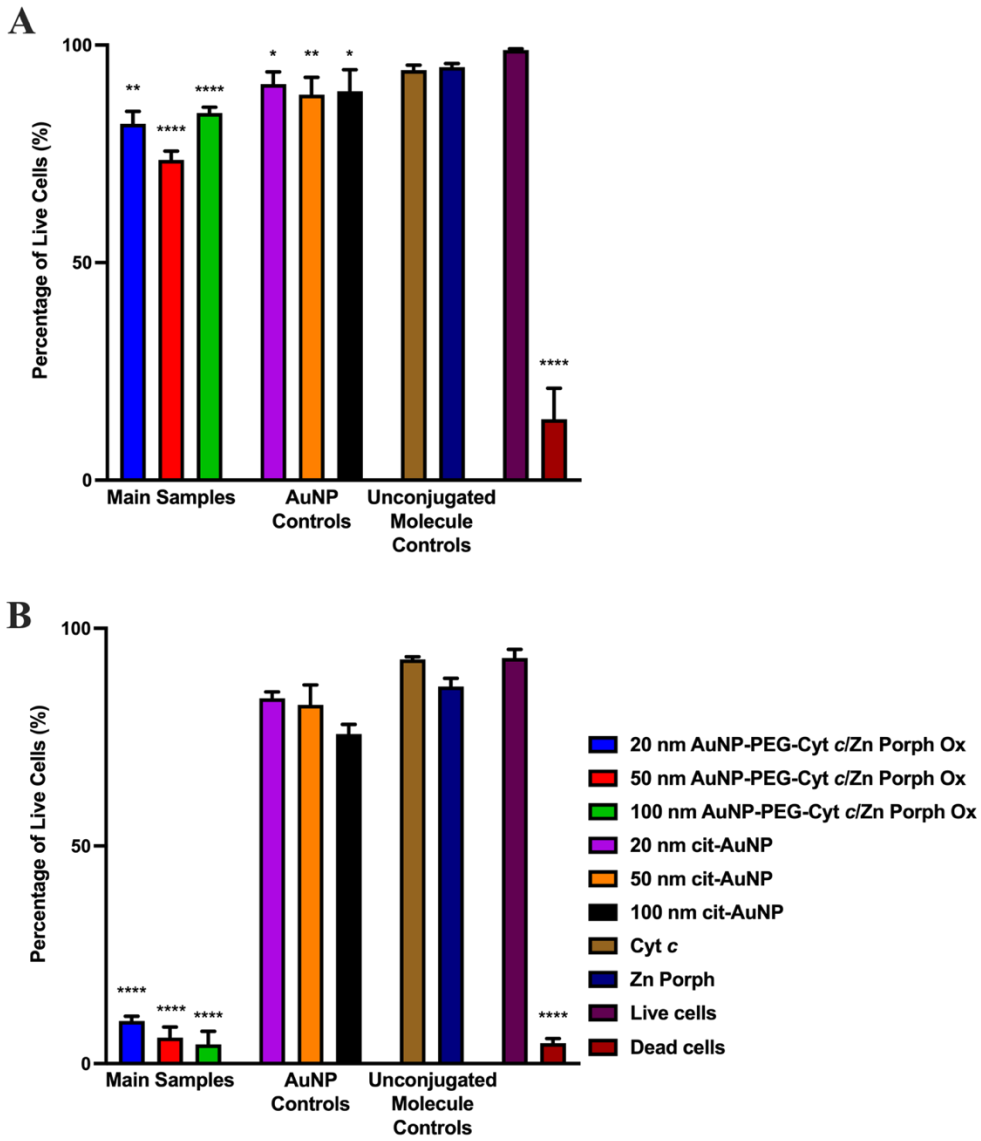


Figure 62. Live/Dead determination of MCF-7 cells containing AuNP-PEG-Cyt *c*/Zn Porph Ox normalised for AuNPs at 20 μg/mL. Before treatment (A) and after treatment with monochromatic Amber light from Lumidox® II 96-position amber LED array at 55 mW for 60 minutes (B). P<0.05=* P<0.005=** P<0.0005=*** P<0.00005=****

The same experiment outlined above was conducted for the 20, 50, and 100 nm AuNP-MUA-Cyt *c*/Zn Porph Ox Cov (main samples), 20, 50, and 100 cit-AuNPs (AuNP controls), and Cyt *c* and Zn Porph (unconjugated molecule controls) (Figure 63A-B). The overlays of Hoechst (coloured green) and PI (coloured red) before and after treatment are shown in Figure SI 15A-F. The effectiveness of the treatment was evaluated using live and dead MCF-7 cell controls. The AuNP and unconjugated molecule controls used in Figure 62A-B were also used here since the experiments were conducted simultaneously. A small decrease in the percentage of live cells was observed for the untreated MCF-7 cells in both the main samples and AuNP controls (Figure 63A), likely due to cellular stress from the uptake of AuNPs. After treatment with the amber LED array for 60 minutes, the main samples showed a significant reduction in the amount of live MCF-7 cells, when compared to the AuNP and unconjugated molecule controls (Figure 63B); this can be attributed to the activation of Cyt *c* via Zn Porph triggered by the irradiation. A similar result was seen in Figure 62B.

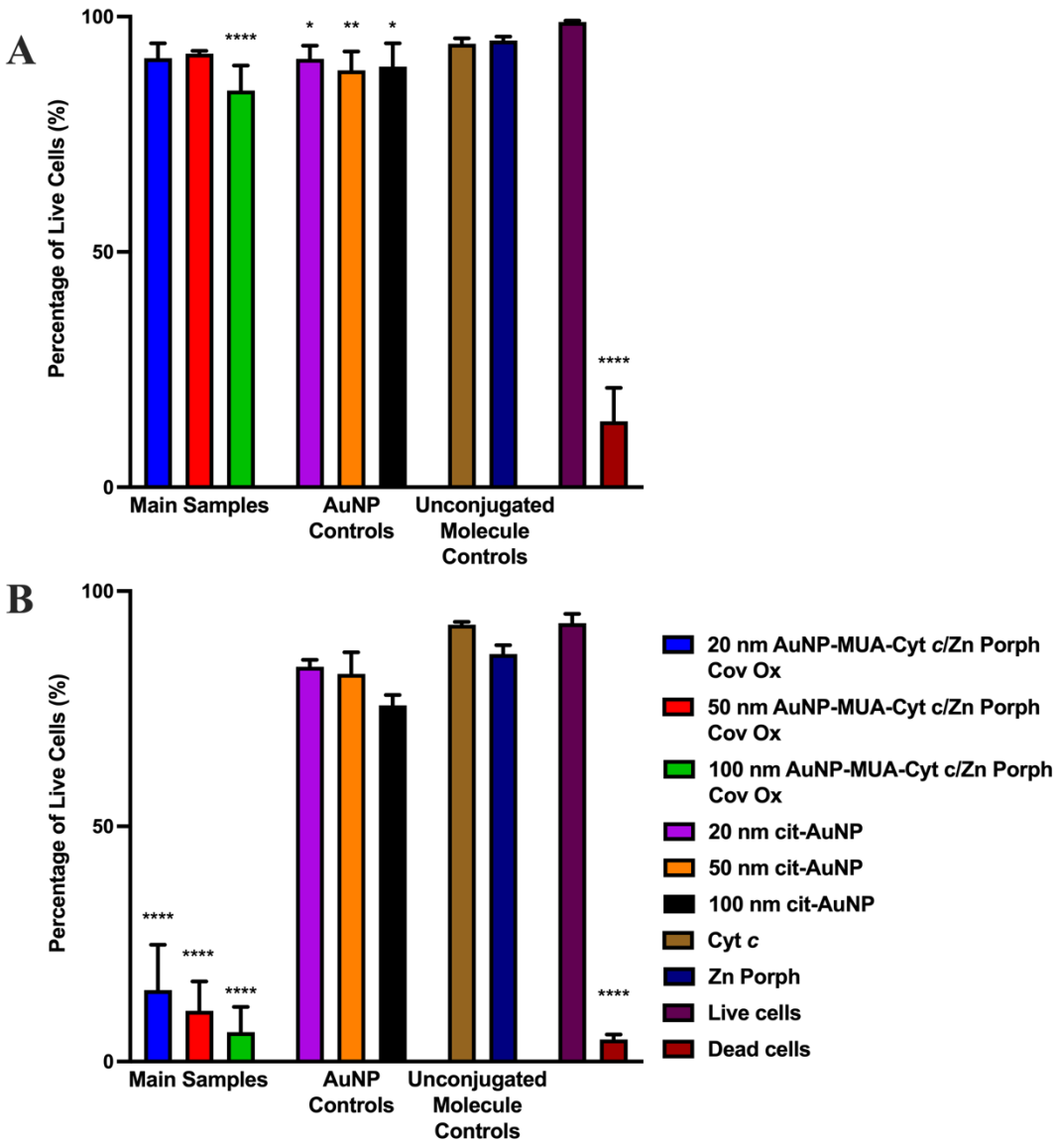


Figure 63. Live/Dead determination of MCF-7 cells containing AuNP-MUA-Cyt *c*/Zn Porph Ox Cov normalised for AuNPs at 20 μg/mL. Before treatment (A) and after treatment with monochromatic amber light from Lumidox® II 96-position amber LED array at 55 mW for 60 minutes (B). P<0.05=* P<0.005=** P<0.0005=*** P<0.00005=****

The percentage of live MCF-7 cells containing 20, 50 and 100 nm AuNP-MUA-Cyt *c*/Zn Porph Ox Electro (main samples) was also determined before and after a 60-minute treatment with the amber LED array, as shown in Figure 64A-B. The overlays of Hoechst (colourised green) and PI (colourised red) before treatment are displayed in Figure SI 16A-C, and those after treatment are shown in Figure S4D-F. The live, dead, AuNP and unconjugated molecule controls used are the same as those in Figure 62A-B and Figure 63A-B, since the experiments were conducted simultaneously. The results from this experiment align with those from Figure 62A-B and Figure 63A-B, indicating that without treatment, the MCF-7 cells exhibited only a minor decrease in the percentage of living cells, similar to that seen in the reduction of AuNP main samples and controls. However, after the 60-minute treatment, the percentage of live cells in the main samples significantly decreased when compared to the AuNP and unconjugated molecule controls (Figure 27B). This finding supports the activation of Cyt *c* via Zn Porph's capacity to transfer energy/electrons to Cyt *c* during the 60-minute amber LED array treatment.

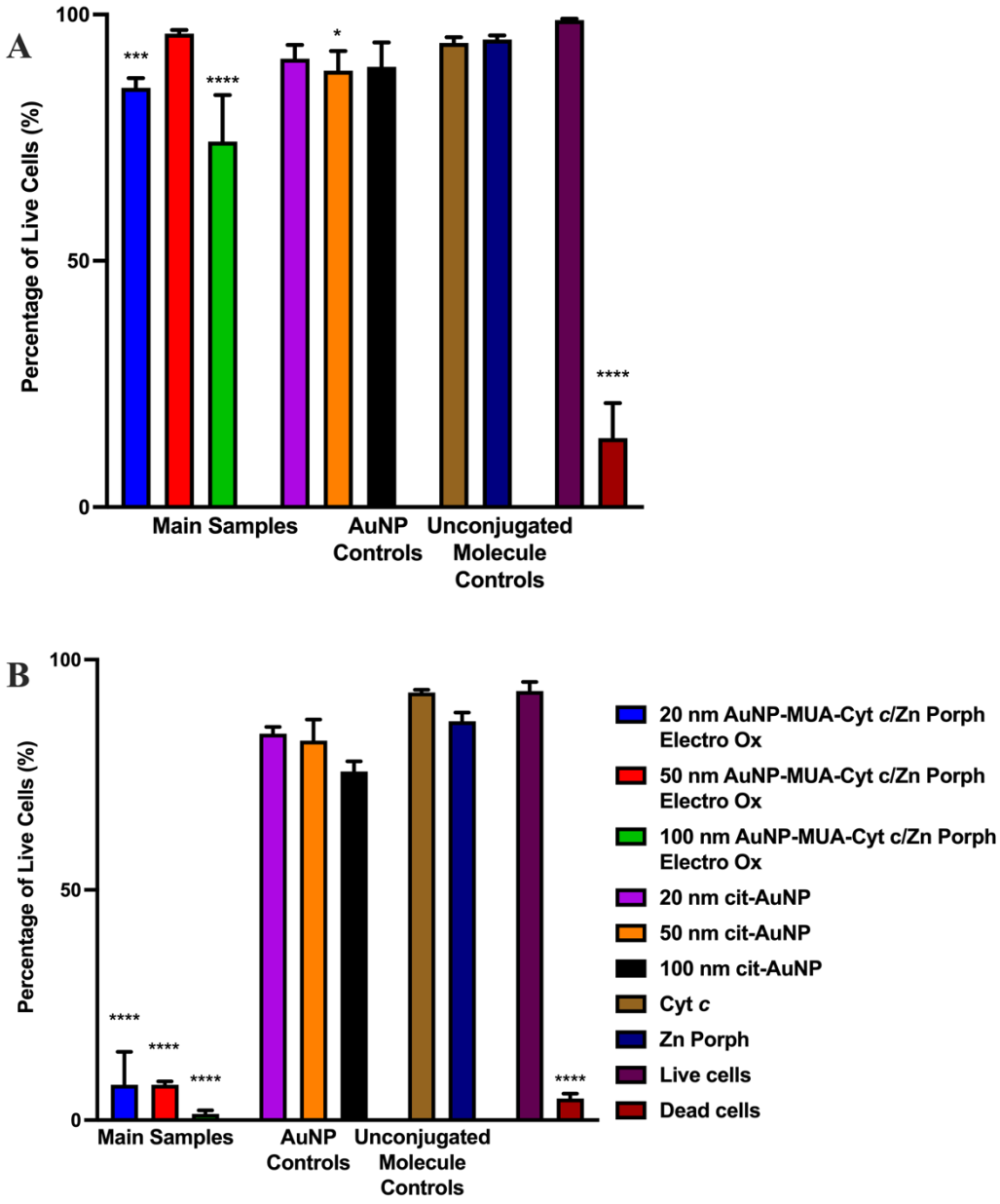


Figure 64. Live/Dead determination of MCF-7 cells containing AuNP-MUA-Cyt *c*/Zn Porph Ox Electro normalised for AuNPs at 20 µg/mL. Before treatment (A) and after treatment with monochromatic Amber light from Lumidox® II 96-position Amber LED array at 55 mW for 60 minutes (B). P<0.05=* P<0.005=** P<0.0005=*** P<0.00005=****

This study presents findings that contradict the data observed in section 4.8, where the PrestoBlue assay suggested that the ligand and conjugation strategy employed to bind molecules to AuNPs can impact the system's ability to induce apoptosis. Specifically, the results here show that the conjugation of AuNP-PEG-Cyt *c*/Zn Porph Ox, AuNP-MUA-Cyt *c*/Zn Porph Ox Cov and AuNP-MUA-Cyt *c*/Zn Porph Ox Electro does not affect the ability of Cyt *c* and Zn Porph to induce apoptosis in MCF-7 cells when activated using the amber LED array. The DNS assay results suggest that the proposed cancer treatment is effective at inducing cellular death, only when activated by a light stimulus of a specific wavelength.

Furthermore, the data presented in

Figure 65 indicates that the heterogeneous rate constant of Cyt *c* conjugated to 20, 50, and 100 nm multifunctionalised AuNPs does not significantly affect the percentage of live cells. These findings also suggest that the orientation of Cyt *c* has no significant influence on its ability to induce apoptosis via activation triggered by an amber light stimulus.

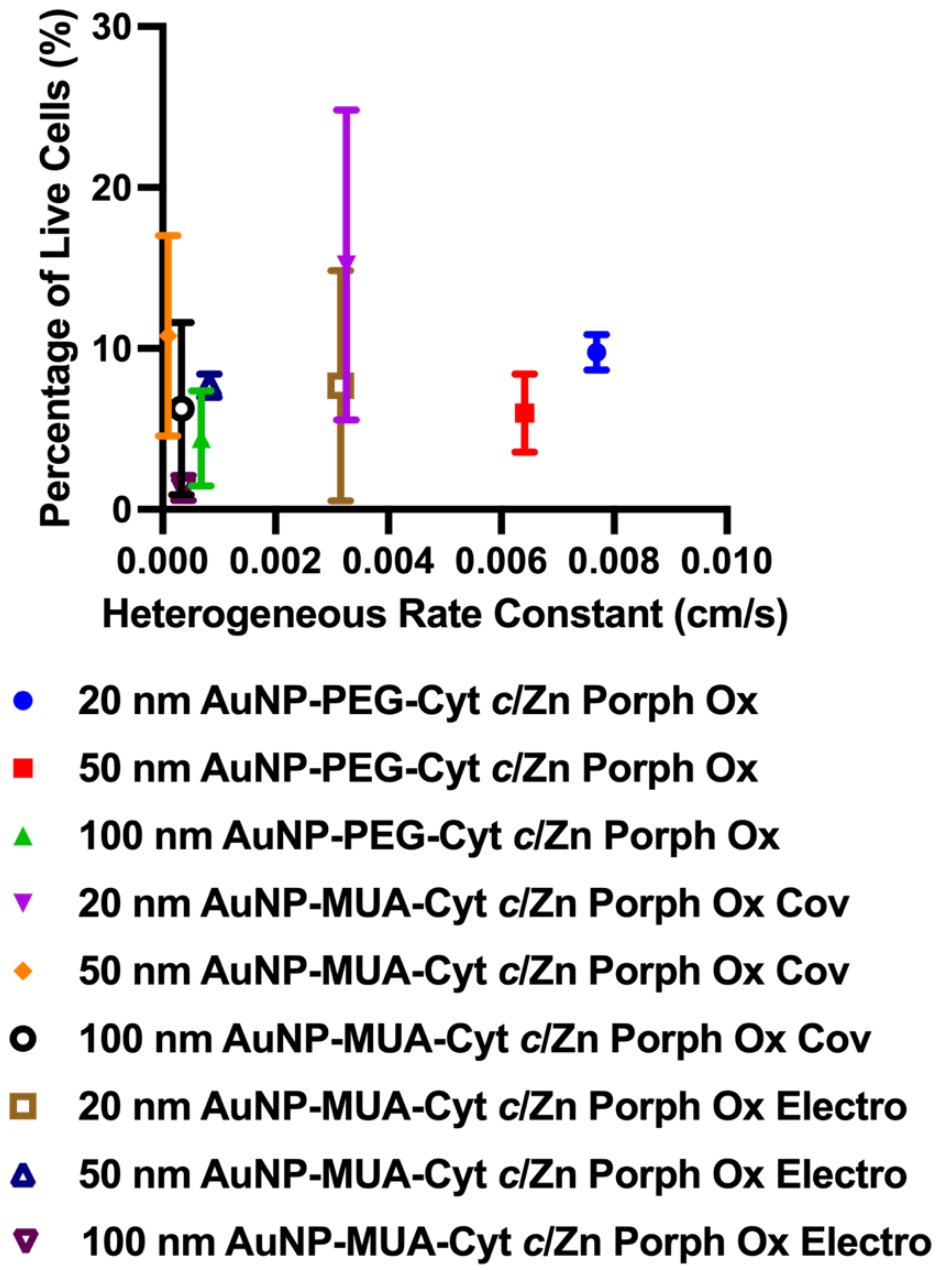


Figure 65. Percentage of Live cells versus the heterogeneous rate constant for Cyt *c* conjugated to 20, 50 and 100 nm AuNP-PEG-Cyt *c*/Zn Porph Ox, AuNP-MUA-Cyt *c*/Zn Porph Ox Cov and AuNP-MUA-Cyt *c*/Zn Porph Ox Electro.

4.8.2. Singlet Oxygen Detection of MCF-7 Cells Inoculated with Multifunctionalised AuNPs and Controls with and without Treatment with an Amber LED Array.

In order to verify that the multifunctionalised AuNPs were responsible for inducing apoptosis through Cyt *c* and Zn Porph interactions, an experiment was conducted to investigate whether intracellular $^1O_2$ was produced by the Zn Porph in the system, after 60 minutes of irradiation. However, the images obtained from singlet oxygen analysis did not show a significant increase in MCF-7 cells containing controls when compared to AuNP-PEG-Cyt *c*/Zn Porph Ox, AuNP-MUA-Cyt *c*/Zn Porph Ox Cov and AuNP-MUA-Cyt *c*/Zn Porph Ox Electro (Figure 66A-H, Figure 67A-F, Figure 687A-F, and Figure 698A-F). These findings suggest that the elevated cell deaths caused by the multifunctionalised AuNPs were not the result of increased singlet oxygen production thus can, it can be concluded that the cellular death was solely the result of Cyt *c* activation via light stimulus as the hypothetical method would be the result of the excitated Zn Porph providing Cyt *c* with enough energy to become 'activated' (reduction of Cyt *c*) and initiate cell death.

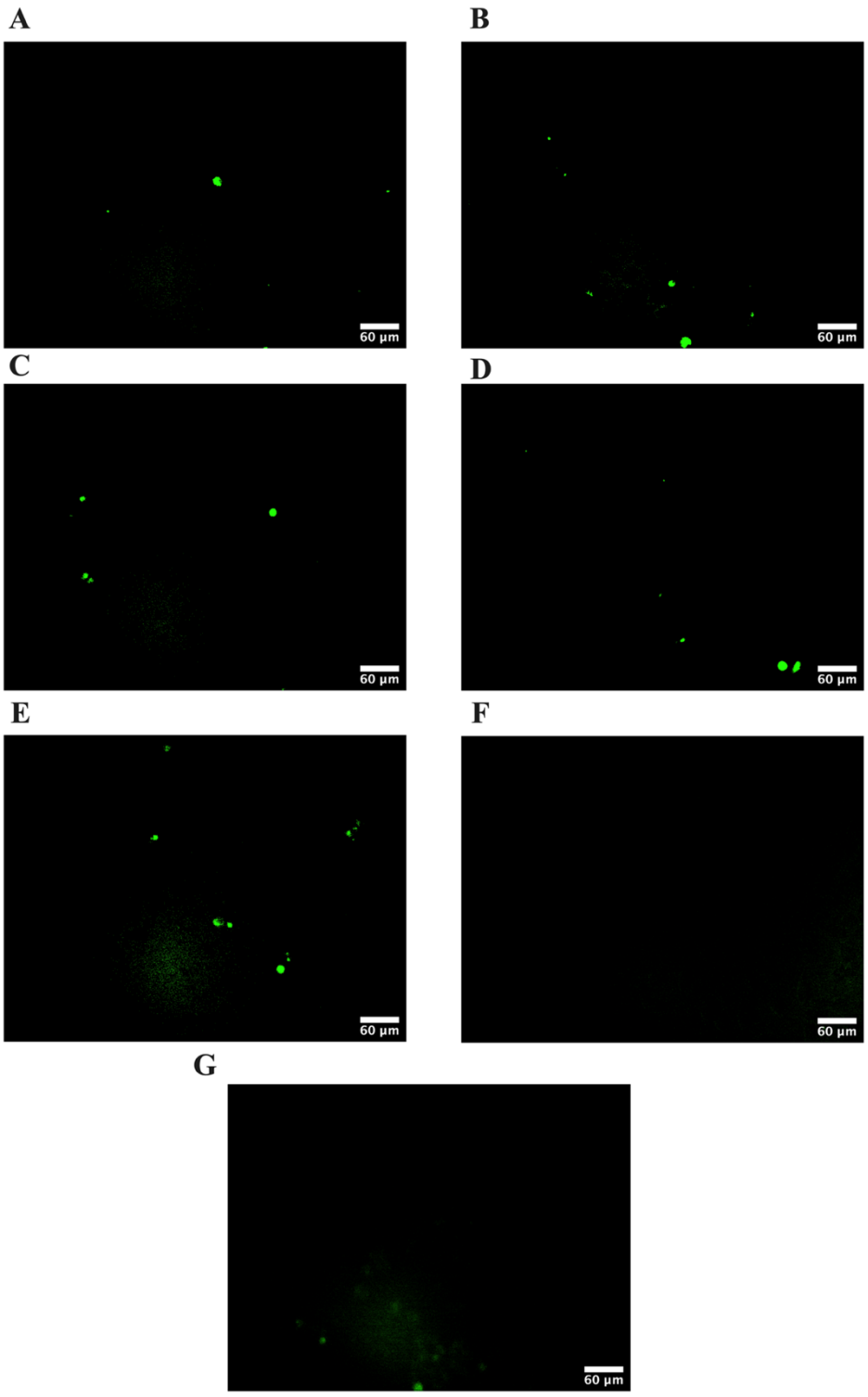


Figure 66: Singlet oxygen detection of MCF-7 cells containing AuNPs multifunctionalised of 20 nm cit-AuNPs (A), 50 nm cit-AuNPs (B), 100 nm cit-AuNPs (C), Cyt *c* 2 µM (D), Zn Porph 2 µM (E), live cells (F), and dead cells (G) normalised for

AuNPs at 20 µg/mL after treatment with monochromatic Amber light from Lumidox® II 96-position Amber LED array at 55 mW for 60 minutes.

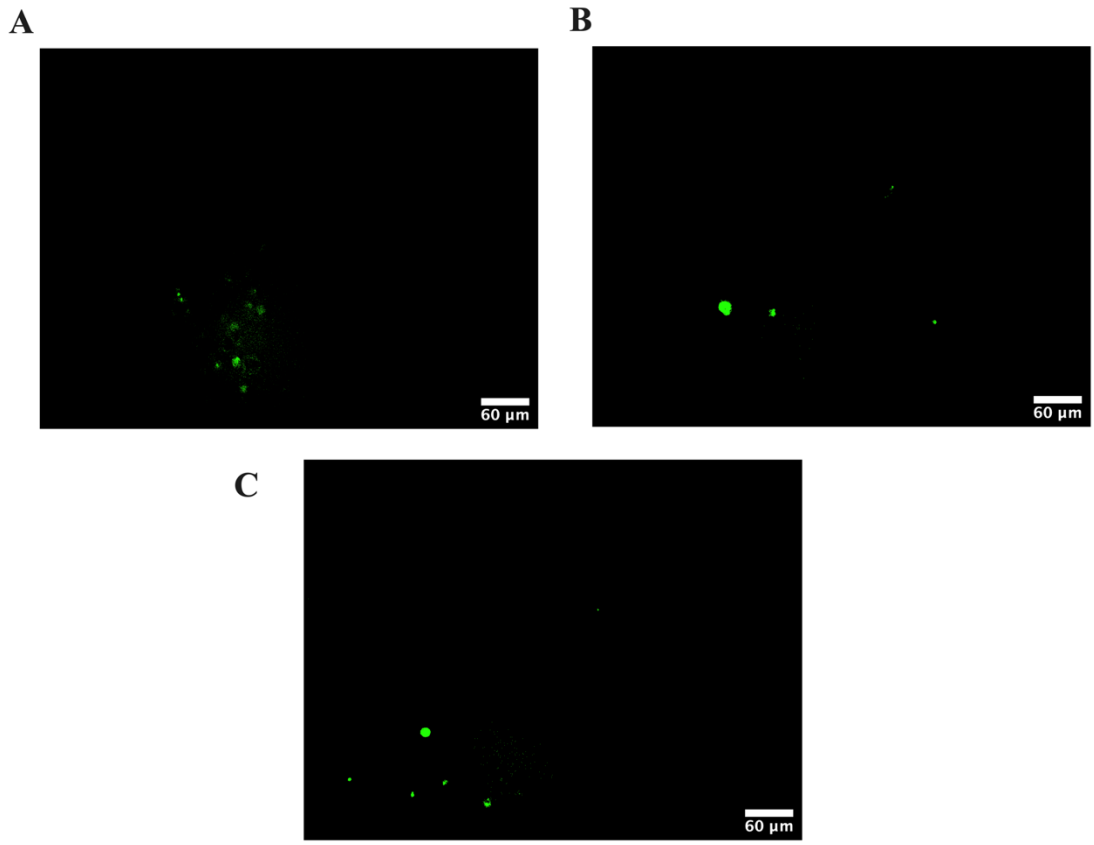


Figure 67: Singlet oxygen detection of MCF-7 cells containing AuNP-PEG-Cyt *c*/Zn Porph Ox normalised for AuNPs at 20 µg/mL after treatment with monochromatic Amber light from Lumidox® II 96-position Amber LED array at 55 mW for 60 minuets. 20 nm AuNP-PEG-Cyt *c*/Zn Porph (A), 50 nm AuNP-PEG-Cyt *c*/Zn Porph (B) and 100 nm AuNP-PEG-Cyt *c*/Zn Porph (C).

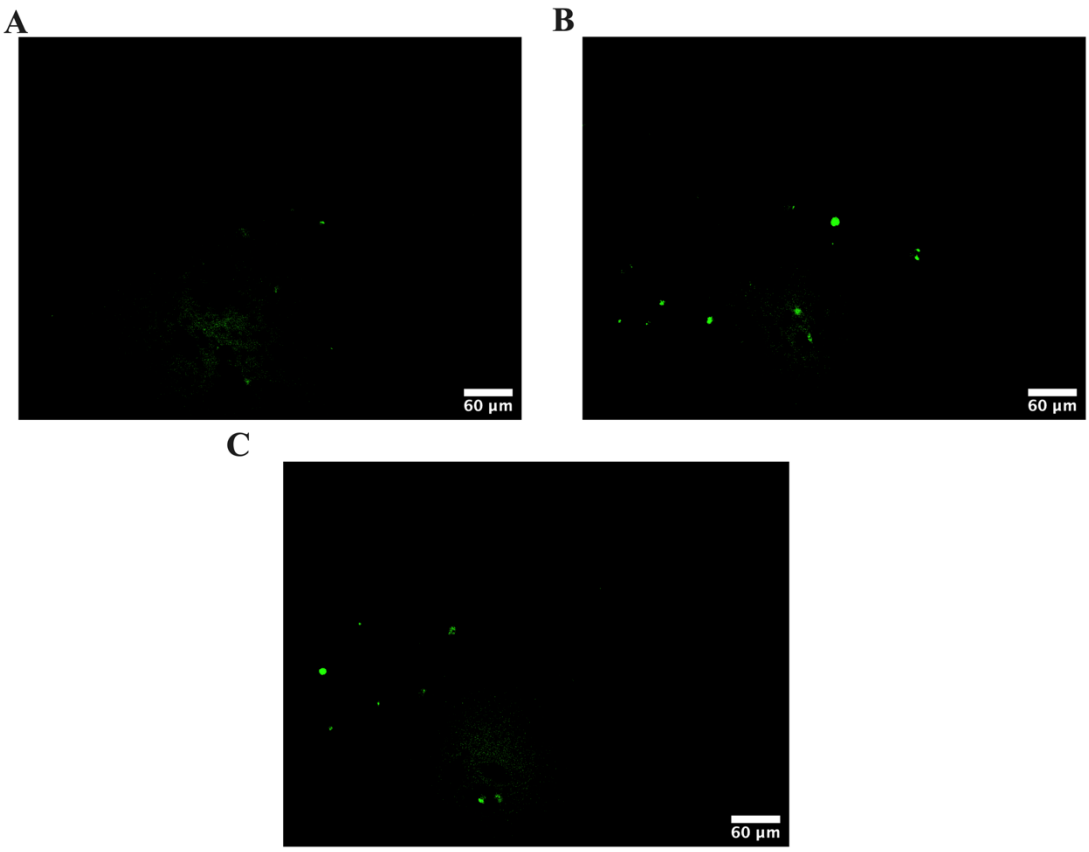


Figure 68. Singlet oxygen detection of MCF-7 cells containing AuNP-MUA-Cyt *c*/Zn Porph Ox Cov normalised for AuNPs at 20 µg/mL before and after treatment with monochromatic Amber light from Lumidox® II 96-position Amber LED array at 55 mW for 60 minuets. Before treatment, 20 nm AuNP-MUA-Cyt *c*/Zn Porph Cov (A), 50 nm AuNP-PEG-Cyt *c*/Zn Porph Cov (B) and 100 nm AuNP-PEG-Cyt *c*/Zn Porph Cov (C).

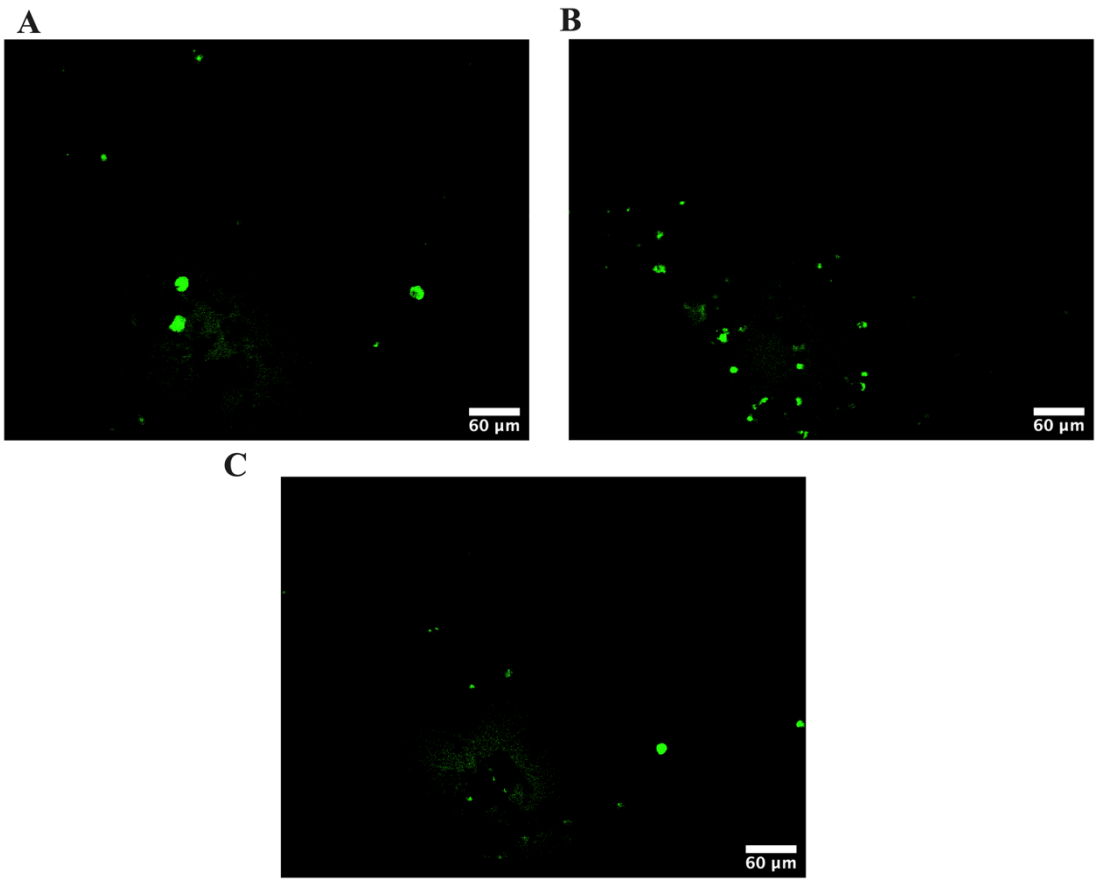


Figure 69. Singlet oxygen detection of MCF-7 cells containing AuNP-MUA-Cyt *c*/Zn Porph Ox Electro normalised for AuNPs at 20 µg/mL before and after treatment with monochromatic Amber light from Lumidox® II 96-position Amber LED array at 55 mW for 60 minutes. 20 nm AuNP-MUA-Cyt *c*/Zn Porph Electro (A), 50 nm AuNP-PEG-Cyt *c*/Zn Porph Electro (B) and 100 nm AuNP-PEG-Cyt *c*/Zn Porph Electro (C).

4.9. Conclusion

To surmmarise, this chapter demonstrated that the multifunctionalised AuNP cancer treatment induced cellular death only when exposed to an amber light LED array.

The uptake of multifunctionalised AuNPs into MCF-7 cells was evaluated using ICP-MS, and it was observed that covalent conjugation methods reduced the number of AuNPs per cell, especially for smaller AuNPs. Nevertheless, confocal microscopy showed that all multifunctionalised AuNPs were internalised with no visible AuNPs attached to the outside of the cells.

The peroxide activity of Cyt *c* increased consistently with a rise in AuNP diameter, suggesting that the heme ring of Cyt *c* is more accessible within larger AuNPs, or that the larger AuNPs themselves aid the peroxidase activity of Cyt *c*.

The results from the PrestoBlue assay indicated that primarily, it was the 100 nm AuNP-MUA-Cyt *c*/Zn Porph Electro that was most effective in reducing the metabolic activity of MCF-7 cells after treatment. The main 20 and 50 nm AuNP samples, as well as the controls containing only cit-AuNPs and unconjugated molecules, contrastingly appeared to show an apparent increase in metabolic activity in MCF-7 cells. This effect can be attributed to the enhancing effect that small AuNPs can have on fluorescence intensity, artificially increasing the apparent metabolic activity. The observation suggests that there is a significant amount of fluorescent overlap between the molecule causing fluorescence in PrestoBlue and the multifunctionalised AuNPs. Therefore, PrestoBlue may not be an ideal method for this study.

The live/dead study demonstrated that the addition of 20, 50, and 100 nm AuNPs multifunctionalised with Cyt *c* Ox and Zn Porph significantly decreased the percentage of live cells within samples after only 60 minutes of treatment with the amber LED array. The AuNP and unconjugated molecule controls were not significantly different from the live cells' control. The percentage of live MCF-7 cells after 60 minutes of irradiation with

the primary AuNP samples was compared to the heterogeneous rate constant calculated in the previous chapter and showed no apparent link, indicating that neither the heterogeneous rate constant nor orientation of Cyt *c* conjugated to the multifunctionalised AuNPs play a significant role in the apoptotic ability of this cancer treatment. The singlet oxygen produced after 60 minutes of irradiation of MCF-7 cells containing the primary samples and controls also showed no significant difference in fluorescence intensity, so cannot be attributed to the large increase in cellular death seen within the primary AuNP samples and the controls.

Ultimately, this chapter concludes that AuNPs multifunctionalised with Cyt *c* and Zn Porph are internalised into MCF-7 cells successfully and have the ability to induce cell death when triggered via an amber light source.

5. Conclusion and Future Work

5.1. Introduction

The work in this thesis has attempted to show the development of a novel cancer treatment, utilising AuNPs to deliver Cyt *c* and Zn Porph to cancerous cells and cause cell death, when activated via a monochromatic light source. This final chapter discusses the findings of this research and suggests work which would further the development of this cancer treatment.

5.2. Main Findings

5.2.1. Chapter 2 - Synthesis and Characterisation of AuNPs Multifunctionalised with Cyt *c* and Porphyrins

In Chapter 2, AuNPs with specific sizes of 20, 50, and 100 nm were successfully synthesised and functionalised with Cyt *c* and Zn Porph. A comprehensive characterisation strategy was employed, leveraging the strengths of techniques such as DLS, Zeta potential, UV-Vis absorption spectroscopy, TEM and XPS, providing a multifaceted view of the functionalised particles. Importantly, the conjugation of Cyt *c* and Zn Porph to the AuNPs was accomplished without inducing any aggregation, ensuring the integrity of the AuNPs. A pivotal development in this work was the introduction of a novel method for deconvoluting UV-Vis absorption spectra. This innovative approach allows for the precise determination of the concentration of Cyt *c* and Zn Porph, as well as the accurate quantification of molecules bound to the AuNPs.

A significant limitation encountered during this research was the need to synthesise a substantial quantity of AuNPs in-house. One of the initial attractions of AuNPs stemmed from their commercial availability; preliminary experiments that are not documented in

this thesis utilised these commercially available AuNPs. However, during conjugation processes using carbodiimide chemistry, these AuNPs exhibited surprising instability, contrary to existing literature. This instability prompted a shift in approach, necessitating the in-house synthesis of AuNPs for the remainder of the project. Freshly synthesised AuNPs showcased superior stability, implying that commercially available variants may have been produced considerably earlier and thus lack the required stability for the purposes of this work. Stability of the AuNPs is also an important consideration in regards to the future clinical applicability of this treatment.

5.2.2. Chapter 3 - Structural and Electrochemical Analysis of Gold Nanoparticles Functionalised with Cytochrome *c* and Zinc Porphyrin

In Chapter 3, the electrochemical properties of Cyt *c* and Zn Porph were assessed both before and after their conjugation to AuNPs, giving insight on significant molecular structural changes. Following conjugation to AuNPs, Cyt *c* underwent noticeable changes in both its secondary and tertiary structures, as determined by CD. Interestingly, amongst the explored methods, the thiol-PEG-carboxyl functionalised AuNPs retained a structure closest to native Cyt *c*, especially when compared to MUA-based conjugation techniques. A critical observation was the pronounced structural changes Cyt *c* underwent when conjugated to larger AuNPs, highlighting the significance of packing density. Contrary to initial hypotheses, covalent conjugation of Cyt *c* showcased less structural change than electrostatic conjugation of Cyt *c* bound to AuNPs using MUA. Notably, post-conjugation CD spectra of all Cyt *c* variants mirrored that of Cyt *c* in its reduced form, suggesting an inherent reduction process during functionalisation. The structural alterations observed in Cyt *c* upon functionalisation with AuNPs can likely be attributed to its interactions with AuNPs. This theory is supported by the pronounced structural changes evident when using MUA as a SAM, as Cyt *c* resides much closer to the AuNPs' surface than when using thiol-PEG-carboxyl as a SAM. It is this proximity which potentially leads to electrostatic interactions between the amino acids of Cyt *c* and the electron rich AuNPs. However, a notable drawback of employing metallic NPs, including AuNPs, is their electron rich

surface which can inadvertently influence protein structure—a challenge not typically encountered with polymeric NPs or vesicles.

The ToF-SIMS analyses confirmed the orientation of Cyt *c* upon conjugation, with a majority retaining their orientation, as previously documented. Any deviations were linked more to the ligand, specifically MUA, than the conjugation technique itself, again suggesting influence from the AuNPs on Cyt *c*. A significant challenge presented by this system stemmed from the electron rich nature of AuNPs combined with the redox-active nature of Cyt *c* and Zn Porph R, which resulted in considerable noise during CV. This made it difficult to discern accurate redox peaks. To navigate this challenge, this work details a novel DPV approach to accurately identify redox peaks and combines equations to enable the calculation of electron transfer rates. The latter providing insights into the effects of conjugation to AuNPs on the redox capabilities of Cyt *c* and Zn Porph. The electron transfer rates for Cyt *c*, represented by k^0 values, did show reductions after conjugation, presumably from observed structural alterations. Zn Porph remained largely unaffected. Despite these variations, the enduring redox capabilities of both Cyt *c* and Zn Porph post-conjugation suggest their potential application for hypothesised light-triggered activation was still a possibility.

5.2.3. Chapter 4 - Biological Studies on MCF-7 Cells after Incubation of Gold Nanoparticles Functionalised with Cyt C and Zinc Porphyrin

In Chapter 4, the efficacy of the multifunctionalised AuNP cancer treatment in inducing cellular death is assessed. The uptake dynamics of the multifunctionalised AuNPs into MCF-7 cells showed that while covalent conjugation methods did lead to a reduced uptake, especially for smaller AuNPs, the conjugation method did not hamper the overarching goal, as every type of the multifunctionalised AuNPs were internalised by the cells, to varying degrees of success. This was visually confirmed through confocal microscopy, where no AuNPs were found adhered to the outer cellular surface.

Peroxidase assays showed an interesting correlation emergence between the peroxide activity of Cyt *c* and the diameter of AuNP. As the size of the AuNPs increased, there was a consistent elevation in the peroxide activity of Cyt *c*. This opens the possibility that either the heme ring of Cyt *c* becomes more accessible when conjugated to larger AuNPs, or that the intrinsic properties of larger AuNPs augment the peroxidase activity of Cyt *c*.

A significant limitation of this AuNP system was its continual interference with the PrestoBlue assay, causing misleading indications of cellular metabolic activity even in the absence of cells. This interference appears to stem from the electron-rich nature of the AuNPs. Such complications could potentially be sidestepped with the use of alternative NPs, such as polymeric NPs which exhibit this characteristic.

The effectiveness of the cancer treatment detailed in this work was evidenced in a live/dead study using fluorescence microscopy. The study illustrated a notable decrease in the live cell percentage following a 60-minute treatment with the amber LED array, using 20, 50, and 100 nm AuNPs multifunctionalised with Cyt *c* and Zn Porph. As all the multifunctionalised AuNPs produced an effective treatment, neither the heterogeneous rate constant nor the orientation of Cyt *c* conjugated to the multifunctionalised AuNPs can be shown to have a marked impact on the treatment's apoptotic capabilities.

In summarising these findings, it is evident that when functionalised with Cyt *c* and Zn Porph, AuNPs not only successfully infiltrate MCF-7 cells but when activated via an amber light source, they pose as a potent agent in inducing cellular death. This work ultimately provides a basis for a cancer treatment that can be initiated wirelessly.

5.3. Future Work

This research did ultimately achieve the goals it set out in synthesising and functionalising AuNPs that can initiate cell death when triggered via light, however, there are still many routes to be explored in gaining a deeper understanding of the mechanism involved in the

initiation of Cyt *c* by Zn Porph. Whilst optimising the treatment for more effective cell killing is of key importance.

Developing a way to actively target cancer cells was initially a key aspect of this project but due to the effects of COVID-19 the lab time was negatively impacted, the extended delivery times of items (the result of Covid-19 and BREXIT) after lab work was resumed compounded the effects of the reduced lab time and so the active targeting approach had to be abandoned and just rely on the passive targeting observed as a result of EPR in cancer cells. The targeting method hypothesised was simple, boronic acid has been previously shown to reversibly interact with the diol group found in sugars, sialic acid is a sugar residue that is upregulated on 40-60% of cancer cell types and is classed as a key indicator of the disease. The interaction between boronic acids and sialic acid has been previously reported for its potential in targeted cancer treatment (Matsumoto et al., 2017, Dobie and Skropeta, 2021, Khan et al., 2020). For the system described in this work Zn Porph would be decorated with 3 boronic acid groups and one amino group (for conjugation) with the intention that when functionalised on AuNPs would bind to the sialic acids upregulated on the surface of cancer cells to increase internalisation of the multifunctionalised AuNPs into cells. No supplier was found that could supply a porphyrin of this description with a Zn atom at the centre of the porphyrin ring and the synthesis and purification would have taken too long due to the restricted lab time , however it would have been a great addition to this work.

The lab time restrictions affected the biological work as more work in regard to the metabolic assay and caspase 3 assay would have provided useful data. The metabolic assay data shown in this work may have been influenced by the fluorescence of Zn Porph as a small emission was observed in the same region used on the plate reader for the assay so it would have been useful to compare the results from the presto blue assay to the MTT assay. Conducting the caspase 3 assays would have helped to confirm if the cell death mechanism was apoptosis or if it was caused by another mechanism. Caspase 3 is a part of the apoptotic cascade so its presence is increase when a cell undergoes apoptosis (Butterick et al., 2014), this would have been a useful assay so the mechanism could be

definitively confirmed instead of hypothesised. Previous work in the Rawson group has shown that the caspase 3 activity of in U251 cells increased after Cyt *c* conjugated to AuNPs were internalised into the cells.

During the functionalisation process the goal was to conjugate as much Cyt *c* as possible to ensure that a large amount of Cyt *c* was being delivered to each cell, working on the hypothesis that there must be a threshold that needs to be supposed to initiate the apoptotic process. A recent paper by the Rawson group (Jain et al., 2023) used a much lower concentration of Cyt *c* per AuNP to maintain a monolayer and was still able to initiate cellular death (using electricity rather than light), therefore, an interesting piece of future work would be to modulate the concentration of Cyt *c* conjugated to AuNPs to find the threshold of Cyt *c* required to initiate apoptosis in cells.

Another aspect that could be looked at in the future is the role of the metal ion at the centre of the porphyrin ring, by changing the ion a more optimised apoptosis initiator may be found.

For a more comprehensive biological study different cell line could be used in the future to assess if the treatment is as effective as it was in MCF-7 cells. This would then lead to a better understanding of the mechanisms that are taking place when the treatment is initiated with a light source. Using more cell lines would also increase researchers confidence in the treatment potentially enabling real world application of the treatment.

5.4. Conclusion

The work detailed in this thesis shows the potential of AuNPs functionalised with Cyt *c* and Zn Porph for a novel cancer treatment. The treatment utilises the apoptotic ability of Cyt *c* when bound to AuNPs and internalised in cancer cells, monochromatic light triggers the initiation of cell death.

The AuNPs used in this work were synthesised at sizes 20, 50, and 100 nm. The subsequent functionalisation with Cyt *c* and Zn Porph using different ligands and conjugation methods was then characterised using DLS, Zeta potential, UV-Vis absorption spectroscopy, TEM and XPS confirming the structural integrity and successful conjugation. A novel method to deconvolute UV-Vis absorption spectra was developed to enable accurate Cyt *c* and Zn Porph quantification.

The next part of the study analysed the electrochemical characteristics of Cyt *c* and Zn Porph before and after conjugation to AuNPs. It was revealed that Cyt *c* underwent significant structural changes when conjugated to AuNPs, with thiol-PEG-carboxyl-functionalised AuNPs causing the least alterations. Contrary to expectations, covalent bonding methods resulted in fewer changes than electrostatic methods. The choice of ligand, especially MUA, heavily influenced these structural adjustments and the density of arrangement on AuNPs. Following attachment, k^0 values of Cyt *c* declined, but those of Zn Porph remained stable. Notably, the redox properties of both Cyt *c* and Zn Porph remained post-AuNP conjugation.

The final part of this work was assessing if the multifuntionalised AuNPs when added to MCF-7 cells could induce cell death when activated via monochromatic light. ICP-MS revealed that using covalent bonding techniques decreased the amount of AuNPs in each cell, particularly with smaller-sized AuNPs. Yet, confocal imaging revealed successful internalisation of the multifunctionalised AuNPs, with none remaining externally on the cell surface. .The peroxidase activity of Cyt *c* displayed a direct correlation with increasing AuNP size. This suggests either a heightened accessibility to the heme ring of Cyt *c* when conjugated to larger AuNPs or an inherent capability of the larger AuNPs to enhance the peroxidase activity of Cyt *c*. The PrestoBlue assay results indicated potential interference due to fluorescence amplification by smaller AuNPs, rendering it possibly unsuitable for this research. A live/dead analysis highlighted the effectiveness of AuNPs with Cyt *c* and Zn Porph in significantly reducing the live cell count upon light exposure. However, neither the rate constant nor the orientation of Cyt *c* on the AuNPs was found to play a substantial role in this cell-killing effect.

.

This thesis establishes a foundational framework for a wireless cancer treatment harnessing the capabilities of Cyt *c*, revealing significant potential for targeted cell death activation. There remains ample opportunity to refine this treatment, particularly in calibrating the precise concentrations of Cyt c and Zn Porph to ascertain the optimal therapeutic dosage. The primary objective—to create a wirelessly activated nanoparticle system for efficient cancer cell eradication—has been achieved. It is the aspiration that this research will not only contribute meaningfully to the realm of oncology but also pave the way for advancements in innovative cancer therapies.

6. Supporting Information

Table SI 1: The wavelength of the Surface Plasma Resonance peaks in relationship to the size of the AuNPs (Haiss et al., 2007).

λspr / nm	**d / nm**	**λspr / nm**	**d / nm**	**λspr / nm**	**d / nm**
525.0	32	534.9	58	552.1	84
525.6	34	535.9	60	553.8	86
526.2	36	536.9	62	555.7	88
526.8	38	538.0	64	557.6	90
527.5	40	539.2	66	559.6	92
528.2	42	540.4	68	561.7	94
528.9	44	541.6	70	563.9	96
529.6	46	542.9	72	566.2	98
530.4	48	544.3	74	568.6	100
531.2	50	545.7	76	571.1	102
532.1	52	547.2	78	573.7	104
533.0	54	548.8	80	576.5	106
533.9	56	550.4	82	579.3	108

Table SI 2: The relationship between AuNPs diameter and extinction coefficient (Haiss et al., 2007).

d / nm	ε_{450} / $M^{-1}cm^{-1}$	d / nm	ε_{450} / $M^{-1}cm^{-1}$	d / nm	ε_{450} / $M^{-1}cm^{-1}$
2	4.25E+05	35	3.21E+09	68	2.50E+10
3	1.49E+06	36	3.52E+09	69	2.61E+10
4	3.62E+06	37	3.84E+09	70	2.71E+10
5	7.20E+06	38	4.18E+09	71	2.82E+10
6	1.26E+07	39	4.54E+09	72	2.93E+10
7	2.03E+07	40	4.92E+09	73	3.05E+10
8	3.07E+07	41	5.32E+09	74	3.16E+10
9	4.43E+07	42	5.74E+09	75	3.28E+10
10	6.15E+07	43	6.18E+09	76	3.40E+10
11	8.27E+07	44	6.65E+09	77	3.52E+10
12	1.09E+08	45	7.13E+09	78	3.64E+10
13	1.39E+08	46	7.65E+09	79	3.77E+10
14	1.76E+08	47	8.18E+09	80	3.89E+10
15	2.18E+08	48	8.74E+09	81	4.02E+10
16	2.67E+08	49	9.32E+09	82	4.14E+10
17	3.24E+08	50	9.92E+09	83	4.27E+10
18	3.87E+08	51	1.06E+10	84	4.40E+10
19	4.60E+08	52	1.12E+10	85	4.53E+10
20	5.41E+08	53	1.19E+10	85	4.53E+10
21	6.31E+08	54	1.26E+10	86	4.65E+10
22	7.31E+08	55	1.33E+10	87	4.78E+10
23	8.42E+08	56	1.41E+10	88	4.91E+10
24	9.64E+08	57	1.48E+10	89	5.04E+10
25	1.10E+09	58	1.57E+10	90	5.17E+10
26	1.24E+09	59	1.65E+10	91	5.30E+10
27	1.40E+09	60	1.73E+10	92	5.43E+10
28	1.58E+09	61	1.82E+10	93	5.56E+10
29	1.76E+09	62	1.91E+10	94	5.69E+10
30	1.96E+09	63	2.00E+10	95	5.82E+10
31	2.18E+09	64	2.10E+10	96	5.94E+10
32	2.41E+09	65	2.19E+10	97	6.07E+10
33	2.66E+09	66	2.29E+10	98	6.19E+10
34	2.93E+09	67	2.40E+10	99	6.31E+10
35	3.21E+09	68	2.50E+10	100	6.44E+10

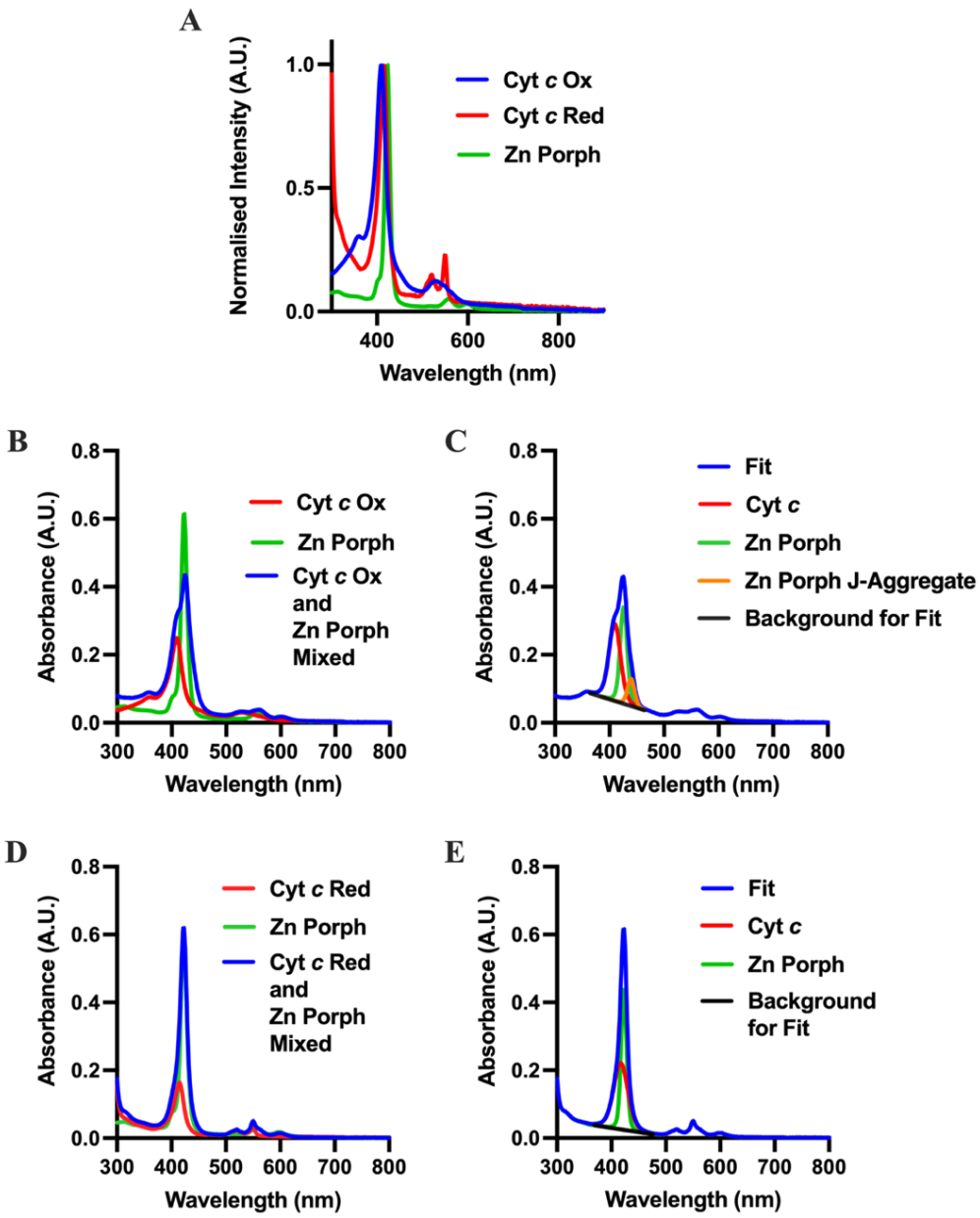


Figure SI 1. Ultraviolet-Visible absorption spectra of (A) Cyt *c* Ox, Cyt *c* Red and Zn Porph free in solution with normalized intensity. (B) Cyt *c* Ox and Zn Porph mixed and independently free in solution at 2.5 mM. (C) Cyt *c* Red and Zn Porph mixed and independently free in solution at 2.5 mM. (D) Deconvolution and fitted spectra of Cyt *c* Ox and Zn Porph mixed to reveal hidden spectra of Cyt *c* and Zn Porph individual components. (E) Deconvolution and fitted spectra of Cyt *c* Red and Zn Porph mixed to reveal hidden spectra of Cyt *c* and Zn Porph individual components.

Table SI 3. AuNP, Cyt *c* and Zn Porph concentration and number of molecules calculated from the UV-Vis absorption spectra of Figure 15A and B

	AuNP		**Cyt C**				**Zn Porph/Porph**				
Sample	Concentration (nM)	Number of Molecules	Concentration (μM)	Number of Molecules	Number Per AuNP	Percentage Coverage (%)	Concentration (μM)	Number of Molecules	No. of molecules Per AuNP	Free Zn Porph Concentration (μM)	Percentage Coverage (%)
20 nm AuNP-PEG-*Cyt* c /Zn Porph (Figure 15A **)**	1.21	$7.30x10^{14}$	0.42	$2.53x10^{17}$	346	29.22 346 /(SA=4026.39 nm^2/3.4 nm (diameter of Cyt *C*))	1.30	$7.83x10^{17}$	1073	-	42.64 1073 /(SA=4026.39 nm^2/1.6 nm (maximum width of Zn Porph))
20 nm AuNP-PEG-Cyt *c*/Zn Porph-S2 (Figure 15B**)**	0.26	$1.55x10^{14}$	0.40	$2.40x10^{17}$	1545	130.46 1545/ (SA=4026.39 nm^2/3.4 nm (diameter of Cyt *C*))	1.16	$6.99x10^{17}$	4500	1.11	178.82 4500/ (SA=4026.39 nm^2/1.6 nm (maximum width of Zn Porph))
50 nm AuNP-PEG-Cyt *c*/Porph(Figure 24)	0.0096	$5.79x10^{12}$	0.11	$6.73x10^{16}$	23259	581.39 (SA=13601.97 nm^2/3.4 nm (diameter of Cyt *C*))/23259	0.17	$1.02x10^{17}$	35168		413.68 35168/(SA=13601.97 nm^2/1.6 nm (maximum width of Zn Porph))

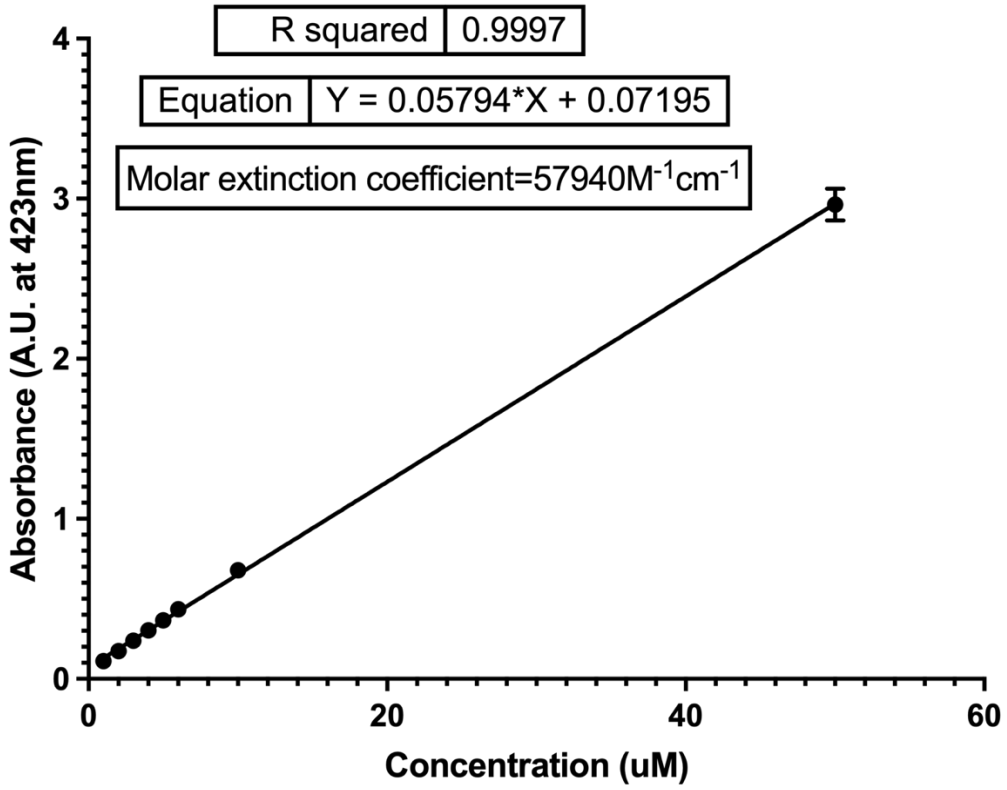


Figure SI 2. The concentration plot used to calculate the extinction coefficient of Zn Porph

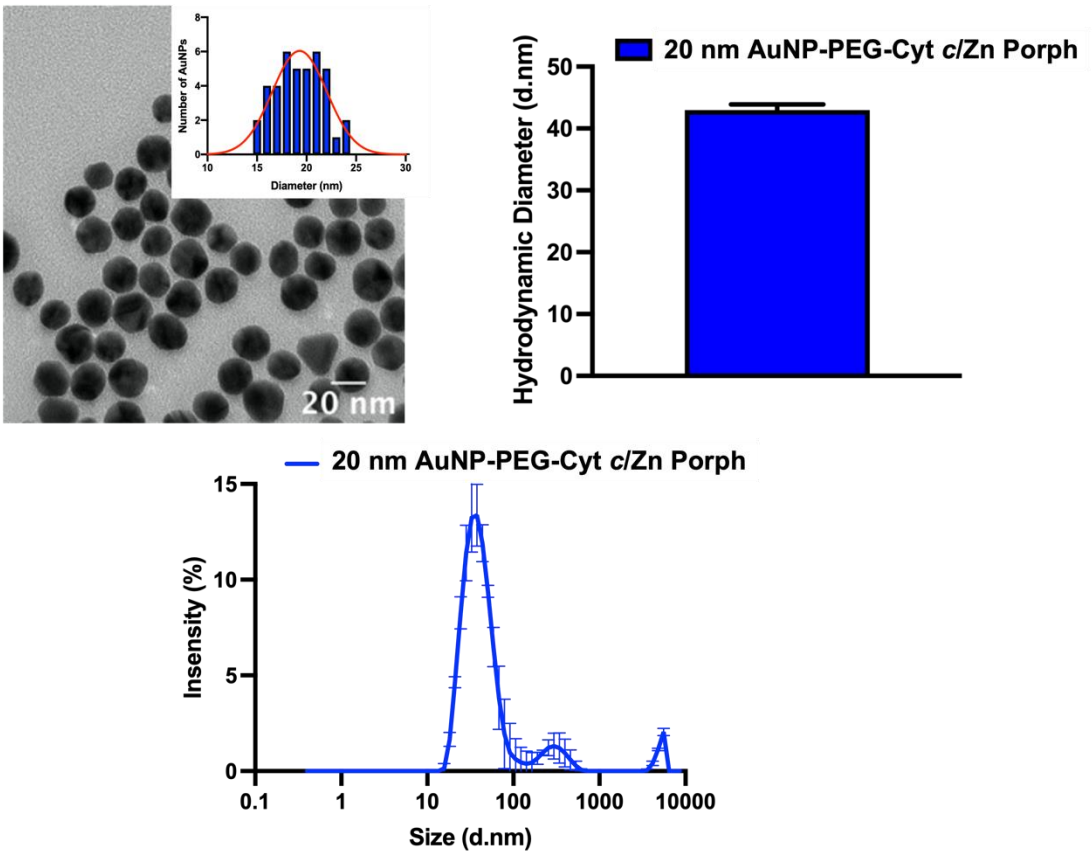


Figure SI 3. Physico-chemical characterization of 20 nm AuNP-PEG-Cyt *c*/Zn Porph-S2 from Figure 15B with TEM and cumulative frequency distribution calculated from 40 AuNPs (A), DLS average diameter (B) and DLS intensity profile (C).

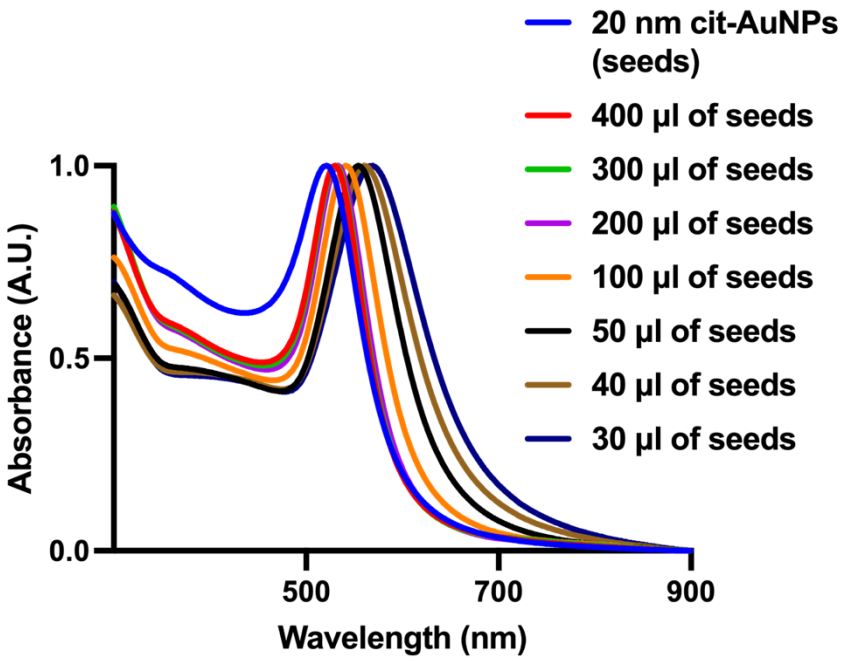


Figure SI 4. UV-Visible absorption spectra of AuNPs synthesised by adding different volumes of 20 nm cit-AuNP seeds (A). Visual representation of the colour change observed from the synthesised AuNPs as the volume of seeds was decreased from 400 µL (left) to 30 µL (right) (B).

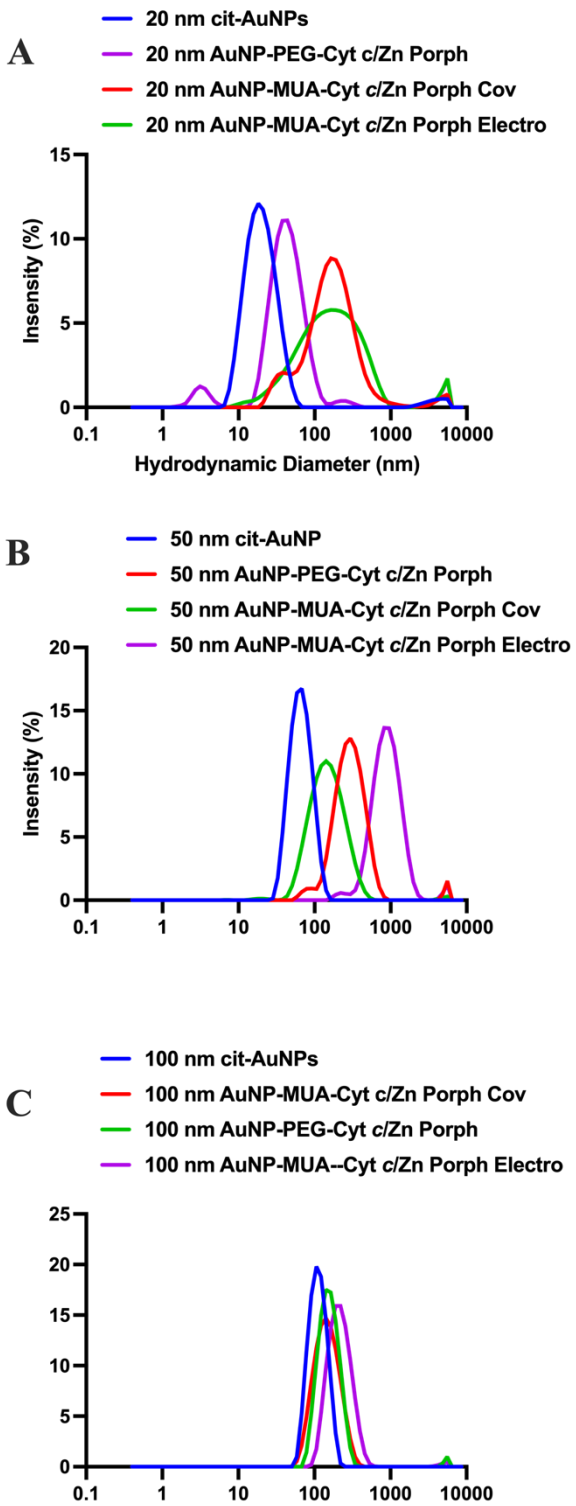


Figure SI 5: Hydrodynamic diameter of 20 nm (A), 50 nm (B) and 100 nm (C) AuNPs before and after functionalisation.

Table SI 4. Size and concentration of synthesised AuNPs calculated from the UV-Vis absorption spectra from Figure SI 4 (Haiss et al., 2007).

SPR	Size (nm)	Volume of 20 nm cit-AuNPs (μL)
521	17	-
529	45	400
530	47	300
532	52	200
541	69	100
554	87	50
560	93	40
569	101	30

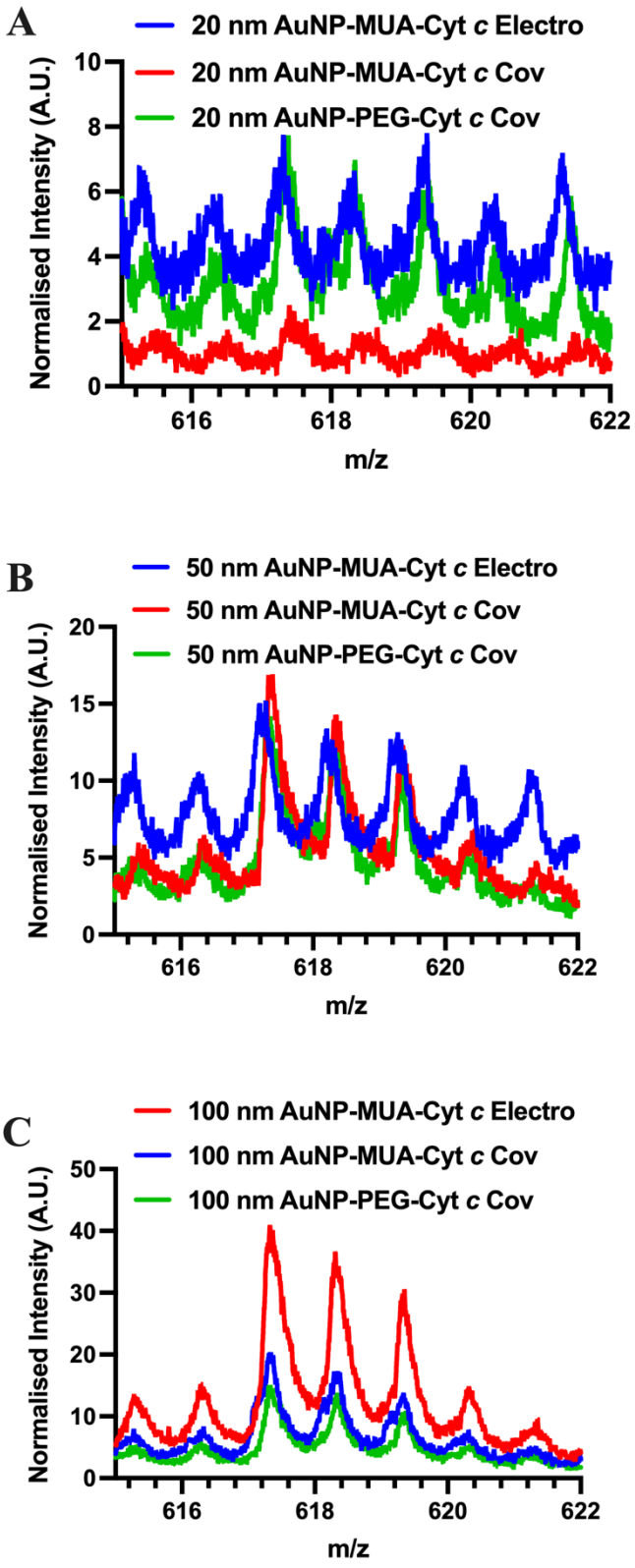


Figure SI 6. ToF-SIMS peak intensities spectra from heme ring fragment of Cyt *c* bound multifunctionalised AuNP sample.

Table SI 5: Concentration of Cyt *c* oxidised and Zn Porph bound to multifunctionalised AuNPs of various sizes and conjugated using different mechanisms, were determined. The concentration of Cyt *c* was normalised in the samples to 2 μM.

Sample	Average Concentration of Cyt *c* (μμM)	Average Concentration of Zn Porph (μM)
20 nm AuNP-PEG-Cyt c/Zn Porph Ox	2	1.47
20 nm AuNP-MUA-Cyt c/Zn Porph Cov Ox	2	23.3
20 nm AuNP-MUA-Cyt c/Zn Porph Ox Electro	2	5.56
50 nm AuNP-PEG-Cyt c/Zn Porph Ox	2	3.21
50 nm AuNP-MUA-Cyt c/Zn Porph Ox Cov	2	17.36
50 nm AuNP-MUA-Cyt c/Zn Porph Ox Electro	2	2.29
100 nm AuNP-PEG-Cyt c/Zn Porph Ox	2	5.04
100 nm AuNP-MUA-Cyt c/Zn Porph Cov Ox	2	7.94
100 nm AuNP-MUA-Cyt c/Zn Porph Ox Electro	2	31.80
Cyt *c*	2	-
Zn Porph	-	2

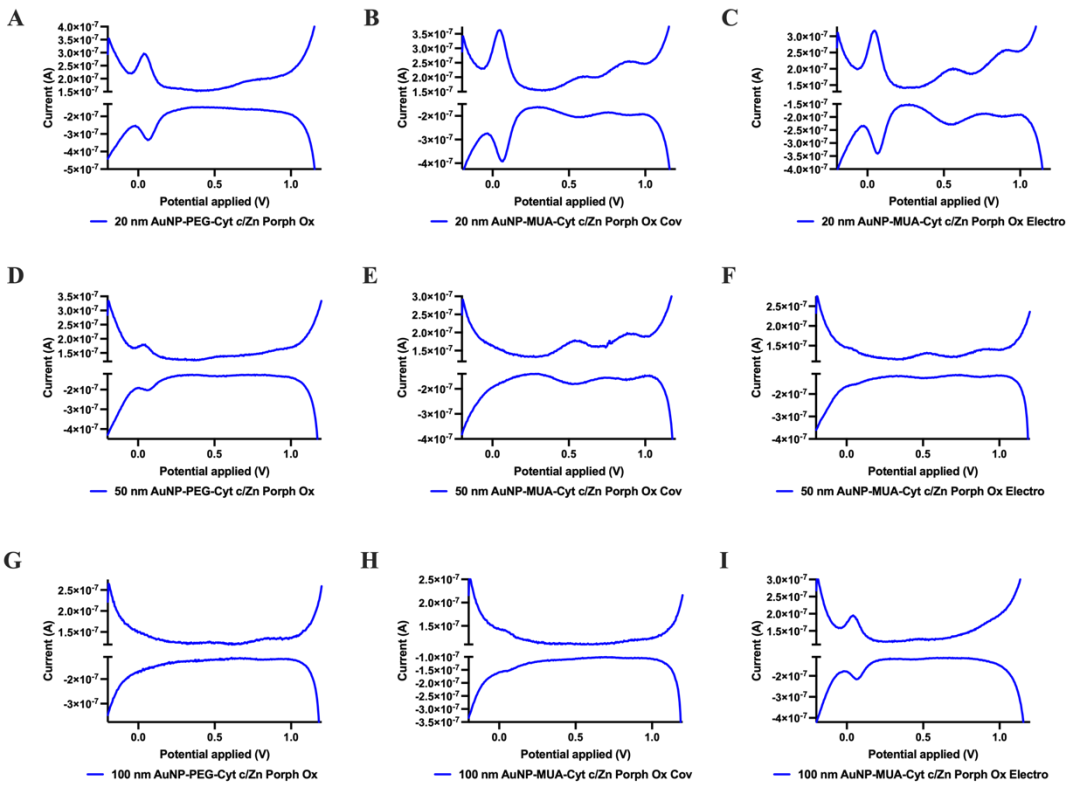


Figure SI 7. DPV of 20, 50 and 100 nm AuNPs multifucntionalised with Cyt *c* and Zn Porph using thiol-PEG-carboxyl covalently and MUA covalently and electrostatically. 20 nm AuNP-PEG-Cyt *c*/Zn Porph Ox (A), 20 nm AuNP-MUA-Cyt *c*/Zn Porph Ox Cov (B), 20 nm AuNP-MUA-Cyt *c*/Zn Porph Ox Electro (C), 50 nm AuNP-PEG-Cyt *c*/Zn Porph Ox (D), 50 nm AuNP-MUA-Cyt *c*/Zn Porph Ox Cov (E), 50 nm AuNP-MUA-Cyt *c*/Zn Porph Ox Electro (F), 100 nm AuNP-PEG-Cyt *c*/Zn Porph Ox (G), 100 nm AuNP-MUA-Cyt *c*/Zn Porph Ox Cov (H) and 20 nm AuNP-MUA-Cyt *c*/Zn Porph Ox Electro (I).

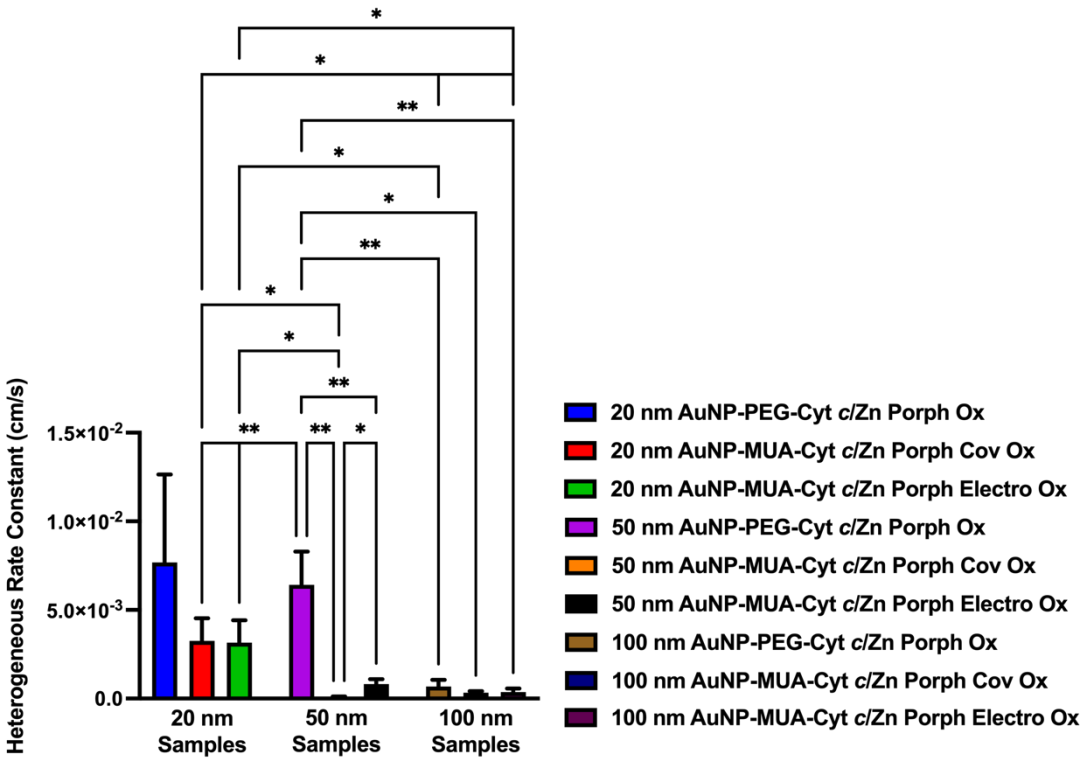


Figure SI 8. Heterogenous rate constant (k^0) of Cyt *c* oxidised conjugated to multifunctionalised AuNPs with Zn Porph. AuNPs of 20, 50 and 100 nm were functionalised with different ligands and conjugations methods. The k^0 values were compared to each other using a one-way ANOVA with a post-Tukey test . Determined by DPV.

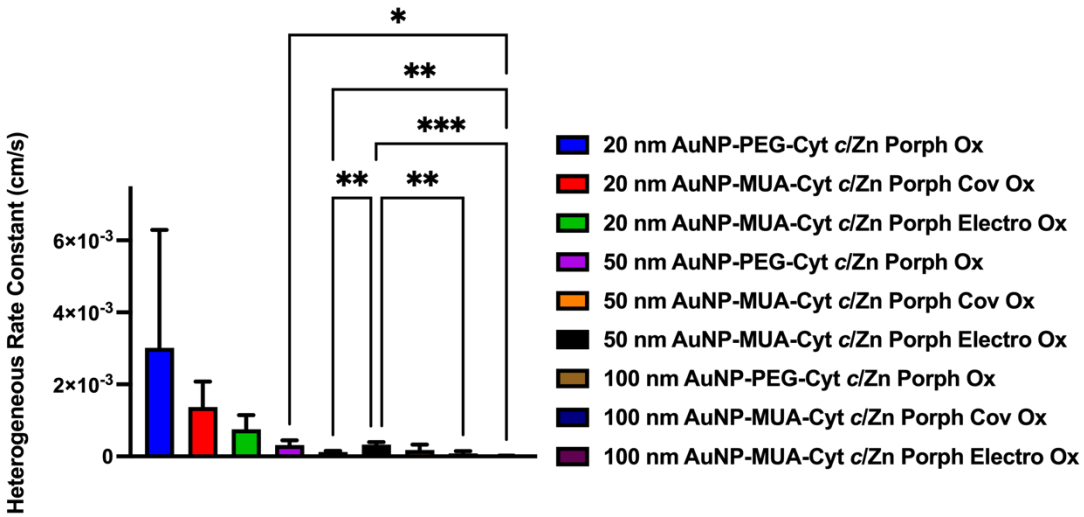


Figure SI 9. Heterogenous rate constant (k^0) of Zn Porph conjugated to multifunctionalised AuNPs with Zn Porph. AuNPs of 20, 50 and 100 nm were functionalised with different ligands and conjugations methods. The k^0 values were compared to each other using a one-way ANOVA with a post-Tukey test . Determined by DPV.

Table SI 6: Mass of Au calculated via ICP-MS of multifunctionalised AuNPs with Cyt *c* and Zn Porph conjugated using HS-PEG-COOH from

Figure 39A.

Sample	Mass of Au (μg)	Number of AuNPs in cells	Number of AuNPs per cell
20 nm AuNP-PEG-Cyt *c*/Zn Porph Ox	0.09 ± 0.02	1.13 x 10^9	7001
50 nm AuNP-PEG-Cyt *c*/Zn Porph Ox	1.43 ± 0.38	1.13 x 10^9	7025
100 nm AuNP-PEG-Cyt *c*/Zn Porph Ox	2.98 ± 1.07	2.95 x 10^8	1828
20 nm AuNP-PEG-Cyt *c*/Zn Porph Ox Supernatant	2.76 ± 0.25	-	-
50 nm AuNP-PEG-Cyt *c*/Zn Porph Ox Supernatant	0.91 ± 0.25	-	-

100 nm AuNP-PEG-Cyt *c*/Zn Porph Ox Supernatant	0.90 ± 0.07	-	-

Table SI 7: Mass of Au calculated via ICP-MS of multifunctionalised AuNPs with Cyt *c* and Zn Porph conjugated using MUA covalently from

Figure 39B.

Sample	Mass of Au (μg)	Number of AuNPs in cells	Number of AuNPs per cell
20 nm AuNP-MUA-Cyt *c*/Zn Porph Ox Cov	0.11 ± 0.04	1.37×10^9	6828
50 nm AuNP-MUA-Cyt *c*/Zn Porph Ox Cov	2.01 ± 0.00	1.59×10^9	7960
100 nm AuNP-MUA-Cyt *c*/Zn Porph Ox Cov	14.24 ± 1.64	1.41×10^9	7046
20 nm AuNP-MUA-Cyt *c*/Zn Porph Ox Cov Supernatant	4.37 ± 1.98	-	-
50 nm AuNP-MUA-Cyt *c*/Zn Porph Ox Cov Supernatant	2.67 ± 1.14	-	-
100 nm AuNP-MUA-Cyt *c*/Zn Porph Ox Cov Supernatant	1.21 ± 0.07	-	-

Table SI 8: Mass of Au calculated via ICP-MS of multifunctionalised AuNPs with Cyt *c* and Zn Porph conjugated using MUA covalently from

Figure 39C. Controls of 20, 50 and 100 nm cit-AuNPs were also included from Figure 39C.

Sample	Mass of Au (μg)	Number of AuNPs in cells	Number of AuNPs per cell
20 nm AuNP-MUA-Cyt *c*/Zn Porph Ox Electro	10.00 ± 3.81	1.24×10^{11}	853073
50 nm AuNP-MUA-Cyt *c*/Zn Porph Ox Electro	16.56 ± 5.61	1.31×10^{10}	90412
100 nm AuNP-MUA-Cyt *c*/Zn Porph Ox Electro	11.84 ± 2.57	1.17×10^{9}	8080
20 nm AuNP-MUA-Cyt *c*/Zn Porph Ox Cov Supernatant	1.83 ± 0.16	-	-
50 nm AuNP-MUA-Cyt *c*/Zn Porph Ox Electro Supernatant	1.15 ± 0.26	-	-
100 nm AuNP-MUA-Cyt *c*/Zn Porph Ox Electro Supernatant	2.09 ± 2.04	-	-
20 nm cit-AuNP	15.14	-	-
50 nm cit-AuNP	19.77	-	-
100 nm cit-AuNPs	17.62	-	-

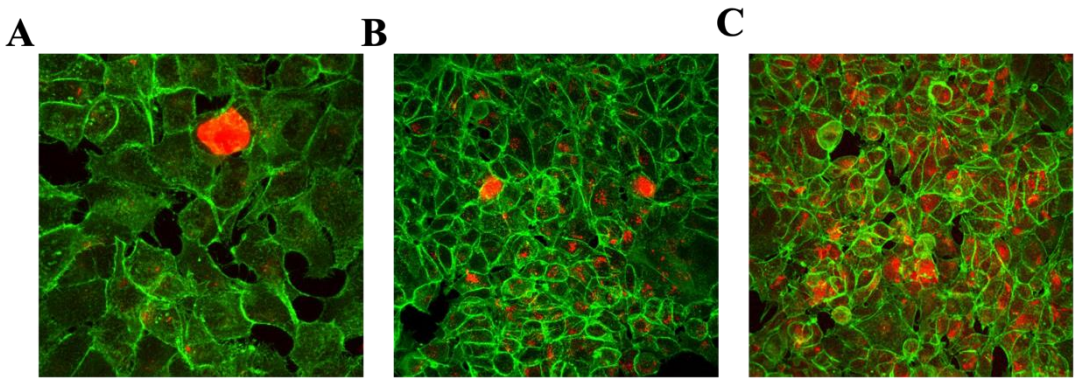


Figure SI 10: Z-stack overlay for maximum intensity for 20 nm AuNP-PEG-Cyt *c*/Zn Porph (A), 20 nm AuNP-MUA-Cyt *c*/Zn Porph Cov (B) and 20 nm AuNP-MUA-Cyt *c*/Zn Porph Electro (C).

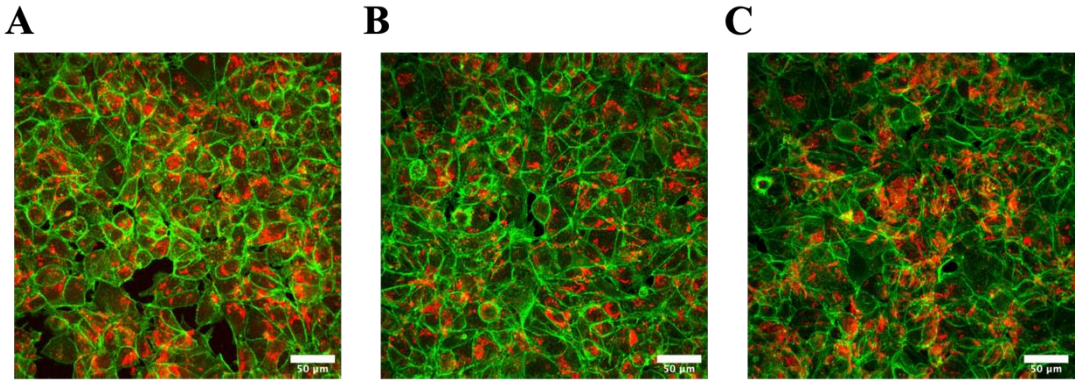


Figure SI 11: Z-stack overlay for maximum intensity for 50 nm AuNP-PEG-Cyt *c*/Zn Porph (A), 50 nm AuNP-MUA-Cyt *c*/Zn Porph Cov (B) and 50 nm AuNP-MUA-Cyt *c*/Zn Porph Electro (C).

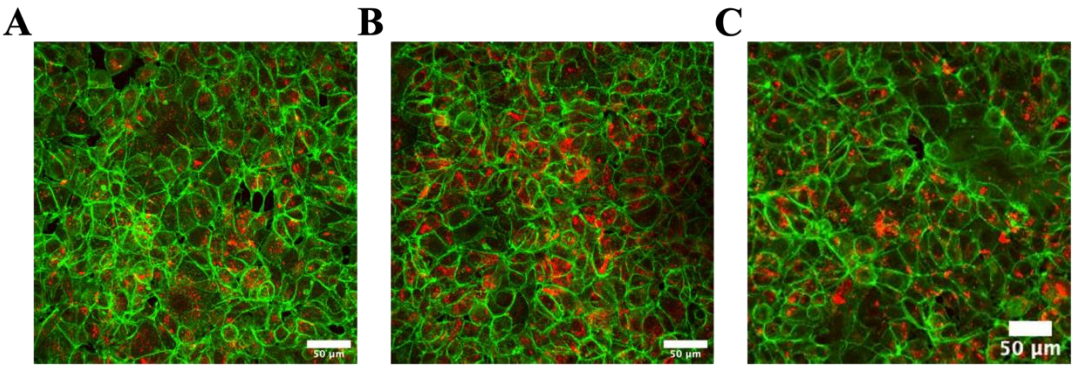


Figure SI 12: Z-stack overlay for maximum intensity for 100 nm AuNP-PEG-Cyt *c*/Zn Porph (A), 100 nm AuNP-MUA-Cyt *c*/Zn Porph Cov (B) and 100 nm AuNP-MUA-Cyt *c*/Zn Porph Electro (C).

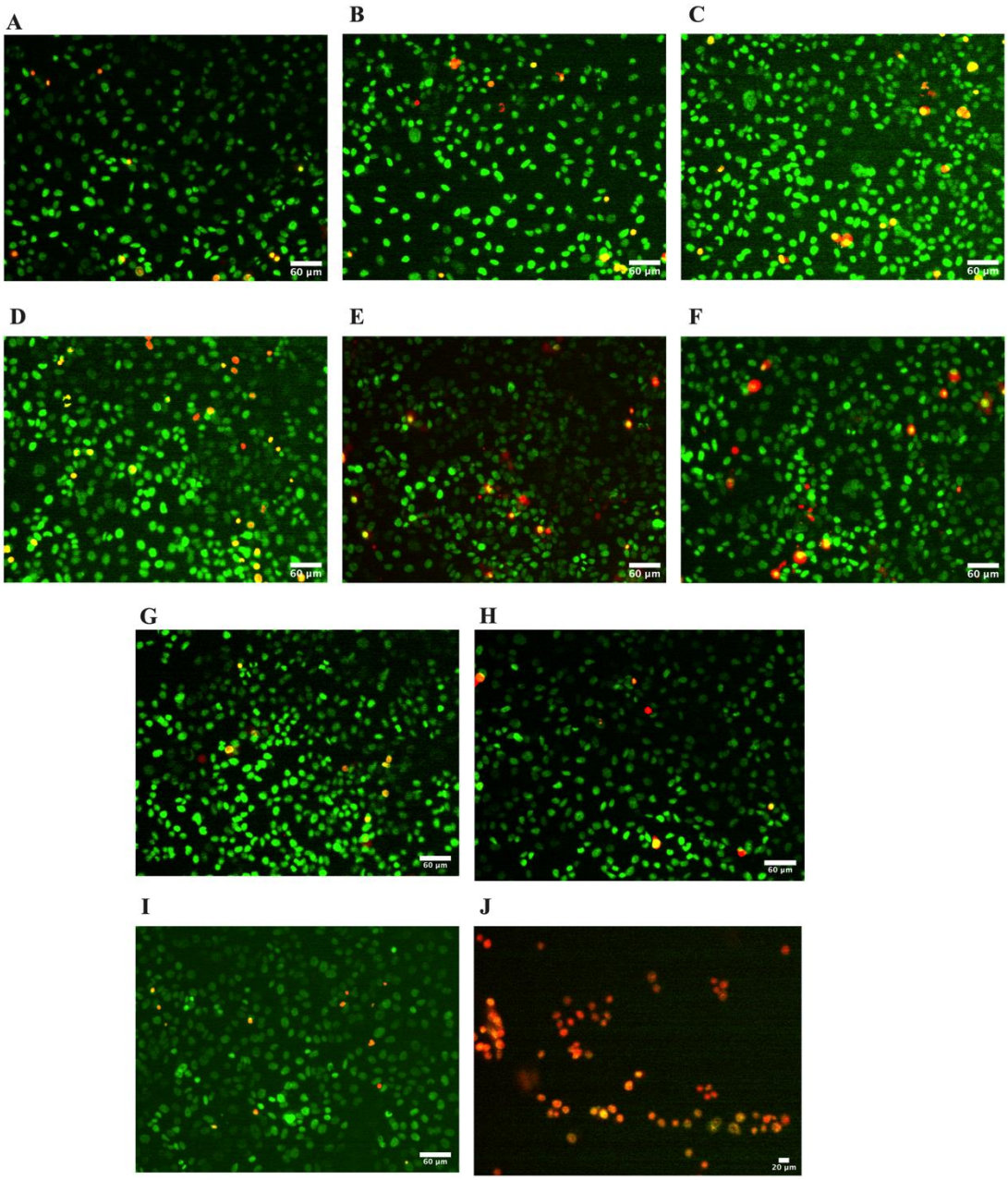


Figure SI 13. Fluorescence microscopy images of Live/Dead determination of MCF-7 cells containing AuNP-PEG-Cyt *c*/Zn Porph Ox normalised AuNPs at 20 µg/mL, before treatment. 20 nm AuNP-PEG-Cyt *c*/Zn Porph (A), 50 nm AuNP-PEG-Cyt *c*/Zn Porph (B), 100 nm AuNP-PEG-Cyt *c*/Zn Porph (C), 20 nm cit-AuNP (D), 50 nm cit-AuNP (E), 100 nm cit-AuNP (F), Cyt *c* 1 µM (G), Zn Porph 1 µM (H), Live control MCF-7 cells (I) and dead control MCF-7 cells.

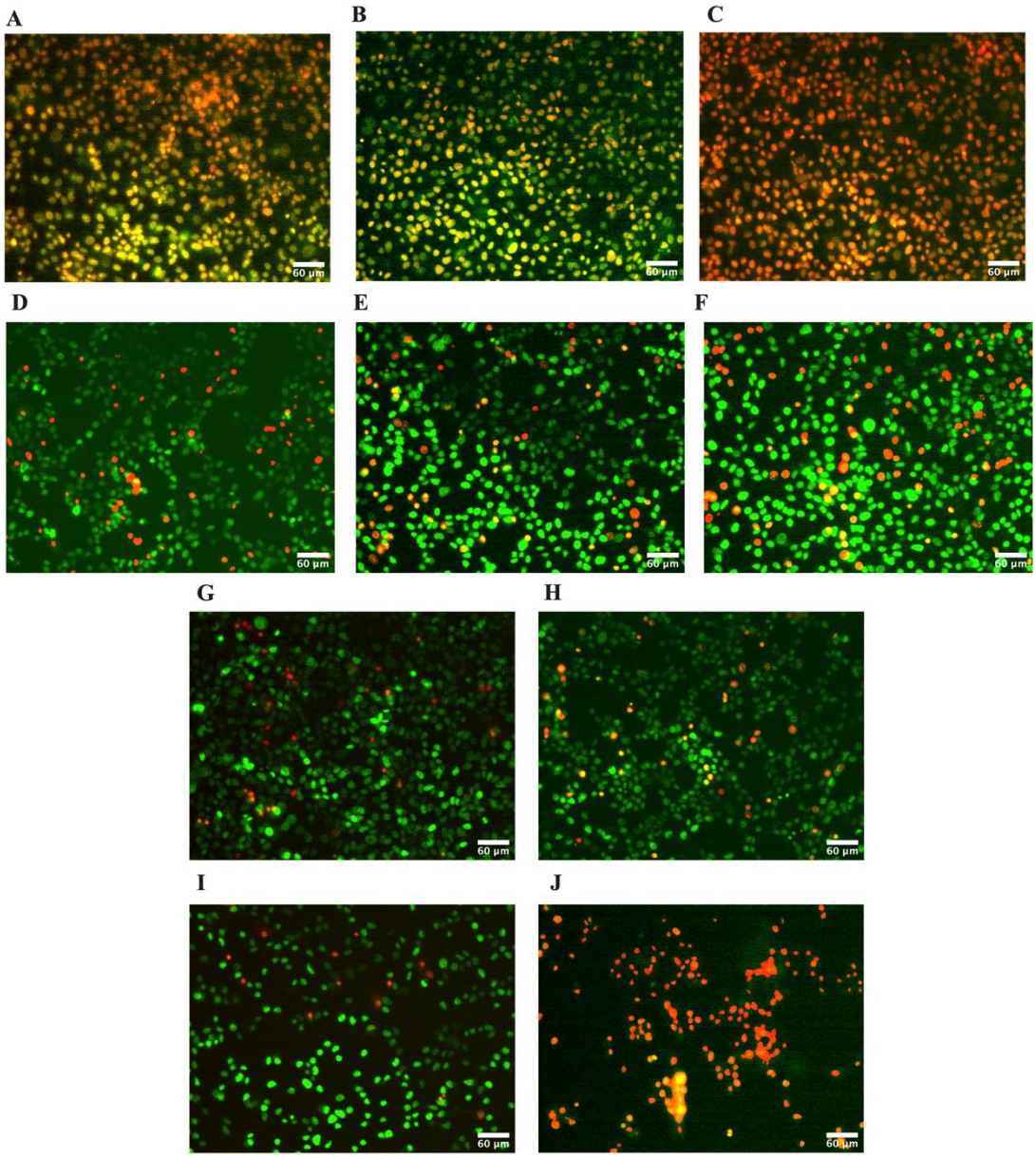


Figure SI 14. Fluorescence microscopy images of Live/Dead determination of MCF-7 cells containing AuNP-PEG-Cyt *c*/Zn Porph Ox normalised for AuNPs at 20 µg/mL after treatment with monochromatic Amber light from Lumidox® II 96-position Amber LED array at 55 mW for 60 minuets. 20 nm AuNP-PEG-Cyt *c*/Zn Porph (A), 50 nm AuNP-PEG-Cyt *c*/Zn Porph (B), 100 nm AuNP-PEG-Cyt *c*/Zn Porph (C), 20 nm cit-AuNP (D), 50 nm cit-AuNP (E), 100 nm cit-AuNP (F), Cyt *c* 1 µM (G), Zn Porph 1 µM (H), Live control MCF-7 cells (I) and dead control MCF-7 cells.

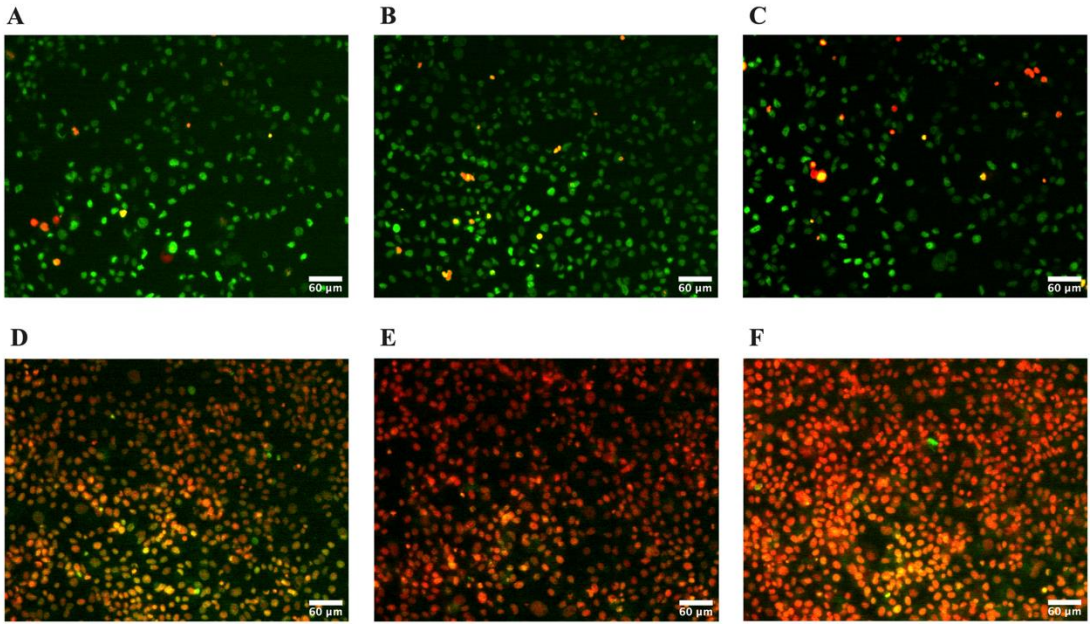


Figure SI 15. Fluorescence microscopy images of Live/Dead determination of MCF-7 cells containing AuNP-MUA-Cyt *c*/Zn Porph Ox covalently conjugated, normalised for AuNPs at 20 µg/mL before and after treatment with monochromatic Amber light from Lumidox® II 96-position Amber LED array at 55 mW for 60 minutes. Before treatment, 20 nm AuNP-MUA-Cyt *c*/Zn Porph Ox Cov (A), 50 nm AuNP-MUA-Cyt *c*/Zn Porph Ox Cov (B), 100 nm AuNP-MUA-Cyt *c*/Zn Porph Ox Cov (C). After treatment, 20 nm AuNP-MUA-Cyt *c*/Zn Porph Ox Cov (D), 50 nm AuNP-MUA-Cyt *c*/Zn Porph Ox Cov (E) and 100 nm AuNP-MUA-Cyt *c*/Zn Porph Ox Cov (F). Controls are included in Figure SI 13 and Figure SI 14.

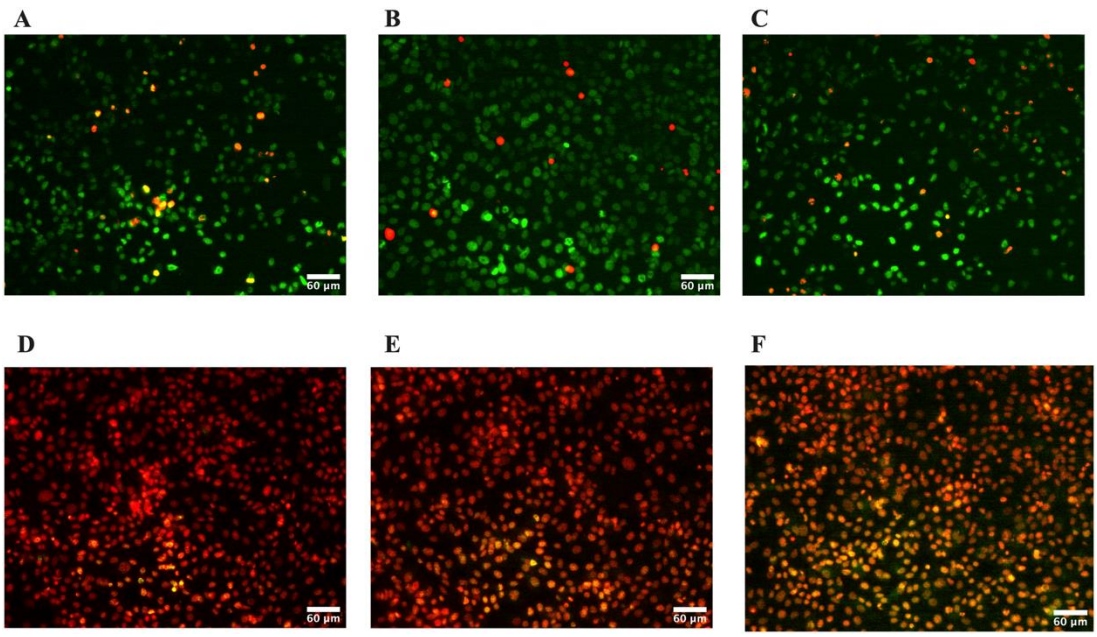


Figure SI 16. Fluorescence microscopy images of Live/Dead determination of MCF-7 cells containing AuNP-MUA-Cyt *c*/Zn Porph Ox electrostatically conjugated, normalised for AuNPs at 20 µg/mL before and after treatment with monochromatic Amber light from Lumidox® II 96-position Amber LED array at 55 mW for 60 minutes. Before treatment, 20 nm AuNP-MUA-Cyt *c*/Zn Porph Electro (A), 50 nm AuNP-MUA-Cyt *c*/Zn Porph Electro (B), 100 nm AuNP-MUA-Cyt *c*/Zn Porph Electro (C). After treatment, 20 nm AuNP-MUA-Cyt *c*/Zn Porph Electro (D), 50 nm AuNP-PEG-Cyt *c*/Zn Porph Electro (E) and 100 nm AuNP-PEG-Cyt *c*/Zn Porph Electro (F). Controls are included in Figure SI 13 and Figure SI 14.

7. References

ABRAHAMSE, H. & HAMBLIN, M. R. 2016. New photosensitizers for photodynamic therapy. *The Biochemical journal,* 473**,** 347-364.

AGHAMIRI, Z. S., MOHSENNIA, M. & RAFIEE-POUR, H.-A. 2018. Immobilization of cytochrome c and its application as electrochemical biosensors. *Talanta,* 176**,** 195-207.

AGHEBATI-MALEKI, A., DOLATI, S., AHMADI, M., BAGHBANZHADEH, A., ASADI, M., FOTOUHI, A., YOUSEFI, M. & AGHEBATI-MALEKI, L. 2020. Nanoparticles and cancer therapy: Perspectives for application of nanoparticles in the treatment of cancers. *Journal of cellular physiology,* 235**,** 1962-1972.

AIKENS, C. M. 2018. Electronic and Geometric Structure, Optical Properties, and Excited State Behavior in Atomically Precise Thiolate-Stabilized Noble Metal Nanoclusters. *Accounts of Chemical Research,* 51**,** 3065-3073.

AL-NASIRY, S., GEUSENS, N., HANSSENS, M., LUYTEN, C. & PIJNENBORG, R. 2007. The use of Alamar Blue assay for quantitative analysis of viability, migration and invasion of choriocarcinoma cells. *Human reproduction,* 22**,** 1304-1309.

AL-SHAKARCHI, W., ALSURAIFI, A., ABED, M., ABDULLAH, M., RICHARDSON, A., CURTIS, A. & HOSKINS, C. 2018. Combined Effect of Anticancer Agents and Cytochrome C Decorated Hybrid Nanoparticles for Liver Cancer Therapy. *Pharmaceutics,* 10**,** 48.

ALARGOVA, R. G., BHATT, K. H., PAUNOV, V. N. & VELEV, O. D. 2004. Scalable Synthesis of a New Class of Polymer Microrods by a Liquid–Liquid Dispersion Technique. *Advanced Materials,* 16**,** 1653-1657.

ALBANESE, A., TANG, P. S. & CHAN, W. C. 2012. The effect of nanoparticle size, shape, and surface chemistry on biological systems. *Annual review of biomedical engineering,* 14**,** 1-16.

ALBERTS, B. 2017. *Molecular Biology of the Cell*, W.W. Norton.

ALEA-REYES, M. E., PENON, O., GARCÍA CALAVIA, P., MARÍN, M. J., RUSSELL, D. A. & PÉREZ-GARCÍA, L. 2018. Synthesis and in vitro phototoxicity of multifunctional Zn(II)meso-tetrakis(4-carboxyphenyl)porphyrin-coated gold nanoparticles assembled via axial coordination with imidazole ligands. *Journal of Colloid and Interface Science,* 521**,** 81-90.

ALI, E. S., SHARKER, S. M., ISLAM, M. T., KHAN, I. N., SHAW, S., RAHMAN, M. A., UDDIN, S. J., SHILL, M. C., REHMAN, S., DAS, N., AHMAD, S., SHILPI, J. A., TRIPATHI, S., MISHRA, S. K. & MUBARAK, M. S. 2021. Targeting cancer cells with nanotherapeutics and nanodiagnostics: Current status and future perspectives. *Seminars in cancer biology,* 69**,** 52-68.

ALVAREZ-PAGGI, D., HANNIBAL, L., CASTRO, M. A., OVIEDO-ROUCO, S., DEMICHELI, V., TÓRTORA, V., TOMASINA, F., RADI, R. & MURGIDA, D. H. 2017. Multifunctional Cytochrome c: Learning New Tricks from an Old Dog. *Chemical Reviews,* 117**,** 13382-13460.

ALYOUSEF, H., ALOTAIBI, B. M., BEN YAHIA, M., ALANAZI, M. M. & ALSAIF, N. A. 2021. New insights on microscopic properties of metal-

porphyrin complexes attached to quartz crystal sensor. *Scientific Reports,* 11**,** 8316.
AMENDOLA, V. & MENEGHETTI, M. 2009. Size Evaluation of Gold Nanoparticles by UV−vis Spectroscopy. *The Journal of Physical Chemistry C,* 113**,** 4277-4285.
AMENDOLA, V., PILOT, R., FRASCONI, M., MARAGÒ, O. M. & IATÌ, M. A. 2017. Surface plasmon resonance in gold nanoparticles: a review. *Journal of Physics: Condensed Matter,* 29**,** 203002.
ANNADHASAN, M., KASTHURI, J. & RAJENDIRAN, N. 2015. Green synthesis of gold nanoparticles under sunlight irradiation and their colorimetric detection of Ni 2+ and Co 2+ ions. *RSC Advances,* 5**,** 11458-11468.
ARRUEBO, M., VILABOA, N., SÁEZ-GUTIERREZ, B., LAMBEA, J., TRES, A., VALLADARES, M. & GONZÁLEZ-FERNÁNDEZ, A. 2011. Assessment of the evolution of cancer treatment therapies. *Cancers,* 3**,** 3279-3330.
ASLAN, B., OZPOLAT, B., SOOD, A. K. & LOPEZ-BERESTEIN, G. 2013. Nanotechnology in cancer therapy. *Journal of drug targeting,* 21**,** 904-913.
AUGUSTINE, R., HASAN, A., PRIMAVERA, R., WILSON, R. J., THAKOR, A. S. & KEVADIYA, B. D. 2020. Cellular uptake and retention of nanoparticles: Insights on particle properties and interaction with cellular components. 25**,** 101692.
AVISHEK CHAKRABORTY AND ANKITA DAS AND SREYAN RAHA AND ANANYA, B. 2020. Size-dependent apoptotic activity of gold nanoparticles on osteosarcoma cells correlated with SERS signal. *Journal of Photochemistry and Photobiology B: Biology,* 203**,** 111778.
BAIO, J. E., WEIDNER, T., RAMEY, D., PRUZINSKY, L. & CASTNER, D. G. 2013. Probing the orientation of electrostatically immobilized cytochrome C by time of flight secondary ion mass spectrometry and sum frequency generation spectroscopy. *Biointerphases,* 8**,** 18.
BAKER JR, J. R. 2009. Dendrimer-based nanoparticles for cancer therapy. *ASH Education Program Book,* 2009**,** 708-719.
BALTRUSAITIS, J., USHER, C. R. & GRASSIAN, V. H. 2007. Reactions of sulfur dioxide on calcium carbonate single crystal and particle surfaces at the adsorbed water carbonate interface. *Physical Chemistry Chemical Physics,* 9**,** 3011-3024.
BARCELO-BOVEA, V., DOMINGUEZ-MARTINEZ, I., JOAQUIN-OVALLE, F., AMADOR, L. A., CASTRO-RIVERA, E., MEDINA-ÁLVAREZ, K., MCGORON, A., GRIEBENOW, K. & FERRER-ACOSTA, Y. 2020. Optimization and Characterization of Protein Nanoparticles for the Targeted and Smart Delivery of Cytochrome c to Non-Small Cell Lung Carcinoma. *Cancers (Basel),* 12.
BARD, A. J. & FAULKNER, L. R. 2002. *Electrochemical Methods: Fundamentals and Applicaitons, 2e Student Solutions Manual*, Wiley.
BARD, A. J., FAULKNER, L. R. & WHITE, H. S. 2022. *Electrochemical Methods: Fundamentals and Applications*, Wiley.
BARFIDOKHT, A., CIAMPI, S., LUAIS, E., DARWISH, N. & GOODING, J. J. 2013. Distance-Dependent Electron Transfer at Passivated Electrodes Decorated by Gold Nanoparticles. *Analytical Chemistry,* 85**,** 1073-1080.
BATHINAPATLA, A., KANCHI, S., SINGH, P., SABELA, M. I. & BISETTY, K. 2016. An ultrasensitive performance enhanced novel cytochrome c biosensor

for the detection of rebaudioside A. *Biosensors and Bioelectronics,* 77**,** 116-123.
BATRAKOVA, E. V. & KIM, M. S. 2015. Using exosomes, naturally-equipped nanocarriers, for drug delivery. *Journal of Controlled Release,* 219**,** 396-405.
BELU, A. M., GRAHAM, D. J. & CASTNER, D. G. 2003. Time-of-flight secondary ion mass spectrometry: techniques and applications for the characterization of biomaterial surfaces. *Biomaterials,* 24**,** 3635-3653.
BERA, K., MAITI, S., MAITY, M., MANDAL, C. & MAITI, N. C. 2018. Porphyrin-Gold Nanomaterial for Efficient Drug Delivery to Cancerous Cells. *ACS omega,* 3**,** 4602-4619.
BERNARDINI, S., TIEZZI, A., LAGHEZZA MASCI, V. & OVIDI, E. 2018. Natural products for human health: an historical overview of the drug discovery approaches. *Natural product research,* 32**,** 1926-1950.
BHALLA, N., JOLLY, P., FORMISANO, N. & ESTRELA, P. 2016. Introduction to biosensors. *Essays Biochem,* 60**,** 1-8.
BIEDULSKA, M., JAKÓBCZYK, P., SOSNOWSKA, M., DEC, B., MUCHLIŃSKA, A., ZACZEK, A. J., NIDZWORSKI, D. & BOGDANOWICZ, R. 2021. Cytocompatibility of stabilized black phosphorus nanosheets tailored by directly conjugated polymeric micelles for human breast cancer therapy. *Scientific Reports,* 11**,** 9304.
BOBER, Z., BARTUSIK-AEBISHER, D. & AEBISHER, D. 2022. Application of Dendrimers in Anticancer Diagnostics and Therapy. *Molecules,* 27.
BRANDENBERGER, C., MÜHLFELD, C., ALI, Z., LENZ, A.-G., SCHMID, O., PARAK, W. J., GEHR, P. & ROTHEN-RUTISHAUSER, B. 2010. Quantitative Evaluation of Cellular Uptake and Trafficking of Plain and Polyethylene Glycol-Coated Gold Nanoparticles. *Small,* 6**,** 1669-1678.
BRAY, F., LAVERSANNE, M., WEIDERPASS, E. & SOERJOMATARAM, I. 2021. The ever-increasing importance of cancer as a leading cause of premature death worldwide. *Cancer,* 127**,** 3029-3030.
BROWN, G. C. & BORUTAITE, V. 2008. Regulation of apoptosis by the redox state of cytochrome c. *Biochimica et Biophysica Acta (BBA) - Bioenergetics,* 1777**,** 877-881.
BRUST, M., WALKER, M., BETHELL, D., SCHIFFRIN, D. J. & WHYMAN, R. 1994. Synthesis of thiol-derivatised gold nanoparticles in a two-phase Liquid–Liquid system. *Journal of the Chemical Society, Chemical Communications***,** 801-802.
BUTTERICK, T. A., DUFFY, C. M., LEE, R. E., BILLINGTON, C. J., KOTZ, C. M. & NIXON, J. P. 2014. Use of a caspase multiplexing assay to determine apoptosis in a hypothalamic cell model. *J Vis Exp*.
CAESAR, C. E. B., ESBJÖRNER, E. K., LINCOLN, P. & NORDÉN, B. 2009. Assigning membrane binding geometry of cytochrome C by polarized light spectroscopy. *Biophysical journal,* 96**,** 3399-3411.
CAI, J., YANG, J. & JONES, D. 1998. Mitochondrial control of apoptosis: the role of cytochrome c. *Biochimica et Biophysica Acta (BBA) - Bioenergetics,* 1366**,** 139-149.
CARNOVALE, C., BRYANT, G., SHUKLA, R. & BANSAL, V. 2019. Identifying Trends in Gold Nanoparticle Toxicity and Uptake: Size, Shape, Capping Ligand, and Biological Corona. *ACS Omega,* 4**,** 242-256.
CASALETTO, M. P., LONGO, A., MARTORANA, A., PRESTIANNI, A. & VENEZIA, A. M. 2006. XPS study of supported gold catalysts: the role of

Au0 and Au+δ species as active sites. *Surface and Interface Analysis,* 38**,** 215-218.
CASTNER, D. G., HINDS, K. & GRAINGER, D. W. 1996. X-ray photoelectron spectroscopy sulfur 2p study of organic thiol and disulfide binding interactions with gold surfaces. *Langmuir,* 12**,** 5083-5086.
CHAKRABORTY, S. & RAHMAN, T. 2012. The difficulties in cancer treatment. *Ecancermedicalscience,* 6**,** ed16.
CHAUDHURI, A., BATTAGLIA, G. & GOLESTANIAN, R. 2011. The effect of interactions on the cellular uptake of nanoparticles. *Physical biology,* 8**,** 046002.
CHAUVET, A. A. P., AL HADDAD, A., KAO, W.-C., VAN MOURIK, F., HUNTE, C. & CHERGUI, M. 2015. Photo-induced dynamics of the heme centers in cytochrome bc1. *Physical Chemistry Chemical Physics,* 17**,** 2143-2151.
CHEN, F., LI, X., HIHATH, J., HUANG, Z. & TAO, N. 2006. Effect of Anchoring Groups on Single-Molecule Conductance: Comparative Study of Thiol-, Amine-, and Carboxylic-Acid-Terminated Molecules. *Journal of the American Chemical Society,* 128**,** 15874-15881.
CHEN, H., KOU, X., YANG, Z., NI, W. & WANG, J. 2008. Shape-and size-dependent refractive index sensitivity of gold nanoparticles. *Langmuir,* 24**,** 5233-5237.
CHEN, X., FERRIGNO, R., YANG, J. & WHITESIDES, G. M. 2002. Redox Properties of Cytochrome c Adsorbed on Self-Assembled Monolayers: A Probe for Protein Conformation and Orientation. *Langmuir,* 18**,** 7009-7015.
CHENG, Z., LI, M., DEY, R. & CHEN, Y. 2021. Nanomaterials for cancer therapy: current progress and perspectives. *Journal of Hematology & Oncology,* 14**,** 85.
CHITHRANI, B. D., GHAZANI, A. A. & CHAN, W. C. 2006. Determining the size and shape dependence of gold nanoparticle uptake into mammalian cells. *Nano letters,* 6**,** 662-668.
COLLEONI, M., SUN, Z., PRICE, K. N., KARLSSON, P., FORBES, J. F., THÜRLIMANN, B., GIANNI, L., CASTIGLIONE, M., GELBER, R. D., COATES, A. S. & GOLDHIRSCH, A. 2016. Annual Hazard Rates of Recurrence for Breast Cancer During 24 Years of Follow-Up: Results From the International Breast Cancer Study Group Trials I to V. *J Clin Oncol,* 34**,** 927-35.
COLLINSON, M., BOWDEN, E. F. & TARLOV, M. J. 1992. Voltammetry of covalently immobilized cytochrome c on self-assembled monolayer electrodes. *Langmuir,* 8**,** 1247-1250.
COMPTON, R. G. & BANKS, C. E. 2018. *Understanding voltammetry,* World Scientific.
COMSA, S., CIMPEAN, A. M. & RAICA, M. 2015. The Story of MCF-7 Breast Cancer Cell Line: 40 years of Experience in Research. *Anticancer Res,* 35**,** 3147-54.
CONNER, S. D. & SCHMID, S. L. 2003. Regulated portals of entry into the cell. *Nature,* 422**,** 37-44.
CORRALES, D. G., ROJAS, N. F., VINDAS, G. S., MUÑOZ, M. S., ROJAS, M. C., BRENES, D. M., SALAS, M. F. R. & REDONDO, G. M. 2022. Dendrimers and their applications. *Journal of Drug Delivery and Therapeutics,* 12**,** 151-158.

DANAEI, M., DEHGHANKHOLD, M., ATAEI, S., HASANZADEH DAVARANI, F., JAVANMARD, R., DOKHANI, A., KHORASANI, S. & MOZAFARI, M. R. 2018. Impact of Particle Size and Polydispersity Index on the Clinical Applications of Lipidic Nanocarrier Systems. *Pharmaceutics,* 10.

DAS, S. K., MENEZES, M. E., BHATIA, S., WANG, X. Y., EMDAD, L., SARKAR, D. & FISHER, P. B. 2015. Gene therapies for cancer: strategies, challenges and successes. *Journal of cellular physiology,* 230**,** 259-271.

DE JONG, W. H. & BORM, P. J. 2008. Drug delivery and nanoparticles:applications and hazards. *Int J Nanomedicine,* 3**,** 133-49.

DE VOLDER, M. F. L., TAWFICK, S. H., BAUGHMAN, R. H. & HART, A. J. 2013. Carbon Nanotubes: Present and Future Commercial Applications. *Science,* 339**,** 535-539.

DEBELA, D. T., MUZAZU, S. G., HERARO, K. D., NDALAMA, M. T., MESELE, B. W., HAILE, D. C., KITUI, S. K. & MANYAZEWAL, T. 2021. New approaches and procedures for cancer treatment: Current perspectives. *SAGE Open Med,* 9**,** 20503121211034366.

DELINOIS, L. J., DE LEÓN-VÉLEZ, O., VÁZQUEZ-MEDINA, A., VÉLEZ-CABRERA, A., MARRERO-SÁNCHEZ, A., NIEVES-ESCOBAR, C., ALFONSO-CANO, D., CARABALLO-RODRÍGUEZ, D., RODRIGUEZ-ORTIZ, J., ACOSTA-MERCADO, J., BENJAMÍN-RIVERA, J. A., GONZÁLEZ-GONZÁLEZ, K., FERNÁNDEZ-ADORNO, K., SANTIAGO-PAGÁN, L., DELGADO-VERGARA, R., TORRES-ÁVILA, X., MASER-FIGUEROA, A., GRAJALES-AVILÉS, G., MÉNDEZ, G. I. M., SANTIAGO-PAGÁN, J., NIEVES-SANTIAGO, M., ÁLVAREZ-CARRILLO, V., GRIEBENOW, K. & TINOCO, A. D. 2021. Cytochrome c: Using Biological Insight toward Engineering an Optimized Anticancer Biodrug. *Inorganics,* 9**,** 83.

DEVIA, A., BENAVIDES, V., CASTILLO, H. A. & QUINTERO, J. 2006. Effects of the Substrate Temperature in AuN Thin Films by Means of X-Ray Diffraction. *AIP Conference Proceedings,* 875**,** 258-261.

DHIMAN, H. K., RAY, A. R. & PANDA, A. K. 2004. Characterization and evaluation of chitosan matrix for in vitro growth of MCF-7 breast cancer cell lines. *Biomaterials,* 25**,** 5147-5154.

DOBIE, C. & SKROPETA, D. 2021. Insights into the role of sialylation in cancer progression and metastasis. *British Journal of Cancer,* 124**,** 76-90.

DONG, X., SUN, Z., WANG, X. & LENG, X. 2017. An innovative MWCNTs/DOX/TC nanosystem for chemo-photothermal combination therapy of cancer. *Nanomedicine: Nanotechnology, Biology and Medicine,* 13**,** 2271-2280.

DOUGLAS, K. L., PICCIRILLO, C. A. & TABRIZIAN, M. 2008. Cell line-dependent internalization pathways and intracellular trafficking determine transfection efficiency of nanoparticle vectors. *European Journal of Pharmaceutics and Biopharmaceutics,* 68**,** 676-687.

DUMBRAVA, E. I. & MERIC-BERNSTAM, F. 2018. Personalized cancer therapy-leveraging a knowledge base for clinical decision-making. *Cold Spring Harb Mol Case Stud,* 4.

DYKMAN, L. A. & KHLEBTSOV, N. G. 2011. Gold nanoparticles in biology and medicine: recent advances and prospects. *Acta naturae,* 3**,** 34-55.

ECK, M. 2014. *Performance enhancement of hybrid nanocrystal-polymer bulk heterojunction solar cells : aspects of device efficiency, reproducibility, and stability.*
ECKERMANN, A. L., FELD, D. J., SHAW, J. A. & MEADE, T. J. 2010. Electrochemistry of redox-active self-assembled monolayers. *Coord Chem Rev,* 254**,** 1769-1802.
ELGRISHI, N., ROUNTREE, K. J., MCCARTHY, B. D., ROUNTREE, E. S., EISENHART, T. T. & DEMPSEY, J. L. 2018. A Practical Beginner's Guide to Cyclic Voltammetry. *Journal of Chemical Education,* 95**,** 197-206.
ELLIOTT, A. D. 2020. Confocal Microscopy: Principles and Modern Practices. *Curr Protoc Cytom,* 92**,** e68.
EMA, M., GAMO, M. & HONDA, K. 2017. A review of toxicity studies on graphene-based nanomaterials in laboratory animals. *Regulatory Toxicology and Pharmacology,* 85**,** 7-24.
ESCUDERO-FRANCOS, M. A., CEPAS, V., GONZALEZ-MENENDEZ, P., BADÍA-LAÍÑO, R., DIAZ-GARCIA, M. E., SAINZ, R. M., MAYO, J. C. & HEVIA, D. 2017. Cellular uptake and tissue biodistribution of functionalized gold nanoparticles and nanoclusters. *Journal of Biomedical Nanotechnology,* 13**,** 167-179.
FERRARI, M. 2005. Cancer nanotechnology: opportunities and challenges. *Nature reviews cancer,* 5**,** 161-171.
FISHER, W. R., TANIUCHI, H. & ANFINSEN, C. B. 1973. On the Role of Heme in the Formation of the Structure of Cytochrome c. *Journal of Biological Chemistry,* 248**,** 3188-3195.
FONIN, A. V., SULATSKAYA, A. I., KUZNETSOVA, I. M. & TUROVEROV, K. K. 2014. Fluorescence of dyes in solutions with high absorbance. Inner filter effect correction. *PloS one,* 9**,** e103878-e103878.
FRANCISCO, A. P., BOTEQUIM, D., PRAZERES, D. M. F., SERRA, V. V., COSTA, S. M. B., LAIA, C. A. T. & PAULO, P. M. R. 2019. Extreme Enhancement of Single-Molecule Fluorescence from Porphyrins Induced by Gold Nanodimer Antennas. *The Journal of Physical Chemistry Letters,* 10**,** 1542-1549.
FU, G., LIU, W., FENG, S. & YUE, X. 2012. Prussian blue nanoparticles operate as a new generation of photothermal ablation agents for cancer therapy. *Chemical communications,* 48**,** 11567-11569.
FUJITA, Y. & MYERS, J. 1965. Light-induced cytochrome c redox reactions by a cell-free preparation of Anabaena cylindrica. *Archives of Biochemistry and Biophysics,* 112**,** 519-523.
FULTON, M. D. & NAJAHI-MISSAOUI, W. 2023. Liposomes in Cancer Therapy: How Did We Start and Where Are We Now. *Int J Mol Sci,* 24.
GAO, H., SHI, W. & FREUND, L. B. 2005. Mechanics of receptor-mediated endocytosis. *Proceedings of the National Academy of Sciences,* 102**,** 9469-9474.
GARAB, G. & VAN AMERONGEN, H. 2009. Linear dichroism and circular dichroism in photosynthesis research. *Photosynth Res,* 101**,** 135-46.
GARCÍA CALAVIA, P., BRUCE, G., PÉREZ-GARCÍA, L. & RUSSELL, D. A. 2018. Photosensitiser-gold nanoparticle conjugates for photodynamic therapy of cancer. *Photochem Photobiol Sci,* 17**,** 1534-1552.

GARRIDO, C., GALLUZZI, L., BRUNET, M., PUIG, P. E., DIDELOT, C. & KROEMER, G. 2006. Mechanisms of cytochrome c release from mitochondria. *Cell Death And Differentiation,* 13**,** 1423.
GEISSLE, D., NIRMALANANTHAN-BUDAU, N., SCHOLTZ, L., TAVERNARO, I. & RESCH-GENGER, U. 2021. Analyzing the surface of functional nanomaterials—how to quantify the total and derivatizable number of functional groups and ligands. *Microchimica Acta,* 188**,** 321.
GIBSON, J. D., KHANAL, B. P. & ZUBAREV, E. R. 2007. Paclitaxel-functionalized gold nanoparticles. *Journal of the American Chemical Society,* 129**,** 11653-11661.
GOENKA, S., SANT, V. & SANT, S. 2014. Graphene-based nanomaterials for drug delivery and tissue engineering. *Journal of Controlled Release,* 173**,** 75-88.
GOTTSTEIN, C., WU, G., WONG, B. J. & ZASADZINSKI, J. A. 2013. Precise Quantification of Nanoparticle Internalization. *ACS Nano,* 7**,** 4933-4945.
GRAY, E. P., COLEMAN, J. G., BEDNAR, A. J., KENNEDY, A. J., RANVILLE, J. F. & HIGGINS, C. P. 2013. Extraction and Analysis of Silver and Gold Nanoparticles from Biological Tissues Using Single Particle Inductively Coupled Plasma Mass Spectrometry. *Environmental Science & Technology,* 47**,** 14315-14323.
GREENFIELD, N. J. 2006. Using circular dichroism spectra to estimate protein secondary structure. *Nat Protoc,* 1**,** 2876-90.
GRIMSLEY, G. R. & PACE, C. N. 2004. Spectrophotometric determination of protein concentration. *Curr Protoc Protein Sci,* Chapter 3**,** Unit 3.1.
GROSVENOR, A. P., KOBE, B. A., BIESINGER, M. C. & MCINTYRE, N. S. 2004. Investigation of multiplet splitting of Fe 2p XPS spectra and bonding in iron compounds. *Surface and Interface Analysis,* 36**,** 1564-1574.
GUO, C., WANG, J., CHEN, X., LI, Y., WU, L., ZHANG, J. & TAO, C.-A. 2018. Construction of a Biosensor Based on a Combination of Cytochrome c, Graphene, and Gold Nanoparticles. *Sensors,* 19.
HA, C. E. & BHAGAVAN, N. V. 2023. Chapter 4 - Three-dimensional structure of proteins and disorders of protein misfolding. *In:* HA, C. E. & BHAGAVAN, N. V. (eds.) *Essentials of Medical Biochemistry (Third Edition).* San Diego: Academic Press.
HAISS, W., THANH, N. T. K., AVEYARD, J. & FERNIG, D. G. 2007. Determination of Size and Concentration of Gold Nanoparticles from UV−Vis Spectra. *Analytical Chemistry,* 79**,** 4215-4221.
HIBBERT, D. B. 1993. Introduction to electrochemistry. *Introduction to electrochemistry.* London: Macmillan Education UK.
HICKS, J. M., WONG, Z. Y., SCURR, D. J., SILMAN, N., JACKSON, S. K., MENDES, P. M., AYLOTT, J. W. & RAWSON, F. J. 2017. Tailoring the Electrochemical Properties of Carbon Nanotube Modified Indium Tin Oxide via in Situ Grafting of Aryl Diazonium. *Langmuir,* 33**,** 4924-4933.
HILLAIREAU, H. & COUVREUR, P. 2009. Nanocarriers' entry into the cell: relevance to drug delivery. *Cellular and Molecular Life Sciences,* 66**,** 2873-2896.
HIROTO, S., MIYAKE, Y. & SHINOKUBO, H. 2017. Synthesis and Functionalization of Porphyrins through Organometallic Methodologies. *Chemical Reviews,* 117**,** 2910-3043.
HOSTA-RIGAU, L., OLMEDO, I., ARBIOL, J., CRUZ, L. J., KOGAN, M. J. & ALBERICIO, F. 2010. Multifunctionalized Gold Nanoparticles with Peptides

Targeted to Gastrin-Releasing Peptide Receptor of a Tumor Cell Line. *Bioconjugate Chemistry,* 21**,** 1070-1078.
HU, X., ZHANG, Y., DING, T., LIU, J. & ZHAO, H. 2020. Multifunctional Gold Nanoparticles: A Novel Nanomaterial for Various Medical Applications and Biological Activities. *Frontiers in Bioengineering and Biotechnology,* 8.
HUANG, X. & EL-SAYED, M. A. 2010. Gold nanoparticles: Optical properties and implementations in cancer diagnosis and photothermal therapy. *Journal of Advanced Research,* 1**,** 13-28.
HUANG, Z., LIU, B. & LIU, J. 2020. Enhancing the peroxidase-like activity and stability of gold nanoparticles by coating a partial iron phosphate shell. *Nanoscale,* 12**,** 22467-22472.
IMBRAGUGLIO, D., GIOVANNOZZI, A. & ROSSI, A. 2013. *Nanometrology*.
IMESCH, P., SCHEINER, D., SZABO, E., FINK, D. & FEDIER, A. 2013. Conjugates of cytochrome c and antennapedia peptide activate apoptosis and inhibit proliferation of HeLa cancer cells. *Experimental and therapeutic medicine,* 6**,** 786-790.
IQBAL, M. A., MD, S., SAHNI, J. K., BABOOTA, S., DANG, S. & ALI, J. 2012. Nanostructured lipid carriers system: recent advances in drug delivery. *Journal of drug targeting,* 20**,** 813-830.
JAIN, A., GOSLING, J., LIU, S., WANG, H., STONE, E. M., CHAKRABORTY, S., JAYARAMAN, P.-S., SMITH, S., AMABILINO, D. B., FROMHOLD, M., LONG, Y.-T., PÉREZ-GARCÍA, L., TURYANSKA, L., RAHMAN, R. & RAWSON, F. J. 2023. Wireless electrical–molecular quantum signalling for cancer cell apoptosis. *Nature Nanotechnology*.
JAIN, A., TRINDADE, G. F., HICKS, J. M., POTTS, J. C., RAHMAN, R., HAGUE, R. J. M., AMABILINO, D. B., PÉREZ-GARCÍA, L. & RAWSON, F. J. 2021. Modulating the biological function of protein by tailoring the adsorption orientation on nanoparticles. *Journal of Colloid and Interface Science,* 587**,** 150-161.
JAIN, S., HIRST, D. G. & O'SULLIVAN, J. M. 2012. Gold nanoparticles as novel agents for cancer therapy. *The British journal of radiology,* 85**,** 101-113.
JAMES, N., COKER, R., TOMLINSON, D., HARRIS, J., GOMPELS, M., PINCHING, A. & STEWART, J. 1994. Liposomal doxorubicin (Doxil): an effective new treatment for Kaposi's sarcoma in AIDS. *Clinical oncology,* 6**,** 294-296.
JARA, N., MILÁN, N. S., RAHMAN, A., MOUHEB, L., BOFFITO, D. C., JEFFRYES, C. & DAHOUMANE, S. A. 2021. Photochemical Synthesis of Gold and Silver Nanoparticles-A Review. *Molecules,* 26.
JAZAYERI, M. H., AMANI, H., POURFATOLLAH, A. A., PAZOKI-TOROUDI, H. & SEDIGHIMOGHADDAM, B. 2016. Various methods of gold nanoparticles (GNPs) conjugation to antibodies. *Sensing and Bio-Sensing Research,* 9**,** 17-22.
JENSEN, P. S., CHI, Q., GRUMSEN, F. B., ABAD, J. M., HORSEWELL, A., SCHIFFRIN, D. J. & ULSTRUP, J. 2007. Gold nanoparticle assisted assembly of a heme protein for enhancement of long-range interfacial electron transfer. *The Journal of Physical Chemistry C,* 111**,** 6124-6132.
JEYARAM, A. & JAY, S. M. 2018. Preservation and storage stability of extracellular vesicles for therapeutic applications. *The AAPS journal,* 20**,** 1-7.
JO, Y., WOO, J. S., LEE, A. R., LEE, S. Y., SHIN, Y., LEE, L. P., CHO, M. L. & KANG, T. 2022. Inner-Membrane-Bound Gold Nanoparticles as Efficient

Electron Transfer Mediators for Enhanced Mitochondrial Electron Transport Chain Activity. *Nano Lett,* 22**,** 7927-7935.
JU, S. & YEO, W.-S. 2012. Quantification of proteins on gold nanoparticles by combining MALDI-TOF MS and proteolysis. *Nanotechnology,* 23**,** 135701.
KAGAN, V. E., BORISENKO, G. G., TYURINA, Y. Y., TYURIN, V. A., JIANG, J., POTAPOVICH, A. I., KINI, V., AMOSCATO, A. A. & FUJII, Y. 2004. Oxidative lipidomics of apoptosis: redox catalytic interactions of cytochrome c with cardiolipin and phosphatidylserine. *Free Radical Biology and Medicine,* 37**,** 1963-1985.
KAGAN, V. E., TYURIN, V. A., JIANG, J., TYURINA, Y. Y., RITOV, V. B., AMOSCATO, A. A., OSIPOV, A. N., BELIKOVA, N. A., KAPRALOV, A. A. & KINI, V. 2005. Cytochrome c acts as a cardiolipin oxygenase required for release of proapoptotic factors. *Nature chemical biology,* 1**,** 223-232.
KALIMUTHU, P., HEATH, M. D., SANTINI, J. M., KAPPLER, U. & BERNHARDT, P. V. 2014. Electrochemically driven catalysis of Rhizobium sp. NT-26 arsenite oxidase with its native electron acceptor cytochrome c552. *Biochimica et Biophysica Acta (BBA) - Bioenergetics,* 1837**,** 112-120.
KALIMUTHU, P. & JOHN, S. A. 2010. Studies on ligand exchange reaction of functionalized mercaptothiadiazole compounds onto citrate capped gold nanoparticles. *Materials Chemistry and Physics,* 122**,** 380-385.
KAPARA, A., BRUNTON, V., GRAHAM, D. & FAULDS, K. 2020. Investigation of cellular uptake mechanism of functionalised gold nanoparticles into breast cancer using SERS. *Chem Sci,* 11**,** 5819-5829.
KARAJIĆ, A., MERZEAU, P., SURANITI, E., GOUNEL, S., JAILLET, C., KUHN, A. & MANO, N. 2020. Enzymatic glucose-oxygen biofuel cells for highly efficient interfacial corrosion protection. *ACS Applied Energy Materials,* 3**,** 4441-4448.
KATHIRESAN, M. & ENGLISH, A. M. 2017. LC-MS/MS suggests that hole hopping in cytochrome c peroxidase protects its heme from oxidative modification by excess H 2 O 2. *Chemical Science,* 8**,** 1152-1162.
KATZ, E. & WILLNER, I. 2003. A biofuel cell with electrochemically switchable and tunable power output. *J Am Chem Soc,* 125**,** 6803-13.
KELEŞTEMUR, S., ALTUNBEK, M. & CULHA, M. 2017. Influence of EDC/NHS coupling chemistry on stability and cytotoxicity of ZnO nanoparticles modified with proteins. *Applied Surface Science,* 403**,** 455-463.
KELLY, K. L., CORONADO, E., ZHAO, L. L. & SCHATZ, G. C. 2003. The optical properties of metal nanoparticles: the influence of size, shape, and dielectric environment. ACS Publications.
KHALIL, C., MOUSSA, M., AZAR, A., TAWK, J., HABBOUCHE, J., SALAMEH, R., IBRAHIM, A. & ALAAEDDINE, N. 2019. Anti-proliferative effects of mesenchymal stem cells (MSCs) derived from multiple sources on ovarian cancer cell lines: an in-vitro experimental study. *Journal of Ovarian Research,* 12**,** 1-12.
KHAN, A., RASHID, R., MURTAZA, G. & ZAHRA, A. 2014. Gold nanoparticles: synthesis and applications in drug delivery. *Tropical journal of pharmaceutical research,* 13**,** 1169-1177.
KHAN, T., IGARASHI, K., TANABE, A., MIYAZAWA, T., FUKUSHIMA, S., MIURA, Y., MATSUMOTO, Y., YAMASOBA, T., MATSUMOTO, A., CABRAL, H. & KATAOKA, K. 2020. Structural Control of Boronic Acid

Ligands Enhances Intratumoral Targeting of Sialic Acid To Eradicate Cancer Stem-like Cells. *ACS Applied Bio Materials*.
KHOURY, R. A., RANASINGHE, J. C., DIKKUMBURA, A. S., HAMAL, P., KUMAL, R. R., KARAM, T. E., SMITH, H. T. & HABER, L. H. 2018. Monitoring the Seed-Mediated Growth of Gold Nanoparticles Using in Situ Second Harmonic Generation and Extinction Spectroscopy. *The Journal of Physical Chemistry C,* 122**,** 24400-24406.
KIM, Y., KANG, B., AHN, H. Y., SEO, J. & NAM, K. T. 2017. Plasmon Enhanced Fluorescence Based on Porphyrin-Peptoid Hybridized Gold Nanoparticle Platform. *Small,* 13.
KIMLING, J., MAIER, M., OKENVE, B., KOTAIDIS, V., BALLOT, H. & PLECH, A. 2006. Turkevich method for gold nanoparticle synthesis revisited. *J Phys Chem B,* 110**,** 15700-7.
KISIELIUTE, A., POPOV, A., APETREI, R.-M., CÂRÂC, G., MORKVENAITE-VILKONCIENE, I., RAMANAVICIENE, A. & RAMANAVICIUS, A. 2019. Towards microbial biofuel cells: Improvement of charge transfer by self-modification of microoganisms with conducting polymer–Polypyrrole. *Chemical Engineering Journal,* 356**,** 1014-1021.
KITT, J. P., BRYCE, D. A., MINTEER, S. D. & HARRIS, J. M. 2017. Raman Spectroscopy Reveals Selective Interactions of Cytochrome c with Cardiolipin That Correlate with Membrane Permeability. *Journal of the American Chemical Society,* 139**,** 3851-3860.
KOU, J., DOU, D. & YANG, L. 2017. Porphyrin photosensitizers in photodynamic therapy and its applications. *Oncotarget,* 8**,** 81591-81603.
KRPETIĆ, Ž., PORTA, F., CANEVA, E., DAL SANTO, V. & SCARÌ, G. 2010. Phagocytosis of Biocompatible Gold Nanoparticles. *Langmuir,* 26**,** 14799-14805.
KUHN, D. A., VANHECKE, D., MICHEN, B., BLANK, F., GEHR, P., PETRI-FINK, A. & ROTHEN-RUTISHAUSER, B. 2014. Different endocytotic uptake mechanisms for nanoparticles in epithelial cells and macrophages. *Beilstein Journal of Nanotechnology,* 5**,** 1625-1636.
KUILLA, T., BHADRA, S., YAO, D., KIM, N. H., BOSE, S. & LEE, J. H. 2010. Recent advances in graphene based polymer composites. *Progress in polymer science,* 35**,** 1350-1375.
KUMAR, D. R., MANOJ, D. & SANTHANALAKSHMI, J. 2014. Au–ZnO bullet-like heterodimer nanoparticles: synthesis and use for enhanced nonenzymatic electrochemical determination of glucose. *RSC Advances,* 4**,** 8943-8952.
KWIATKOWSKI, S., KNAP, B., PRZYSTUPSKI, D., SACZKO, J., KĘDZIERSKA, E., KNAP-CZOP, K., KOTLIŃSKA, J., MICHEL, O., KOTOWSKI, K. & KULBACKA, J. 2018. Photodynamic therapy – mechanisms, photosensitizers and combinations. *Biomedicine & Pharmacotherapy,* 106**,** 1098-1107.
LACERDA, S. H. D. P., PARK, J. J., MEUSE, C., PRISTINSKI, D., BECKER, M. L., KARIM, A. & DOUGLAS, J. F. 2010. Interaction of Gold Nanoparticles with Common Human Blood Proteins. *ACS Nano,* 4**,** 365-379.
LAKOWICZ, J. R. 1999. Instrumentation for fluorescence spectroscopy. *Principles of fluorescence spectroscopy***,** 25-61.
LAKOWICZ, J. R. 2007. *Principles of Fluorescence Spectroscopy,* Springer US.

LARSSON, S., RYDÉN, T., HOLST, U., OREDSSON, S. & JOHANSSON, M. 2008. Estimating the total rate of DNA replication using branching processes. *Bull Math Biol,* 70**,** 2177-94.
LAVAGNINI, I., ANTIOCHIA, R. & MAGNO, F. 2004. An Extended Method for the Practical Evaluation of the Standard Rate Constant from Cyclic Voltammetric Data. *Electroanalysis,* 16**,** 505-506.
LAWRENCE, A., JONES, C. M., WARDMAN, P. & BURKITT, M. J. 2003. Evidence for the role of a peroxidase compound I-type intermediate in the oxidation of glutathione, NADH, ascorbate, and dichlorofluorescin by cytochrome c/H2O2: implications for oxidative stress during apoptosis. *Journal of Biological Chemistry,* 278**,** 29410-29419.
LAWRENCE, K. P., DOUKI, T., SARKANY, R. P. E., ACKER, S., HERZOG, B. & YOUNG, A. R. 2018. The UV/Visible Radiation Boundary Region (385–405 nm) Damages Skin Cells and Induces "dark" Cyclobutane Pyrimidine Dimers in Human Skin in vivo. *Scientific Reports,* 8**,** 12722.
LEE, S., TAK, E., LEE, J., RASHID, M., MURPHY, M. P., HA, J. & KIM, S. S. 2011. Mitochondrial H2O2 generated from electron transport chain complex I stimulates muscle differentiation. *Cell research,* 21**,** 817-834.
LEMA, C., VARELA-RAMIREZ, A. & AGUILERA, R. J. 2011. Differential nuclear staining assay for high-throughput screening to identify cytotoxic compounds. *Curr Cell Biochem,* 1**,** 1-14.
LÉVY, R., SHAHEEN, U., CESBRON, Y. & SÉE, V. 2010. Gold nanoparticles delivery in mammalian live cells: a critical review. *Nano Rev,* 1.
LI, C., CHAI, O. J. H., YAO, Q., LIU, Z., WANG, L., WANG, H. & XIE, J. 2021a. Electrocatalysis of gold-based nanoparticles and nanoclusters. *Materials Horizons,* 8**,** 1657-1682.
LI, K., LI, Y., SHELTON, J. M., RICHARDSON, J. A., SPENCER, E., CHEN, Z. J., WANG, X. & WILLIAMS, R. S. 2000. Cytochrome c Deficiency Causes Embryonic Lethality and Attenuates Stress-Induced Apoptosis. *Cell,* 101**,** 389-399.
LI, S., ZHANG, L., WANG, T., LI, L., WANG, C. & SU, Z. 2015. The facile synthesis of hollow Au nanoflowers for synergistic chemo-photothermal cancer therapy. *Chemical Communications,* 51**,** 14338-14341.
LI, S. L., JIANG, P., JIANG, F. L. & LIU, Y. 2021b. Recent advances in nanomaterial-based nanoplatforms for chemodynamic cancer therapy. *Advanced Functional Materials,* 31**,** 2100243.
LIANG, S., DENG, X., MA, P. A., CHENG, Z. & LIN, J. 2020. Recent advances in nanomaterial-assisted combinational sonodynamic cancer therapy. *Advanced Materials,* 32**,** 2003214.
LIM, J., KOSTIAINEN, M., MALY, J., DA COSTA, V. C., ANNUNZIATA, O., PAVAN, G. M. & SIMANEK, E. E. 2013. Synthesis of large dendrimers with the dimensions of small viruses. *Journal of the American Chemical Society,* 135**,** 4660-4663.
LIM, Z.-Z. J., LI, J.-E. J., NG, C.-T., YUNG, L.-Y. L. & BAY, B.-H. 2011. Gold nanoparticles in cancer therapy. *Acta Pharmacologica Sinica,* 32**,** 983-990.
LINK, S. & EL-SAYED, M. A. 2000. Shape and size dependence of radiative, non-radiative and photothermal properties of gold nanocrystals. *International reviews in physical chemistry,* 19**,** 409-453.

LIU, C.-G., HAN, Y.-H., KANKALA, R. K., WANG, S.-B. & CHEN, A.-Z. 2020. Subcellular performance of nanoparticles in cancer therapy. *International Journal of Nanomedicine*, 675-704.

LIU, H., YAMAMOTO, H., WEI, J. & WALDECK, D. H. 2003. Control of the Electron Transfer Rate between Cytochrome c and Gold Electrodes by the Manipulation of the Electrode's Hydrogen Bonding Character. *Langmuir,* 19**,** 2378-2387.

LU, X.-Y., WU, D.-C., LI, Z.-J. & CHEN, G.-Q. 2011. Chpater 7 - Polymer Nanoparticles. *In:* VILLAVERDE, A. (ed.) *Progress in Molecular Biology and Translational Science.* Academic Press.

LUCKY, S. S., SOO, K. C. & ZHANG, Y. 2015. Nanoparticles in Photodynamic Therapy. *Chemical Reviews,* 115**,** 1990-2042.

LUM, C. T., WONG, A. S.-T., LIN, M. C. M., CHE, C.-M. & SUN, R. W.-Y. 2013. A gold(iii) porphyrin complex as an anti-cancer candidate to inhibit growth of cancer-stem cells. *Chemical Communications,* 49**,** 4364-4366.

LUO, L., WANG, H., TIAN, W., LI, X., ZHU, Z., HUANG, R. & LUO, H. 2021. Targeting ferroptosis-based cancer therapy using nanomaterials: strategies and applications. *Theranostics,* 11**,** 9937.

MA, X. & YU, H. 2006. Global burden of cancer. *The Yale journal of biology and medicine,* 79**,** 85-94.

MAITI, N. C., MAZUMDAR, S. & PERIASAMY, N. 1998. J- and H-Aggregates of Porphyrin−Surfactant Complexes: Time-Resolved Fluorescence and Other Spectroscopic Studies. *The Journal of Physical Chemistry B,* 102**,** 1528-1538.

MALEKIGORJI, M., HOSKINS, C., CURTIS, T. & VARBIRO, G. 2014. Enhancement of the cytotoxic effect of anticancer agent by cytochrome C functionalised hybrid nanoparticles in hepatocellular cancer cells. *Journal of Nanomedicine Research,* 1.

MALIK, S., MUHAMMAD, K. & WAHEED, Y. 2023. Nanotechnology: A Revolution in Modern Industry. *Molecules,* 28.

MANICKAM, P., KAUSHIK, A., KARUNAKARAN, C. & BHANSALI, S. 2017. Recent advances in cytochrome c biosensing technologies. *Biosensors and Bioelectronics,* 87**,** 654-668.

MASOOD, F. 2016. Polymeric nanoparticles for targeted drug delivery system for cancer therapy. *Materials Science and Engineering: C,* 60**,** 569-578.

MASOUDIPOUR, E., KASHANIAN, S. & MALEKI, N. 2017. A targeted drug delivery system based on dopamine functionalized nano graphene oxide. *Chemical Physics Letters,* 668**,** 56-63.

MATSUMOTO, A., STEPHENSON-BROWN, A. J., KHAN, T., MIYAZAWA, T., CABRAL, H., KATAOKA, K. & MIYAHARA, Y. 2017. Heterocyclic boronic acids display sialic acid selective binding in a hypoxic tumor relevant acidic environment. *Chem Sci,* 8**,** 6165-6170.

MAYERHÖFER, T. G., MUTSCHKE, H. & POPP, J. 2016. Employing Theories Far beyond Their Limits—The Case of the (Boguer-) Beer–Lambert Law. *ChemPhysChem,* 17**,** 1948-1955.

MCCLELLAND, L. J., MOU, T. C., JEAKINS-COOLEY, M. E., SPRANG, S. R. & BOWLER, B. E. 2014. Structure of a mitochondrial cytochrome c conformer competent for peroxidase activity. *Proc Natl Acad Sci U S A,* 111**,** 6648-53.

MELANCON, M. P., LU, W., ZHONG, M., ZHOU, M., LIANG, G., ELLIOTT, A. M., HAZLE, J. D., MYERS, J. N., LI, C. & STAFFORD, R. J. 2011.

Targeted multifunctional gold-based nanoshells for magnetic resonance-guided laser ablation of head and neck cancer. *Biomaterials,* 32**,** 7600-7608.
MÉNDEZ, J., MORALES CRUZ, M., DELGADO, Y., FIGUEROA, C. M., ORELLANO, E. A., MORALES, M., MONTEAGUDO, A. & GRIEBENOW, K. 2014. Delivery of chemically glycosylated cytochrome c immobilized in mesoporous silica nanoparticles induces apoptosis in HeLa cancer cells. *Molecular pharmaceutics,* 11**,** 102-111.
MENG, J., YANG, M., JIA, F., KONG, H., ZHANG, W., WANG, C., XING, J., XIE, S. & XU, H. 2010. Subcutaneous injection of water-soluble multi-walled carbon nanotubes in tumor-bearing mice boosts the host immune activity. *Nanotechnology,* 21**,** 145104.
MEZIADI, A., ZUBERI, N., DE HAAN, H. W. & GAUTHIER, M. A. 2022. Overcoming PEG─Protein Mutual Repulsion to Improve the Efficiency of PEGylation. *Biomacromolecules,* 23**,** 4948-4956.
MICHAELIDES, E. E. 2015. Brownian movement and thermophoresis of nanoparticles in liquids. *International Journal of Heat and Mass Transfer,* 81**,** 179-187.
MIDELET, J., EL-SAGHEER, A. H., BROWN, T., KANARAS, A. G. & WERTS, M. H. V. 2017. The Sedimentation of Colloidal Nanoparticles in Solution and Its Study Using Quantitative Digital Photography. *Particle & Particle Systems Characterization,* 34**,** 1700095.
MIESZAWSKA, A. J., MULDER, W. J. M., FAYAD, Z. A. & CORMODE, D. P. 2013. Multifunctional gold nanoparticles for diagnosis and therapy of disease. *Molecular pharmaceutics,* 10**,** 831-847.
MILES, D. T. & MURRAY, R. W. 2003. Temperature-Dependent Quantized Double Layer Charging of Monolayer-Protected Gold Clusters. *Analytical Chemistry,* 75**,** 1251-1257.
MILLO, D., RANIERI, A., GROSS, P., LY, H. K., BORSARI, M., HILDEBRANDT, P., WUITE, G. J. L., GOOIJER, C. & ZWAN, G. V. D. 2009. Electrochemical Response of Cytochrome c Immobilized on Smooth and Roughened Silver and Gold Surfaces Chemically Modified with 11-Mercaptounodecanoic Acid. *The Journal of Physical Chemistry C,* 113**,** 2861-2866.
MODY, V. V., SIWALE, R., SINGH, A. & MODY, H. R. 2010. Introduction to metallic nanoparticles. *J Pharm Bioallied Sci,* 2**,** 282-9.
MOHAMED, M. S., VEERANARAYANAN, S., POULOSE, A. C., NAGAOKA, Y., MINEGISHI, H., YOSHIDA, Y., MAEKAWA, T. & KUMAR, D. S. 2014. Type 1 ribotoxin-curcin conjugated biogenic gold nanoparticles for a multimodal therapeutic approach towards brain cancer. *Biochimica et Biophysica Acta (BBA) - General Subjects,* 1840**,** 1657-1669.
MOHAMMADI, A., MOGHADDAM, A. B., AHADI, S., DINARVAND, R. & KHODADADI, A. A. 2011. Application of cobalt oxide nanoparticles as an electron transfer facilitator in direct electron transfer and biocatalytic reactivity of cytochrome c. *Journal of Applied Electrochemistry,* 41**,** 115-121.
MOLINA, A., LABORDA, E., MARTÍNEZ-ORTIZ, F., BRADLEY, D. F., SCHIFFRIN, D. J. & COMPTON, R. G. 2011. Comparison between double pulse and multipulse differential techniques. 659**,** 12-24.
MONTIS, C., GENERINI, V., BOCCALINI, G., BERGESE, P., BANI, D. & BERTI, D. 2018. Model lipid bilayers mimic non-specific interactions of

gold nanoparticles with macrophage plasma membranes. *Journal of colloid and interface science,* 516**,** 284-294.
MOSLEH-SHIRAZI, S., ABBASI, M., MOADDELI, M. R., VAEZ, A., SHAFIEE, M., KASAEE, S. R., AMANI, A. M. & HATAM, S. 2022. Nanotechnology Advances in the Detection and Treatment of Cancer: An Overview. *Nanotheranostics,* 6**,** 400-423.
MOZAFARI, M. R. 2005. Liposomes: an overview of manufacturing techniques. *Cellular and molecular biology letters,* 10**,** 711.
MUKHA, I., KHODKO, A., VITYUK, N., SEVERYNOVSKA, O., PIVOVARENKO, V., KACHALOVA, N., SMIRNOVA, N. & EREMENKO, A. 2020. Light-driven formation of gold/tryptophan nanoparticles. *Applied Nanoscience,* 10**,** 2827-2833.
MUKHERJEE, S., MUKHERJEE, A., BHAGI-DAMODARAN, A., MUKHERJEE, M., LU, Y. & DEY, A. 2015. A biosynthetic model of cytochrome c oxidase as an electrocatalyst for oxygen reduction. *Nature communications,* 6**,** 8467-8467.
MUÑOZ, R., SINGH, D. P., KUMAR, R. & MATSUDA, A. 2019. Graphene oxide for drug delivery and cancer therapy. *Nanostructured polymer composites for biomedical applications***,** 447-488.
MURGIDA, D. H. & HILDEBRANDT, P. 2001. Active-Site Structure and Dynamics of Cytochrome c Immobilized on Self-Assembled Monolayers—A Time-Resolved Surface Enhanced Resonance Raman Spectroscopic Study. *Angewandte Chemie International Edition,* 40**,** 728-731.
MURPHY, M., THEYAGARAJAN, K., GANESAN, P., SENTHILKUMAR, S. & THENMOZHI, K. 2019. Electrochemical biosensor for the detection of hydrogen peroxide using cytochrome c covalently immobilized on carboxyl functionalized ionic liquid/multiwalled carbon nanotube hybrid. *Applied Surface Science,* 492**,** 718-725.
MURTHY, K. V. R. & VIRK, H. 2013. *Luminescence Phenomena: An Introduction*.
NAM, J., WON, N., JIN, H., CHUNG, H. & KIM, S. 2009. pH-Induced Aggregation of Gold Nanoparticles for Photothermal Cancer Therapy. *Journal of the American Chemical Society,* 131**,** 13639-13645.
NARDIN, S., MORA, E., VARUGHESE, F. M., D'AVANZO, F., VACHANARAM, A. R., ROSSI, V., SAGGIA, C., RUBINELLI, S. & GENNARI, A. 2020. Breast Cancer Survivorship, Quality of Life, and Late Toxicities. *Front Oncol,* 10**,** 864.
NEEVES, K. B., SAWYER, A. J., FOLEY, C. P., SALTZMAN, W. M. & OLBRICHT, W. L. 2007. Dilation and degradation of the brain extracellular matrix enhances penetration of infused polymer nanoparticles. *Brain research,* 1180**,** 121-132.
NEGAHDARY, M., RAD, S., NOUGHABI, M. T., SARZAEEM, A., NOUGHABI, S. P., MIRZAEINASAB, F., MAZDAPOUR, M. & AMRAEIFARD, S. 2012. Design a hydrogen peroxide biosensor by cytochrome c and cadmium oxide Nanoparticles and its application in diagnostic cancer cells. *Advanced Studies in Biology,* 4**,** 103-118.
NEJATI, K., DADASHPOUR, M., GHARIBI, T., MELLATYAR, H. & AKBARZADEH, A. 2022. Biomedical Applications of Functionalized Gold Nanoparticles: A Review. *Journal of Cluster Science,* 33**,** 1-16.
NIKZAMIR, M., HANIFEHPOUR, Y., AKBARZADEH, A. & PANAHI, Y. 2021. Applications of Dendrimers in Nanomedicine and Drug Delivery: A Review.

Journal of Inorganic and Organometallic Polymers and Materials, 31**,** 2246-2261.
NIZA, E., OCAÑA, A., CASTRO-OSMA, J. A., BRAVO, I. & ALONSO-MORENO, C. 2021. Polyester Polymeric Nanoparticles as Platforms in the Development of Novel Nanomedicines for Cancer Treatment. *Cancers,* 13**,** 3387.
NOIREAUX, J., GRALL, R., HULLO, M., CHEVILLARD, S., OSTER, C., BRUN, E., SICARD-ROSELLI, C., LOESCHNER, K. & FISICARO, P. 2019. Gold Nanoparticle Uptake in Tumor Cells: Quantification and Size Distribution by sp-ICPMS. *Separations,* 6**,** 3.
O'NEAL, D. P., HIRSCH, L. R., HALAS, N. J., PAYNE, J. D. & WEST, J. L. 2004. Photo-thermal tumor ablation in mice using near infrared-absorbing nanoparticles. *Cancer Letters,* 209**,** 171-176.
OH, N. & PARK, J. H. 2014. Endocytosis and exocytosis of nanoparticles in mammalian cells. *Int J Nanomedicine,* 9 Suppl 1**,** 51-63.
OUYANG, X., TELLI, M. L. & WU, J. C. 2019. Induced pluripotent stem cell-based cancer vaccines. *Frontiers in Immunology,* 10**,** 1510.
OVIEDO-ROUCO, S., PEREZ-BERTOLDI, J. M., SPEDALIERI, C., CASTRO, M. A., TOMASINA, F., TORTORA, V., RADI, R. & MURGIDA, D. H. 2020. Electron transfer and conformational transitions of cytochrome c are modulated by the same dynamical features. *Archives of Biochemistry and Biophysics,* 680**,** 108243.
OW, Y.-L. P., GREEN, D. R., HAO, Z. & MAK, T. W. 2008. Cytochrome c: functions beyond respiration. *Nature Reviews Molecular Cell Biology,* 9**,** 532.
OZGEN, P. S. O., ATASOY, S., KURT, B. Z., DURMUS, Z., YIGIT, G. & DAG, A. 2020. Glycopolymer decorated multiwalled carbon nanotubes for dual targeted breast cancer therapy. *Journal of materials chemistry B,* 8**,** 3123-3137.
PADMA, V. V. 2015. An overview of targeted cancer therapy. *BioMedicine,* 5**,** 1-6.
PANT, D., VAN BOGAERT, G., DIELS, L. & VANBROEKHOVEN, K. 2010. A review of the substrates used in microbial fuel cells (MFCs) for sustainable energy production. *Bioresource technology,* 101**,** 1533-1543.
PANYAM, J., DALI, M. M., SAHOO, S. K., MA, W., CHAKRAVARTHI, S. S., AMIDON, G. L., LEVY, R. J. & LABHASETWAR, V. 2003. Polymer degradation and in vitro release of a model protein from poly (D, L-lactide-co-glycolide) nano-and microparticles. *Journal of controlled release,* 92**,** 173-187.
PARK, S., LEE, W. J., PARK, S., CHOI, D., KIM, S. & PARK, N. 2019. Reversibly pH-responsive gold nanoparticles and their applications for photothermal cancer therapy. *Scientific Reports,* 9**,** 20180.
PATIL, T., GAMBHIR, R., VIBHUTE, A. & TIWARI, A. P. 2023. Gold Nanoparticles: Synthesis Methods, Functionalization and Biological Applications. *Journal of Cluster Science,* 34**,** 705-725.
PAWAR, S., BHATTACHARYA, A. & NAG, A. 2019. Metal-Enhanced Fluorescence Study in Aqueous Medium by Coupling Gold Nanoparticles and Fluorophores Using a Bilayer Vesicle Platform. *ACS Omega,* 4**,** 5983-5990.
PEDERSEN, R. N., ESEN, B. Ö., MELLEMKJÆR, L., CHRISTIANSEN, P., EJLERTSEN, B., LASH, T. L., NØRGAARD, M. & CRONIN-FENTON, D.

2021. The Incidence of Breast Cancer Recurrence 10-32 Years After Primary Diagnosis. *JNCI: Journal of the National Cancer Institute,* 114**,** 391-399.
PEGTEL, D. M. & GOULD, S. J. 2019. Exosomes. *Annual review of biochemistry,* 88**,** 487-514.
PESSOA, J. 2022. Cytochrome c in cancer therapy and prognosis. *Bioscience Reports,* 42.
PETROVIĆ, J., CLARK, R. A., YUE, H., WALDECK, D. H. & BOWDEN, E. F. 2005. Impact of Surface Immobilization and Solution Ionic Strength on the Formal Potential of Immobilized Cytochrome c. *Langmuir,* 21**,** 6308-6316.
PLOWMAN, B. J., MAHAJAN, M., O'MULLANE, A. P. & BHARGAVA, S. K. 2010. Electrochemical detection of dopamine and cytochrome c at a nanostructured gold electrode. *Electrochimica Acta,* 55**,** 8953-8959.
POCHAPSKI, D. J., CARVALHO DOS SANTOS, C., LEITE, G. W., PULCINELLI, S. H. & SANTILLI, C. V. 2021. Zeta Potential and Colloidal Stability Predictions for Inorganic Nanoparticle Dispersions: Effects of Experimental Conditions and Electrokinetic Models on the Interpretation of Results. *Langmuir,* 37**,** 13379-13389.
PONS, T., UYEDA, H. T., MEDINTZ, I. L. & MATTOUSSI, H. 2006. Hydrodynamic dimensions, electrophoretic mobility, and stability of hydrophilic quantum dots. *The Journal of Physical Chemistry B,* 110**,** 20308-20316.
POTTS, J. C., JAIN, A., AMABILINO, D. B., RAWSON, F. J. & PÉREZ-GARCÍA, L. 2023. Molecular Surface Quantification of Multifunctionalized Gold Nanoparticles Using UV–Visible Absorption Spectroscopy Deconvolution. *Analytical Chemistry*.
PTASZEK, M. 2013. Chapter Three - Rational Design of Fluorophores for In Vivo Applications. *In:* MORRIS, M. C. (ed.) *Progress in Molecular Biology and Translational Science.* Academic Press.
PUJALS, S., FERNÁNDEZ-CARNEADO, J., LÓPEZ-IGLESIAS, C., KOGAN, M. J. & GIRALT, E. 2006. Mechanistic aspects of CPP-mediated intracellular drug delivery: relevance of CPP self-assembly. *Biochim Biophys Acta,* 1758**,** 264-79.
QIAN, H., ZHU, M., WU, Z. & JIN, R. 2012. Quantum Sized Gold Nanoclusters with Atomic Precision. *Accounts of Chemical Research,* 45**,** 1470-1479.
QUINTANA, C., CIFUENTES, M. P. & HUMPHREY, M. G. 2020. Transition metal complex/gold nanoparticle hybrid materials. *Chemical Society Reviews,* 49**,** 2316-2341.
RAMALINGAM, V. 2019. Multifunctionality of gold nanoparticles: Plausible and convincing properties. *Advances in Colloid and Interface Science,* 271**,** 101989.
RAMANAVICIUS, A., KAUSAITE-MINKSTIMIENE, A., MORKVENAITE-VILKONCIENE, I., GENYS, P., MIKHAILOVA, R., SEMASHKO, T., VORONOVIC, J. & RAMANAVICIENE, A. 2015. Biofuel cell based on glucose oxidase from Penicillium funiculosum 46.1 and horseradish peroxidase. *Chemical Engineering Journal,* 264**,** 165-173.
RATTANAPINYOPITUK, K., SHIMADA, A., MORITA, T., SAKURAI, M., ASANO, A., HASEGAWA, T., INOUE, K. & TAKANO, H. 2014. Demonstration of the clathrin- and caveolin-mediated endocytosis at the maternal-fetal barrier in mouse placenta after intravenous administration of gold nanoparticles. *J Vet Med Sci,* 76**,** 377-87.

RIBEIRO, A. M., VEIGA, F. & FIGUEIRAS, A. 2017. Chapter 3 - Biodegradable polymeric nanostructures: design and advances in oral drug delivery for neurodegenerative disorders. *In:* ANDRONESCU, E. & GRUMEZESCU, A. M. (eds.) *Nanostructures for Oral Medicine.* Elsevier.

RODRIGUES, M., CALPENA, A. C., AMABILINO, D. B., RAMOS-LÓPEZ, D., DE LAPUENTE, J. & PÉREZ-GARCÍA, L. 2014. Water-soluble gold nanoparticles based on imidazolium gemini amphiphiles incorporating piroxicam. *RSC Advances,* 4**,** 9279-9287.

RODRIGUEZ-GARRAUS, A., AZQUETA, A., VETTORAZZI, A. & LOPEZ DE CERAIN, A. 2020. Genotoxicity of silver nanoparticles. *Nanomaterials,* 10**,** 251.

ROMANOVSKAIA, E., SLOVENSKÝ, P., KALANTARIAN, S. M., LAUNDRY-MOTTIAR, L., ROMANOVSKI, V., HALAMA, M., AUINGER, M. & HEDBERG, Y. S. 2022. Electrochemical Estimations of the Gold Nanoparticle Size Effect on Cysteine-Gold Oxidation. *Journal of The Electrochemical Society,* 169**,** 021501.

ROMINIYI, O., VANDERLINDEN, A., CLENTON, S. J., BRIDGEWATER, C., AL-TAMIMI, Y. & COLLIS, S. J. 2021. Tumour treating fields therapy for glioblastoma: current advances and future directions. *British Journal of Cancer,* 124**,** 697-709.

ROSSI, G. & MONTICELLI, L. 2016. Gold nanoparticles in model biological membranes: A computational perspective. *Biochimica et Biophysica Acta (BBA) - Biomembranes,* 1858**,** 2380-2389.

SABOURIAN, P., YAZDANI, G., ASHRAF, S. S., FROUNCHI, M., MASHAYEKHAN, S., KIANI, S. & KAKKAR, A. 2020. Effect of Physico-Chemical Properties of Nanoparticles on Their Intracellular Uptake. *International Journal of Molecular Sciences,* 21**,** 8019.

SAHAKYAN, N., HADDAD, A., RICHARDSON, S., FORCHA-ETIEUNDEM, V., CHRISTOPHER, L., ALHARBI, H. & CAMPBELL, R. 2017. Personalized Nanoparticles for Cancer Therapy: A Call for Greater Precision. *Anticancer Agents Med Chem,* 17**,** 1033-1039.

SAMAD, A., SULTANA, Y. & AQIL, M. 2007. Liposomal drug delivery systems: an update review. *Current drug delivery,* 4**,** 297-305.

SAMUKAITE BUBNIENE, U., ZUKAUSKAS, S., RATAUTAITE, V., VILKIENE, M., MOCKEVICIENE, I., LIUSTROVAITE, V., DROBYSH, M., LISAUSKAS, A., RAMANAVICIUS, S. & RAMANAVICIUS, A. 2022. Assessment of Cytochrome c and Chlorophyll a as Natural Redox Mediators for Enzymatic Biofuel Cells Powered by Glucose. *Energies,* 15**,** 6838.

SANDERSON, M. J., SMITH, I., PARKER, I. & BOOTMAN, M. D. 2014. Fluorescence microscopy. *Cold Spring Harb Protoc,* 2014**,** pdb.top071795.

SANJUAN-ALBERTE, P., ALEXANDER, M. R., HAGUE, R. J. M. & RAWSON, F. J. 2018. Electrochemically stimulating developments in bioelectronic medicine. 4**,** 1.

SANJUAN-ALBERTE, P., JAIN, A., SHAW, A. J., ABAYZEED, S. A., DOMÍNGUEZ, R. F., ALEA-REYES, M. E., CLARK, M., ALEXANDER, M. R., HAGUE, R. J. M., PÉREZ-GARCÍA, L. & RAWSON, F. J. 2019. Wireless Nanobioelectronics for Electrical Intracellular Sensing. *ACS Applied Nano Materials,* 2**,** 6397-6408.

SANTRA, S., KAITTANIS, C. & PEREZ, J. M. 2010. Cytochrome C encapsulating theranostic nanoparticles: a novel bifunctional system for targeted delivery of therapeutic membrane-impermeable proteins to tumors and imaging of cancer therapy. *Molecular pharmaceutics,* 7**,** 1209-1222.

SCHÄFFLER, M., SOUSA, F., WENK, A., SITIA, L., HIRN, S., SCHLEH, C., HABERL, N., VIOLATTO, M., CANOVI, M., ANDREOZZI, P., SALMONA, M., BIGINI, P., KREYLING, W. G. & KROL, S. 2014. Blood protein coating of gold nanoparticles as potential tool for organ targeting. *Biomaterials,* 35**,** 3455-66.

SCHIRRMACHER, V. 2019. From chemotherapy to biological therapy: A review of novel concepts to reduce the side effects of systemic cancer treatment (Review). *International journal of oncology,* 54**,** 407-419.

SCHLESINGER, M. 2008. Modern Applications of Electrochemical Technology. *In:* VAYENAS, C. G., WHITE, R. E. & GAMBOA-ALDECO, M. E. (eds.) *Modern Aspects of Electrochemistry.* New York, NY: Springer New York.

SCOLARO, L. M., ROMEO, A., CASTRICIANO, M. A. & MICALI, N. 2005. Unusual optical properties of porphyrin fractal J-aggregates. *Chemical Communications***,** 3018-3020.

SELMI, M., BIN DUKHYIL, A. A. & BELMABROUK, H. 2019. Numerical analysis of human cancer therapy using microwave ablation. *Applied Sciences,* 10**,** 211.

SENAPATI, S., MAHANTA, A. K., KUMAR, S. & MAITI, P. 2018. Controlled drug delivery vehicles for cancer treatment and their performance. 3**,** 7.

SHARMA, B., JAIN, A., PÉREZ-GARCÍA, L., WATTS, J. A., RAWSON, F. J., CHAUDHARY, G. R. & KAUR, G. 2022. Metallocatanionic vesicle-mediated enhanced singlet oxygen generation and photodynamic therapy of cancer cells. *Journal of Materials Chemistry B,* 10**,** 2160-2170.

SHEORAN, S., ARORA, S., SAMSONRAJ, R., GOVINDAIAH, P. & VUREE, S. 2022. Lipid-based nanoparticles for treatment of cancer. *Heliyon,* 8**,** e09403.

SHI, L., ZHANG, J., ZHAO, M., TANG, S., CHENG, X., ZHANG, W., LI, W., LIU, X., PENG, H. & WANG, Q. 2021. Effects of polyethylene glycol on the surface of nanoparticles for targeted drug delivery. *Nanoscale,* 13**,** 10748-10764.

SHILO, M., MOTIEI, M., HANA, P. & POPOVTZER, R. 2014. Transport of nanoparticles through the blood–brain barrier for imaging and therapeutic applications. *Nanoscale,* 6**,** 2146-2152.

SIGGEL, U., BINDIG, U., ENDISCH, C., KOMATSU, T., TSUCHIDA, E., VOIGT, J. & FUHRHOP, J.-H. 1996. Photophysical and photochemical properties of porphyrin aggregates. *Berichte der Bunsengesellschaft für physikalische Chemie,* 100**,** 2070-2075.

SIMON, J., FLAHAUT, E. & GOLZIO, M. 2019. Overview of Carbon Nanotubes for Biomedical Applications. *Materials,* 12**,** 624.

SKOOG, D. A., HOLLER, F. J. & CROUCH, S. R. 2007. *Principles of Instrumental Analysis,* Thomson Brooks/Cole.

SLEE, E. A., HARTE, M. T., KLUCK, R. M., WOLF, B. B., CASIANO, C. A., NEWMEYER, D. D., WANG, H.-G., REED, J. C., NICHOLSON, D. W., ALNEMRI, E. S., GREEN, D. R. & MARTIN, S. J. 1999. Ordering the Cytochrome c–initiated Caspase Cascade: Hierarchical Activation of Caspases-2, -3, -6, -7, -8, and -10 in a Caspase-9–dependent Manner. *Journal of Cell Biology,* 144**,** 281-292.

SLOWING, I. I., TREWYN, B. G. & LIN, V. S. Y. 2007. Mesoporous Silica Nanoparticles for Intracellular Delivery of Membrane-Impermeable Proteins. *Journal of the American Chemical Society,* 129**,** 8845-8849.

SONG, J., LU, C., LESZEK, J. & ZHANG, J. 2021. Design and Development of Nanomaterial-Based Drug Carriers to Overcome the Blood–Brain Barrier by Using Different Transport Mechanisms. *International Journal of Molecular Sciences,* 22**,** 10118.

SOUSA DE ALMEIDA, M., SUSNIK, E., DRASLER, B., TALADRIZ-BLANCO, P., PETRI-FINK, A. & ROTHEN-RUTISHAUSER, B. 2021. Understanding nanoparticle endocytosis to improve targeting strategies in nanomedicine. *Chemical Society Reviews,* 50**,** 5397-5434.

SOUSA, F., MANDAL, S., GARROVO, C., ASTOLFO, A., BONIFACIO, A., LATAWIEC, D., MENK, R. H., ARFELLI, F., HUEWEL, S., LEGNAME, G., GALLA, H.-J. & KROL, S. 2010. Functionalized gold nanoparticles: a detailed in vivo multimodal microscopic brain distribution study. *Nanoscale,* 2**,** 2826-2834.

SOUSA, L. M., VILARINHO, L. M., RIBEIRO, G. H., BOGADO, A. L. & DINELLI, L. R. 2017. An electronic device based on gold nanoparticles and tetraruthenated porphyrin as an electrochemical sensor for catechol. *Royal Society open science,* 4**,** 170675.

SOUZA, L. R. R., DA SILVA, V. S., FRANCHI, L. P. & DE SOUZA, T. A. J. 2018. Toxic and beneficial potential of silver nanoparticles: the two sides of the same coin. *Cellular and molecular toxicology of nanoparticles***,** 251-262.

SREERAMA, N., VENYAMINOV, S. Y. & WOODY, R. W. 2000. Estimation of Protein Secondary Structure from Circular Dichroism Spectra: Inclusion of Denatured Proteins with Native Proteins in the Analysis. *Analytical Biochemistry,* 287**,** 243-251.

SRIVASTAVA, S., FRANKAMP, B. L. & ROTELLO, V. M. 2005. Controlled plasmon resonance of gold nanoparticles self-assembled with PAMAM dendrimers. *Chemistry of materials,* 17**,** 487-490.

STONE, J., JACKSON, S. & WRIGHT, D. 2011. Biological applications of gold nanorods. *WIREs Nanomedicine and Nanobiotechnology,* 3**,** 100-109.

SU, K.-H., WEI, Q.-H., ZHANG, X., MOCK, J., SMITH, D. R. & SCHULTZ, S. 2003. Interparticle coupling effects on plasmon resonances of nanogold particles. *Nano letters,* 3**,** 1087-1090.

SU, Y.-H., KE, Y.-F., CAI, S.-L. & YAO, Q.-Y. 2012. Surface plasmon resonance of layer-by-layer gold nanoparticles induced photoelectric current in environmentally-friendly plasmon-sensitized solar cell. *Light: Science & Applications,* 1**,** e14-e14.

SUN, S., MENDES, P., CRITCHLEY, K., DIEGOLI, S., HANWELL, M., EVANS, S. D., LEGGETT, G. J., PREECE, J. A. & RICHARDSON, T. H. 2006. Fabrication of Gold Micro- and Nanostructures by Photolithographic Exposure of Thiol-Stabilized Gold Nanoparticles. *Nano Letters,* 6**,** 345-350.

SZTANDERA, K., GORZKIEWICZ, M. & KLAJNERT-MACULEWICZ, B. 2019. Gold Nanoparticles in Cancer Treatment. *Molecular Pharmaceutics,* 16**,** 1-23.

SZUNERITS, S., SPADAVECCHIA, J. & BOUKHERROUB, R. 2014. Surface plasmon resonance: signal amplification using colloidal gold nanoparticles for enhanced sensitivity. *Reviews in Analytical Chemistry,* 33**,** 153-164.

TAGHDISI, S. M., DANESH, N. M., LAVAEE, P., EMRANI, A. S., HASSANABAD, K. Y., RAMEZANI, M. & ABNOUS, K. 2016. Double targeting, controlled release and reversible delivery of daunorubicin to cancer cells by polyvalent aptamers-modified gold nanoparticles. *Mater Sci Eng C Mater Biol Appl,* 61**,** 753-61.

TARPANI, L., BELLEZZA, F., SASSI, P., GAMBUCCI, M., CIPICIANI, A. & LATTERINI, L. 2019. New Insights on the Effects of Surface Functionalization on the Peroxidase Activity of Cytochrome c Adsorbed on Silica Nanoparticles. *The Journal of Physical Chemistry B*.

THAMBILIYAGODAGE, C. 2022. Ligand exchange reactions and PEG stabilization of gold nanoparticles. *Current Research in Green and Sustainable Chemistry,* 5**,** 100245.

TODERAS, F., BAIA, M., MANIU, D. & ASTILEAN, S. 2008. Tuning the plasmon resonances of gold nanoparticles by controlling their size and shape. *Journal of optoelectronics and advanced materials,* 10**,** 2282-2284.

TOLLEFSON, E. J., ALLEN, C. R., CHONG, G., ZHANG, X., ROZANOV, N. D., BAUTISTA, A., CERDA, J. J., PEDERSEN, J. A., MURPHY, C. J., CARLSON, E. E. & HERNANDEZ, R. 2019. Preferential Binding of Cytochrome c to Anionic Ligand-Coated Gold Nanoparticles: A Complementary Computational and Experimental Approach. *ACS Nano,* 13**,** 6856-6866.

TOMASETTI, L. & BREUNIG, M. 2018. Preventing obstructions of nanosized drug delivery systems by the extracellular matrix. *Advanced healthcare materials,* 7**,** 1700739.

TORCHILIN, V. P. 2005. Recent advances with liposomes as pharmaceutical carriers. *Nature reviews Drug discovery,* 4**,** 145-160.

TRABBIC, K. R., KLESKI, K. A. & BARCHI, J. J. 2021. Stable Gold-Nanoparticle-Based Vaccine for the Targeted Delivery of Tumor-Associated Glycopeptide Antigens. *ACS Bio & Med Chem Au,* 1**,** 31-43.

TSOLEKILE, N., NAHLE, S., ZIKALALA, N., PARANI, S., SAKHO, E. H. M., JOUBERT, O., MATOETOE, M. C., SONGCA, S. P. & OLUWAFEMI, O. S. 2020. Cytotoxicity, fluorescence tagging and gene-expression study of CuInS/ZnS QDS - meso (hydroxyphenyl) porphyrin conjugate against human monocytic leukemia cells. *Scientific Reports,* 10**,** 4936.

TSUKUDA, T. 2012. Toward an Atomic-Level Understanding of Size-Specific Properties of Protected and Stabilized Gold Clusters. *Bulletin of the Chemical Society of Japan,* 85**,** 151-168.

TURKEVICH, J., STEVENSON, P. C. & HILLIER, J. 1951. A study of the nucleation and growth processes in the synthesis of colloidal gold. *Discussions of the Faraday Society,* 11**,** 55-75.

VAN TRAN, V., MOON, J.-Y. & LEE, Y.-C. 2019. Liposomes for delivery of antioxidants in cosmeceuticals: Challenges and development strategies. *Journal of Controlled Release,* 300**,** 114-140.

VEITCH, N. C. 2004. Horseradish peroxidase: a modern view of a classic enzyme. *Phytochemistry,* 65**,** 249-259.

VELASCO-AGUIRRE, C., MORALES, F., GALLARDO-TOLEDO, E., GUERRERO, S., GIRALT, E., ARAYA, E. & KOGAN, M. J. 2015. Peptides and proteins used to enhance gold nanoparticle delivery to the brain: preclinical approaches. *International journal of nanomedicine,* 10**,** 4919.

VENTON, B. J. & DISCENZA, D. J. 2020. Chapter 3 - Voltammetry. *In:* PATEL, B. (ed.) *Electrochemistry for Bioanalysis.* Elsevier.
VILLARREAL, E., LI, G. G., ZHANG, Q., FU, X. & WANG, H. 2017. Nanoscale Surface Curvature Effects on Ligand–Nanoparticle Interactions: A Plasmon-Enhanced Spectroscopic Study of Thiolated Ligand Adsorption, Desorption, and Exchange on Gold Nanoparticles. *Nano Letters,* 17**,** 4443-4452.
VINOGRADOV, S. & ZAND, R. 1968. Circular dichroism studies: I. Cytochrome c. *Archives of biochemistry and biophysics,* 125**,** 902-910.
VOLKOV, A. N., NICHOLLS, P. & WORRALL, J. A. 2011. The complex of cytochrome c and cytochrome c peroxidase: the end of the road? *Biochimica et Biophysica Acta (BBA)-Bioenergetics,* 1807**,** 1482-1503.
VOLLATH, D., FISCHER, F. D. & HOLEC, D. 2018. Surface energy of nanoparticles - influence of particle size and structure. *Beilstein J Nanotechnol,* 9**,** 2265-2276.
WAN, P., WANG, Y., JIANG, Y., XU, H. & ZHANG, X. 2009. Fabrication of Reactivated Biointerface for Dual-Controlled Reversible Immobilization of Cytochrome c. *Advanced Materials,* 21**,** 4362-4365.
WANG, H., JOHS, A., BROWNING, J. F., TENNANT, D. A. & LIANG, L. 2019. Electrochemical properties of the interaction between cytochrome c and a hematite nanowire array electrode. *Bioelectrochemistry,* 129**,** 162-169.
WANG, R., LV, Q., MENG, W., TAN, Q., ZHANG, S., MO, X. & YANG, X. 2014. Comparison of mammosphere formation from breast cancer cell lines and primary breast tumors. *J Thorac Dis,* 6**,** 829-37.
WANG, S.-H., LEE, C.-W., CHIOU, A. & WEI, P.-K. 2010. Size-dependent endocytosis of gold nanoparticles studied by three-dimensional mapping of plasmonic scattering images. *Journal of Nanobiotechnology,* 8**,** 33.
WANG, Z., TIRUPPATHI, C., MINSHALL, R. D. & MALIK, A. B. 2009. Size and Dynamics of Caveolae Studied Using Nanoparticles in Living Endothelial Cells. *ACS Nano,* 3**,** 4110-4116.
WEINER, A. L. 1994. Liposomes for protein delivery: selecting manufacture and development processes. *Immunomethods,* 4**,** 201-209.
WEINKAM, P., ZIMMERMANN, J. R., ROMESBERG, F. E. & WOLYNES, P. G. 2010. The folding energy landscape and free energy excitations of cytochrome c. *Accounts of chemical research,* 43**,** 652-660.
WELLER, M., OVERTON, T., ROURKE, J. & ARMSTRONG, F. 2014. *Inorganic Chemistry*, OUP Oxford.
WHITE, D. R. 1990. Standard potential of the silver-silver chloride electrode and mean activity coefficient of hydrochloric acid in 10 wt% sucrose/water from 0 to 25°C. *Food Chemistry,* 37**,** 1-11.
WILSCHEFSKI, S. C. & BAXTER, M. R. 2019. Inductively Coupled Plasma Mass Spectrometry: Introduction to Analytical Aspects. *Clin Biochem Rev,* 40**,** 115-133.
WILSON, B. K. & PRUD'HOMME, R. K. 2021. Nanoparticle size distribution quantification from transmission electron microscopy (TEM) of ruthenium tetroxide stained polymeric nanoparticles. *Journal of Colloid and Interface Science,* 604**,** 208-220.
WRIGHT, S. J. & WRIGHT, D. J. 2002. Chapter 1 - Introduction to Confocal Microscopy. *In:* MATSUMOTO, B. (ed.) *Methods in Cell Biology.* Academic Press.

XIAO, T., HUANG, J., WANG, D., MENG, T. & YANG, X. 2020. Au and Au-Based nanomaterials: Synthesis and recent progress in electrochemical sensor applications. *Talanta,* 206**,** 120210.
XIE, X., LIAO, J., SHAO, X., LI, Q. & LIN, Y. 2017. The Effect of shape on Cellular Uptake of Gold Nanoparticles in the forms of Stars, Rods, and Triangles. *Scientific Reports,* 7**,** 3827.
XU, G. & CHANCE, M. R. 2007. Hydroxyl radical-mediated modification of proteins as probes for structural proteomics. *Chemical reviews,* 107**,** 3514-3543.
XU, M., MCCANNA, D. J. & SIVAK, J. G. 2015. Use of the viability reagent PrestoBlue in comparison with alamarBlue and MTT to assess the viability of human corneal epithelial cells. *Journal of Pharmacological and Toxicological Methods,* 71**,** 1-7.
XU, X., TIAN, B., KONG, J., ZHANG, S., LIU, B. & ZHAO, D. 2003. Ordered mesoporous niobium oxide film: a novel matrix for assembling functional proteins for bioelectrochemical applications. *Advanced Materials,* 15**,** 1932-1936.
YADAV, N., KHATAK, S. & SARA, U. S. 2013. Solid lipid nanoparticles-a review. *Int. J. Appl. Pharm,* 5**,** 8-18.
YAGATI, A. K., LEE, T., MIN, J. & CHOI, J.-W. 2012. Electrochemical performance of gold nanoparticle–cytochrome c hybrid interface for H2O2 detection. *Colloids and Surfaces B: Biointerfaces,* 92**,** 161-167.
YANG, N. J. & HINNER, M. J. 2015. Getting across the cell membrane: an overview for small molecules, peptides, and proteins. *Methods Mol Biol,* 1266**,** 29-53.
YEH, Y.-C., CRERAN, B. & ROTELLO, V. M. 2012. Gold nanoparticles: preparation, properties, and applications in bionanotechnology. *Nanoscale,* 4**,** 1871-1880.
YIN, V., SHAW, G. S. & KONERMANN, L. 2017. Cytochrome c as a Peroxidase: Activation of the Precatalytic Native State by H2O2-Induced Covalent Modifications. *Journal of the American Chemical Society,* 139**,** 15701-15709.
YIN, Y., WU, P., LÜ, Y., DU, P., SHI, Y. & CAI, C. 2007. Immobilization and direct electrochemistry of cytochrome c at a single-walled carbon nanotube-modified electrode. *Journal of Solid State Electrochemistry,* 11**,** 390-397.
YUAN, W., ZHANG, J., SHEN, P. K. & LI, C. M. 2016. Self-assembled CeO2 on carbon nanotubes supported Au nanoclusters as superior electrocatalysts for glycerol oxidation reaction of fuel cells. *Electrochimica Acta,* 190**,** 817-828.
ZENG, J., YANG, W., SHI, D., LI, X., ZHANG, H. & CHEN, M. 2018. Porphyrin Derivative Conjugated with Gold Nanoparticles for Dual-Modality Photodynamic and Photothermal Therapies In Vitro. *ACS Biomaterials Science & Engineering,* 4**,** 963-972.
ZHANG, J., HUANG, Z., XIE, Y. & JIANG, X. 2022. Modulating the catalytic activity of gold nanoparticles using amine-terminated ligands. *Chemical Science,* 13**,** 1080-1087.
ZHANG, L., GU, F., CHAN, J., WANG, A., LANGER, R. & FAROKHZAD, O. 2008. Nanoparticles in medicine: therapeutic applications and developments. *Clinical pharmacology & therapeutics,* 83**,** 761-769.

ZHANG, L., HU, D., SALMAIN, M., LIEDBERG, B. & BOUJDAY, S. 2019. Direct quantification of surface coverage of antibody in IgG-Gold nanoparticles conjugates. *Talanta,* 204**,** 875-881.
ZHANG, Q., LI, R.-X., CHEN, X., HE, X.-X., HAN, A.-L., FANG, G.-Z., LIU, J.-F. & WANG, S. 2017. Study of Efficiency of Coupling Peptides with Gold Nanoparticles. *Chinese Journal of Analytical Chemistry,* 45**,** 662-667.
ZHAO, M.-X., CAI, Z.-C., ZHU, B.-J. & ZHANG, Z.-Q. 2018. The Apoptosis Effect on Liver Cancer Cells of Gold Nanoparticles Modified with Lithocholic Acid. *Nanoscale research letters,* 13**,** 304-304.
ZHIVOTOVSKY, B., ORRENIUS, S., BRUSTUGUN, O. T. & DØSKELAND, S. O. 1998. Injected cytochrome c induces apoptosis. *Nature,* 391**,** 449-450.
ZHU, A., TIAN, Y., LIU, H. & LUO, Y. 2009. Nanoporous gold film encapsulating cytochrome c for the fabrication of a H2O2 biosensor. *Biomaterials,* 30**,** 3183-3188.
ZIELIŃSKA, A., CARREIRÓ, F., OLIVEIRA, A. M., NEVES, A., PIRES, B., VENKATESH, D. N., DURAZZO, A., LUCARINI, M., EDER, P., SILVA, A. M., SANTINI, A. & SOUTO, E. B. 2020. Polymeric Nanoparticles: Production, Characterization, Toxicology and Ecotoxicology. *Molecules,* 25.
ZOLGHADR, A. R. & MOOSAVI, S. S. 2019. Interactions of neutral gold nanoparticles with DPPC and POPC lipid bilayers: simulation and experiment. *RSC Adv,* 9**,** 5197-5205.